Vortex Dynamics and Superconducting Phase Diagrams in Ta_xGe_{1-x}/Ge Multilayers with Coplanar Defects

by

Andreas Engel

A thesis
submitted to the Victoria University of Wellington
in fulfilment of the requirements for the degree of
Doctor of Philosophy
in Physics

Victoria University of Wellington
August 2001

"Curiosity is a delicate little plant which, aside from stimulation, stands mainly in need of freedom."

Albert Einstein

Thesis typeset using LaTeX2ε

Abstract

The superconducting phase diagrams of amorphous multilayered Ta_xGe_{1-x}/Ge thin films have been studied over a large range of temperatures and magnetic fields by means of dc electrical transport measurements. These superconducting films belong to the class of extremely type-II superconductors, for which a multitude of superconducting phases has been predicted and experimentally verified. A thorough understanding of these phase diagrams is indispensable for future successful applications of high-temperature superconductors since some of the observed phases severely limit the zero-resistance current-carrying capacity of these materials. The Ta_xGe_{1-x}/Ge films in this study were prepared by vapour deposition under high vacuum conditions. The Ta-content varied between $x = 0.31$ and 0.37 and individual layer thicknesses ranged from about 3 to 15 nm. Tilting the sample substrates during the deposition resulted in coplanar defects with variable orientation and structure depending on the tilting angle. This way it was possible to study the interplay between magnetic flux lines and the material structure and defect morphology, respectively. Films with thin insulating Ge layers and thus strong interlayer coupling showed three dimensional behaviour over the complete range of fields and temperatures. The coplanar defect structure was able to extend the zero-resistance phase to significantly higher fields and temperatures for magnetic fields co-aligned with the defects. Strong support for the existence of a low-temperature glass phase was found in the case of aligned and misaligned magnetic fields. Increasing the insulating layer thickness lead to a cross-over to 2D behaviour depending on temperature and field as well as field orientation with respect to the defects. In the 2D phase regions the low-temperature zero-resistance glass phase may have disappeared entirely. Current-voltage characteristics measured in the low-temperature glass phases showed significant differences between the strongly and weakly coupled films. However the detailed temperature and field dependence of these current-voltage curves at low temperatures cannot be explained satisfactorily with existing theoretical models.

This page is intentionally left blank.

Acknowledgements

It is my pleasure to thank all the people who were involved in this project and helped me one way or the other during the process of gathering the data and writing it all up. Most and above all, I would like to thank my supervisor Prof. Joe Trodahl for offering me this project and his advice and encouragement over the whole period it took me to complete this research. Generous financial support by Victoria University was greatly appreciated. Thank you very much as well to Prof. John Abele and his students for taking a considerable amount of the data in Portland, and especially for his hospitality and good company during my stays in Portland and Dave Smith for his great help in the lab.

Prof. Paul Munroe and Sergey Rubanov from the Electron Microscope Unit at the University of New South Wales in Australia helped a great deal to elucidate the microscopic structure of the films with their fantastic TEM images, and Andreas Markwitz and John Kennedy from the Institute of Geological and Nuclear Sciences in New Zealand were very cooperative in performing RBS measurements in order to determine the chemical composition. A big thank you goes to the staff at Victoria University who helped with many of the more technical issues encountered, too many to name them all, although one stands out: Alan Rennie who was always there to help as much as he could. Big support came also from the Materials Physics Group at Industrial Research, thanks especially to Bob Buckley as the most important contact person and source of advice at IRL, Ross Exley for helping to prepare the TEM samples, Jock Sinclair for many 100 liters of liquid helium, and Ursula Muavae for her help printing this thesis.

Many thanks to my fellow students, most of all to Olly Pantoja and Neil Kemp; it was my privilege to share an office room with them, and Olly was always a good resource when it came to solving computer problems. Special thanks to Ben Ruck for introducing me into the mysterious physics of vortices in TaGe during the final weeks of his PhD project and also for his very critical but extremely helpful reading of the theory and results chapters. And I would like to thank everybody else who read parts of the manuscript and corrected many of the spelling, grammar and style errors, but have not been acknowledged by name so far: Ocean Mercier, Darryl Squires, and Kim Rupp.

Last but not least, I would like to say thank you to my parents and family. After all, it was their support and belief in my abilities that enabled me to study physics and pursue a carrier in science.

This page is intentionally left blank.

Contents

List of Figures

List of Tables

List of Symbols

symbol	description
a	numerical constant
a_0	vortex separation
AC	anti-columnar direction
$\vec{B}, B$	magnetic flux density
B_{sb}, B_{lb}	small (sb) and large (lb) bundle lower field boundary
b	numerical constant
C	columnar direction
$c, \tilde{c}$	general constant
c_L	Lindemann number
D	dimension
d	superconducting layer separation
$d_{\mathrm{i}}, d_{\mathrm{sc}},$	thickness of insulating and superconducting layers
d_{tot}	total film thickness
$\vec{E}, E$	electric field (vector, norm)
E_0, E_1	projectile energies before and after scattering
E_k	vortex kink energy
$\mathcal{E}_{\mathrm{pin}}$	pinning energy
$\mathcal{E}_{\pm}$	vortex glass scaling functions
e	electron charge
$F_{\mathrm{2D}}, F_{\mathrm{3D}}$	universal functions fluctuation conductivity
F_L, f_L	Lorentz force, per unit length
$\mathcal{F}$	free energy functional
$\mathcal{F}_{\pm}$	Bose-glass scaling functions
f_{pin}	pinning strength
G_{VG}	vortex glass correlation function
$\mathcal{G}_{\pm}$	Bose-glass angular scaling functions
Gi	Ginzburg number
$\vec{H}, H$	magnetic field (vector, norm)
H_c	thermodynamic critical field
H_{c1}	lower critical field
H_{c2}	upper critical field
$H_{c2\perp}, H_{c2\parallel}$	perpendicular and parallel upper critical field

symbol	description
h	Planck's constant
I	electric current
I_x	cross-over current
$\vec{J}, J$	current density
$\vec{J}_s, J_s$	superconducting current density
J_c	critical current density
J_0	depairing current density
J_c, J_c^{sv}	critical current density, single vortex
J_x	cross-over current density
K	kinematic factor
k_B	Boltzmann constant
L	length of vortex segment
L_c, L_c^{sv}	collective pinning length, for single vortex
l	conduction path length, mean free path
l_{el}, l_{in}	elastic and inelastic mean free path
$l_\perp, l_\parallel$	transverse and longitudinal wandering length
M, m	effective mass in uniaxial systems
M_P, M_T	mass of projectile and target atom, resp.
m_e	electron mass
m_x, m_y, m_z	effective mass along crystallographic x, y, z-direction
$m_{\mu\nu}$	effective mass tensor
$N_{\mathrm{Ta}}, N_{\mathrm{Ge}}$	number of atoms per area for Ta and Ge
n_e	electron density
n_i	defect density
n_s	number density of superconducting charge carriers
p	pressure
R	resistance
R_c	vortex bundle correlation length
$\vec{r}, r$	space coordinate (2D and 3D)
r_{cr}	dimensional cross-over ratio
s	gradient of upper critical field
T	temperature
T_{BG}	Bose-glass melting temperature
$T_c, T_c(0)$	critical temperature in zero magnetic field
T_{cr}	dimensional cross-over temperature
T_{dp}	depinning temperature
T_g	vortex glass melting temperature
T_m	melting temperature
T_λ	superfluid transition temperature of liquid ^{4}He
t	reduced temperature, backscattering depth
$t_{\mathrm{Ta}}, t_{\mathrm{Ge}}$	evaporation time for Ta and Ge
U, U_c	pinning energy, collective pinning energy
U_A	activation energy for flux motion

symbol	description
U_{dis}	activation energy for unbound dislocations
U_{pl}	activation energy for plastic deformations
u	thermal displacement
V	voltage
V_c	vortex bundle correlation volume
$\vec{v}, v$	vortex velocity
v_F	Fermi velocity
w	conduction path width
x	Ta concentration/crystallographic x-direction
Z_P, Z_T	atomic number of projectile and target atom, resp.
z	vortex glass dynamic critical exponent
z'	Bose-glass dynamic critical exponent
α	evaporation angle
β	columnar angle
γ	anisotropy ratio
γ_{dis}	disorder parameter
δ	variation of oxygen content
ϵ_l	single vortex line tension
ϵ_r	pinning potential
ϵ_ϑ	angular-dependent anisotropy parameter
ε_0	dielectric constant
η	friction coeffcient, demagnetising factor
θ	angle between c-axis (film normal) and applied magnetic field, backscattering angle
θ_c	critical lock-in angle
ϑ	angle between applied magnetic field and ab-plane
κ	Ginzburg-Landau parameter
λ, λ_0	magnetic penetration depth, at zero temperature
λ_{ab}, λ_c	λ in ab-plane and c-direction, resp.
λ_L	London penetration depth
μ	glass exponent
$\mu_0 = 4\pi \times 10^{-7}$	magnetic permeability
ν	vortex glass static critical exponent
ν'	Bose-glass static critical exponent
ν_0	glass exponent
ξ, ξ_0	coherence length, at zero temperature
ξ_{ab}, ξ_c	ξ in ab-plane and c-direction, resp.
ξ_{BCS}	BCS coherence length
ξ_{VG}	vortex glass correlation length
$\pi = 3.14159\ldots$	
ρ	resistivity
ρ_{FFF}	free flux flow resistivity
ρ_N	normal resistivity

symbol	description
σ	conductivity
$\sigma_{\text{2D}}, \sigma_{\text{3D}}$	2D and 3D fluctuation conductivity
σ_N	normal conductivity
$\mathrm{d}\sigma/\mathrm{d}\Omega$	differential scattering cross-section
τ	mean scattering time
τ_{VG}	vortex glass relaxation time
τ_{BG}	Bose-glass relaxation time
Φ_0	flux quantum
ϕ	phase of order parameter
χ	disorder parameter (columnar defects)
Ψ	complex order parameter
$\mathrm{d}\Omega$	solid angle of particle detector
$\vec{\nabla}$	Nabla operator
$\propto$	proportional to

Chapter 1

Introduction

90 years ago in 1911, H. Kamerlingh Onnes studied the resistivity of mercury at low temperatures. After he had succeeded in liquefying helium three years earlier he could reach temperatures below $4\,\mathrm{K}$ and that is when he discovered a sudden drop in resistivity over several orders of magnitude within a very narrow temperature range [1]. He soon named the phenomenon *superconductivity* and measuring the low-temperature resistance for other materials many more metals and alloys were found since then to be superconducting below a well-defined critical temperature T_c.

It was also noted very early that a high electric current or the application of a magnetic field can destroy the property of zero-resistance current transport. But it would take more than 20 years before the other hallmark of superconductivity was discovered in 1933, the Meissner-effect[1] [2]. Contrary to a *perfect conductor* which would preserve the magnetic field at the moment it loses its resistance and resist any change of the magnetic field, a superconductor actively repels a not too large magnetic field in its superconducting state. This is independent of whether there was a magnetic field when it turned superconducting or if the field was switched on later. The fact that the magnetic state of the superconductor does not depend on its history suggested that it was a new distinct thermodynamic phase of matter, separated from the normal-conducting phase by a thermodynamic phase-transition.

---

[1] The effect is sometimes referred to as Meissner-Ochsenfeld effect, after the two scientists W. Meissner and R. Ochsenfeld who made the discovery.

Two years later the first successful phenomenological theory of superconductivity was published by F. and H. London [3] describing both characteristics of a superconductor, zero resistance and the Meissner-effect. The second of the London-equations also introduced an important length-scale, the London penetration depth λ_L. Since the magnetic field at the surface of a superconductor cannot vanish abruptly, it penetrates the material decaying exponentially over a typical distance which can be as short as some ten nanometers for elemental superconductors.

Although the London-theory is adequate to describe superconductors in the Meissner phase, it can not describe the superconductivity usually observed in alloys. Their critical magnetic field is often much higher than for elemental superconductors, but the Meissner-effect is not observed over the whole superconducting phase. Today, these materials are usually known as type-II superconductors and are characterised by two critical fields. The first or lower critical field marks the phase boundary for the Meissner-effect. Above it and below the upper critical field the magnetic field can penetrate the interior of the superconductor and form the mixed phase. The resulting mean-field phase diagram is shown in figure 1.1. But the magnetic field does not enter the superconductor homogeneously, instead it penetrates the bulk along linear tubes surrounded by circular screening currents which confine the field to these tubes. These magnetic field structures are called flux lines or, synonymously, vortices. Near the center of the flux carrying regions the superconductivity is suppressed due to the high flux density, but this *trade-off* allows the rest of the material to remain superconducting at much higher fields than type-I superconductors for which it is all or nothing: no resistance and Meissner-effect or normal conducting.

In 1950 V. L. Ginzburg and L. D. Landau presented a theory of the superconducting phase transition based on Landau's theory for continuous phase transitions [4] that is applicable on both types of superconductors and it proved itself to be especially valuable to describe the mixed phase of type-II superconductors between the lower and upper critical field. They defined a superconducting order parameter which is finite in the superconducting phase and zero in the
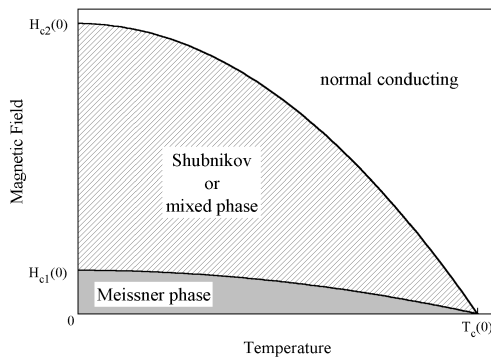
Figure 1.1: Mean-field phase diagram for type-II superconductors. The Meissner-effect exists only below the lower critical field line $H_{c1}(T)$. Over a large portion (for extremely type-II sc it is almost all) of the phase diagram the magnetic field penetrates the superconductor in the form of flux lines and forms the Shubnikov or mixed phase.

normal phase. The squared norm of the order parameter, which is a complex function of temperature and field, can be identified with the number density of superconducting electrons in the material. Starting with an appropriately chosen Hamiltonian-type of functional for the order parameter type-II superconductors can be described in great detail, especially in magnetic fields close to the upper critical field near the phase transition.

With the Ginzburg-Landau (GL) theory a new important parameter of superconductors was introduced, the coherence length ξ. It describes the length scale over which the order parameter can vary, for example at the interface between a superconducting and normal material. Among other things this implies that superconductivity can *leak* into normal conducting or even insulating materials. The GL-theory is also able to define and quantify the difference between type-I and II superconductors. Defining the dimensionless Ginzburg-Landau parameter $\kappa = \lambda/\xi$ type-I superconductors are those materials for which $\kappa \lesssim 1$, and consequently $\lambda > \xi$ for type-II[2].

Although the GL-theory is still very successfully applied to a wide range of problems in superconductivity, it does not explain the microscopic mechanism responsible for the loss of resistivity. In 1957 J. Bardeen, L. N. Cooper and J. R. Schrieffer (BCS) showed that two electrons in a crystal lattice can overcome their electrostatic repulsion and form a bound electron-pair [5]. These *Cooper-pairs* are effectively bosons, thus the Pauli-exclusion principle is no longer applicable and they can form a macroscopic condensate. Excitations from this ground state need

---

[2] The GL penetration depth λ is related but not equal to the London penetration depth λ_L. At zero temperature the relation is $\lambda_L \approx 1.41\lambda$, see also section 5.1

a minimum excitation energy equal to the pairing energy to break up the electron-pairs. Simply speaking, this energy gap is also the reason for the dissipation-free current transport. The BCS-theory has been verified in great detail for many superconductors; the existence of Cooper-pairs is most convincingly shown by the Josephson-effects, the tunneling phenomena of electron-pairs between two superconductors separated by a thin non-superconducting barrier [6].

The way penetrating flux lines affect the superconducting state can be analysed within the GL-theory. Most importantly, it was realized that the interaction between an applied current and the vortices can lead to the movement of the flux lines. In turn, this movement leads to an electrical field that is oriented in such a way that it slows down the supercurrent, thus it creates resistance. To avoid or minimize the resistance caused by flux motion, the flux lines have to be pinned. This can be achieved by defects in the crystal lattice or other variations of the superconducting parameters. Although the practical critical current density is reduced with respect to the depairing critical current, which is the current density when the Cooper-pairs break up, this has never been a real issue in conventional bulk superconductors. In fact, a lot of the predicted effects of flux motion were experimentally accessible in very thin superconducting films, only.

With the discovery of superconductivity in $Ba_xLa_{5-x}Cu_5O_{5(3-y)}$ by J. G. Bednorz and K. A. Müller in 1986 [7] the era of high-temperature superconductivity began. Until then Nb_3Ge with $T_c \approx 23\,K$ had the highest known critical temperature. Soon after the first report on high-temperature superconductivity similar compounds were synthesized with critical temperatures well above the boiling point of liquid nitrogen $(77\,K)$[3]. However, it did not take long to realize that there are many problems, which have to be overcome before these materials could be used for applications. One of these is the relatively low critical current density, caused by the movement of vortices due to an external current.

The special combination of superconducting parameters makes thermal fluctuations in the high-temperature cuprate superconductors much more important. Firstly, the penetration depth λ is much larger than the coherence length ξ, and

---

[3] An introduction to HTSC, including their crystal structure and many other aspects of these materials can be found in reference [8].

therefore $\kappa \gg 1$ (extremely type-II). This makes flux lines in these materials much harder to pin. Furthermore, the perovskite crystal structure has a layered nature and superconductivity is basically confined to thin CuO_2 layers which are separated by insulating charge reservoirs. This leads to a significant anisotropy of the conductive properties and a further reduction of the pinning potential. And, of course, the much higher temperatures further increase thermal fluctuations. Together, these parameters are the reason for a wealth of experimentally accessible effects resulting in a much more complicated phase diagram than shown in figure 1.1 and renewed interest in the physics of vortices in superconductors [9].

As it turns out pinning by random point defects is not very effective for increasing the critical current density at elevated temperatures and fields in the cuprate superconductors and defect structures which are more adapted to the dimensionality of the flux lines are needed. Grain boundaries, which could be easily produced during the manufacturing process, are not favourable either, because they significantly reduce the intrinsic critical current. The most effective way of improving the critical current and increasing the field and temperature range over which HTSCs show zero resistance, is by artificial columnar defects made by irradiation with high-energy ions. But to elucidate the role the anisotropic crystal structure plays in the way flux lines interact with the defect structure, it would be desirable to have full control over the crystal's anisotropy. Although there are a number of HTSC materials known with a range from weak to strong anisotropy, one is bound by the available materials. Furthermore, these materials differ from each other in more aspects than just their anisotropy.

Artificially grown superlattices of conventional or high-temperature superconductors separated by insulating or normal metallic layers can help in answering some of the open questions. Modern film deposition techniques allow one to make well-defined thin films with thickness ranging from single atomic layers to micrometers. One of the key requirements to be able to observe the phenomena associated with flux motion are a short coherence length and a much larger penetration depth, which is generally fulfilled in amorphous superconductors. Finally, the films need to have some form of extended defects which have a strong flux-

pinning potential and, ideally, flux motion can be studied with and without the pinning sites in effect.

In view of this background, amorphous multilayers made up of superconducting Ta_xGe_{1-x}-alloy and insulating Ge are nearly ideal systems to study some of the known vortex phases and the dynamics of vortices when subjected to an external force[4]. Both the penetration depth and the coherence length in these amorphous superconductors are similar to those found in the two most studied HTSCs, $YBa_2Cu_3O_{7-\delta}$ (YBCO) and $Bi_2Sr_2CaCu_2O_{8+\delta}$ (BSCCO)[5]. The multilayers can be easily produced in a completely amorphous state and the individual layer thicknesses can be varied precisely over a very large range. This enables one to study the vortex physics from strongly coupled three-dimensional to very weakly coupled quasi-two-dimensional films. Furthermore, a very simple technique known as oblique vapour deposition allows one to introduce intrinsic extended defects running across a significant part or even the complete film thickness. These defects oriented at a well-defined angle with respect to the film normal have been proven to be strong flux pinning sites [10]. And the fact that the defects are tilted away from the film normal gives one the opportunity to study the conductive behaviour with the magnetic field co-aligned with the defects and symmetrical to the film normal at large angles to the defects, but otherwise identical circumstances. In the first configuration the defects are able to pin the flux lines along their entire length, the other field orientation, however, should render the pinning sites ineffective.

There are many open questions when it comes to the magnetic behaviour and superconducting phase diagram of extremely type-II superconductors [11]. One of the most interesting problems is whether a truly superconducting phase, i.e. zero resistance in the limit of vanishing driving currents, can exist in the mixed phase of type-II superconductors or if the mixed phase is always characterised by a finite, albeit sometimes very small, ohmic resistance as observed over a

---

[4] Amorphous Ge is generally regarded a semiconductor. But at low temperatures and compared to the superconducting alloy-layers, it can be taken as a good insulator.

[5] For values of the superconducting parameters for these two HTSC materials see for example [9] and references therein.

substantial part of the phase diagram in most HTSCs. Based on an analogy in the theoretical description of magnetic spin-glasses and superconductors M. P. A. Fisher proposed a continuous phase transition from a high-temperature vortex phase with finite ohmic resistance into a low-temperature phase with vanishing linear resistance [12]. Despite intense research over the last decade many aspects of the proposed glass transition are still not well understood. Does the vortex glass phase really exist? If it exists, how is its nature influenced by the material anisotropy and the pinning defect geometry? How can the transition line in the phase diagram be moved to higher magnetic fields and temperatures? What is the best arrangement of defect structures for the most effective flux pinning? These are just some of the questions for which the above introduced multilayered Ta_xGe_{1-x}/Ge superconductors should be especially suited to help on getting a better understanding of the underlying physics.

This report is organized as follows. After this introduction the preparation of the multilayered Ta_xGe_{1-x}/Ge thin films will be discussed followed by the techniques used to characterise the microstructure and the results of these investigations will be given. The fourth chapter will deal with the experimental apparatus and setup used to study the superconducting phase diagram. The next chapter will present the theoretical models necessary to understand the experimental results and some background knowledge on related strongly type-II superconductors. The experimental results obtained during this project and their analysis will be discussed next before conclusions will be drawn in the last chapter.

This page is intentionally left blank.

Chapter 2

Sample Preparation

As outlined in the introduction the aim of this project was to study the superconducting phase-diagram of layered, strongly type-II superconductors with deliberately introduced extended defect structures. The combined experience of many years of research in thin amorphous films of Ge, Ta, and their alloys allowed us to manufacture well-defined multilayered films of Ta_xGe_{1-x}/Ge with a Ta-content of approximately 30% ($x = 0.3$). Previous studies [13] have found a maximum $T_c \approx 2.8\,K$ for TaGe-alloys of this composition (see also figure 2.1), thus allowing us to trace a good part of the superconducting phase diagram in a ^{4}He-bath cryostat. The equipment used for the sample preparation made it possible to achieve very low pressures during the actual film manufacturing process to reduce unwanted impurities, to control the layer thickness, and to introduce the above mentioned correlated defects. Details of the setup and the process are discussed in the following.

2.1   UHV vacuum system

The *Varian FC-12E Ultra High Vacuum System* provided the desired low pressures (base pressure $p \lesssim 10^{-7}\,Pa = 10^{-9}\,mbar$) and the means to make well-defined layered films of Ta_xGe_{1-x}/Ge . It is a completely oil-free vacuum system that uses a combination of adsorption pumps, ionisation pumps and titanium sublimation pumps[1].

---

[1] For an explanation of the principles of those vacuum pumps and general considerations in vacuum technology see for example [15]
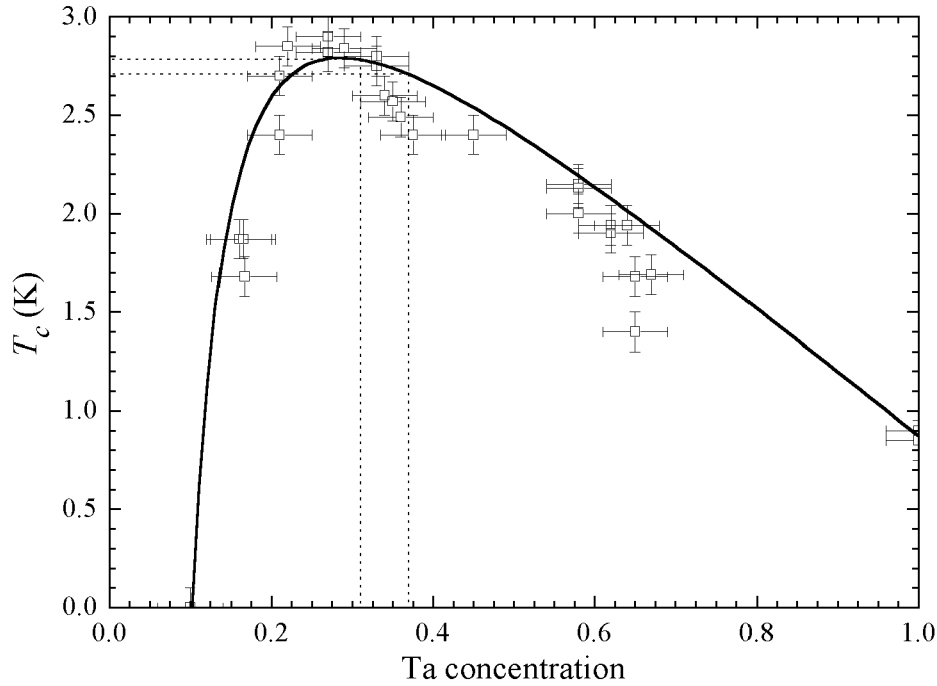
Figure 2.1: Transition temperature for amorphous Ta_xGe_{1-x} alloys with changing Ta concentration. For Ta concentrations of approximately 30 % the alloys show a maximum T_c of just under 3 K. The solid line is a guide to the eye. The range of Ta concentrations for the alloy layers in multilayered samples used in this study is indicated by the vertical dotted lines and the horizontal dotted lines give the range of transition temperatures expected for these alloys assuming the guideline is a good approximation. Plot includes data from reference [13] and unpublished data [14] recorded by Adrian Durham and Kieren Newell.

A typical pump-down cycle started with a careful visual inspection of the vacuum chamber and the installations inside the chamber, and any dust or excess material was removed using a vacuum cleaner. The cleaned sample substrates (see section 2.2) were placed inside the chamber. After closing the UHV-chamber, initial rough pumping with an oil-free rotary pump was followed by pumping with the two adsorption pumps. The entire system had been wrapped in heating coils and insulation thus allowing for heating of the system to 80° C to 100° C. Further pumping cycles at these elevated temperatures removed more gas from the system to the effect that the pressure dropped down into the 10^{-3} Pa range after the system had cooled to room temperature (RT), again.

At this stage the ionisation pumps could be switched on and the pressure rapidly dropped a further 2 orders of magnitude. Then it was necessary to bake

the system at around 100° C for at least 48 hours. Gaseous or other contaminations trapped on the surfaces and in the bulk of the source materials could be removed by applying low power levels to the evaporation sources during this period. Once the whole system cooled to RT the pressure dropped to approximately 10^{-7} Pa or less[2].

After that procedure the vacuum system was basically ready for an evaporation. However, the pressure rise under evaporation conditions had to be checked, that is both sources were heated to operational levels and the pressure rise was monitored. The titanium sublimation pump was also checked at this time. Initial switch-on of the sublimation pump usually led to a short but sharp pressure rise. After these operations the pressure dropped very rapidly to its base value again and evaporation could begin.

2.2   Oblique-Incidence Vapour Deposition

Conventional vapour deposition of thin films is made with the incoming particle flux normal to the substrate resulting in an anisotropy of the films primarily due to their 2D or quasi-2D character. Repositioning the source or tilting the substrate in such a way that there is a finite angle α between the film normal and the flux direction results in highly anisotropic thin films evident in their optical [16–19], magnetic [20, 21], electrical [19, 20, 22] and mechanical [23] properties. The following section will briefly discuss this phenomenon, a review of which can be found in [24].
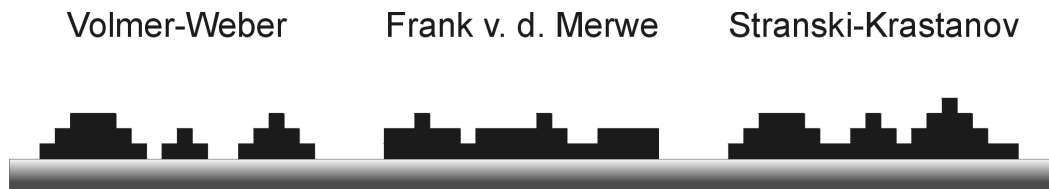
Figure 2.2: Schematical description of early stages of thin film growth modes.

Phenomenologically, one can distinguish between three different film growth

---

[2] The current through the ion pumps was used as a pressure gauge. It was calibrated down to 10^{-9} Torr $= 1.333 * 10^{-7}$ Pa and the pressure reading for the base pressure was usually below the calibrated range.

modes (figure 2.2): 3D island growth (Volmer-Weber), layer-by-layer growth (Frank van der Merwe), and an intermediate mode where first a continuous layer forms followed by island growth (Stranski-Krastanov). The growth mode is dependent on the interrelation of the surface free energy of the substrate, the deposit and the substrate-deposit interface. Except for the Frank van der Merwe-growth mode, island formation and subsequent island growth determine the film morphology.

For normal-incidence evaporation amorphous or multi-crystalline films form with grain boundaries approximately normal to the film plane. Tilting the incident beam away from the film normal results in a shadowing effect, schematically shown in figure 2.3 for a hard sphere model and with incoming particles sticking to where they first impinged on the substrate. The exact film microstructure depends on various parameters such as the sticking coefficient, the capture radius, and adatom mobility. Crucial to the formation of a leaning columnar-like structure is a limited adatom mobility, usually given for amorphous films, that prohibits the wandering of additional adatoms into the shadowed regions.
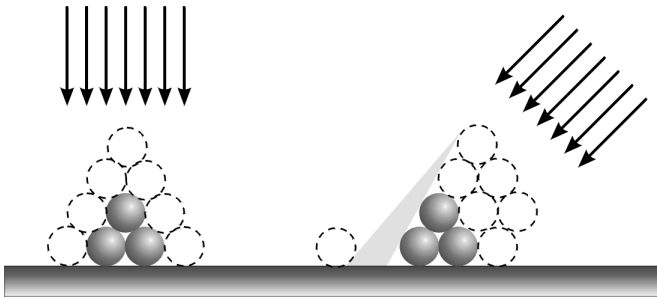
Figure 2.3: Shadowing-effect for oblique vapour deposition. On the left, the situation for a normal-incident vapour beam is shown; the islands grow isotropically in all directions. If the incident beam is off the normal direction a shadowed region forms (light grey in picture).

Numerous theoretical [25], experimental [21, 26], and simulation-type studies [27, 28] have been published that look at the growth and formation of the columnar microstructure. Given appropriate and realistic parameters all these studies show the formation of a low density or void network that surrounds an array of nearly parallel uniformly sized rods of higher density. For the incident vapour beam orientated at an angle α to the film normal the columns will grow at an angle $\beta < \alpha$ in the evaporation plane (see figure 2.4). Empirical studies suggest the following relation between those two angles:
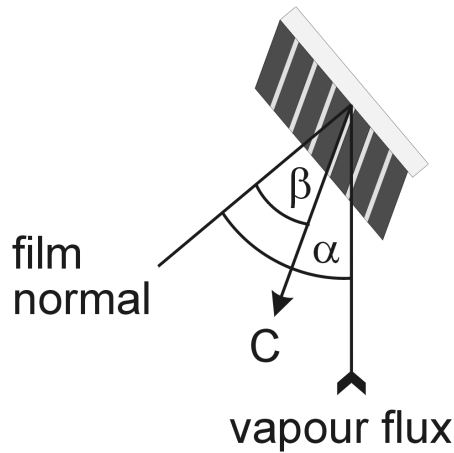
Figure 2.4: Definition of the evaporation angle α and β, orientation of the columnar structure. Note that the columnar direction C is always closer to the film normal than the incoming flux direction.

$$c \times \tan\beta = \tan\alpha, \tag{2.1}$$

with c being a constant for a wide range of angles α. Originally, a value for $c = 2$ was published [29], more generally c is a material-dependent parameter in many cases roughly equal 2. In addition to the growth direction of the columnar structure, the size and separation of the columns also depend on the evaporation angle α, with a larger α producing smaller and better separated columns.

2.3 Vapour Deposition Setup and Procedure

The setup for the multilayer evaporation was relatively simple and the layering could be controlled by a shutter mechanism. A schematic setup is shown in figure 2.5. For a general overview of thin film deposition see for example [30, 31].

For the Ge-source, resistive heating was sufficient to achieve desired evaporation rates[3]. High-purity (99.999 %) Ge chunks of a few mm^3 size were placed in a tungsten boat, which had to be replaced frequently to avoid boat breakage during evaporations. Because of its high melting temperature, Ta-evaporation required the use of an electron gun (*2kW Varian e-Gun*). As source material a 10 mm diameter Ta rod (purity 99.95 %) was available from which a small disc was cut and placed in the e-gun crucible.

Evaporation rates were controlled using two *Sycon Instruments STC-200/SQ*

---

[3] For key material parameters of the raw materials see Appendix C.
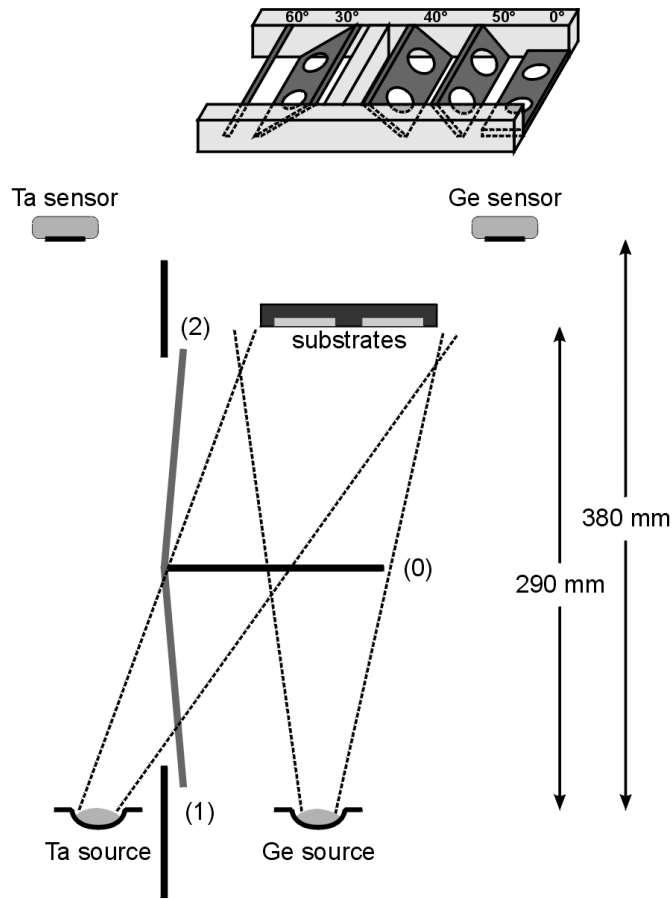
Figure 2.5: Schematic setup for oblique vapour deposition (not to scale). At the bottom are the two vapour sources for tantalum and germanium, respectively. The shutter in its three basic positions "0" (closed), "1" (Ge) and "2" (Ta_xGe_{1-x}/Ge) was used to control the layering and layer thickness. At the top are the quartz-microbalances to monitor and control evaporation rates. Above this is a perspective drawing of the substrate holder and arrangement. Tilting angles are indicated.

Deposition Rate Controllers in conjunction with two suitable quartz crystal rate monitors, one for each source. Geometrical constraints made it impossible to mount the rate monitors the same distance from the sources as the substrates. However, the *Sycon* deposition rate controllers allow for a correction by a tooling factor and, therefore, read the actual deposition rate at the substrates. Details of how to obtain the tooling factor are given in reference [32]. The short and long term stability of the evaporation rates were typically within $\pm 10\%$.

The films were deposited onto glass substrates. Commercially available microscope slides were cut and polished to circular discs of about 18 mm diameter. To ensure smooth and well-defined films the discs were thoroughly cleaned before

they were placed in the UHV-chamber. At first, they were immersed in acetone and placed in an ultrasonic bath for at least 15 minutes. This was followed by similar baths in iso-propanol and ethanol, respectively. In between the discs were rinsed under distilled water. They were then taken from the ethanol bath and dried under a stream of dry nitrogen gas, inspected for any visual scratches or dust, and placed on the sample tray. The pump down cycle was then initiated as described above.

The sample tray could hold up to 10 discs at five different evaporation angles of 0°, 30°, 40°, 50°, and 60°; two discs at each angle placed next to each other (see also figure 2.5). No substrate cooling was necessary to obtain amorphous multilayered films. This way we could produce a set of 10 multilayered films under identical vacuum conditions, having very similar layering, but different columnar microstructure. Of course, the layer thickness varied with the cosine of the evaporation angle[4]. In addition, the substrates were all placed at slightly different distances and angles to the evaporation sources. Most notably, this leads to deviations in the desired chemical composition of the alloy-layers. Törnquist [22] studied this effect for a very similar setup and found a variation in Ta concentration of less than 10 %. The chemical composition for all films investigated was determined using Rutherford Backscattering after completing conductance measurements (see section 3.1).

The evaporation process and consequently the layering of the films was controlled by a hand-operated shutter (figure 2.5). Initially, the shutter was in its "closed" or "0" position and was held there until evaporation rates for both sources had stabilised to their desired value. The rates were chosen so that the alloy-layers were made of approximately 30 % Ta and 70 % Ge, respectively. The evaporation rate was maintained at a maximum in order to minimize contamination by residual gas. The limiting factor was the Ta-evaporation rate due to its high vaporisation temperature. Best results were achieved with evaporation rates of 1.0 Å/s for Ta and 2.5 Å/s for Ge. Once these evaporation rates were reached a several nanometer thick bottom Ge-layer was deposited. The idea was that

---

[4] This assumes no or negligible changes in mean density. In section 3.2, layer thicknesses and the range of evaporation angles for which this assumption holds are discussed.

any adsorbed gases or water would react with germanium and then be covered by pure Ge. Thereafter, the multilayer process started by switching the shutter between positions "1", pure Ge, and "2", TaGe-alloy at predefined time intervals. Another relatively thick Ge-layer was put on top to protect the film with a germanium-oxide layer once the specimens were taken out of the vacuum and were exposed to atmospheric conditions. Exposure to atmosphere was minimized by storing the samples under a rough vacuum at a pressure of the order of mPa.
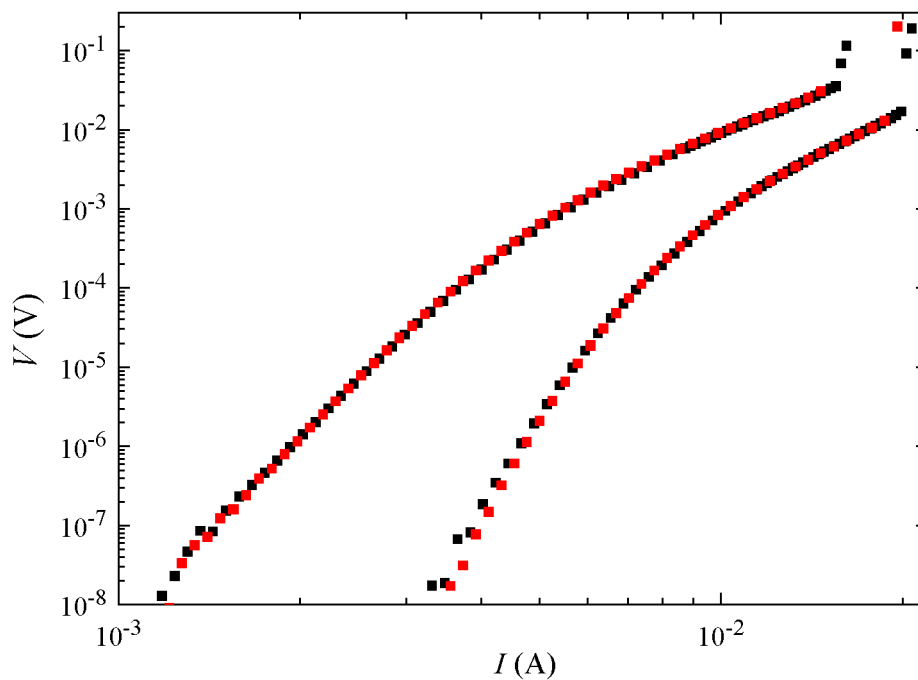
Figure 2.6: Double-logarithmic IV curves taken for one sample (J40) at a temperature of $1.70\,\mathrm{K}$, and magnetic fields equal to 0.3 (right) and $0.5\,\mathrm{T}$ (left), respectively. The red curves were first taken in Wellington and about 8 months later the measurements were repeated in Portland (black data).

However, the films proved to be very stable over time, even when exposed to atmospheric conditions for extended periods of time. In figure 2.6, two sets of IV-curves taken at the same temperature and two different magnetic fields are shown. The first set (red data in figure) was taken using the IRL-setup (see chapter 4) in Wellington, New Zealand. Before and after the experiments the film was stored under rough vacuum conditions as described above. Eight months later the film was taken to Portland, USA, to extend the measurements to higher fields and

lower temperatures. On the way to Portland, the sample had to be exposed to atmosphere for several days, and to check consistency some of the New Zealand measurements were repeated. The results are the two black curves in figure 2.6, which are almost identical to the red data taken several months earlier.

This page is intentionally left blank.

Chapter 3

Sample Characterisation

It was the purpose of this study to investigate the influence and interplay of layering and defect structure, respectively, on the Shubnikov-phase in type-II superconductors and the phase transition from a strongly pinned vortex glass phase to an unpinned vortex liquid in particular. To be able to draw definite conclusions it is, therefore, a prerequisite to have a detailed knowledge of the films' microstructure, that is the individual layer thicknesses and in our case the orientation and structure of the deliberately introduced extended defects. Furthermore, the superconducting properties of the Ta_xGe_{1-x}-alloy depend on the Ta-concentration x, which means the chemical composition of the superconducting layers had to be determined. The latter was done using the Rutherford Backscattering (RBS) technique and information about the films' microstructure was obtained from transmission electron microscopy (TEM). Both methods will be described briefly and the results discussed.

3.1   Rutherford Backscattering Spectroscopy

RBS is based on the famous experiment by E. Rutherford in which he observed the scattering of alpha particles from a gold foil and through this greatly helped to clarify the atomic structure, and which is not unlike playing pool billiard on an atomic level. A monoenergetic beam of ions is targeted at a sample surface and the recoil energy of the ions is analysed, thus giving information about the elements present and their depth profile. A very detailed description of the technique and analysis of RBS spectra is given in reference [33].

Because the interaction between the beam ions and the target nuclei can usually be described by a simple Coulomb interaction, the recoil energy and the scattering cross section can be calculated from first principles. The kinetic energy of the ions after the scattering can be characterised by the kinematic factor defined as $K = E_1/E_0$, where E_0 and E_1 are the energies before and after the collision, respectively. K is only dependent on the mass ratio M_P of the projectile and M_T of the target atoms and the scattering angle θ, see also figure 3.1:

$$K = \left[\frac{\sqrt{1 - (M_P/M_T)^2 \sin^2\theta} + (M_P/M_T)\cos\theta}{1 + (M_P/M_T)} \right]^2 . \tag{3.1}$$

From equation 3.1 can be seen that K is smallest for $\theta = 180°$ and increases with increasing target mass for a given projectile mass. The θ dependence also means that the best energy discrimination is given for angles near $180°$ and detectors are positioned at large angles without blocking the incident beam, hence the name *backscattering* spectrometry. The energy lost by the projectile during the scattering event is of course transferred to the target atom. This can lead to structural changes of the target material[1].
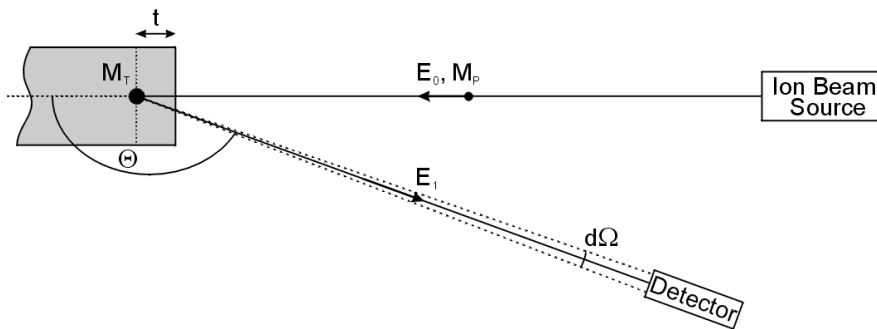
Figure 3.1: Principle RBS setup. The ion beam source creates a monoenergetic parallel beam of ions (mass M_P, energy E_0) that is aimed at the target. The detector is positioned at an angle θ as close to $180°$ as possible (see text). The detector's signal is then determined by the target atoms' mass M_T, their density at a depth t and the detector's solid angle $d\Omega$. Because the distance between detector and target is much larger than common target thicknesses, the angle θ is well defined.

---

[1] Though it might have been desirable to know the chemical composition before conductivity measurements, RBS spectra were taken afterwards to eliminate effects caused by the exposure to the high energy helium ions.

The differential scattering cross section is in addition dependent on the energy of the incoming ions and the atomic numbers Z_P and Z_T of projectile and target, respectively:

$$\frac{d\sigma}{d\Omega} = \left(\frac{Z_P Z_T e^2}{16\pi\varepsilon_0 E_0} \right)^2 \frac{4}{\sin^4\theta} \frac{\left(\sqrt{1 - [(M_P/M_T)\sin\theta]^2} + \cos\theta \right)^2}{\sqrt{1 - [(M_P/M_T)\sin\theta]^2}}. \tag{3.2}$$

From this equation follows that it is favourable to use projectiles with higher atomic number and that it is easier to detect atoms with high atomic number Z. Furthermore, $d\sigma/d\Omega \propto E_0^{-2}$ which leads to a higher sensitivity at lower energies.

The depth information comes from electronic scattering of the projectile ions as they pass through the target material before and after the scattering event. This electronic scattering leads to a gradual decrease in energy, but does not change the direction of the ions. The stopping power is itself energy dependent but for thin enough films it can be taken constant before and after the backscattering event, respectively.

The spectra were recorded at the *Institute of Geological and Nuclear Sciences* in Lower Hutt, New Zealand using a 3 MV Van-de-Graaff accelerator and a standard RBS setup. ^{4}He$^+$-ions with an initial energy of 2.7 MeV were used as projectiles, directed at the target film at normal incidence, which was placed in high vacuum. At an angle of 165° a surface barrier detector (SBD, FHWM = 15 keV) was employed to measure the energy of the backscattered He-ions. The data was digitized and stored for later analysis with standard RUMP (Rutherford Universal Manipulation Program) software by *Computer Graphics Service* [34]. The program allows one to simulate the spectra by entering the composition and thickness of the film and compare the simulated spectrum to the recorded one.

In figure 3.2 a typical spectrum together with the final simulation spectrum is shown. The x-axis is linear in energy and could be scaled in MeV using the kinematic factor K for Ta and Ge, respectively, but this is not necessary to analyse the spectrum. Tantalum is the atom with the highest atomic mass in the films, thus the broad peak at the far right corresponds to He-ions scattered at Ta-atoms. The next peak at lower energies can thus be identified to be coming
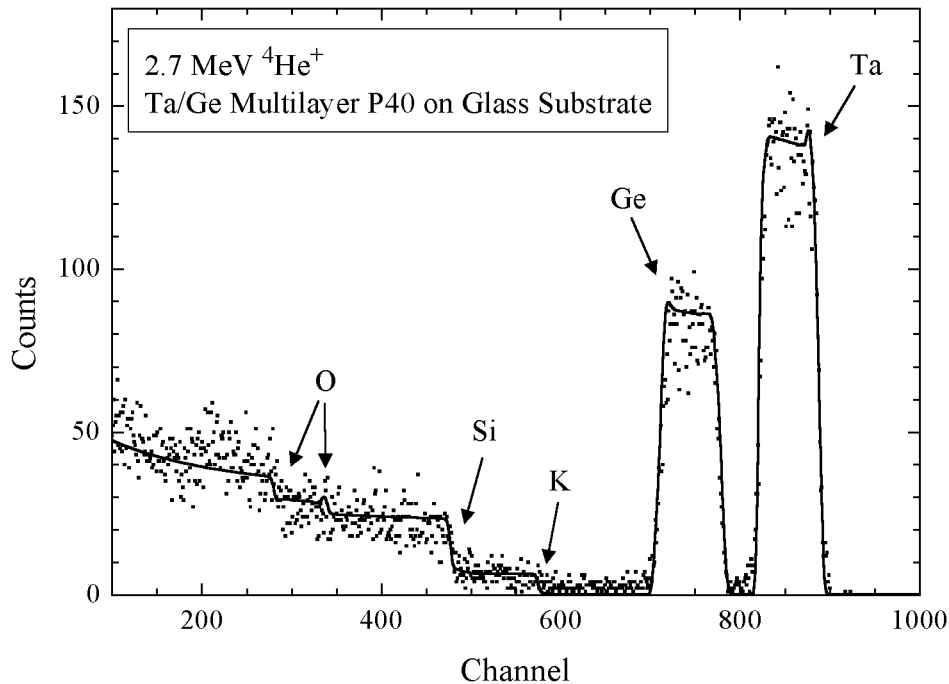
Figure 3.2: RBS spectrum for sample P40 (dots) and simulated spectrum (solid line). The two broad peaks at channel numbers 750 and 850 correspond to Ge and Ta, respectively, present in the multilayered film. The terraces at lower energies are due to the glass substrate.

from scattering events at germanium. The terraces at lower energies are caused by elements present in the glass substrate, mainly K, Si and O. There is a small hardly visible peak in the recorded spectrum but present in the simulation that corresponds to oxygen in the top germanium layer of the films. This topmost layer was oxidized when the film was first exposed to atmosphere. Although the depth-resolution was not high enough to resolve the individual layers of the films, it was still necessary to compose the film of several sublayers (typically 5 + substrate) in order to successfully simulate the spectra. From the simulation data it was then possible to calculate the relative composition of the Ta/Ge-film averaged over the film thickness. The quantity directly accessible from the simulations are atoms per square-centimeter[2]. Typical values were in the range of 10^{17} to 10^{18} atoms/cm^2.

Knowing the evaporation times for Ta and Ge it is possible to calculate the

---

[2] 10^{15} atoms/cm^2 are roughly equivalent to one monolayer of densely packed atoms.
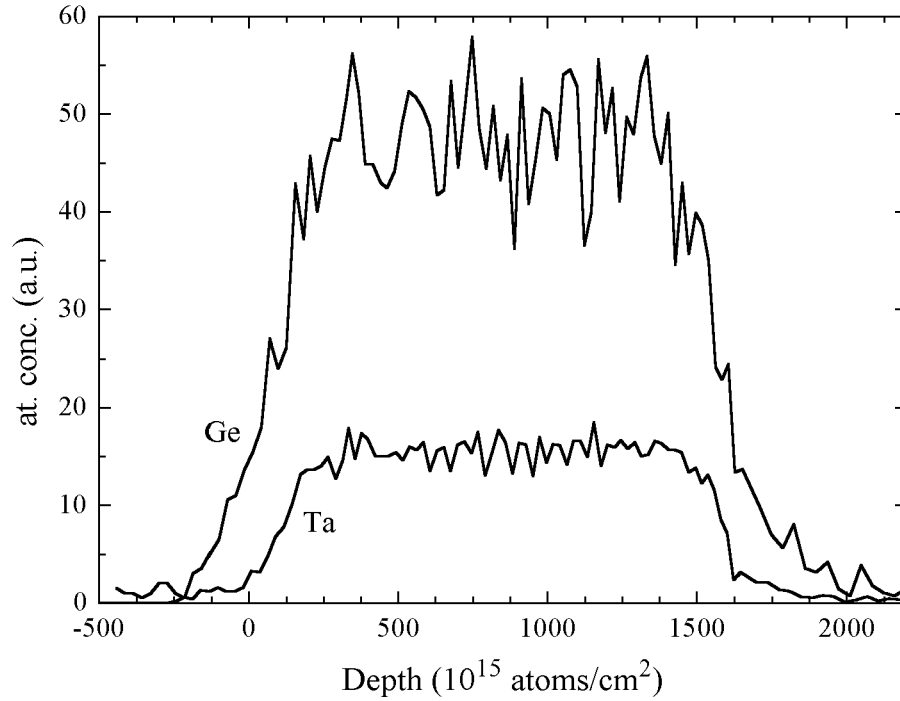
Figure 3.3: The depth profile of Ta and Ge for P40 as determined from the RBS spectrum figure 3.2. The depth scale is still given in atoms/cm^2 because the mass density is not known for sure.

chemical composition of the superconducting layers via the following equation

$$\frac{N_{\mathrm{Ta}}}{N_{\mathrm{Ge}}}\frac{t_{\mathrm{Ge}}}{t_{\mathrm{Ta}}} = \frac{x}{1-x}, \tag{3.3}$$

where N_{Ta} and N_{Ge} are the number of atoms per area determined from the simulations for tantalum and germanium, respectively, t_{Ta} and t_{Ge} are the evaporation times for the two elements. t_{Ge} is the total evaporation time for Ge, including the time needed for the bottom and top layers, and t_{Ta} is the time for the alloy layers only. x is the atomic fraction of Ta in the superconducting alloy layers; x values for all six principle samples in this study are given in table 3.1.

The RUMP program allows the transformation of the spectra into a depth profile, showing the relative content of the film constituents at a given film depth. Knowing the mass density of the film, this information could be given in nanometers, for example, but analysis of TEM images in the following section will prove that the density of these films may be significantly different from the bulk value.

Thus, in figure 3.3 this information for sample P40 is still given as a function of atoms/cm^2. The film surface is at the x-axis value $x = 0$ and $x \approx 1600$ marks the film substrate interface. It can easily be seen that the overall Ge-thickness is more than for Ta, reflecting the pure bottom and top Ge-layers. There is still no evidence of the layering, in fact the concentration for Ta and Ge are relatively constant, although there is considerable scatter in the Ge-data. Previously, a similar Ta_xGe_{1-x}/Ge film was checked for contaminations by other elements using particle induced x-ray emission[3]. But all the trace elements found in the signal could be tracked down to be part of the glass substrate.

3.2   Transmission Electron Microscopy

Just as well as light is used in traditional microscopes electrons can be used in an electron microscope, but with much higher magnification, under favourable conditions even atomic resolution is possible. The method of TEM will be briefly introduced, for a thorough discussion of the technique see for example reference [37]. A schematic setup of a TEM is shown in figure 3.4. The setup is very similar to optical microscopes and the resulting images contrast areas depending on their '*electron absorbance*[4]. However, the electrons are not really absorbed, but rather lost through large-angle scattering outside the objective aperture or through inelastic scattering being brought to focus on a plane far distant from the image plane. Since electrons are strongly interacting with condensed matter, the mean penetration lengths are very short of the order of 100 nm or less[5] and the specimens have to be prepared as very thin cross-sections with thicknesses comparable to the penetration length.

---

[3] In PIXE the x-ray spectrum emitted after inner-shell excitations by energetic ions is analysed. Every element is characterised by a unique *fingerprint* of x-ray wavelengths. The technique is also sensitive at low concentrations. See for example [35, 36])

[4] That is for microscopes operated in the bright-field mode. Analogous to optical microscopes, a TEM can also be operated in the dark-field mode. In the latter mode differences in the phase of the electrons are imaged. An introduction to phase-sensitive electron microscopy can be found in [38]

[5] The penetration length is strongly energy dependent and has a minimum of < 1 nm for low energy electrons of about 50 eV making low energy electrons a very sensitive probe for surface effects.

Electron Gun

Condenser 1

Condenser 2

Objective

Specimen

Objective
Aperture

Intermediate
Lens

1st

Image

2nd

Projector Lens

Image
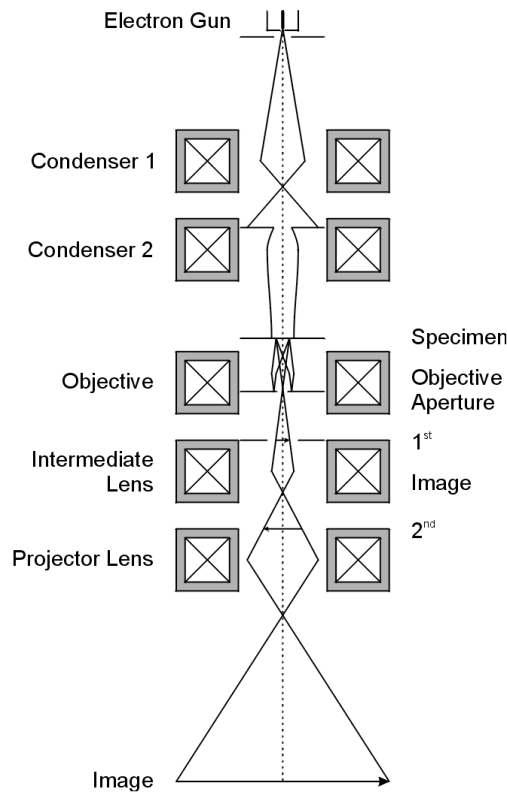
Figure 3.4: Schematic drawing of a typical setup for a TEM in bright-field mode. The paths for the electrons are also indicated. Electron lenses are realized through magnetic fields; the coils producing the required fields are indicated. Additional analyzing equipment (X-ray detectors, electron energy-spectrometer,...) are often included, but not shown in this drawing.

The preparation of the samples in this study followed a routine suggested by P. Munroe [39]. After a protecting gold layer was deposited on top of the film a small piece, about $1\,\mathrm{mm}$ long and $0.5 - 0.7\,\mathrm{mm}$ thick was cut from the glass disc using a diamond wire saw. In order to be able to not only see the layering of the film, but also the columnar structure the cross-section had to be taken for the evaporation plane and the sample had to be aligned carefully for this cutting process. Standard grinding equipment was used to thin down the specimen to the final thickness of $\approx 20 - 25\,\mu\mathrm{m}$. To ensure the two faces are parallel and smooth the specimen was glued to one leg of a tripod (figure 3.5) which was constantly leveled and a succession of ever finer diamond grinding papers ensured optically
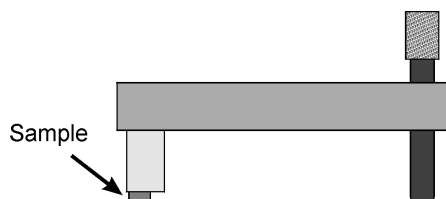
Sample

Figure 3.5: Schematic edge-on view of the tripod for grinding. The sample is glued to the detachable front leg so that it can be put under a microscope and the sample thickness be controlled. The two back legs (only one of them is shown) are adjustable in length to ensure the sample faces are always parallel as it is thinned down.

flat surfaces. The thickness was controlled by focusing on the tripod leg and the specimen surface in a measuring microscope, respectively. In figure 3.6 an edge-on photo was taken through the microscope. In places the gold film obviously chipped off, but the underlying superconducting multilayered film usually seemed to be still intact. For comparison a $80\,\mu$m Cu-wire was laid across[6].
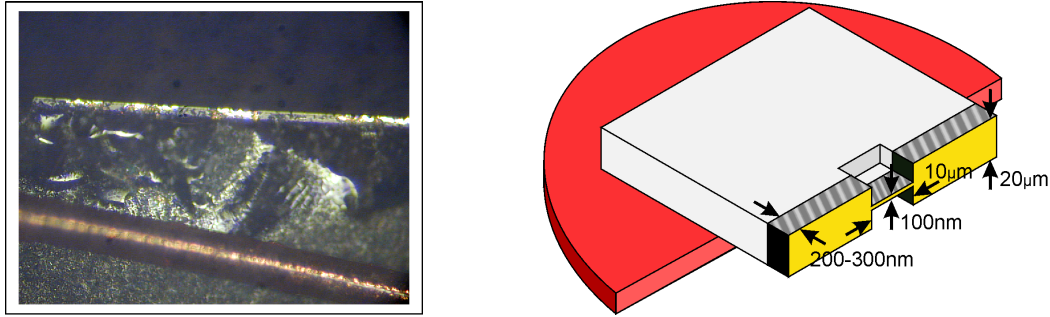
Figure 3.6: The left photo is an edge-on view of the sample still glued to the tripod's leg. The relatively bright areas are the remaining gold film. Across the bottom of the image is a $80\,\mu$m Cu-wire. The drawing on the right is a schematic view of the sample when it is readily prepared for TEM and glued to the specimen-mount (red) . It is not to scale, approximate dimensions are given in the figure, the overall size of the specimen is about 1×1 mm.

Mounted on a TEM specimen-mount it was sent to the *Electron Microscope Unit* at the *University of New South Wales* in Australia where the final preparation and electron microscopy was done. Using a focused ion beam which can be positioned and aimed at the target very precisely two trenches from either side were formed and only a very thin electron transparent section left standing for the TEM investigations. Next to the photograph in figure 3.6 a schematic drawing of the resulting sample geometry is shown. The microscope used for the investigations was a *Philips CM200 field emission gun TEM* operated at $200\,$kV with a maximum resolution of $0.24\,$nm. Digital images were analysed using *Image-Pro Plus* from *Media Cybernetics*.

In figure 3.7 digital images of all six principle samples used in this study are reproduced. On top of all films remnants of the protective gold and additional platinum layer deposited prior to the ion milling are identified as a dark layer. The layering of the Ta_xGe_{1-x}/Ge films is clearly visible in all images with the

---

[6] Bear in mind that it appears a little bit bigger, because it is out-of-focus.
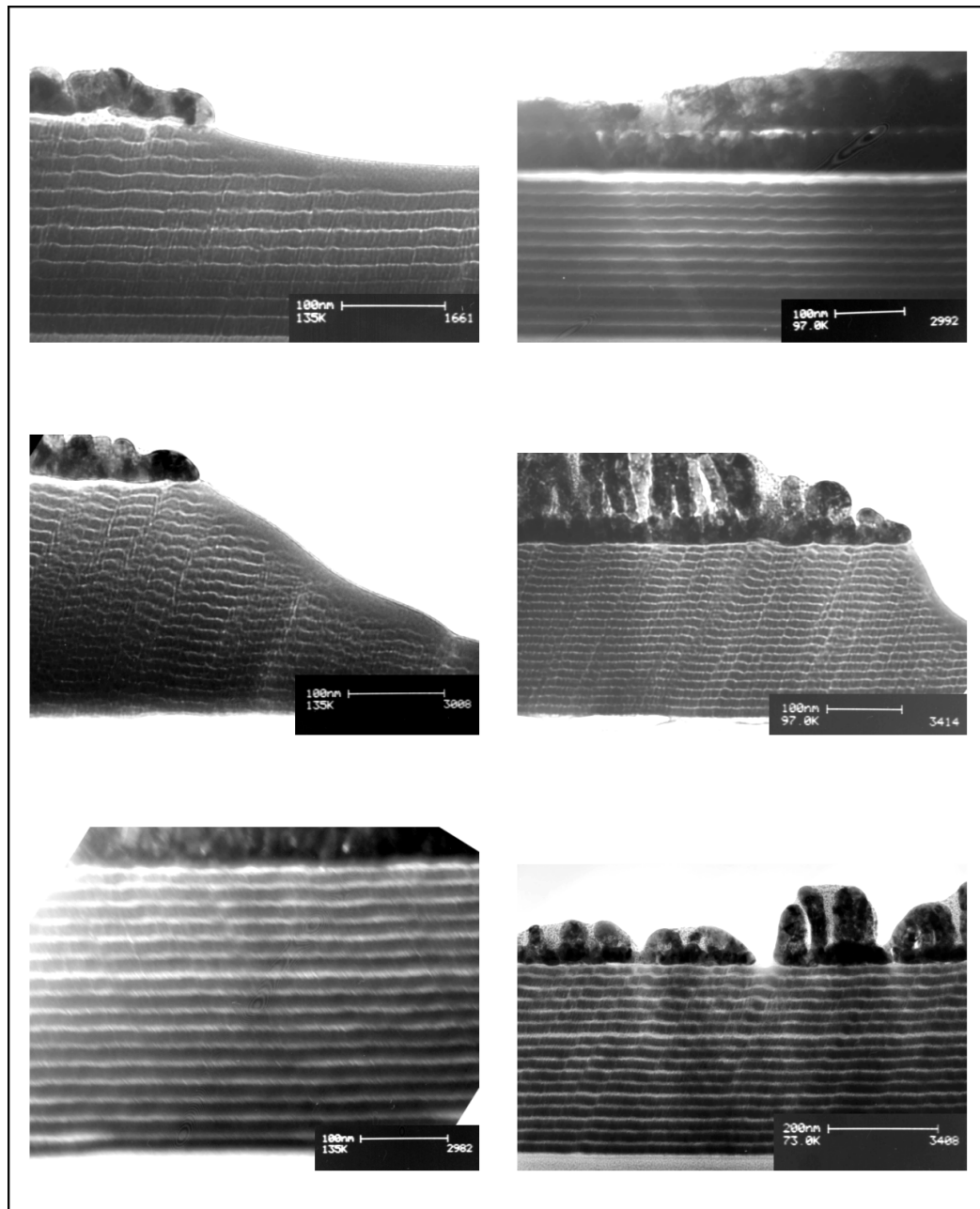
Figure 3.7: Comparison of TEM images of the six principle samples; top row: C40 (left), C30 (right); middle row: J40, J50; bottom row: P40, P50.

brighter layers identified as the pure Ge-layers. The columnar microstructure is also apparent in these or similar images for all films, but for C30. In none of the images taken from C30 was any additional structure visible except for the layering. In all images an intensity gradient from higher intensity at the top to lower intensity at the bottom can be seen, which is due to a slightly increasing thickness of the cross-section towards the glass substrate. Thus in some images the structure of the films towards the bottom end becomes less visible.

In figure 3.8 the intensity along a line perpendicular to the film P40 is plotted versus the relative position starting at the top of the film. The individual layers are easily recognizable as maxima and minima, respectively, as well as the regularity of the layering. Such intensity plots were used to determine the overall thickness of the films. The thickness of the individual layers was determined by marking the interfaces along a line perpendicular to the film and measuring the distance between those marks using the image analysis software. For that purpose contrast and intensity of the images was adjusted until the interfaces were most easily identified. This was done for a number of lines at different positions in the image and the results averaged. The columnar direction was determined by drawing straight lines along clearly identifiable defects and measuring their angle with respect to the well-defined glass surface. Numerical values are given in table 3.1. The error in the overall thickness of the films is estimated to be $1 - 2\,\mathrm{nm}$ or less than $1\,\%$ and probably the same error margins have to be assumed for the thickness of the individual layers. The columnar orientation is less well defined and a distribution of angles roughly between $\pm 3°$ from the averaged angle seems to be reasonable.

It is very interesting to compare the film thicknesses with those expected from the evaporation parameters and the tilting angle of the substrates. If the material density is not significantly changed by the oblique evaporation the thickness should simply scale proportional to the cosine of the tilting angle. For those samples evaporated at 30° and 40° that is confirmed exactly to within our uncertainties. The films deposited at 50° tilting angle, however, are much thicker than expected from this simple assumption. P50 is even thicker than the corre-
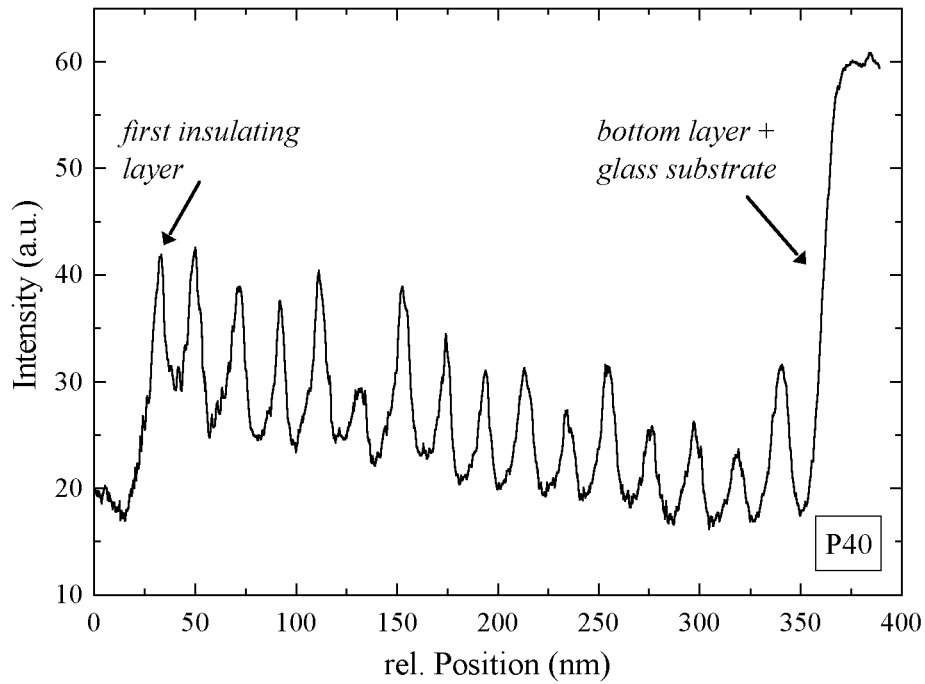
Figure 3.8: Intensity across multilayer P40. The intensity was measured along a line perpendicular to the film. The measurement starts at an arbitrary position in the protective Au/Pt layer (very low intensity) and extends into the glass substrate (very high intensity). The insulating Ge layers are the maxima separated by the low intensity in the TaGe-alloy layers.

sponding film P40. Therefore, the average material density must have decreased significantly. Further evidence that the film growth process changes for tilting angles $\alpha > 40°$ comes from a comparison of the columnar angles β. If we first compare the columnar angles for those samples evaporated at an deposition angle of 40° we have to conclude that the constant c in equation 2.1 is dependent on the layering and possibly on the tantalum content in the alloy layers. Nevertheless, the columnar angle for the '50°-samples' is expected to be significantly larger compared to the corresponding samples prepared with smaller tilting angle. However, for those samples studied there is no significant difference in the columnar angle between samples from the same evaporation but different tilting angles.

Unfortunately, further detailed characterisation of the defects proved to be difficult. It can be estimated that their typical thickness is of the order of a few

nanometers, but their mean spacing (or the mean size of the columns) cannot be determined reliably. A coarse estimate puts the typical column size for the samples deposited at 40° and 50° tilting angle at between 10 and 100 nm. No estimate was possible for C30, since no columnar structure was visible. A close inspection of, for example the images for J40 and J50, reveals that not all defects are spanning the complete film thickness, still there seems to be no significant change in defect density between the bottom and top of the films. For all films a general trend to increasing interface mixing and increased corrugation at the interfaces from bottom to top can be seen. This is not unexpected, because the films start to grow from a relatively flat glass surface. The statistical nature of the columnar film growth will lead to more corrugated surfaces which in turn will also favour mixing between individual layers.

3.3 Sample Characterisation Summary

	x	#	d_i [nm]	d_{sc} [nm]	d_{tot} [nm]	β	l [mm]	w [mm]
C30	0.31	12	3.4	15.6	225	—	6.81	1.64
C40	0.32	12	3.5	13.6	203	19.5°	6.72	1.57
J40	0.35	20	3.1	8.8	236	26.8°	7.34	1.94
J50	0.33	20	3.6	8.0	228	26.6°	6.86	1.64
P40	0.37	16	7.5	13.0	321	25.5°	6.97	1.67
P50	0.34	16	6.8	14.9	341	26.4°	6.67	1.84

Table 3.1: Summary of the physical characteristics for all six principle samples in this study. Values were derived as described in the preceding sections on RBS and TEM. x gives the Ta concentration in the superconducting layers and the third column labelled '#' gives the number of superconducting layers in the films. d_i, d_{sc}, and d_{tot} are the insulating and superconducting layer thickness and the total film thickness, respectively. β is the columnar angle measured with respect to the film normal. Dimensions of the conduction path, l and w, were measured using a microscope. Uncertainties are of the order of 0.04 mm for the width and 0.3 mm for the length; uncertainties for the other quantities are given in the text.

Chapter 4

Experimental Setup

The superconducting phase diagrams of the $\mathrm{Ta_{0.3}Ge_{0.7}/Ge}$ films were studied by measuring DC resistances and current-voltage characteristics in magnetic fields applied at different angles deliberately chosen with respect to the films' anisotropies. Careful design of the experimental setup allowed us to conduct the measurements with high sensitivity and accuracy in both temperature and resistance.

Two very similar setups were used, one at Victoria University laboratories at Industrial Research Ltd., Wellington, New Zealand, (IRL-setup) and the other at Lewis & Clark College, Portland, Oregon (Portland-setup). Both setups will be described in detail with emphasis on the differences between the two.

4.1   System Requirements

The films measured had critical temperatures in zero-applied magnetic fields $T_c(0)$ between approximately 2.0 and 2.7 K depending on the details of the film's microstructure and chemical composition. Therefore, the measurements were done in two ^{4}He-bath cryostats which could be operated down to 1.45 and 1.20 K, respectively. In order to trace large portions of the magnetic phase diagrams, large magnetic fields of the order of Tesla had to be applied; a conventional electromagnet and a superconducting magnet system were used. Because of the large and fundamental anisotropies of our samples it was further necessary to be able to freely orientate the magnetic field with respect to the film's geometry.

Because of the narrow temperature regime of only $\approx 1\,\mathrm{K}$ the temperature

31

had to be measured with high sensitivity and reasonable accuracy. Furthermore, temperature stability over extended periods of time was paramount as some of the experiments had to be done at constant T and sometimes high power inputs. High precision and accuracy was also required for the DC conductance measurements. A 4-point conductance bridge was used and great care was taken to reduce electro-thermal effects and noise.

4.2   Cryostat and Magnet Setup

IRL-setup   The IRL-setup consisted of an *Oxford Instruments MD4* cryostat fitted with a 40 cm long tail which was suspended in a *Varian V-3603 12-INCH Magnet* (fig. 4.1). The *MD4* cryostat is made of a 3.0 l liquid nitrogen reservoir as a heat shield for the 2.8 l liquid helium reservoir and a common vacuum jacket provides the necessary thermal isolation. The sample space inside the tail is shielded from room temperature by a copper heat shield in good thermal contact with the nitrogen tank. The inner diameter of the tail is just over 18 mm, to fit the 18 mm sample discs. Through a pumping line the liquid helium space was connected to a single stage rotary pump to reach temperatures as low as ≈ 1.4 K. Three differently sized valves in parallel were used to regulate the pumping speed and thus adjust the cooling rate and hold the temperature constant, respectively. Later, an electrically controllable *Cryo Industries Micro Valve* was installed as a fourth parallel valve. Together with a *MKS Baratron Type 626A Absolute Pressure Transducer* and a personal computer it helped to maintain a constant pressure[1] and thus constant temperature. Additionally, the pressure reading was used as a secondary thermometer at temperatures below 4.2 K.

Prior to cooling down, the common vacuum jacket for the liquid nitrogen and the liquid helium reservoir was pumped to $\approx 10^{-3}$ Pa or less with an oil diffusion pump to assure good thermal isolation. Cooling down from room temperature was done by adding liquid nitrogen the night before. Through radiative cooling

---

[1] Because of the limited maximum flow rate through the *Micro Valve*, this worked well for a limited temperature range between approximately 1.8 and 2.1 K, only. However, the computer program developed for that purpose had a graphical display of pressure vs time that made any drifts in vapour pressure/temperature easily visible at any temperature.
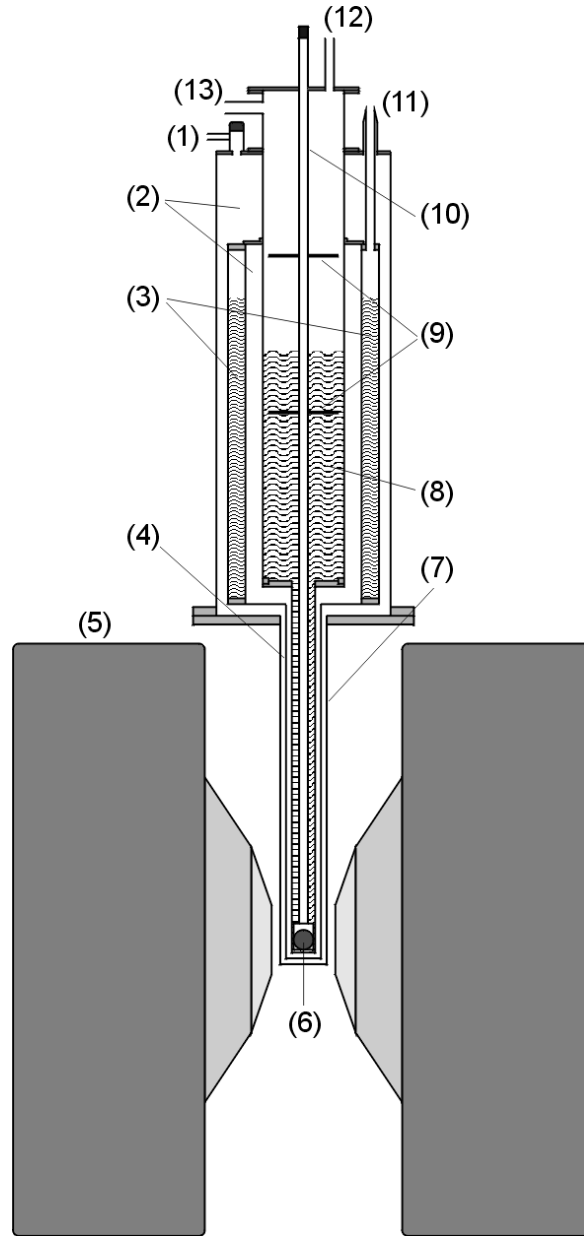
Figure 4.1: Schematic drawing of the *Oxford* cryostat and the *Varian* magnet (not to scale). (1) vacuum pumping port. (2) common vacuum jacket. (3) liquid nitrogen reservoir. (4) 77 K heat shield (5) rotatable electro-magnet. (6) sample. (7) cryostat tail. (8) liquid helium reservoir. (9) radiation shields. (10) cryostat insert and sample mount. (11) liquid nitrogen filling port. (12) liquid helium filling port. (13) helium vapour pumping port.

the sample space which held helium exchange gas reached around $100\,\mathrm{K}$ the next morning when liquid helium transfer started. This relatively slow cooling procedure reduced the chance of cracks in the film due to thermal stresses and a dense set of high-temperature resistance data could be obtained.

A liquid helium fill usually lasted for one day's experiments. Three $680\,\Omega$ carbon resistors along the sample holder (see section 4.3) were used as helium level sensors. At around $4.2\,\mathrm{K}$ they show a sharp resistance increase to about $20\,\mathrm{k\Omega}$. This means that when the liquid helium level dropped lower than one of the resistors its resistance dropped rapidly thus giving an indication of the approximate helium level.

The *V-3603* magnet is part of a *Varian V-4502-15 EPR Spectrometer System* for electron spin resonance (ESR) measurements installed at IRL. The ESR capabilities of the system were never used for this study, but the system's excellent magnetic field stability and homogeneity made it ideal for the in-field conductance measurements. The water-cooled magnet has a maximum power-supply limited field of $1.0\,\mathrm{T}$ and is fully rotatable by $190°$ which is a sufficient angular range due to sample symmetries. The field could be set with the *Varian Fieldial Magnetic Field Regulator* with an accuracy of $0.1\,\%$ and a sensitivity of $0.5\,\mathrm{ppm}$ for $\pm 10\,\%$ line or load changes from mean. The approximately $6.5\,\mathrm{cm}$ air gap between the tapered pole caps is wide enough for the cryostat's tail to fit in to. The magnetic field homogeneity over the sample space is better than $10\,\mathrm{ppm}$ for a field of $340\,\mathrm{mT}$.

Portland-setup   The major difference in this setup compared to the previous one is the *Janis Research Company 14CNDT Supervaritemp* cryostat with a fixed *Cryomagnetics Inc.* NbTi superconducting magnet; a sketch is shown in fig. 4.2.

The principle cryostat design is very similar, it also has a liquid nitrogen reservoir as a heat shield, separated by a common vacuum from the liquid helium dewar which also holds the superconducting magnet. Additionally, this *Janis*-cryostat has a separate, $44.45\,\mathrm{mm}$ diameter sample space connected to the main helium reservoir by a capillary and needle valve. Because of the relatively large heat capacity of the magnet, the cool-down procedure was a little bit different.
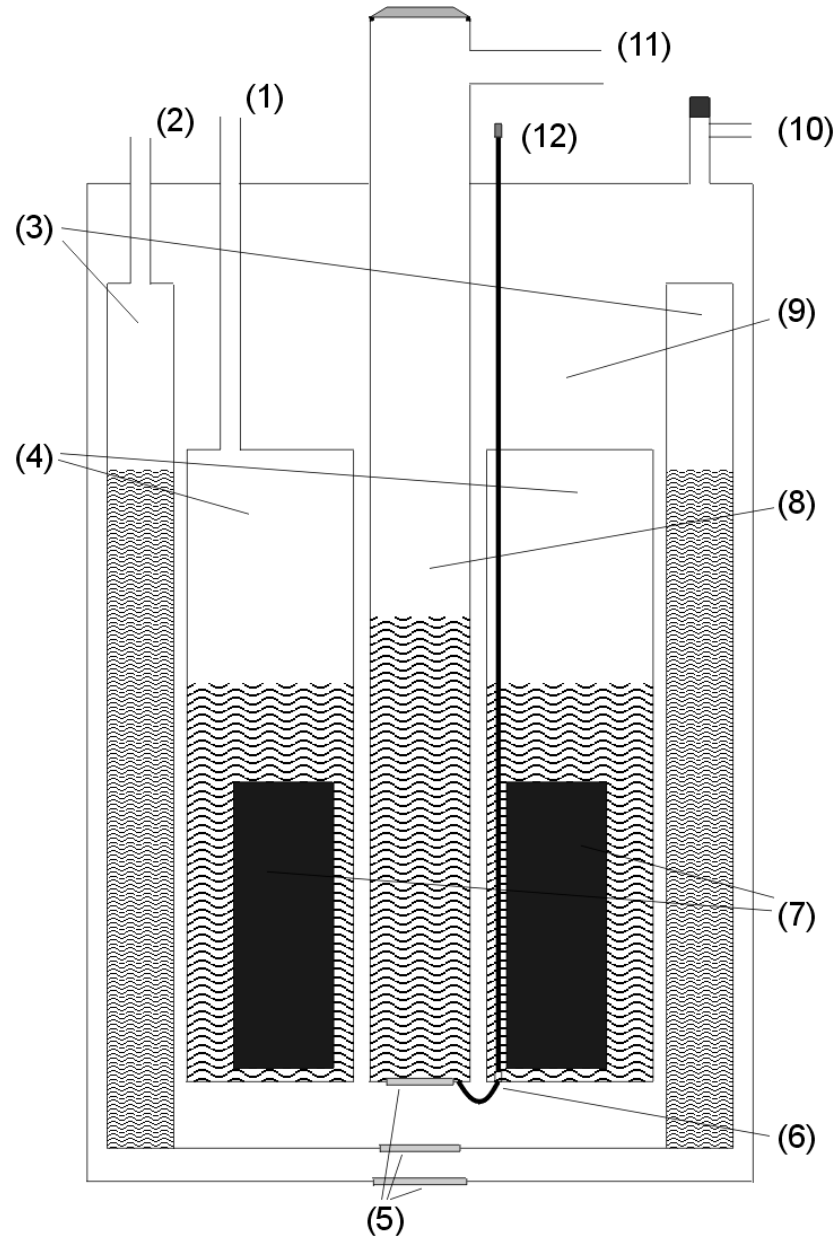
Figure 4.2: Sketch of the *Janis* cryostat. (1) liquid helium filling port. (2) liquid nitrogen filling port. (3) liquid nitrogen reservoirs. (4) liquid helium reservoir. (5) optical windows. Not in use for these experiments and therefore covered to reduce heat input. (6) needle valve and capillary connecting liquid helium reservoir and sample space. (7) superconducting magnet submerged in liquid helium. (8) sample space. (9) vacuum. (10) vacuum pumping port. (11) sample space pumping port. (12) needle valve control. Not shown is the cryostat insert and sample mount.

After thoroughly pumping the vacuum jacket, liquid nitrogen was filled into both the nitrogen and helium reservoirs. Once the magnet was cooled down to near 77 K the liquid nitrogen was blown out of the magnet space and any remaining nitrogen gas pumped out. At this point the sample space was flushed with helium gas and great care had to be taken that the needle valve was nitrogen-free as well, which could otherwise block the valve once it is frozen at liquid helium temperatures. Then liquid helium transfer started and as soon as liquid had been collected in the magnet space the needle valve was opened to allow first helium gas and later liquid to cool the inner space.

Liquid levels in the nitrogen and helium reservoirs were monitored electronically. The helium level in the sample space was monitored by means of a set of 4 resistors which change resistance rapidly near the boiling point of helium as described above. The sample space can hold approximately 1 l liquid helium that lasts for several hours under normal operating conditions.

Temperatures below 4.2 K were again reached by pumping on the helium vapour and regulating the pumping speed through a set of parallel valves. To increase the temperature range over which automatic temperature stabilization with the *Cryo Industries Micro Valve* was possible a set of 3 such valves was used. A particularily powerful single stage *Kinney* rotary pump and large diameter pipes extended the accessible temperature range down to about 1.2 K.

The superconducting magnet can achieve a maximum field of 9.3 T at the center of the bore with a homogeneity better than 100 ppm over the sample area. The magnet's excitation current was controlled by a *IPS-100* superconducting magnet power supply. The output current has a stability of better than 50 ppm per hour and a noise level less than 100 mA peak to peak. For measurements at constant field the magnet can be put into persistent mode where the current circulates in the superconducting coils making full use of zero resistance. In this mode the noise level is of course further reduced. Output current and thus magnetic field can be set to an accuracy of about 0.1 %. Of course, with this setup the magnetic field cannot be rotated relative to the film orientation, because the magnets orientation is fixed inside the cryostat, hence the sample holder had to

be designed to allow free rotation of the film, see section 4.3.

4.3   Sample Holder
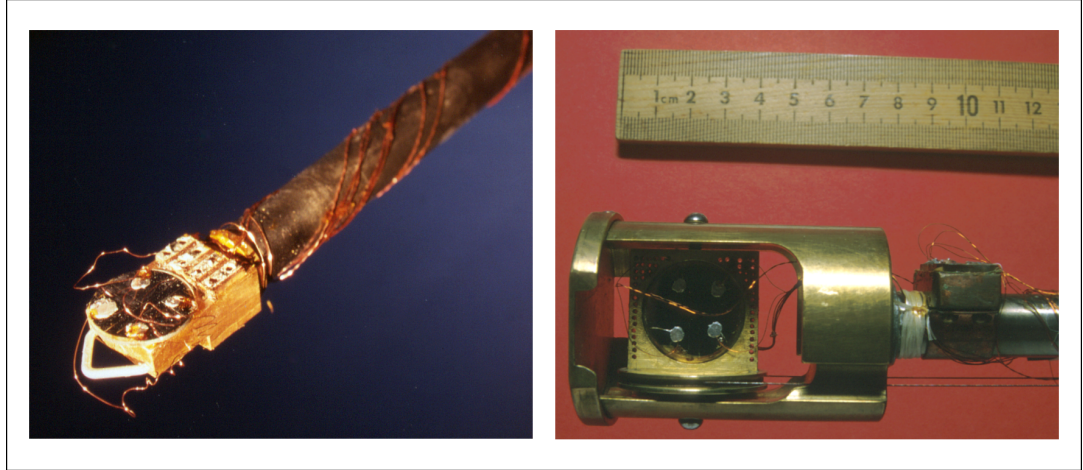
Figure 4.3: Photos of the IRL- (left) and Portland-sample holder (right). The bottom end of the cryostat inserts is shown. The dimensions of the copper block onto which the sample is glued has approximate dimensions 25 mm long and 15 mm wide (left image). In the right image the rotatable sample mount is shown. Its dimensions are indicated by the ruler.

IRL-sample holder   The sample holder or cryostat insert is used to hold and position the sample inside the cryostat and make the connection to the outside world. A photograph is shown in figure 4.3. The holder had been designed to reduce both thermal energy input and voltage noise [32].

A long thin-walled stainless steel tube connected a copper block onto which the sample was glued using *Ge 7031 varnish* and the top flange. This way the sample was directly immersed in the liquid helium which has several advantages. First of all, it greatly improves thermal contact with the temperature bath, directly between the sample and the liquid helium and through the copper block, a fact very important at high measurement currents when a large thermal power input has to be dissipated. Furthermore, below $T_\lambda = 2.17\,\mathrm{K}$ when liquid helium becomes superfluid it offered excellent temperature stability because of the unique properties of superfluid helium.[2] The temperature stability achieved be-

---

[2] For an introduction to superfluidity and the properties of superfluid helium-3 and -4 as well as a comparison of superfluidity versus superconductivity see for example [40].

low T_λ was well within ± 1 mK and about ± 3 mK for $T > T_\lambda$. Because the only soldered connections on the leads for measuring sample and thermometer voltages (see below) are immersed in liquid helium as well, voltage noise through thermal fluctuations is effectively minimized.

A *Lakeshore* carbon-glass thermometer (*CGR-1-1000*, serial number *C16322*, calibration report 253413) was mounted to the back of the copper block. This type of thermometer was chosen because of its high dR/dT below 4 K and its low magneto-resistance in fields up to about 1 T. The temperature accuracy is dependent on many factors; in the most interesting temperature range (1.5 – 4.0 K) it is mainly limited by the accuracy of the constant current source and varies between ± 7 mK (4.0 K) and ± 15 mK (1.5 K). For details see appendix A.

To reduce thermal voltage effects the sample and temperature sensor voltage leads were continuous 80 μm diameter, twisted pair copper leads all the way from the solder pads to the voltmeter. Using copper clips at the input to the voltmeter there were only mechanical copper to copper connections outside the helium bath. Current contacts and the contacts to the He-level sensors, where thermo-effects are not important, were made with 0.132 mm diameter, twisted pair constantan wire thus reducing power input through thermal conduction. The two baffles along the stainless steel tube effectively reduced power input to the helium bath by reducing radiative and convective heating.

Portland-sample holder In designing the sample holder for the Portland-setup the same principles were followed in reducing heat input to the system and reducing voltage noise and thermal effects. Thus the only real difference is the need to be able to rotate the sample instead of the magnet.

The brass manufactured rotatable sample mount is shown in figure 4.3. It is connected to an axle at the top of the insert via a strained stainless steel wire. The top axle was rotated with a goniometer and allowed the sample to be oriented relative to the magnetic field to within $\pm 0.1°$.

Temperature measurements were done with a *Lakeshore* carbon-glass thermometer *CGR-250*, serial number *11057*, in conjunction with a *Lakeshore DRC-91C Temperature Controller*. The temperature controller uses AC currents to

measure sensor resistance and internally stored calibration data to calculate temperature. The use of the *CGR-250* series thermometer ensured that the thermometer resistance stayed at reasonable levels even below 1.4 K. This way self-heating could be avoided while still keeping a very high sensitivity (up to ± 0.1 mK) and overall accuracy (of the order of ± 10 mK).

4.4 Measurement Setup
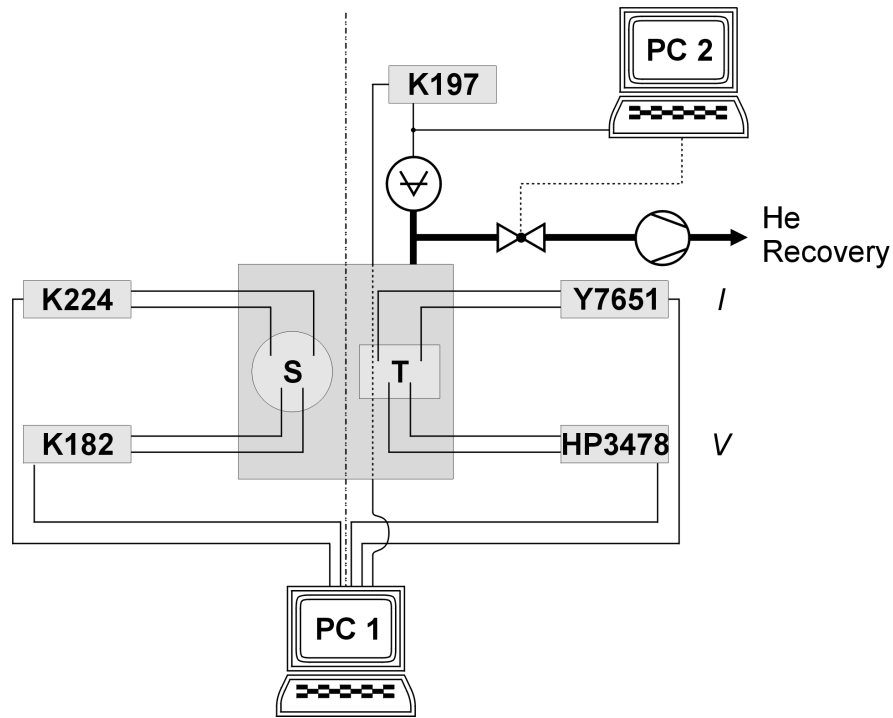
Figure 4.4: Schematic drawing of the setup for the conductance and temperature measurements. Left of the center line are the current-source (Keithley 224) and voltmeter (Keithley 182) for the sample conductance measurements; to the right are the equipment used for temperature control and monitoring. The set of valves to control the temperature is represented by only one valve symbol and the dotted line symbolizes the limited automatic control by PC 2. PC 1 was used to control the experiments and collect all relevant data: sample current and voltage, temperature and helium vapour pressure.

IRL-measurements The measurement setup can be divided into two parts: the DC resistance measurements of the sample and the temperature measurement, the latter being a DC resistance measurement with subsequent conversion according to the calibration sheets to the corresponding temperature. Addition-

ally, at temperatures below $4.2\,\mathrm{K}$ the helium vapour pressure could be used as a secondary thermometer.

The sample conductivity was measured in a 4-point geometry with the conductance path about $6-7\,\mathrm{mm}$ long and $2\,\mathrm{mm}$ wide scratched into the film (see also table 3.1). To apply the measurement current a *Keithley 224 Programmable Current Source* was used. It provided very accurate and completely PC-controlled excitation currents from as small as $100\,\mathrm{nA}$ up into the mA-range (for specifications see appendix B). The voltage drop along the conduction path was measured using a *Keithley 182 Sensitive Digital Voltmeter* with nanovolt resolution. This high resolution was desirable to measure very small resistances in the superconducting state.

These highly anisotropic films offer a multitude of possibilities on how to apply current and magnetic field with respect to the sample geometry which allow different aspects of the physics of these systems to be explored. For this study it was chosen to apply the external current parallel to the film plane and perpendicular to the evaporation plane, which is defined by the surface normal and the direction of the incoming particles during evaporation. The magnetic field was then applied in the evaporation plane and could be rotated in such a way that it was always parallel to this plane and thus perpendicular to the applied current. As will be discussed later in chapter 5 and 6, there were two field directions of special interest. Firstly, field direction parallel to the columnar microstructure, in which case the magnetic flux lines can take full advantage of the extended defects and they are pinned effectively. This direction will later be referred to as columnar (C) direction. The other field orientation that was studied extensively was symmetric to C with respect to the film normal at large angles to the defects. This way the films conductive behaviour could be studied under identical conditions only that the defect structure was rendered ineffective as a pinning potential. This second field orientation will be called anti-columnar (AC). Figure 4.5 schematically visualizes the geometry with respect to the film and defect structure.

For the temperature measurements the previously used home-made constant
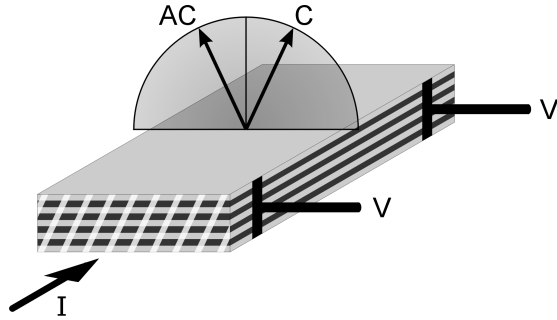
Figure 4.5: Schematical drawing of the measurement geometry, showing the applied current parallel to the film and perpendicular to the magnetic field that could be rotated in the evaporation plane. The two field orientations parallel to the defect structure (C) and symmetric at large angles to the defects (AC) are indicated as well as the terminals V to measure the voltage drop along the current path.

current source was replaced by a *Yokogama 7651 Programmable DC Source* to reduce current noise and offer better control. Its output current was software controlled to avoid self-heating of the thermometer and yet to have maximum possible temperature sensitivity and accuracy. Due to the thermometer's high resistance a *Hewlett Packard 3478A Digital Multimeter* in its DC voltage mode offered good enough resolution for the desired temperature sensitivity (see appendix A and section 4.3).

Three different measurements were realized, that were all controlled and the data collected by PC 1:

- resistance versus temperature at constant field magnitude & direction (T-sweeps)

- resistance versus field direction at constant temperature and field magnitude (Rotations)

- voltage versus current at constant temperature and field magnitude & direction (I-sweeps)

The software performing these tasks was written in *Turbo Pascal*. It set the excitation currents for the resistance measurements of sample and thermometer, and read corresponding voltages. To eliminate voltage offsets due to thermal effects, the current direction was reversed after the first reading and the average of both taken as the true voltage. The helium vapour pressure (read as voltage and converted to true pressure) was stored in a computer file together with sample current, voltage, resistance (not for I-sweeps), temperature (calculated from the

given Chebychev-polynomial) and field. The most important data (e.g. V vs I and T) were also graphically displayed on the computer screen for immediate verification.

Field magnitude and direction had to be set manually and the respective software variable set via the keyboard. Because automated temperature control was very limited, this had to be done manually as well. However, PC 2 was used to read the helium vapour pressure and display a graph pressure versus time. This greatly helped to maintain roughly constant cooling and heating rates and improved the temperature stability for measurements when constant temperature was required. For T-sweeps it was important to adjust the cooling (or heating) rate so that a dense set of data points could be obtained and to minimize temperature gradients having sample and thermometer in good thermal equilibrium.

Portland-measurements   The Portland-measurements setup is slightly simplified by the use of the *Lakeshore* temperature controller. It replaces the current source and voltmeter for temperature measurements of the IRL-setup. The software was programmed using *LabVIEW* but offered essentially the same control over the experiments with the additional feature that the magnetic field magnitude could be read by the software. However, when the magnet was operated in persistent mode, the field magnitude had to be entered manually.

Chapter 5

Theoretical Predictions and Background

The research area of superconductivity attracts a lot of attention from theorists and experimentalists alike, because of the many fundamental issues raised, but not least due to the technological potential of superconducting materials. This leads to a large and ever increasing number of publications on superconductivity and related areas. In this chapter the theoretical background will be developed as far as it is necessary to interpret and understand the experimental results presented in the following chapter.

5.1 Ginzburg-Landau Theory

One of the earliest successful phenomenological descriptions of superconductivity was given by F. and H. London in 1935 [3]. They introduced the following two equations now known as the London equations:

$$\vec{E} = \mu_0 \lambda_L^2 \frac{\partial}{\partial t}\left(\vec{J_s}\right), \tag{5.1}$$

$$\vec{B} = -\lambda_L^2 \left(\vec{\nabla} \times \vec{J_s}\right), \tag{5.2}$$

with the London penetration depth

$$\lambda_L = \sqrt{\frac{m_e}{\mu_0 n_e e^2}}, \tag{5.3}$$

and m_e the mass of an electron, e the elementary charge and n_e the number density of superconducting electrons. The first of the London equations describes perfect conductivity and the second, together with the Maxwell equation $\vec{\nabla} \times \vec{B} = \mu_0 \vec{J}_s$, describes the Meissner effect, which gives λ_L the meaning of a penetration depth of an applied magnetic field at the surface of the superconductor.

Although the London equations adequately describe a superconductor's response to electro-magnetic fields when in the Meissner phase, they fail when dealing with type-II superconductors in the mixed phase between the lower and upper critical fields. In 1950 Ginzburg and Landau applied Landau's general theory of phase transitions to superconductors. They introduced a complex superconducting order parameter Ψ and expressed the free-energy functional in terms of a series expansion of this order parameter and applied fields [4]. Originally a phenomenological theory which does not explain the microscopic origin of superconductivity, it was later shown [41] that it is a limiting case of the microscopic theory published several years later [5]. Because it is mathematically much simpler than the microscopic theory it has been employed very successfully to describe a wide variety of effects associated with superconductivity. Since the free-energy functional is a series expansion in Ψ it is strictly valid only in the vicinity of the superconducting transition, that is $T_c - T \ll T_c$.

Variation of the GL functional with respect to the order parameter and the vector potential leads to a set of differential equations. Solving these differential equations gives the order parameter and vector potential for a given situation and set of boundary conditions. The complex order parameter Ψ is commonly interpreted as a pseudo-wave function of the superconductor and as such can be related to the number density of superconducting charge carriers

$$|\Psi|^2 = n_s, \tag{5.4}$$

where $n_s = n_e/2$, since the superconducting charge carriers are electron pairs (see section 5.2). The differential equations mentioned above can be characterised by two parameters. The first one describes the length scale over which the order parameter can vary in magnitude, the GL coherence length ξ:

$$\xi^2(T) = \xi^2(0)\frac{1}{t},$$
(5.5)

with $t = 1 - T/T_c(0)$ the reduced temperature and $\xi(0)$ the coherence length at $T = 0\,\mathrm{K}$. $\xi(0)$ has to be distinguished from the microscopic coherence length $\xi_{BCS} \approx 1.36\xi(0)$. Within the GL theory the temperature dependence of the second parameter, the penetration length λ, takes on the following form:

$$\lambda^2(T) = \lambda^2(0)\frac{1}{t},$$
(5.6)

again, the extrapolated value at zero temperature $\lambda(0)$ is proportional to the microscopic value $\lambda_L \approx 1.41\lambda(0)$. Equations 5.5 and 5.6 have the same temperature dependence, therefore we can define the temperature independent GL parameter[1]

$$\kappa = \frac{\lambda}{\xi}.$$
(5.7)

Whenever superconducting and normal regions are next to each other[2] there is a domain wall energy associated with the interface. It can be shown that the domain wall energy changes sign from positive for $\kappa < 1/\sqrt{2}$ (type-I) to negative energies for larger κ (type-II). Because of the positive domain wall energy in type-I superconductors the Meissner phase is always stable up to the critical field. Abrikosov [43] showed that for type-II superconductors there is a field range between the lower H_{c1} and upper critical field H_{c2} in which it is energetically favourable if an applied magnetic field penetrates the bulk of the superconductor along tubes that are confined by circulating supercurrents. The condition that the complex order parameter $\Psi = |\Psi|\exp(i\phi)$ must be single valued leads naturally to the quantization of the magnetic flux. For a complete circulation of the flux line, the phase ϕ can only change by an integral multiple of 2π leading to the following expression for the flux quantum[3]:

---

[1] κ is only temperature independent within the valid temperature range for the GL-theory, i.e. near T_c.

[2] This can happen for any superconductor with non-zero demagnetising factor in a strong enough magnetic field. This intermediate state of superconductors is discussed in e.g. [42].

$$\Phi_0 = \frac{h}{2e} = 2.07 \times 10^{-15}\,\text{Wb}. \tag{5.8}$$

The interactions between vortices themselves and between vortices and the underlying superconducting material lead to the realization of a multitude of vortex phases and phase transitions; some of which will be discussed in later sections.

Within the GL-theory the critical magnetic fields for type-II superconductors can be expressed as a function of ξ and λ. The thermodynamic critical field, which in type-I superconductors is the field at which superconductivity breaks down, is given by:

$$\mu_0 H_c = \frac{\Phi_0}{2\sqrt{2}\pi\lambda\xi}. \tag{5.9}$$

In type-II superconductors the lower and upper critical field are much more relevant. The lower critical field H_{c1} is defined as the field value at which the first vortex enters the bulk and the Meissner effect is destroyed:

$$\mu_0 H_{c1} = \frac{\Phi_0}{4\pi\lambda^2}\ln\frac{\lambda}{\xi}. \tag{5.10}$$

The upper critical field is then the field value at which superconductivity finally vanishes and the material turns normal. Its value is only dependent on the coherence length

$$\mu_0 H_{c2} = \frac{\Phi_0}{2\pi\xi^2} \;\propto\; t = 1 - \frac{T}{T_c(0)}, \tag{5.11}$$

and the relative values of the critical fields is solely given by the GL parameter κ:

$$\frac{H_{c2}}{H_c} = \sqrt{2}\kappa \quad\text{and}\quad \frac{H_{c1}}{H_c} = \frac{\sqrt{2}\ln\kappa}{2\kappa}. \tag{5.12}$$

Since the two parameters λ and ξ are of such importance especially when it comes

---

[3] That the denominator in equation 5.8 is $2e$ instead of e is a direct consequence of the formation of electron pairs in the superconducting phase.
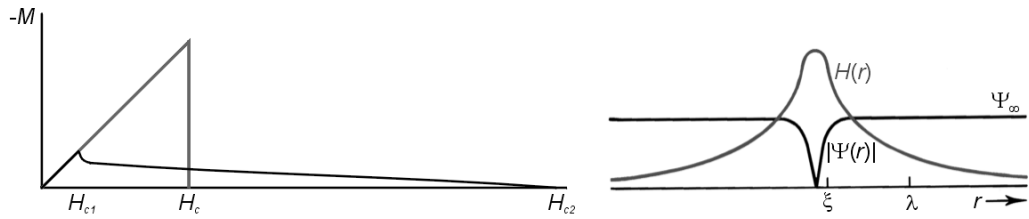
Figure 5.1: Magnetisation and the structure of an isolated vortex. On the left hand side magnetisation curves for type-I and II ($\kappa \approx 2.5$) superconductors with the same thermodynamic critical field H_c are compared. The graph on the right shows the spatial variation of the order parameter $|\Psi|$ and the microscopic magnetic field near an isolated vortex. The magnetic field decays over a typical distance λ whereas the superconducting electron pair density $n_s = |\Psi|^2$ goes to zero within a core radius ξ (here: $\kappa \approx 8$, from [42]).

to the structure of vortices, it helps to look at the right part of figure 5.1 in order to get a better feeling for their physical meaning. This shows the situation for an isolated vortex in a strongly type-II material. Over a typical length scale ξ the density of superconducting electron pairs drops from its equilibrium value far away from the vortex to zero at the vortex core. On the other hand, the magnetic field associated with the flux line decays over a typical distance λ. Also shown in figure 5.1 is a comparison of magnetisation curves for type-I and II superconductors with the same thermodynamic critical field H_c. In type-II superconductors, the Meissner-effect is destroyed at the relatively small field of H_{c1}, but at the cost of penetrating flux lines superconductivity can exist up to the much larger field value of H_{c2}.

Equation 5.11 implies that the upper critical field would increase linearly with decreasing temperature all the way to $T = 0\,\mathrm{K}$. Experimentally one finds that the upper critical field $H_{c2}(T)$ lies below the extrapolated value from equation 5.11 for temperatures T well below $T_c(0)$. Far more detailed microscopic theories are needed to describe the behaviour at low temperatures, such as that given by Werthamer et al. [44] who give a value for $H_{c2}(0)$ that is a factor 0.69 below the extrapolated value in the most simple case and compare it to measurements.

So far the discussion has been limited to isotropic superconductors to keep the argumentation as simple as possible. Anisotropy can be included in the GL free energy functional by replacing the scalar effective electron mass m by the

effective mass tensor $m_{\mu\nu}$. In the especially interesting case of uniaxial systems, that is, layered materials of alternating superconducting and normal layers to which the cuprate HTSCs belong, the effective masses along the principal axes of the system (symmetry axis $\parallel z$) become $m_x = m_y = m$ and $m_z = M$ with a mass anisotropy ratio defined by $\gamma^2 = m/M < 1$. An immediate consequence of the anisotropy is that λ, ξ and also the upper and lower critical fields depend on the magnetic field orientation relative to the superconductor's symmetry axis.

Following the convention for HTSCs the subscripts ab denote the in-plane parameters and c the characteristic length scales perpendicular to the superconducting planes. Similarly, the symbols $\perp$ and $\parallel$ are used to distinguish between magnetic fields applied perpendicular and parallel to the superconducting planes, respectively. It follows that the anisotropy ratio γ can also be expressed by the following ratios:

$$\gamma = \frac{\lambda_{ab}}{\lambda_c} = \frac{\xi_c}{\xi_{ab}} = \frac{H_{c2\perp}}{H_{c2\parallel}}. \tag{5.13}$$

Qualitatively, this can be understood by considering a magnetic field applied parallel to the superconducting layers. Since the screening currents surrounding the flux line have to cross the insulating layers, the critical current will be reduced, leading to an increased penetration length $\lambda_c > \lambda_{ab}$. On the other hand, this also leads to a shorter coherence length perpendicular to the layered structure $\xi_c < \xi_{ab}$.

Calculating any quantity from the anisotropic GL-functional for arbitrary field orientations is usually very tricky. Based on a scaling approach G. Blatter *et al.* [45] have demonstrated a convenient method to obtain the general result for arbitrary field orientations for quantities for which the isotropic result is already known. Assume the quantity $\tilde{Q}$ is known for isotropic superconductors, and one is interested in the corresponding $Q(\vartheta)$ as a function of magnetic field direction for the uniaxially anisotropic case, then one has to simply apply the following transformation:

$$Q(\vartheta, H, T, \xi, \lambda, \gamma, f_{\text{pin}}) = s_Q \tilde{Q}(\epsilon_\vartheta H, \gamma T, \xi_{ab}, \lambda_{ab}, \gamma f_{\text{pin}}), \tag{5.14}$$

with $\epsilon_\vartheta^2 = \gamma^2 \cos^2 \vartheta + \sin^2 \vartheta$ and $s_Q = 1/\epsilon_Q$ for $Q \equiv H$ the magnetic field, and $s_Q = \gamma$ for all other variables. ϑ is the angle between the applied field and the ab-plane, and f_{pin} is a measure of the pinning strength which will be discussed in section 5.5.1. In the isotropic expression the in-plane values ξ_{ab} and λ_{ab} have to be used. Applying relation 5.14 to the upper critical field yields

$$\mu_0 H_{c2}(\vartheta) = \frac{1}{\epsilon_\vartheta} \frac{\Phi_0}{2\pi \xi_{ab}^2}, \tag{5.15}$$

$$= \frac{1}{\left(\cos^2 \vartheta + \frac{1}{\gamma^2} \sin^2 \vartheta\right)^{1/2}} \frac{\Phi_0}{2\pi \xi_{ab} \xi_c}, \tag{5.16}$$

which reduces to

$$\mu_0 H_{c2\parallel} = \frac{\Phi_0}{2\pi \xi_{ab} \xi_c}, \tag{5.17}$$

$$\mu_0 H_{c2\perp} = \frac{\Phi_0}{2\pi \xi_{ab}^2}, \tag{5.18}$$

for parallel and perpendicular applied fields, respectively.

Another useful parameter within the GL-theory should be introduced here, the Ginzburg number, which can be expressed as

$$Gi = \frac{1}{2} \left(\frac{k_B T_c(0)}{4\pi \mu_0 H_c^2(0) \gamma \xi^3(0)} \right)^2 \tag{5.19}$$

$$\approx 10^{-7} \frac{\kappa^4 T_c^2(0)}{\gamma^2 H_{c2}(0)}, \tag{5.20}$$

where k_B is the Boltzmann constant. It is simply defined as the ratio of thermal energy to the superconducting condensation energy within a volume given by the coherence length ξ^3. Therefore it is a measure of the importance of thermal effects; the larger the Ginzburg number the more important thermal fluctuations become in determining the physical properties of the superconductor. From equation 5.19 it is obvious that Gi is strongly dependent on the critical temperature $T_c(0)$, but it is even more strongly dependent on the GL-parameter, with $Gi \propto \kappa^4$.

Additionally, anisotropic superconductors ($\gamma < 1$) are more susceptible to thermal fluctuations than isotropic. Altogether this means that the cuprate HTSCs are influenced by thermal excitations over a very large part of their superconducting phase diagram, but even LTSCs can show significant thermal fluctuations, given that their GL-parameter κ is large enough.

The above discussion is valid for superconductors for which the anisotropy is not too great, that is, they can still be treated as homogeneous materials. Other models have been developed to treat the case of extreme anisotropy, such as the Lawrence-Doniach (LD) model [46]. In the LD-model discrete superconducting layers separated by insulating layers are stacked on top of each other and the GL energy functional has to be replaced by a sum over contributions from the individual superconducting layers. Whether the discrete LD model or the anisotropic GL approach has to be adopted for a certain superconductor is often decided according to the dimensionless ratio

$$r_{cr} = \frac{2\xi_c(0)^2}{d^2},\tag{5.21}$$

where d is the superconducting layer separation. For $r_{cr} \gg 1$ the anisotropic continuum description is always correct, for $r_{cr} \ll 1$ on the other hand, a crossover from 3D to 2D-behaviour occurs at a certain temperature, which can be estimated as $T_{cr} = (1 - r_{cr})T_c$. However, even below this cross-over temperature T_{cr} many properties can still be described adequately within the anisotropic GL-theory. Therefore, the LD model will not be described in detail; a comprehensive review can be found in reference [9].

One consequence of the discrete model will be mentioned however, because of its relevance in understanding the experimental results in chapter 6. When the superconducting layers are separated by relatively thick insulating or normal conducting layers, the formation of an Abrikosov vortex is only possible within the superconducting layers. These vortices are generally called *pancake* vortices, due to their flat shape. Within the same layer repulsive interactions for pancake vortices with equal orientation persist, leading to various possible configurations, as will be discussed below in sections 5.4 and following. Pancake vortices in

different layers will also interact with each other, but their interaction will be
attractive in general. A long-range interaction is caused by the magnetic field
associated with each pancake vortex. On short length scales of the order of the
coherence length ξ_c perpendicular to the layers, there is also a so called Josephson-
coupling acting as a strong attractive force lining them up as a stack of pancake
vortices [9, 47] (see also figure 5.2).
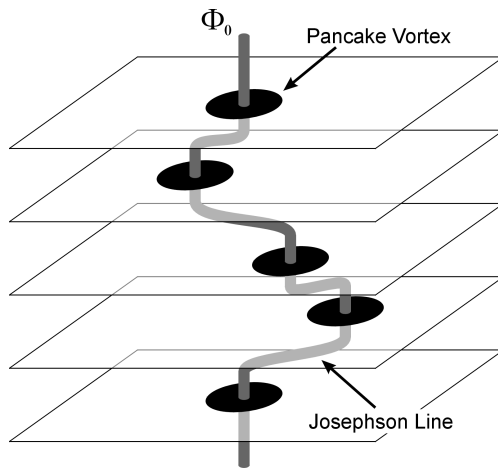
Figure 5.2: A flux line in a strongly lay-
ered superconductor is made up of pancake
vortices in the superconducting layers in-
terconnected by Josephson lines.

Josephson-coupling is due to tunneling of superconducting Cooper-pairs be-
tween superconductors in close proximity. Consider two superconductors joined
by a thin layer of insulating or normal-conducting material. This layer is equiva-
lent to an energy barrier for the superconducting electron-pairs, but the laws of
quantum mechanics allow them to penetrate a certain distance into this "forbid-
den" region, and if the layer is thin enough to tunnel through the energy barrier.
Within the GL-theory this means that the phase ϕ of the complex pseudo-wave
functions Ψ in the two superconductors have a well-defined relation that can be
expressed in terms of their difference $\Delta\phi$. Josephson in 1962 first theoretically
considered such a situation and came up with a number of interesting effects, now
known as the Josephson-effects [6] which have been applied in a number of very
sensitive voltage and magnetic field measuring devices (see for example [42] or for
more in depth treatment [48]). In the case of multilayered superconductors the
tunneling of electron-pairs between neighboring superconducting layers leads to
the above mentioned attractive force between pancake vortices in different layers
and their tendency to line up along the applied field direction. However, the exact

arrangement depends on the relative strength of interactions within a layer and between adjoining layers, magnetic field direction, temperature and disorder.

The typical length scale for Josephson-coupling is given by the coherence length, and the above defined ratio r_{cr} can serve to characterise the coupling strength. For $r_{cr} \gg 1$ the coupling is very strong, but as r_{cr} drops below unity for increasing layer separation, the coupling strength drops rapidly and the two dimensional character increases.

5.2   Amorphous Superconductors

The microscopic theory of Bardeen, Cooper and Schrieffer (BCS-Theory) [5], which can be applied very successfully to a wide range of elemental and alloy superconductors is based on electron-phonon interactions. At low enough temperatures this attractive interaction eventually overcomes the Coulomb-repulsion between two electrons and leads to the formation of electron pairs, so called Cooper-pairs, which are the superconducting charge carriers. A discussion of superconductivity in amorphous metals can be found in [49], but some basic ideas will be presented below.

In amorphous materials the picture of phonons as the quasi-particle excitations of the lattice vibrations breaks down since the long-range order of an atomic lattice no longer exists and only short-range order over a few interatomic distances remains. However the atoms still vibrate around their equilibrium positions with a broad range of frequencies, leading to the scattering of the conduction electrons and a very strong interaction between the conduction electrons and the atomic cores. In an atomic lattice quasi-particle momentum conservation effectively limits allowed scattering events; in amorphous materials this restriction no longer exists resulting in very short mean free paths for the conduction electrons.

These interactions between the charge carriers and the atoms can still lead to an attractive electron-electron interaction, and hence to the formation of Cooper-pairs. Because of the increased scattering rate amorphous superconductors often belong to the strong-coupling superconductors, and some metals are superconductors in their amorphous state only, for example Bi [49].

The loss of long-range order has some important implications for the super-conducting state, most importantly the coherence length ξ and the penetration depth λ. Inelastic scattering destroys the phase coherence between electrons and thus limits the coherence length ξ to about the mean free path of the electrons[4] which may be as little as a few interatomic distances, i.e. of the order of nanometers. The penetration depth is inversely related to the normal state conductivity resulting in an increased penetration depth for reduced conductivity. Since the conductivity in amorphous conductors is much less than in their crystalline phase, amorphous superconductors are generally type-II, often even extreme type-II superconductors with $\lambda \gg \xi$.

5.3 Conductivity above $\mathbf{T_c}$

In highly disordered or dirty superconductors there are several corrections to the conductivity at low temperatures and close to, but above T_c that go beyond the Boltzmann transport equation. Using a simple model describing current transport in metals Boltzmann arrived at the following equation (see for example [51, 52])

$$\sigma = \frac{n_e e^2 \tau}{m}, \tag{5.22}$$

with n_e the number density of conduction electrons, e the elementary charge, m the electron mass and the scattering time $\tau = l/v_F$ related to the mean free path l and the Fermi velocity v_F. Corrections to above formula can be divided into two groups, those which are present in all highly disordered conductors and others related to superconductivity[5]. In general, all of these corrections are more important in conductors with reduced dimensionality, e.g. thin two-dimensional films or quasi-2D layered materials.

The disorder related corrections to the conductivity are weak localization

---

[4] The mean free path to be used here is the mean displacement between phase breaking scattering events. It can be estimated to be $\sqrt{l_{el} l_{in}}$, where l_{el} and l_{in} are the mean free paths between elastic and inelastic scattering events, respectively. In amorphous Ta this displacement is about 1 nm at 100 K [50] and increases with decreasing temperature.

[5] However, even materials which are normal conducting at $T = 0$ K can have small contributions to their conductivity from superconducting corrections.

(WL) and Coulomb contributions where one has to distinguish between contributions from the particle-hole channel (CPH) and the particle-particle channel (CPP). WL stems from quantum self-interference of the charge carriers and in zero magnetic field gives a negative contribution to the conductivity. Random scattering events lead to a finite probability for self-intersecting current paths. If no inelastic scattering has occurred along this loop this can lead to constructive interference at the intersection. The probability for intersecting electron paths is greatly increased for conductors with reduced dimensionality, thus WL is more important in thin films or layered conductors. However, at very low temperatures spin-orbit scattering can lead to weak anti-localization and an overall positive conductance correction. Both Coulomb interactions CPH and CPP give additional terms which increase the resistance with decreasing temperature. Detailed descriptions of these effects and their temperature and magnetic field dependence can be found in [53, 54]. Detailed studies of conduction processes in amorphous Ta/Ge multilayers have been carried out by Johnson [50].

Even above the critical temperature thermodynamic fluctuations give rise to short-lived virtual Cooper-pairs which increase conductivity and lead to a rounding of the superconducting transition. Aslamazov and Larkin (AL) first calculated this contribution for a thin two-dimensional film in zero magnetic field [55]. It can be derived within the Ginzburg-Landau formalism by allowing non-interacting Gaussian type fluctuations of the order parameter and can be generalized for one, two, and three dimensions [56, 57]. Near T_c they take the following simple forms in two- and three-dimensional, isotropic superconductors:

$$\sigma_{2D}^{AL} = \frac{e^2}{16\hbar d_{sc}}\frac{1}{t}, \tag{5.23}$$

$$\sigma_{3D}^{AL} = \frac{e^2}{32\hbar\xi(0)}\left(\frac{1}{t}\right)^{1/2}, \tag{5.24}$$

where σ_x^{AL} is the fluctuation conductivity in 2D and 3D respectively, giving the total conductivity as $\sigma = \sigma_N + \sigma_x^{AL}$, the sum of the normal-state conductivity and the fluctuation conductivity. In the above equations $t = (T - T_c)/T_c$, $T > T_c$ is the reduced temperature, d_s the film thickness and $\xi(0)$ the zero-temperature

coherence length. An early verification of this kind of behaviour was for example found in thin amorphous bismuth films [58].

There is another term contributing to the fluctuation conductivity above T_c known as Maki-Thompson (MT) fluctuations [57, 59]. Its physical interpretation is much more difficult however, and sometimes called anomalous or indirect fluctuation conductivity. Thompson [57] gives a derivation of the MT-term which in three dimensions has the same temperature dependence as the AL-term adding up to a total fluctuation conductivity of

$$\sigma'_{3D} = \frac{5e^2}{32\hbar\xi(0)} \left(\frac{1}{t}\right)^{1/2} = 5\sigma^{AL}_{3D}. \tag{5.25}$$

The result in two dimensions is much more complicated; first calculations even resulted in infinite contributions at all temperatures. Thompson removed this divergence by introducing an additional pair-breaking rate [57] and could then describe experimental data for many thin film superconductors (e.g. Al [60]). Very close to T_c the MT contribution in two dimensions is negligible but at temperatures farther away from the superconducting transition the MT term becomes dominant and far more important than the AL fluctuation conductivity. A discussion of the origin of MT fluctuation conductivity and the pair-breaking mechanism can be found in [61]. It is also a good review of other effects of thermodynamic fluctuations on the properties of superconducting materials.

So far the focus has been on the conductivity in zero magnetic field and the different contributions of disorder-driven effects and effects due to the virtual formation of Cooper-pairs above T_c. The effects of an external magnetic field will be briefly discussed for the case of fluctuation conductivity above $T_c(H)$. Ullah and Dorsey [62, 63] used the time-dependent GL-theory to calculate various thermal and electrical transport coefficients near $T_c(H)$. For high magnetic fields they obtain the following scaling relation between the fluctuation conductivity in two and three dimensions and the temperature and applied field:

$$\sigma'_{2D} \;=\; \left(\frac{T}{H}\right)^{1/2} F_{2D}\left(a\frac{T - T_c(H)}{(TH)^{1/2}}\right), \qquad (5.26)$$

$$\sigma'_{3D} \;=\; \left(\frac{T^2}{H}\right)^{1/3} F_{3D}\left(b\frac{T - T_c(H)}{(TH)^{2/3}}\right), \qquad (5.27)$$

where a and b are material dependent constants and F_{2D} and F_{3D} are universal functions. These results are derived for the case where the current is perpendicular to the applied field, and in two dimensions the field is perpendicular to the film or the conducting planes in the case of layered materials. For the universal scaling functions $F_{2D}(x)$ and $F_{3D}(x)$, only their asymptotic behaviour for large positive and negative values of x, that is, far from the mean-field transition temperature, are known (see [63]). See section 6.4 on how these scaling relations were used to determine $H_{c2}(T)$ for the superconductors in this study.

5.4 Vortex Physics – The Mixed Phase of Type-II Superconductors

After this short excursion to fluctuation conductivity and the transition into the superconducting state let us return to the mixed or Shubnikov-phase of type-II superconductors. In section 5.1 figure 5.1 we have already seen that the magnetic field associated with a vortex decays over a typical length-scale λ away from the vortex. Details of the functional dependence of the field on the distance r from the center of the vortex can be found in [42], for example. Since in the most common situation the flux has the same direction in all vortices, the magnetic interaction is naturally repulsive. In the case of clean[6] samples this leads to the formation of a regular triangular lattice of flux lines, the Abrikosov lattice [43][7].

---

[6] Clean samples are those with no or only very weak pinning by impurities or other defects. In this case the interaction between vortices is dominated by the above mentioned magnetic interaction over much of their phase diagram.

[7] In his original publication Abrikosov predicted a rectangular lattice, but it was shown later that the triangular lattice is energetically slightly favourable. However, in some superconductors the influence of the underlying atomic structure can not be neglected, and the stable equilibrium configuration may be other than triangular [64,65].

The distance between adjacent vortices can be shown to be

$$a_0 = \sqrt{\frac{2}{\sqrt{3}} \frac{\Phi_0}{B}}. \tag{5.28}$$

It is interesting to note that the upper critical field can be interpreted as the point at which the distance between neighboring flux lines becomes less than the coherence length ξ, meaning that there is no continuous superconducting path through the bulk sample anymore. For the flux line lattice (FLL), well-defined elastic moduli (compression, tilt, and shear modulus) can be found as a function of applied field and intervortex spacing [9].

For strongly type-II superconductors with a large Ginzburg number Gi thermal fluctuations can lead to the melting of the FLL into a vortex liquid. Within elastic theory melting is characterised by a vanishing shear modulus. In the case of vortex matter one expects differences in the magnetic and electrical behaviour as one crosses the melting line. Experimental evidence that the melting transition is a first order phase transition as predicted by theory came from calorimetric measurements [66–68]. For example Schilling *et al.* measured the latent heat required to melt the flux line lattice into a flux liquid. The melting line itself can be described reasonably well applying a Lindemann criterion[8] [9]. Experimentally, the melting transition has been associated with a jump in magnetisation and the so-called peak effect in critical current density. These effects have been found in low-T_c systems such as Nb_3Ge and Mo_3Si [70] and high-temperature superconductors, for example YBCO [71–75] and BSCCO [76]. Structural evidence that these effects are indeed correlated with a solid-to-liquid melting transition, has come very recently from simultaneous neutron diffraction and magnetisation experiments on niobium single crystals [77]. Figure 5.3 shows diffraction patterns for temperatures below and above the melting transition, respectively. At low temperatures the pattern shows the six-fold symmetry of the FLL, at higher temperatures the long-range order is completely destroyed and a diffrac-

---

[8] In 1910 F. Lindemann proposed that a crystalline lattice becomes unstable when the mean-squared amplitude of thermal fluctuations of its constituents increases beyond a certain fraction of the lattice constant: $\langle u^2(T_m) \rangle_{th} \approx c_L^2 a_0^2$ [69]. $c_L \approx 0.1 - 0.3$ is the Lindemann number.

tion pattern unfolds that is very typical for liquids. Hysteresis effects observed in those experiments also confirmed that the vortex lattice melting is a first-order transition.
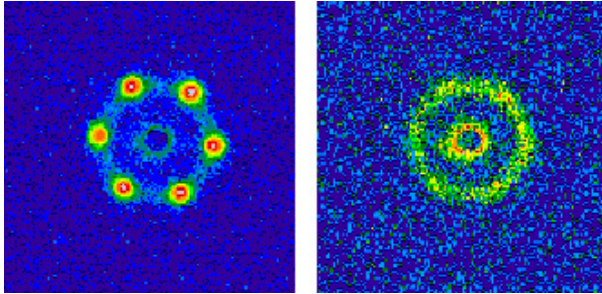
Figure 5.3: Small angle neutron diffraction patterns of vortex lattice (left) and liquid (right). For the lattice the pattern reveals the typical six-fold symmetry, which is completely absent in the liquid phase [77]. Reproduced with the kind permission of X. S. Ling.

Perhaps the major motivation for research in terms of applications of superconductors stems from their ability to carry electrical currents without any dissipation. An upper limit to the maximum dissipation-free current density is set by the depairing current density J_0, which can be estimated from the condition that the self-field of the current at the surface of the superconductor cannot exceed the thermodynamic critical field:

$$J_0 \simeq \frac{H_c}{\lambda}. \tag{5.29}$$

In type-II superconductors the dissipation-free current density can be significantly reduced due to the interaction of an applied current with the flux lines or vortices. It might be expected that, as long as the vortex cores do not overlap, there is always a continuous superconducting path through the material and the applied current would simply avoid the normal-conducting regions. But because the magnetic field extends a distance $\lambda > \xi$ from the vortex, the current has to flow through regions penetrated by magnetic field and there is a Lorentz force on the current and vice versa on the flux lines[9]:

$$\vec{f_L} = \Phi_0 \vec{J} \times \vec{n}, \tag{5.30}$$

---

[9] There is another possible derivation of the force on a vortex in a superfluid, solely based on hydrodynamics and therefore also valid for uncharged superfluids, like superfluid liquid helium. The force is then called Magnus force, but leads to essentially the same result [78]

with $\vec{f}_L$ the Lorentz force per unit length per flux line and $\vec{n}$ a unit vector in the direction of the flux line. Under the action of the Lorentz force the vortices accelerate until they reach a steady-state and the Lorentz force is balanced by a friction force $\vec{F}_\eta = -\eta\vec{v}$ with $\vec{v}$ the average vortex velocity. The flux motion induces an electrical field proportional to the vortex velocity

$$\vec{E} = \vec{B} \times \vec{v}, \tag{5.31}$$

which is parallel to the external current and thus leads to dissipation[10]. The friction coefficient can be calculated and leads to the free flux flow (FFF) resistivity [79]

$$\rho_{\text{FFF}} = \rho_N \frac{B}{\mu_0 H_{c2}}, \tag{5.32}$$

with ρ_N the normal state resistivity. Thus, for a given magnetic field, the resistance decreases only gradually with decreasing temperature as the upper critical field $H_{c2}(T)$ increases. Since the electrical field is proportional to the mean vortex velocity we can regain dissipation-free current transport in the mixed phase by prohibiting flux motion. That this is possible is evident from superconducting magnets used for particle accelerators, or MRI-machines in hospitals, which are all type-II superconductors operated in their mixed phase. In these conventional superconductors[11] sufficient pinning potentials can be achieved by random point defects, such as missing or interstitial atoms, impurities, etc., which cause local variations in the superconducting parameters and thereby generate potential minima which are able to counteract the Lorentz force due to the applied current. Details of flux pinning and the problems faced in layered, extremely type-II superconductors are discussed in more detail in the following section.

---

[10] That the electric field must decelerate the external current rather than accelerate can be seen easily by considering the fact that it would otherwise lead to a highly unstable and rather unphysical situation.

[11] Usually, these are niobium-alloys, like Nb_3Sn or $NbTi$, the material used for the superconducting magnet in this study, see section 4.2.

5.5   Flux Pinning

From the previous discussion it is clear that the useful property of dissipation-free current transport in type-II superconductors is only possible if the vortices can be pinned effectively, and thereby their movement due to the Lorentz force be suppressed. Fortunately, almost any kind of defect or inhomogenity in the crystal structure will achieve this, because this usually leads to a local suppression of the order parameter. Since superconductivity is already suppressed in the core of a flux line there is an attractive interaction between regions of reduced superconductivity and the cores of flux lines. There are two ways in which defects can alter superconductivity. One is by reducing the critical temperature (δT-pinning) and the other is by increasing the effective mass of the electrons through increased scattering (δl-pinning). Though the details of the flux pinning are different, these two mechanisms will not be distinguished in the remainder of this discussion. In fact, for most practical defects it will be a mixture of the two types of pinning.

The dimensionality of the defects does play an important role when it comes to their efficiency in flux pinning and magnetic field orientation. On the one hand there are point defects, 0D objects, realized by impurity atoms or vacancies in the crystal lattice, for example. On the other hand there are correlated defects in one or two dimensions. Examples of one dimensional defects are screw dislocations or columnar defects generated by high-energy ion bombardment. Examples of 2D defects are grain boundaries, twin planes[12] or the defect structure caused by the columnar growth discussed in section 2.2. In general these defects are randomly distributed, thus point defects exhibit no preferred pinning direction, yet one and two dimensional pinning sites are highly anisotropic. They are most effective at preventing flux motion when the flux lines can lock into the direction defined by the defect, i.e. when the defect structure and applied magnetic field are co-aligned.

---

[12] YBCO is not exactly uniaxial, the lattice parameters a and b are slightly different. In a single crystal of YBCO the interface between two domains rotated by 90° thus causes a strain field which leads to a reduction of the superconducting order parameter in the vicinity of this interface.

In the following, the theory of weak collective pinning developed by Larkin and Ovchinnikov [80, 81] will be introduced and the effects of pinning on the liquid and solid vortex phases will be discussed. One important consequence of pinning by randomly distributed defects in three or less dimensions will be the destruction of the long-range order of the vortex lattice, the resulting solid vortex phase is then known as a vortex glass.

5.5.1   Weak Collective Pinning

The simplest situation to introduce the basic concepts of weak collective pinning is an isolated vortex ($a_0 \gg \lambda$) in an isotropic superconductor subject to pinning by randomly distributed point defects. The free energy functional describing the situation with the magnetic field in the z- and the current in the y-direction may be expressed as follows:

$$\mathcal{F}(\vec{u}) = \int \left(\frac{\epsilon_l}{2}(\partial_z \vec{u})^2 + \epsilon_{\text{pin}}(z, \vec{u}) - \vec{f}_L \cdot \vec{u} \right) dz, \qquad (5.33)$$

where $\vec{u}(z)$ is a displacement vector of the flux line. The last term is the free energy due to the Lorentz force acting on the flux line, ϵ_{pin} is the pinning potential and the first term is the contribution from elastic deformations of the flux line, where ϵ_l is the line tension of a flux line:

$$\epsilon_l = \frac{1}{4\pi\mu_0} \left(\frac{\Phi_0}{\lambda} \right)^2 \ln \kappa = \epsilon \ln \kappa, \qquad (5.34)$$

where for later convenience the energy scale $\epsilon = \Phi_0^2/4\pi\mu_0\lambda^2$ has been introduced. When dealing with point defects, the size of the defects is assumed to be much smaller than the core of the vortex, and thus the typical length scale over which the pinning potential is resolved is given by ξ. Individual point defects within a distance ξ from the flux line compete with each other in such a way that only fluctuations in the defect distribution result in a net pinning force. The energy by which a segment of length L of a flux line is pinned is given by

$$\langle \mathcal{E}_{\text{pin}}^2 \rangle^{1/2} \simeq \left(f_{\text{pin}}^2 n_i \xi^2 L \right)^{1/2} \xi \simeq (\gamma_{\text{dis}} L)^{1/2} \xi, \qquad (5.35)$$

where $\langle \ldots \rangle$ denotes the average over the pinning volume given by $\xi^2 L$, f_{pin} is the average pinning force of a single defect, n_i is the defect density, and the disorder parameter is given by $\gamma_{\text{dis}} \simeq f_{\text{pin}}^2 n_i \xi^2$. Equation 5.35 shows that the pinning energy grows only sublinearly with L, but the contribution from the driving Lorentz force grows in direct proportion to L, which means a stiff vortex in a three dimensional superconductor subject to pinning by random point defects will always be unpinned by an external current.

The vortex is, however, an elastic object which can change its shape to find the best pinning potential. This is limited by the line tension of the vortex given in equation 5.34. The main idea of weak collective pinning is that the vortex can be thought of being made up of individual line segments of collective pinning length L_c. L_c is defined as the longitudinal length for which the transverse displacement exceeds the coherence length ξ. Each segment is then pinned independently and can compete with the Lorentz force. A dimensional estimate gives the pinning length for a single vortex as

$$L_c^{sv} \simeq \left(\frac{\epsilon^2 \xi^2}{\gamma_{dis}} \right)^{1/3}, \tag{5.36}$$

and by inserting this result back into equation 5.35 it gives an expression for the pinning energy. Equating the resulting pinning force and the Lorentz force on segments of the length L_c^{sv} allows one to relate the collective pinning length and the critical current density for the case of weakly pinning point defects and small applied fields:

$$J_c^{sv} \simeq J_0 \left(\frac{\xi}{L_c^{sv}} \right)^2. \tag{5.37}$$

For larger applied magnetic fields, interactions between flux lines cannot be ignored and they form vortex bundles, structures of several vortices which are treated as one unit subject to the various forces present. Obviously different length and energy scales have to be considered. In the plane perpendicular to the applied field, ξ is replaced by the lateral dimension R_c of the vortex bundle. The collective pinning length will be dependent in some way on R_c, and the pinning

energy will be determined by the correlation volume $V_c = R_c^2 L_c$. Additionally the elastic properties have to be expressed by the elastic moduli of the flux lattice instead of the line tension of a single vortex. It turns out that one has to distinguish between two different regimes: the small bundle regime when the bundle consists of only a few vortices, or $a_0 < R_c < \lambda$, and the large bundle regime, when the lateral correlation length becomes larger than the penetration length $R_c > \lambda$. Using the same argument as above the critical current density can be calculated by equating the Lorentz and pinning energies:

$$J_c = \frac{U_c}{BV_c\xi}. \tag{5.38}$$

Expressing equation 5.38 as a function of the correlation length R_c it can be shown that $J_c \propto R_c^{-2}$. Therefore, reducing R_c increases the critical current. Naturally this can be achieved by increasing the pinning energy, but also by softening the flux lattice, that is for reduced elastic constants c_{ij}. This allows the flux lines to better accommodate themselves to the pinning potential. This softening of the flux lattice and thereby increased critical current density is used to explain the peak effect associated with the flux lattice melting discussed above in section 5.4. Inserting expressions for the pinning energy U_c and the correlation volume V_c for the respective single vortex, small bundle and large bundle pinning regimes gives the following dependence of the critical current density on the average flux density in the bulk superconductor [9]:

$$J_c(B) \simeq \begin{cases} J_c^{sv} & \text{single vortex,} B < B_{sb} \\[2mm] J_c^{sv} \dfrac{B}{B_{sb}} \exp\left[-2\tilde{c}\left(\dfrac{B}{B_{sb}}\right)^{3/2}\right] & \text{small bundles,} B_{sb} < B < B_{lb} \\[2mm] J_c^{sv} \dfrac{\Phi_0}{\lambda^2} \dfrac{B_{sb}^2}{B^3} & \text{large bundles,} B > B_{lb} \end{cases} \tag{5.39}$$

B_{sb} is the lower boundary of the small bundle pinning regime, $\tilde{c}$ a constant of order unity and J_c^{sv} the single vortex critical current density from equation 5.37. The field-dependence of the critical current is shown schematically in figure 5.4. It is important to note that the already low critical current in the single vortex

regime ($J_c^{sv} \ll J_0$), drops further quickly once the small bundles region is entered ($J_c \propto \exp(-B^{3/2})$). At even higher fields it reduces at a slower algebraic rate $\propto B^{-3}$.
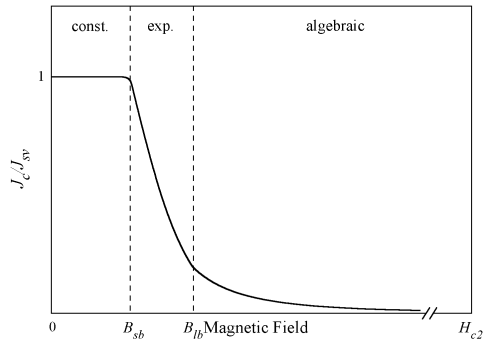

Figure 5.4: Schematic field-dependence of the critical current. At low fields, in the single vortex regime, J_c is field-independent. In an intermediate field range the critical current decays exponentially before crossing over to an algebraic relation at high magnetic fields. Also compare with equations 5.39; the cross-over fields B_{sb} and B_{lb} depend on the disorder and the GL-parameter κ [9].

The above results can be generalized for the case of anisotropic superconductors using the scaling method described above. However, the scaling approach is only applicable for a limited range of magnetic fields. The limits of the scaling approach and a derivation of more general results can be found in [9].

5.5.2   Vortex Creep and Thermal Depinning

Finite temperatures have two effects on the pinning of vortices. Firstly, the flux lines will vibrate about their equilibrium positions, leading to the smoothing of the pinning potential until eventually they will be depinned for temperatures exceeding the depinning temperature T_{dp}. Secondly, thermally activated jumps of the flux lines over the potential barriers lead to the phenomenon of flux creep.

Consider the following situation, sketched in figure 5.5, for an understanding of flux creep: a single vortex in a local minimum of the free energy potential, subject to pinning by randomly distributed defects and a distribution of pinning strengths. Without any transport current applied, the probability for a thermally activated jump over the energy barriers will be equal in any direction, on average. Consequently no net flux flow will occur. The effect an applied current has on the potential landscape is to tilt the whole potential in such a way that the average gradient is proportional to the current density[13]. Now the probability for flux

---

[13] This assumes that the pinning forces are independent of the current density.
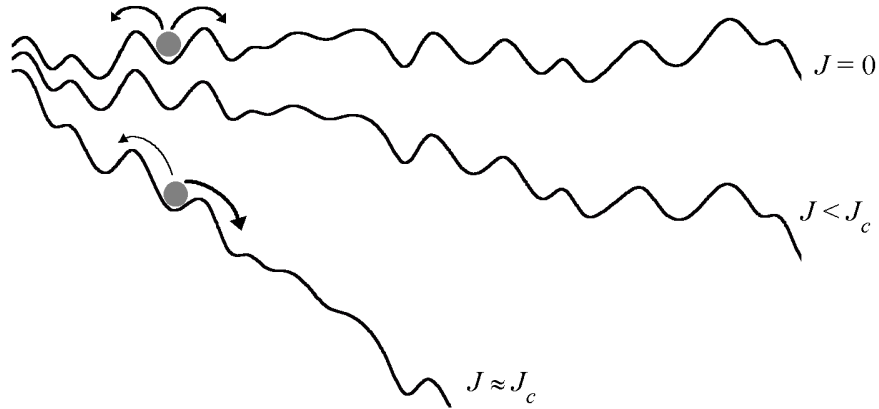
Figure 5.5: Vortex in random pinning potential for various applied current densities J as given in graphic. For zero applied current the vortex sits in a local minimum and the probability for a thermally activated jump in either direction is an average equal. For increasing current densities the probability for a activated jump in the direction of the Lorentz force increases compared with the probability for the opposite direction, which leads to a net flux motion and consequently to electrical resistance.

jumps to occur in the direction of the gradient increases relative to jumps in the opposite direction, which leads ultimately to a net flux motion in the direction of the Lorentz force and therefore energy dissipation. For current densities exceeding the critical current densities calculated in the previous section the potential will effectively flatten out, so that no pinning can occur anymore and flux creep changes into flux flow.

A more detailed investigation of the phenomenon of flux creep was first undertaken by Kim and Anderson [82–84] in conventional type-II superconductors. The Maxwell equation $\vec{\nabla} \times \vec{B} = \mu_0 \vec{J}$ relates a macroscopic or screening current to a vortex density gradient that will decay due to such thermally activated jumps over the pinning barriers. Anderson proposed the following logarithmic decay of a transport current due to flux creep, valid near the critical current density J_c:

$$J(t) = J_c \left[1 - \frac{k_B T}{U_c} \ln \left(1 + \frac{t}{t_0} \right) \right]. \tag{5.40}$$

Here t is the time, t_0 a characteristic decay time and U_c the characteristic pinning energy defined above. This logarithmic decay of a persistent current has been verified experimentally, for example [82]. It has important implications for the

operation of superconducting magnets, like the one used in this study. If the current is close to the critical current J_c, it will drop rather rapidly over a short period of time. But for the next time decade, the total reduction of the persistent current due flux creep will be just the same. Thus, superconducting magnets are operated at persistent currents sufficiently below J_c so that the magnetic field is practically constant over a period of days or longer. M. Tinkham [42] gives an estimate of how long it would take for a persistent current to die out completely if the above equation would hold over the complete range of currents. He comes up with a decay time $\approx 10^{390}$ years (!), thus for any practical application currents not too close to the critical current for depinning are truly persistent, even though the resistance may still be finite.

An interesting question now arises: can a true superconducting state in the mixed phase of type-II superconductors exist, that is, does $\rho \to 0$ in the limit of small applied currents $J \to 0$? For one-dimensional flux lines the pinning barrier will depend on the current density, since not only the height of the barrier will change with current, but also the length of a vortex segment that can jump over the barrier into the next low-lying potential minimum. It can be seen from figure 5.5 already that the potential barrier for vortex creep decreases with increasing current. However in this model the one-dimensional character of the flux lines was neglected. Taking that into account, it follows that for small applied currents the next neighboring configuration that has a similar or lower total energy will be far away. Thus, the total length of the flux line that has to be deformed will be large as well, and consequently the activation energy for such a jump will be high. This is illustrated in the schematic graph 5.6, where the free energy is plotted versus the hopping length for different applied current densities. The optimal hopping length $L_{\text{opt}}(J)$ and the necessary activation energy $U(J)$ is also indicated.

As the current density is increased, the next favourable pinning site will be closer to the original position. This leads to a shorter hopping length and a shorter section of the flux line that needs to hop over a potential barrier, thus the necessary activation energy for the process to happen will be sharply reduced. A
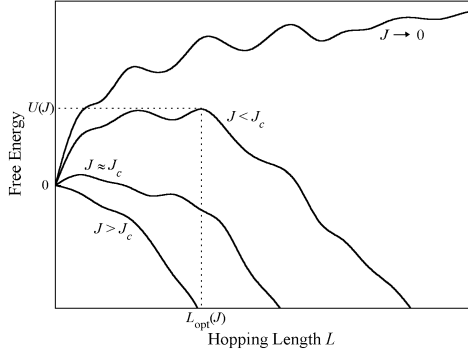
Figure 5.6: Schematic dependence of the energy barrier for thermally activated vortex creep on the length L of the vortex segment for different current regimes. As the current density increases the height of the barrier decreases as well as the optimal length of the vortex segment that can go over the barrier. This leads to a highly non-linear resistive behaviour in the vortex creep regime of the phase diagram.

consequence of this behaviour is that small applied currents probe large distances of the pinning potential to find a new pinning site. On the other hand, applying large current densities, approaching the depinning current density for which the activation energy goes to zero, one looks at the short range pinning landscape.

Dimensional estimates for the dependence of the optimal vortex length on the current density result in an algebraic relation between the pinning energy and applied current

$$U(J) \sim U_c \left(\frac{J_c}{J}\right)^{\mu},\tag{5.41}$$

and the current-voltage characteristics display the following *glassy* behaviour

$$V \propto \exp\left[-\frac{U_c}{k_B T}\left(\frac{J_c}{J}\right)^{\mu}\right].\tag{5.42}$$

The exponent μ depends non-trivially on magnetic field and current [9,85,86]. But in any case, $\mu > 0$ and therefore the pinning barriers diverge and the resistance vanishes in the limit of zero applied current, in contrast to Anderson's original proposal which predicted a finite ohmic resistance down to zero current density. Whether such a *glassy* regime exists or not will be discussed in more detail in section 5.6 on vortex glass theories.

As the thermal displacement $\langle u^2 \rangle_{th}^{1/2}$ grows larger than ξ due to increasing temperature, ξ has to be replaced by the averaged thermal displacement as the shortest relevant length scale determining the pinning potential. Most importantly, the critical current densities in the various flux pinning regimes are re-

duced drastically according to these relations [87, 88]:

$$J_c(T) \propto \begin{cases} \exp\left(-T^3\right) & \text{single vortex and small bundles} \\ T^{-11/2} & \text{large bundles} \end{cases} \tag{5.43}$$

5.5.3   Pinning in Vortex Liquids

It has already been argued above that the flux line lattice in clean superconductors eventually melts into a flux liquid via a first order phase transition at the melting temperature T_m. Apart from the loss of long range order in the spatial positions of the flux lines, the basic difference between the two phases is a vanishing shear modulus in the liquid phase, analogous to the conventional melting transition, for example from ice to water. It is reasonable to assume that the melting temperature $T_m(H)$ is only weakly affected by weak disorder, and even in the presence of a weak pinning potential thermal energy will drive a solid vortex phase, whose nature will be discussed in the next section, into a vortex liquid phase at some field dependent melting temperature. Strong pinning, on the other hand, will shift the melting line to higher temperatures and fields. In many conventional low-temperature type-II superconductors, this occurs to such an extent that the melting transition basically coincides with the upper critical field and the liquid phase is experimentally difficult to observe.

Because of the elastic forces in a vortex solid, it is principally enough to pin just one flux line, although the critical current will be very small and it is desirable to have as many vortices as possible pinned by defects. In the vortex liquid phase this is no longer true and the unpinned vortices dominate the dynamic behaviour. Furthermore, the flux lines sample the pinning potential over a much larger volume given by the thermal displacement $\langle u^2 \rangle_{th}^{1/2} \gtrsim a_0 \gg \xi$, and the question arises whether disorder plays any role at all in vortex liquids. For temperatures just above the melting temperature, the vortex liquid can be considered to be in a highly viscous state and the time scale τ_{pl} for plastic deformations to relax can be much larger than the time scale τ_{th} for short-scale elastic deformations. A dynamic approach [9] identifies this low-temperature liquid phase, or *pinned* vortex

liquid, with vortex flow dominated by large, but finite plastic barriers U_{pl}. These barriers are indeed affected by the disorder and the resistance shows a strong exponential dependence on temperature:

$$\rho \propto \exp\left(-\frac{U_{pl}}{k_B T}\right).\tag{5.44}$$

The relevant barriers in this regime of thermally activated flux flow (TAFF) involve plastic deformations on a length scale equal to the vortex separation a_0. For deformations of such short wavelength, all the elastic moduli are of the same order, thus the energy barriers can be estimated as [89–91]

$$U_{pl} \sim \gamma \epsilon a_0 \propto \frac{T_c - T}{\sqrt{H}}.\tag{5.45}$$

Only for even higher temperatures can the disorder potential be neglected. In this case the unpinned vortex regime is entered and the result for free flux flow is recovered (equation 5.32). In strongly layered superconductors a very different mechanism may dominate the resistance in the thermally activated region. As in ordinary matter flux lines may move away from their equilibrium position or may be even completely missing, creating a vacancy. These defects are known as dislocations and they occur in vortex systems as well. In response to an applied current and the resulting Lorentz-force such dislocations can move, and if there is magnetic flux associated with such a defect structure this will lead to resistance. For topological reasons in 3D superconductors, only dislocations with a net flux equaling zero are allowed. This restriction does not exist in two dimensions, which results in a number of interesting phenomena in thin films or strongly layered superconductors. Feigel'man et al. considered the effects of dislocations on the dynamic behaviour of flux lines [92]. Without going into the details of their theory, they found a thermally activated flux flow region for 2D or quasi-2D superconductors that is mediated by the creation of unbound dislocations, for which they found the following activation energy

$$U_{dis} \simeq \frac{\Phi_0^2 d_{sc}}{32\pi^2 \mu_0 \lambda_{ab}^2(T)} \ln\left(\frac{H_0}{H}\right),\tag{5.46}$$

where d_{sc} is the thickness of a superconducting layer and $H_0 \sim H_{c2}$ is a characteristic magnetic field. Evidence for this kind of flux motion has been found in thin films of a-MoGe [93, 94], very anisotropic multilayers of YBa$_2$Cu$_3$O$_7$/-PrBa$_2$Cu$_3$O$_7$ [95] and also in multilayered Ta$_x$Ge$_{1-x}$/Ge films [32].

Figure 5.7 summarizes the above results for vortex pinning and the different regimes of a three dimensional superconductor in a double logarithmic plot of voltage versus current. For temperatures just below the mean-field transition
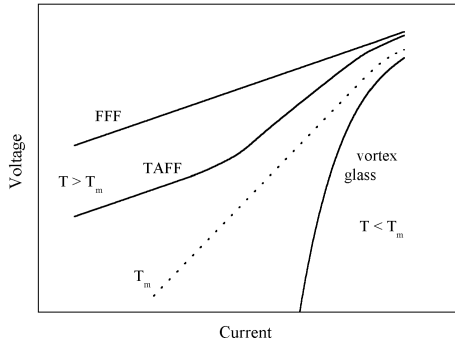

Figure 5.7: Theoretical *IV*-characteristics in a log-log plot summarizing the different regimes of vortex pinning in three-dimensional superconductors.

$H_{c2}(T)$ the flux lines are in their unpinned liquid state and the resistance is given by the Bardeen-Stephen value, equation 5.32. As the temperature is lowered plastic deformations become important and the TAFF-region is entered. At low excitation currents the resistance shows an exponential dependence on temperature and is well below the anticipated free flux-flow value. As the current is increased, smaller and smaller volumes are probed by the current, which effectively reduces the plastic deformation energy barriers and the resistance gradually approaches its free flow value. For temperatures below the melting temperature, the voltage is given by equation 5.42 for the vortex glass phase with zero resistance in the limit of zero applied current. Details of the vortex glass phase, and the transition from the liquid into the glass phase, will be discussed in the next section. For very high applied currents, the velocities of the moving vortices can reach relatively high values. This can lead to a smearing of the pinning potential and experimental measured IV-curves may deviate from the theoretical exponential behaviour. At even higher driving currents an instability can occur that drives the system normal conducting [96] and that has been studied previously for similar Ta$_x$Ge$_{1-x}$/Ge films [32, 97].

5.6 Vortex Glass Theories

So far the discussion has identified several different vortex phases with quite different thermodynamic and electrical properties. The central question of whether there are vortex phases which are truly superconducting, with zero resistance in the limit of zero applied current density, has not been fully answered, although the possibility that flux creep may give vanishing ohmic resistance has been mentioned. What can been said though, is that vortex liquid phases and the flux line lattice in very clean superconductors do have a finite resistance, which can vary from almost normal resistance for unpinned vortices in high magnetic fields, to resistances many orders of magnitude smaller in pinned vortex fluids in the TAFF region. But does the resistance remain finite when the temperature is lowered below the melting temperature and the vortices form an unordered solid phase, as predicted by the Anderson-Kim flux creep theory? Or is this phase characterised by a vanishing ohmic resistance caused by diverging pinning barriers and a *glassy* current-voltage characteristic?

Experimentally, it is extremely difficult, if not impossible, to measure zero resistance, because every real apparatus does have a finite sensitivity and resolution. The best one can do is to give an upper limit of the resistance. Consequently, a different approach to the problem of true superconductivity in the unordered solid vortex phase in the presence of disorder is needed. It is worth mentioning here that this is more a fundamental than technical issue, because the resistances below a temperature dependent critical current, although maybe finite, are so small that they can be neglected. From the applications point of view it is more important to increase these critical currents.

This new approach to the vortex phase and the vortex dynamics below the melting transition in the presence of a pinning potential was developed by Fisher [12] and Fisher *et al.* [98], and is based on similarities between magnetic phases in ordinary matter and vortex phases in superconductors [99]. In superconductors, the phase ϕ of the complex order parameter $\Psi = |\Psi| \exp(i\phi)$ takes the role of the magnetic spin's orientation in ordinary magnetic materials, and various superconducting phases can be mapped to their magnetic counterpart. In the Meissner

phase, for example ϕ takes on the same time-averaged value everywhere in the material, just as the spins in a ferromagnet all point in the same direction. In the flux line lattice the phase ϕ still has long-range order, although in a non-trivial fashion reflecting the other long-range order in the system, the translational order of the positions of the flux lines. This type of long-range order in ϕ can be identified with the magnetic ordering in antiferromagnetic materials.

As the temperature is increased above the Curie or Néel temperature, thermal fluctuations destroy magnetic ordering and the paramagnetic phase is entered. In superconductors this is the vortex fluid phase, when the long-range order of the phase of the superconducting wave-function cannot be established and superconductivity is destroyed. In the presence of disorder the flux lines freeze into a compromise configuration determined by the distribution of random pinning sites. Because the vortices are frozen in position, the phase of the order parameter has again true long-range order, reflecting the vortex arrangement in a complicated way. This kind of order is analogous to the magnetic order in so called *spin glasses* [100, 101], where the magnetic spins are frozen in time, again in a seemingly random way determined in detail by the microscopic interactions of the material. By this analogy the disordered solid vortex phase is called vortex glass phase. The ansatz of the vortex glass theory by Fisher *et al.* is to look for a thermodynamic phase transition from the liquid to the glass phase. If the transition is first order, the resistivity and other properties would change discontinuously at the transition. However, it turns out that it is a continuous phase transition and material properties, the conductivity for example, are expected to obey universal scaling laws.

5.6.1 Point Disorder: 2D and 3D Vortex Glass Theory

The original vortex glass theory was developed for the case of weak pinning by point-like defects with spatial extensions less than the coherence length ξ in every direction. Furthermore, the model neglects the anisotropy introduced by the flux lines, although it may be possible to eliminate the anisotropy by rescaling the lengths (see [98] for details). As a measure of the long-range phase coherence the

following vortex glass (VG) correlation function is defined:

$$G_{\mathrm{VG}}(\vec{r}) = \langle |\langle \Psi^*(\vec{r}') \Psi(\vec{r}' + \vec{r}) \rangle_{\mathrm{th}}|^2 \rangle_{\mathrm{dis}}, \qquad (5.47)$$

where Ψ is the complex order parameter, $\langle \ldots \rangle_{\mathrm{th}}$ is the thermal average, and $\langle \ldots \rangle_{\mathrm{dis}}$ the spatial average over the disorder. In the VG phase G_{VG} takes on a finite constant value for $\vec{r} \to \infty$, but decays exponentially on a length scale of the glass correlation length ξ_{VG} in the vortex liquid phase. The theory of second order or continuous phase transitions predicts that certain variables show universal behaviour in the vicinity of the phase transition. Explicitly, the VG correlation length ξ_{VG} is expected to diverge as the glass melting temperature T_g is approached according to

$$\xi_{\mathrm{VG}}(T) \propto |T - T_g|^{-\nu}, \qquad (5.48)$$

with ν being the static glass exponent. The dynamic response of the system is given by the relaxation time τ_{VG}, which also diverges close to the glass phase characterised by the dynamic critical exponent z

$$\tau_{\mathrm{VG}}(T) \propto \xi_{\mathrm{VG}}^z. \qquad (5.49)$$

From these relations one can get scaling relations for the dynamic response functions. In the following the nonlinear current-voltage characteristics will be considered in detail. Using simple dimensional arguments based on the scaling behaviour of the vector potential $\vec{A}$, the following scaling ansatz is obtained

$$E\xi_{\mathrm{VG}}^{z+1} = \mathcal{E}_{\pm}(J\xi_{\mathrm{VG}}^{D-1}), \qquad (5.50)$$

with D being the dimensionality of the system, $\mathcal{E}_{\pm}$ being universal scaling functions above $(+)$ and below $(-)$ T_g, and E and J are the electric field and current density, respectively. No analytical expression for the scaling functions $\mathcal{E}_{\pm}$ are known, nevertheless using some rather general arguments one can extract a num-

ber of scaling relations which allow the determination of the critical exponents ν and z, as well as the glass melting temperature T_g.

Right at the melting temperature, the correlation length ξ_{VG} diverges and for the electrical field to remain finite, ξ_{VG} has to cancel out on both sides of equation 5.50, hence $\mathcal{E}_{\pm}(x \to \infty) \propto x^{(z+1)/(D-1)}$, which results in a power-law relation between current density and electric field

$$E \propto J^{(z+1)/(D-1)}, \text{ for } T = T_g. \tag{5.51}$$

Thus, a log-log plot of the current-voltage characteristic should be a straight line and the logarithmic gradient $\mathrm{d}\ln V/\mathrm{d}\ln I$ a horizontal line at $y = (z+1)/2$ for $D = 3$. For temperatures $T > T_g$ the system is in the vortex liquid state, showing ohmic resistance for small applied currents. Accordingly, the scaling function is linear in its argument $\mathcal{E}_{+}(x \to 0) \propto x$, which results in the following temperature dependence for the resistance at temperatures above, but close to T_g:

$$\rho \propto \xi_{\text{VG}}^{(D-z-2)} \propto |T - T_g|^{\nu(z+2-D)} \ (T > T_g). \tag{5.52}$$

Below the transition temperature glassy behaviour is expected, $\mathcal{E}_{-}(x \to 0) \propto \exp(-a/x^\mu)$, leading to an exponential dependence of the electrical field on current density

$$E \propto e^{-c(J_c/J)^\mu} \ (T < T_g), \tag{5.53}$$

with $\mu \lesssim 1$. As the current density is increased smaller and smaller volumes are probed by the current. At high current densities the current-voltage curves above and below the glass temperature are expected to show critical power-law behaviour. The critical current density that marks the cross-over from the low current to the high current regime scales again with the correlation length

$$J_x^{\pm} \propto \xi_{\text{VG}}^{(1-D)} \propto |T - T_g|^{\nu(D-1)}. \tag{5.54}$$

At small fields when the glass melting temperature $T_g \rightarrow T_c(0)$, the following power-law behaviour should be observed

$$[T_c(0) - T_g(H)] \propto H^{1/2\nu_0}, \tag{5.55}$$

with $\nu_0 \simeq 2/3$.

For a second order phase transition critical scaling is expected to be universal, that is, the critical exponents ν and z depend only on dimensionality and symmetry and not on magnetic field or temperature, not even the superconducting material itself. If a plot is made of appropriately scaled current-voltage characteristics taken at different temperatures and fields within the critical region near $T_g(H)$, all curves should collapse onto the scaling functions $\mathcal{E}_\pm$ for temperatures above and below the melting temperature, respectively. From equation 5.50, it is obvious that, in order to check the scaling, plotting $(E/J)|T - T_g|^{-\nu(z-D+2)}$ versus $J|T - T_g|^{\nu(1-D)}$ should result in the collapse of all IV-curves onto the two universal functions $\tilde{\mathcal{E}}_\pm$, above and below the transition temperature respectively[14].

Although the above vortex glass theory has been developed for general dimensionality, it applies primarily to 3D superconductors[15]. In 2D or quasi-2D systems the motion of flux carrying unbound dislocations (compare section 5.5.3) extend the vortex liquid phase down to zero temperature with the glass temperature $T_g \equiv 0\,\mathrm{K}$ [9, 98]. This makes it difficult to distinguish vortex glass theory from the Anderson-Kim theory of flux creep. However in VG theory, the critical current density separating linear from nonlinear current-voltage behaviour is expected to scale as $J_x^{2D} \propto T/\xi_{\mathrm{VG}} \propto T^{1+\nu}$ as $T = 0\,\mathrm{K}$ is approached, compared to a linear temperature dependence in the flux creep theory.

A mean-field analysis of the VG transition in 3D succeeded in calculating the critical exponents and was able to verify the scaling relation for the resistance above T_g [102]. The exponents $\nu = 1/2$ and $z = 4$ are identical to those obtained

---

[14] From equation 5.50 one would expect to plot $E\xi_{\mathrm{VG}}^{z+1}$ versus the argument of the scaling function. However, it is common practice to plot the scaled resistivity as given in the text versus the argument of the scaling function $\tilde{\mathcal{E}}_\pm(x) = \mathcal{E}_\pm(x)/x$.

[15] It may also be applied to higher dimensional systems, but that is of rather mathematical interest only.

for Ising spin glasses. By analogy with real spin glasses experimental critical exponents for vortex glasses are expected to be $\nu \approx 1/2 - 1$ and $z \approx 4 - 7$, respectively [98].

Early support for the VG idea came from measurements on YBCO, which were consistent with VG predictions [103, 104]. However, these materials contained twin-planes and the low-temperature glass phase is more appropriately described by a derivation of the VG theory, which will be discussed below. In the meantime many more investigations were undertaken to search for evidence of a VG transition in materials that do not have extended pinning sites like twin-planes. These materials include the common HTSC YBCO [105] and BSCCO [106, 107], but also $Nd_{1.85}Ce_{0.15}CuO_{4\pm\delta}$ [108, 109] and the isotropic HTSC $(K,Ba)BiO_3$ [110, 111] as well as the low-temperature superconductor Mo_3Si [112]. The reported values for the critical exponents ν and z vary substantially, but as P. Voss-de Haan *et al.* [113, 114] have shown, this can be a result of different current and voltage ranges of the measured *IV*-curves and if the analysis relies solely on the scaling collapse of them. The most reliable values suggest $\nu > 1$ and $z > 4$ for most of the systems mentioned above and in line with theoretical predictions. An experiment in particularly strong support of a second-order phase transition below $H_{c2}(T)$ was done by M. Roulin *et al.* They measured specific heat steps in YBCO and identified this transition with the VG melting line [115].

The two dimensional behaviour has been observed as well. In very thin YBCO films [116] and highly anisotropic $Tl_2Ba_2CaCu_2O_8$ [117] the true 2D vortex glass scaling with $T_g = 0$ has been reported, and successively deoxygenated YBCO thin films showed a cross-over from 3D to 2D vortex glass with a quasi-2D intermediate phase [118].

5.6.2   Extended Defects: Bose-Glass Theory

The discussion in the previous sections focused on pinning by point defects, which is generally relatively weak, and for randomly distributed defects it is also isotropic, apart from any anisotropy of the underlying superconductor itself. A major problem in the application of HTSCs is their rather limited critical cur-

rent density J_c, especially in applied magnetic fields and at high temperatures. Although the presence of point-like defects can increase the critical current density significantly [119], they are not effective for increasing the range of magnetic fields over which large critical current densities can be achieved, especially at high temperatures [119, 120]. Much better pinning efficiency is expected for defects whose dimensionality is better adapted to the intrinsic dimensionality of the vortex system, that is, one or two dimensional structures that span a considerable fraction of the superconductor's thickness with typical extensions in the other directions of the order of the coherence length ξ. Examples of 1D defect structures are screw dislocations as observed in thin films of YBCO [121–123] or columnar tracks artificially produced by bombardment with high-energy heavy ions, such as Sn, Xe, Pb, and others [124–126]. Planar pinning sites are realized for twin-planes in YBCO, for example [127, 128]. Theoretical ideas describing pinning by correlated defects have been developed at about the same time as these early experiments [129–132].

For magnetic fields aligned with the correlated defect structure, the pinning force grows on average linearly with the flux line length L, compared with the $L^{1/2}$-growth for point-disorder (section 5.5.1). Furthermore, thermal reduction of the pinning potential is expected to be much more gradual, leading to less reduced critical currents for increased temperatures[16] [9, 125, 133]. The new anisotropy introduced by these extended defects also leads to a wealth of new effects, such as a transverse Meissner effect. In this case a magnetic field applied transverse to the defect orientation is perfectly screened until a critical field is reached due to the locking of the field direction to the defects. In other words there is an infinite tilt modulus c_{44} for tilting angles less than a critical angle θ_c [9]. Another effect is different vortex motion along and perpendicular to the pinning planes. There has even been the suggestion that pinning along the planes could be reduced [134].

Considerable interest exists again in the low-temperature phase of the vortex system. Most importantly, does a zero-resistance phase exist in the presence

---

[16] This is true for not too high temperatures. When the thermal displacement $\langle u \rangle_{\text{th}}^{1/2} > d$ the typical distance between defects the T-dependence becomes more like that for weak collective pinning.

of correlated disorder, and if so, is it any different from the vortex glass phase, which exists when point disorder dominates? Nelson and Vinokur (NV) [131] have developed a scaling theory for correlated disorder quite similar to the VG theory, but with some important differences. Their theory is based on a strong analogy between vortices and 2D-bosons in the presence of a random potential as it is realized for helium films on a rough surface. They predict a low-temperature *Bose-glass* (BG) with flux lines localized on the extended defects separated from an entangled flux fluid of delocalized vortices at higher temperatures by a continuous phase transition. The original BG theory focused on pinning by columnar defects, like those created by ion irradiation, but was extended by Marchetti and Vinokur [132, 135] to also include pinning by coplanar defects.

In the following it will be assumed that the magnetic field is parallel to the defects. NV introduce a root-mean-square transverse wandering length $l_\perp(T)$, which is a measure of how far the flux line has *wandered* from its pinning site in the direction transverse to the applied field. As the transition temperature T_{BG} is approached from below, this length scale is expected to diverge

$$l_\perp(T) \propto |T - T_{\mathrm{BG}}|^{-\nu'}, \tag{5.56}$$

with a static critical exponent ν' different from the corresponding ν in the VG theory. Due to the intrinsic anisotropy of the defects it is necessary to also define a longitudinal length scale $l_\parallel(T)$. The simplest possible choice relates it to the transverse length scale

$$l_\parallel \propto l_\perp^2. \tag{5.57}$$

The typical relaxation time is given by (compare with equation 5.49)

$$\tau_{\mathrm{BG}} \propto l_\perp^{z'}, \tag{5.58}$$

with the new dynamic critical exponent z'. Very similar dimensional arguments result in the new scaling ansatz for Bose-glass scaling

$$El_\perp^{z'+1} = \mathcal{F}_\pm(Jl_\perp l_\parallel), \tag{5.59}$$

with yet another pair of scaling functions $\mathcal{F}_\pm$ above and below the transition temperature, respectively. Taking the limits $x \to 0$ and $x \to \infty$, where x is the argument of the scaling function as above, one gets similar relations from which to determine critical exponents and the transition temperature:

$$E = J^{(z'+1)/3} \text{ for } T = T_{\mathrm{BG}}. \tag{5.60}$$

The resistance above T_{BG} should vanish like

$$\rho \propto |T - T_{\mathrm{BG}}|^{\nu'(z'-2)} \, (T > T_{\mathrm{BG}}), \tag{5.61}$$

and the glassy behaviour below the transition temperature is given equal to equation 5.53

$$E \propto e^{-c(J_c/J)^\mu} \, (T < T_{\mathrm{BG}}) \tag{5.62}$$

with a possibly different glass exponent μ (see below section 5.6.3). The crossover current densities separating critical from noncritical behaviour are given by

$$J_x^\pm \propto (l_\perp l_\parallel)^{-1} \propto |T - T_{\mathrm{BG}}|^{3\nu'}. \tag{5.63}$$

Comparing equations $5.60 - 5.63$ with the corresponding equations $5.51 - 5.54$ for the vortex glass theory one finds that they are very similar. In fact one can get the scaling laws for Bose-glass from the vortex glass equations by setting $D = 4$ and replacing the critical exponents by those for the Bose-glass. It is important, however, to remember that the vortex glass and Bose-glass are two distinct thermodynamic phases. The difference becomes apparent when tilting the magnetic field away from the defect direction. Isotropic pinning by point defects as in the vortex glass phase will lead to a smoothly varying glass melting temperature with

tilting angle θ, only varying due to the possible anisotropy of the superconducting material. By contrast, the BG theory predicts the following scaling relation on how the linear resistance vanishes, depending on temperature and angle between the z-axis (defect direction) and magnetic field

$$\rho(t_{\mathrm{BG}}, \theta) = |t_{\mathrm{BG}}|^{\nu'(z'-2)} \mathcal{G}_{\pm}(\theta|t_{\mathrm{BG}}|^{-\nu'}), \tag{5.64}$$

where $t_{\mathrm{BG}} = (T - T_{\mathrm{BG}})/T_{\mathrm{BG}}$ is the reduced temperature with respect to the Bose-glass transition temperature, and θ the tilting angle. Plotting the transition temperature versus the field perpendicular to the defects results in a sharp cusp, compared to a slowly varying function in the VG theory. Equation 5.64 deviates from the original proposal which had $\theta|t_{\mathrm{BG}}|^{-3\nu'}$ as the argument of the scaling functions $\mathcal{G}_{\pm}$. Lidmar and Malin [136] and NV [137] have published the corrected scaling relation 5.64, where a necessary distinction between the transverse magnetic field $H_{\perp}$ and flux density $B_{\perp}$ is made.

Furthermore, BG theory allows one to estimate the transition temperature in relation to the melting transition T_m of the pure system without defects, based on a Lindemann-criterion. The BG transition temperature can be expressed as a function of the magnetic field and the disorder [9]

$$T_{\mathrm{BG}}(B) \approx \chi T_m(B) + (1 - \chi)T_c \left(1 - \frac{B}{H_{c2}(0)}\right), \quad \left(B > \frac{\Phi_0}{\lambda^2}\right) \tag{5.65}$$

with χ describing the disorder, which in this notation is $\chi = 1$ for the pure system and $\chi \to 0$ in the presence of strong disorder when $T_{\mathrm{BG}}(B) \to T_c(B)$.

The situation when point disorder and extended defects are present was considered by Hwa et $al.$ [138]. In their model, they found that the effect of point disorder can be neglected in most cases. Only for very weak pinning by the correlated compared to the point-like defects the latter will dominate.

As in the case of the VG, many conductivity measurements on a range of different superconducting materials have been interpreted in favour of the existence of a BG. These include studies on ion irradiated YBCO [139, 140] and BSCCO [141] as well as the isotropic (K,Ba)BiO$_3$ [142]. Computer simulations

of appropriate models have also shown a transition into a BG at low temperatures [143, 144]. Convincing evidence for the existence of the BG-phase came from measurements of the characteristic cusp in the transition temperature of twinned YBCO [145] (compare equation 5.64), and the associated screening of a transverse magnetic field, or transverse Meissner effect [146, 147].

5.6.3   Vortex Dynamics in the Glass Phase

The nonlinear dissipation in the glass phase (VG and BG) is caused by vortex excitations, prominent examples being vortex loops, half loops and kinks, depending on sample anisotropy and defect dimensions, for example. For the case of weak collective pinning by point defects, it has been mentioned above (section 5.5.2) that the value of the glass exponent for a given material depends nontrivially on the relevant length scales given by magnetic field, temperature and current density. Thus, the general expectation for the glass exponent μ in the vortex glass is

$$\mu \lesssim 1 \text{ (vortex glass).} \tag{5.66}$$

For vortex dynamics in the Bose-glass phase, more quantitative predictions are possible and some very interesting similarities can be drawn between the dynamics of flux lines and current transport in semiconductors. In figure 5.8 graphical illustrations of the relevant flux line excitations and some of the important length scales are given for columnar pinning [131], as well as coplanar pinning with vortex motion transverse to the pinning planes [132, 135]. In all cases, current densities less than the depinning current density are assumed. If the current density is not too small, half-loop excitations are possible extending a length $l_y < d_r$, d_r being a typical distance between extended defects, perpendicular to the defect and lateral extension l_z, which may be larger than $2l_y$ for the case of anisotropic superconductors. Those half-loops with a radius larger than a critical radius will extend due to the Lorentz-force until the flux line is pinned by a nearby defect. The critical radius is given by the condition that the radial outward Lorentz-force equals the inward force due to the line tension of the
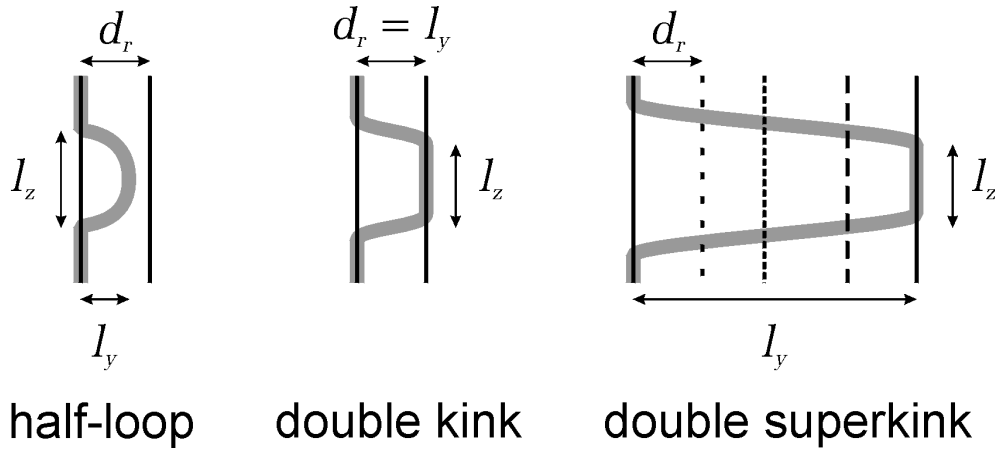
Figure 5.8: Different vortex excitations pinned to extended defects. The black vertical lines represent columnar or cross-sections of coplanar defects with typical spacings d_r. Magnetic field is applied parallel to the defects and flux lines are represented by thick grey lines. The applied current is perpendicular to the paper, such that the Lorentz-force is acting to the right. Typical lengths l_y and l_z for the excitations are also given.

half-loop[17]. For radii smaller than the critical radius, the line tension dominates and the half-loop shrinks back to zero size. The current-voltage characteristic is then given by

$$E/J \approx \tilde{\rho} \exp\left[-\frac{E_k}{k_B T}\frac{J_c}{J}\right] \text{ or } \mu = 1, \qquad (5.67)$$

in equation 5.62, where $\tilde{\rho}$ is a characteristic resistivity, E_k is a typical activation energy, and J_c a current scale. For smaller currents the half-loop excitations are replaced by double-kink or double-superkink excitations. For these excitation modes segments of the flux line tunnel to a neighboring defect through the generation of two kinks, as depicted in figure 5.8. The kink-segments will then spread in opposite directions due to the Lorentz-force, thereby moving the flux line to its new position. If the pinning energies of the individual defects have no or very little dispersion, vortex motion equivalent to nearest-neighbor percolative hopping conductivity in semiconductors is possible with a current-voltage characteristic [9]

---

[17] The same applies to loop excitations as well.

$$E \propto J \exp\left[-\frac{c_p E_k}{k_B T}\right], \tag{5.68}$$

which is actually ohmic. The constant c_p can be obtained from percolation theory [148]. For strong enough dispersion of the pinning energies, the nearest-neighbor pinning site may not be an energetically favourable one, and excitations over larger distances are necessary. The vortex transport is then similar to quantum variable-range hopping (VRH) conductivity in doped semiconductors [148, 149]. In the case of columnar defects the vortex velocity can be calculated analogous to 2D VRH in semiconductors with

$$E/J \approx \tilde{\rho} \exp\left[-\frac{E_k}{k_B T}\left(\frac{J_c}{J}\right)^{1/3}\right] \text{ or } \mu = 1/3, \tag{5.69}$$

with a different current scale J_c and resistivity $\tilde{\rho}$ than in equation 5.67. Vortex dynamics in the presence of coplanar defects corresponds to current transport in 1D semiconductors with the exponent μ differing from the above equation

$$E/J \approx \tilde{\rho} \exp\left[-\frac{E_k}{k_B T}\left(\frac{J_c}{J}\right)^{1/2}\right] \text{ or } \mu = 1/2. \tag{5.70}$$

The activation energy E_k is the energy associated with the creation of the kinks and is given by (see for example [9])

$$E_k = d_r \sqrt{\epsilon_l \epsilon_r(T)}, \tag{5.71}$$

where ϵ_l is the line tension of the flux line, ϵ_r the pinning potential and d_r the mean spacing between defects. For samples of finite thickness, the length scale of half-loop excitations l_z or the longitudinal extension of double-kink structures will grow beyond the sample dimension at low enough currents. As a consequence vortex motion will proceed via rigid transformation of flux lines with a resulting ohmic resistance [9]. A similar scenario is possible in strongly layered superconductors where a description in the form of pancake vortices is more relevant. In

that case ohmic resistance at small currents will set in when the excitations in the z-direction grow beyond the interlayer spacing.

Evidence of VRH processes, responsible for flux creep in the glass phase of type-II superconductors, was found in magnetisation experiments on YBCO with columnar defects [150], and extensive analyses of current-voltage characteristics taken on BSCCO also containing columnar defects [141, 151, 152]. However, measurements of the glass exponent in a YBCO thin film, probably containing twin planes as the dominant pinning sites, revealed a significant temperature and field as well as possibly current dependence of the exponent μ [153].

Chapter 6

Experimental Results and Discussion

In this chapter experimental results are presented for six samples which have been characterised in chapter 3 (see also table 3.1) and which differ from each other in the insulating layer thickness, the pinning strength, and to a lesser extent the superconducting layer thickness.

The detailed analysis below will show that the samples can be divided into two groups according to the Ge-layer thickness. The samples of the first group have thin Ge-layers, and thus strong interlayer coupling. The C-samples with thick superconducting layers as well as the J-samples with thinner TaGe-layers belong to this group. The two P-samples make up the other group of samples having thicker Ge-layers, and consequently weaker interlayer coupling. These differences in coupling between the superconducting layers are reflected in the conducting behaviour in the superconducting mixed phase.

In sections 6.1 to 6.4 the superconducting phase boundaries in the H-T plane will be defined, and important information about the samples anisotropy, resulting from the columnar structure, will be derived. The detailed analysis of the conductivity in the superconducting mixed phase in chapters 6.5 and following will allow us to map different vortex phases in the H-T phase diagram and explain the samples' differences as a consequence of their different microstructure.

The use of SI units would require to write $\mu_0 H$, with $\mu_0 = 4\pi \times 10^{-7}$, for all applied magnetic fields. For convenience and because it is common practice within the scientific community, only the symbol H will be used to refer to the

applied magnetic field in Tesla. Furthermore, as will be seen later, for all the magnetic fields used in this study $B = \mu_0 H$ is a very good approximation for the microscopic field inside the superconducting films.

6.1   Normal State Resistance from 300 K to 4 K

It is helpful and even necessary to have a good understanding of the conduction processes in the normal state of these multilayers, in order to be able to interpret the experimental data below the critical temperature conclusively. We will therefore start by looking at the temperature dependence of the normal state resistance between room temperature (RT) and liquid helium temperature. The data was collected during either cool down or warm up. The cool down cycle had the disadvantage that the cooling rate between liquid nitrogen and liquid helium temperature was too fast to ensure thermal equilibrium. Thus, the data sets obtained during the warm up process were preferred, except for sample C40 for which no data was recorded during warm up.

The resistance versus temperature curves, normalized to the resistance at $T = 0° \mathrm{C} = 273.15 \, \mathrm{K}$ for all six samples, are shown in figure 6.1. For sample C40 the low temperature part is known only approximately, as explained above and indicated by the dashed line. Data points for sample C30 between $\approx 50 \, \mathrm{K}$ and $\approx 90 \, \mathrm{K}$ are also missing, the linear interpolation in this temperature range is again indicated by a dashed line. All samples show a linear temperature dependence between RT and $\approx 30 \, \mathrm{K}$, which has also been measured previously for amorphous Ta/Ge multilayers [50]. Values for the normal state resistivities at zero temperature, linearly extrapolated from resistance data between 150 and 250 K, are given in table 6.1. Comparing the normal state resistivities $\rho_N(0)$ for the samples evaporated at $40°$ and taking into account the different filling factors[1] due to different layering, one finds similar conductivities for the superconducting

---

[1] The resistivities in table 6.1 were calculated using the whole film thickness, including the separating Ge-layers, excluding the top and bottom Ge-layers. But the Ge-layers can be taken as insulating even at elevated temperatures, restricting conduction to the alloy layers. The filling factor gives the relative volume content of the conducting layers with respect to the whole film thickness.

layers, deviating by less than $\pm 5\,\%$ from their mean value. Compared to this mean value for the 40°-samples, the films evaporated at 30° and 50° have approximately $30\,\%$ decreased and increased resistivities, respectively. The alloy layers in the 50°-samples have conductivities very similar to each other as well.
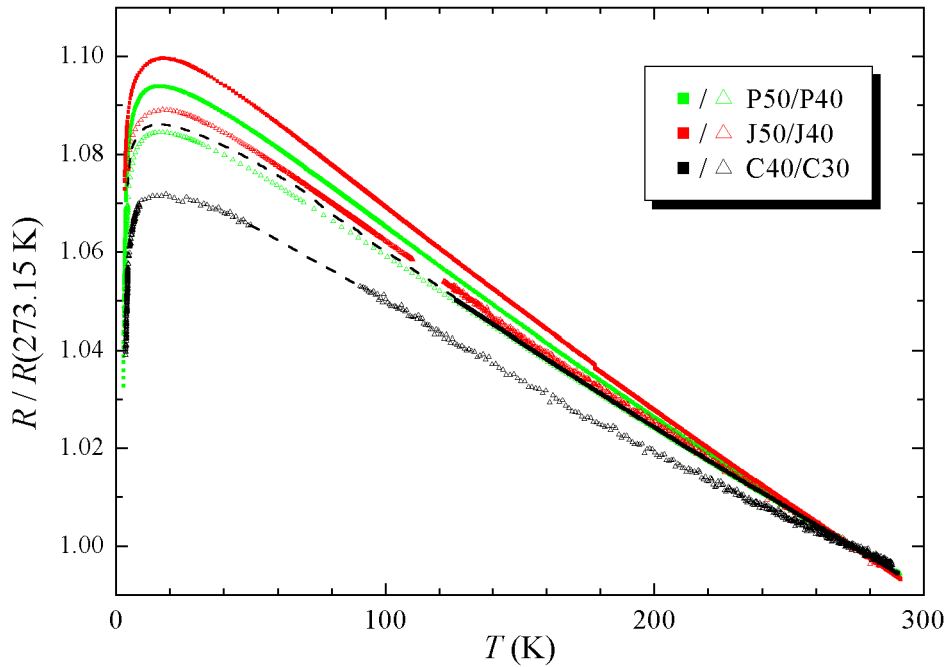

Figure 6.1: Normal state resistance between $300\,\mathrm{K}$ and $4\,\mathrm{K}$ normalized to the resistance at $273.15\,\mathrm{K}$. All samples show a linear temperature dependence down to $\approx 30\,\mathrm{K}$. The negative slope can be explained within the theory of weak localization due to the short mean free paths for the conduction electrons in these amorphous films. The gradient variations reflect differences in the layering and defect structure, and are discussed in the text. For temperatures below $30\,\mathrm{K}$, superconducting fluctuations set in and the films have a maximum resistance for temperatures between 10 and $20\,\mathrm{K}$.

The different temperature gradients also reflect the different layering and defect structures of the films. Let us first compare the three samples evaporated at 40°: C40 and P40 have nearly identical gradients down to $\approx 120\,\mathrm{K}$, and it is reasonable to assume that they remain similar down to at least $30\,\mathrm{K}$. J40 on the other hand exhibits a significantly larger negative gradient. Weak localization is expected to become more important with reduced dimensionality (section 5.3 and [50, 53, 54]), explaining this change in gradient as a consequence of the reduction of the alloy layer thickness in J40 compared to the other two samples.

The differences between samples with similar layering is due to changes in the defect structure. The columnar structure in C30 is much less developed than in C40 (see TEM images in section 3.2 and rotational data in section 6.3 below), which reduces scattering and increases the mean free path of the conduction electrons. A similar argument may be used to explain the steeper gradients for J50 and P50, except that the more pronounced columnar microstructure leads to increased scattering. Analysis of the layer and film thicknesses in section 3.2 revealed a reduced mass density in the films evaporated at 50°. This may give rise to an additional contribution towards electron scattering. They are also expected to have a reduced free electron density what would also contribute to increased resistance and an increased temperature dependence. Further details of the high-temperature conduction mechanism have not been studied.

At around 30 K deviations from the linear behaviour set in, which lead to a maximum resistance for temperatures between 10 and 20 K followed by a sharp drop as the superconducting transition is approached. We attribute the sharp drop to the onset of superconducting fluctuations in these multilayered films. The fluctuations are apparent even at these relatively high temperatures of roughly $10 \times T_c$ because of the high resistances and very short coherence lengths of these materials. The superconducting fluctuations will be discussed in more detail below. Experimental evidence that the deviations from the linear temperature dependence of the resistances are indeed caused by superconducting fluctuations, comes from magnetoresistance measurements by D. Smith on two multilayered films with columnar structure very similar to J40 and P50 in the temperature range 2 to 18 K [154]. At magnetic fields of 7 T the linear temperature dependence extends smoothly to lower temperatures. Just as in the superconducting phase, a magnetic field leads to the suppression of Cooper-pairs even in the fluctuation regime above T_c, and the normal state behaviour is recovered. The high-field measurements by D. Smith also showed that at temperatures $T \ll 10$ K, the resistances increase faster than linearly with decreasing temperature, an effect which has not been explored at this stage, but which is probably due to weak localization or electron-electron correlations at very low temperatures.

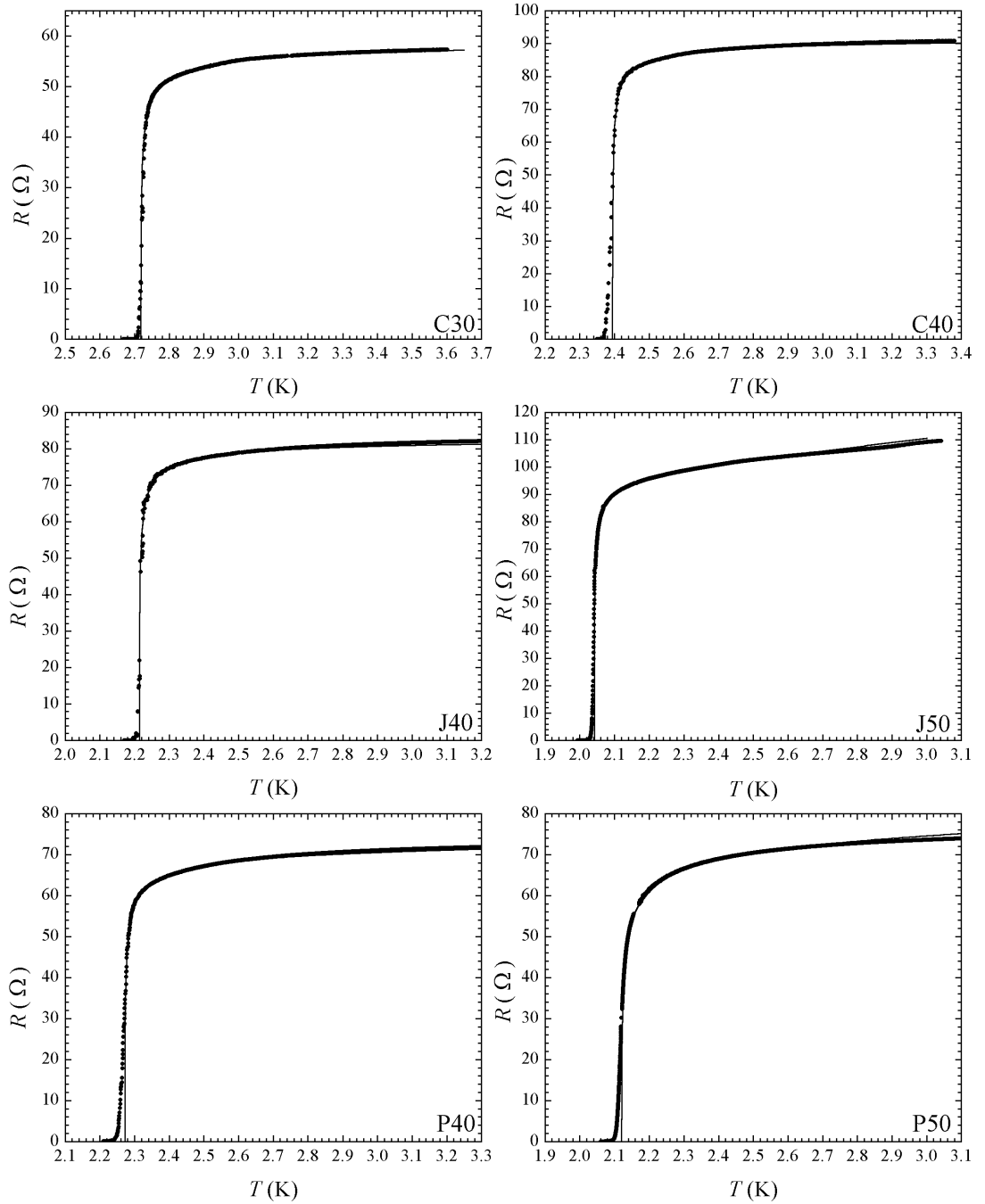# 6.2 Zero-Field Superconducting Transition and Fluctuations

Figure 6.2: Superconducting transition in zero magnetic field for all six samples as labelled in the individual graphs. Note the different resistance and temperature scales, though for easier comparison, the temperature range equals 1.2 K for all graphs. The lines are fits according to fluctuation conductivity theory (eq. 5.25) and are described in detail in the text.

In this section, the zero-field transition temperatures from the normal conducting to the superconducting state will be determined. Despite the importance of $T_c(0)$ as a sample characteristic, this will give a first indication of the samples' dimensionality, according to the fluctuation conductivity theory (section 5.3). In figure 6.2, the low temperature part of the resistance measurements from the previous section are shown for all samples. They all show a sharp drop in resistance at the critical temperature, preceded by significant rounding of the transition for temperatures close to but above T_c, which can be well described within the theory of superconducting fluctuations, as described below. Also, all curves show a more or less pronounced resistive tail for very low resistances. This tail is probably caused by the remnant field of the order of $0.1 - 1\,\text{mT}$ present even when the magnet is switched off[2].

Attempts were made to fit the resistance data according to superconducting fluctuation theory for two and three dimensional systems as discussed in section 5.3. The data were fitted to the sum of normal conductance and a contribution from superconducting fluctuations following equations 5.23 and 5.24 for 2D and 3D. In all cases the equation for 3D superconductors provided a better qualitative description of the data, especially the rounded part near T_c. Consequently, equation 5.25, including the AL and MT contribution, was used to describe the data with the temperature independent pre-factor, the transition temperature and the normal state resistance as fitting parameters. Best fits are shown in figure 6.2 as solid lines. From these fits the critical temperatures $T_c(0)$ and normal state resistances have been extracted, as shown in table 6.1.

The normal state resistances can be compared to the values obtained from the extrapolations of the resistance data down to zero temperature in the previous section 6.1. The results can be categorized into two groups. Samples C30, C40 and J40 fall into the first group for which the two values conform to within less than $2\,\%$. For these samples, the superconducting transition could be fitted

---

[2] The conventional electro-magnet of the IRL-setup naturally has a remnant field caused by the remnant magnetisation of the pole caps. For the Portland-setup the remnant field was not caused by the superconducting magnet itself, but instead by the magnetisation of the iron used in the reinforced concrete of the floor on which the cryostat was standing.

well by assuming a constant normal state resistance for the relevant temperature interval. This is a very good approximation considering the small temperature gradient, which results in a relative change in resistance of the order of $0.01\,\%\,\mathrm{K}^{-1}$. Contrarily, for the remaining three samples, satisfactory fits of equation 5.25 to the data could only be achieved by assuming a positive gradient of the normal state resistance near the critical temperature, compared to the negative gradient observed at higher temperature. For samples P40 and P50, the gradients for which a best fit was obtained equate to relative changes in resistance of 1 and $3\,\%\,\mathrm{K}^{-1}$, respectively, and the normal state resistivities at zero temperature deviate from those determined in section 6.1 by only 4 and $6\,\%$, respectively. From the plot for J50 in figure 6.2, it can already be seen that the resistance data exhibits a significant gradient in this temperature range. The determined zero temperature normal state resistivity is about $30\,\%$ lower than the value extrapolated from resistances at higher temperatures. A possible explanation for this peculiar behaviour could be a significant volume fraction with a much higher critical temperature as would be expected for crystalline material, for example.

Having determined the normal state conductivities, one can calculate the superconducting fluctuation conductivity by subtracting the former from the experimentally measured conductivities. Plotting the fluctuation conductivities obtained this way in a log-log plot versus the reduced temperature, allows a check of the relevant dimensionality of the films, since for three dimensional superconductors the data should describe a straight line with gradient $-1/2$ compared to a slope equal to -1 for 2D superconductors. Such plots are shown in figure 6.3, where the actual experimental data have been multiplied by constant factors to separate the data sets for the different films from one another. For all samples, the fluctuation conductivity σ' can be fitted very well over at least one to two orders of magnitude in reduced temperature t by a straight line with gradient $-1/2$. This confirms the previous assumption of 3D behaviour. These fitted lines also allow a more reliable determination of the temperature independent pre-factor in equation 5.25 than the fitting procedure to the original resistance data. Using these values the superconducting coherence length $\xi(0)$ can be calculated. The
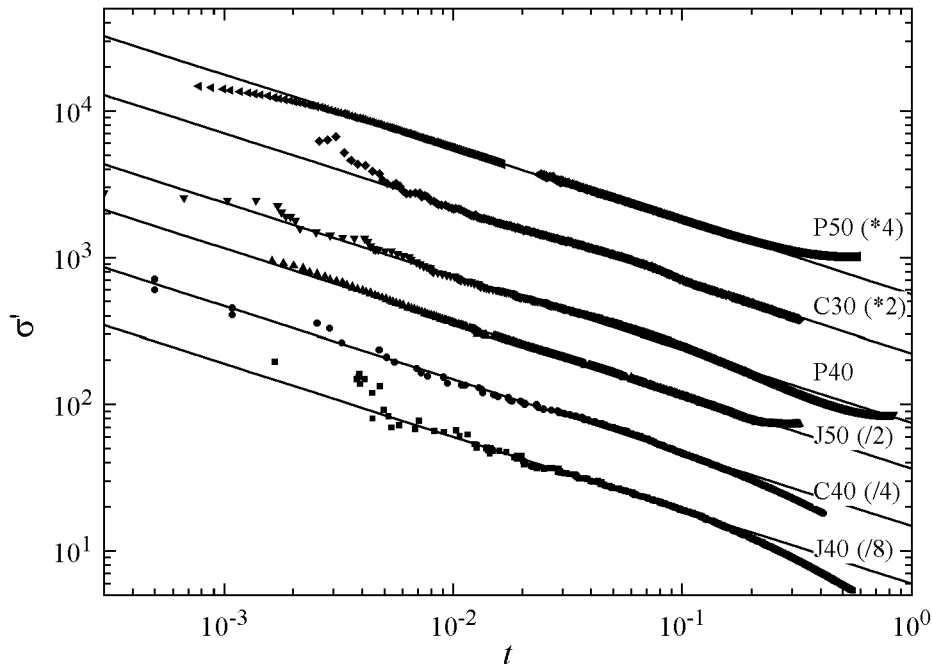
Figure 6.3: Log-log plot of the conductivity contribution from superconducting fluctuations versus the reduced temperature. The data sets are separated from each other by multiplication or division by a constant, as indicated in the graph. The solid lines are fits to the data with a gradient equal to $-1/2$ in this double logarithmic plot, confirming the 3D characteristics of the films.

coherence lengths obtained this way are given in table 6.1. As will be shown later, the films are definitely anisotropic and the question arises whether the determined coherence length is in the ab- or c-direction. An independent determination of ξ_{ab} follows in section 6.4.

As mentioned above, the very short coherence lengths and relatively high resistivities make it possible to observe superconducting fluctuations up to temperatures equal to $10 \times T_c(0)$ and higher. The short coherence length ensures that the fluctuation conductivity gives a contribution to the overall conductivity of approximately 0.1 to 1 % for a reduced temperature $t = 9$ or $T = 10T_c(0)$. The high sensitivity in resistance measurements thus allows us to trace the contribution of short-lived Cooper-pairs up to very high temperatures.

Table 6.1: Film parameters as determined from zero-field resistance versus temperature measurements. The transition temperatures $T_c(0)$ were determined from fitting equation 5.25 as described in the text. The third column gives the normal state resistivity $\rho_N(0)$ as another parameter in the fitting procedure, compared to the same quantity from extrapolations of the resistance data at higher temperatures down to zero temperature. Both methods agree with each other, except for sample J50, for which the value from the resistance data at high temperatures seems to be more reliable. The values of the coherence length $\xi(0)$ in the last column were derived from fitting the conductivity due to superconducting fluctuations directly to equation 5.25, as detailed in the text.

	$T_c(0)$ [K]	$\rho_N(0)$ [$\mu\Omega\,$cm]		$\xi(0)$ [nm]
C30	2.718	325.7	319.7	3.4
C40	2.395	442.0	447.2	6.5
J40	2.214	525.8	527.7	8.0
J50	2.042	450.8	632.8	5.2
P40	2.272	555.3	577.6	5.1
P50	2.121	692.3	737.5	2.7

6.3 Angular Magnetic Field Dependence of the Resistance in the Vortex Liquid Phase

The large anisotropies of the multilayered films are expected to have significant consequences for the conductive behaviour, especially in the mixed phase of the superconducting phase diagram. Furthermore, the columnar microstructure gives rise to an additional anisotropy. This should be evident in the magnetoresistance of the samples for external magnetic fields applied at different directions with respect to the layering and the defect structure. These anisotropies were determined by measuring the resistance as a function of the magnetic field orientation.

Although an exact description of the resistance R as a function of the magnetic field orientation θ is very difficult due to the large number of different vortex phases and range of phenomena which are encountered, a qualitative description of the expected $R(\theta)$ curve is given before the experimental results are discussed. As will be seen from results in later sections, the measurements presented below were taken in the pinned and unpinned vortex liquid phases for magnetic fields normal to the film, equivalent to $\theta = 0°$, that is $R(0)$ is still a significant fraction
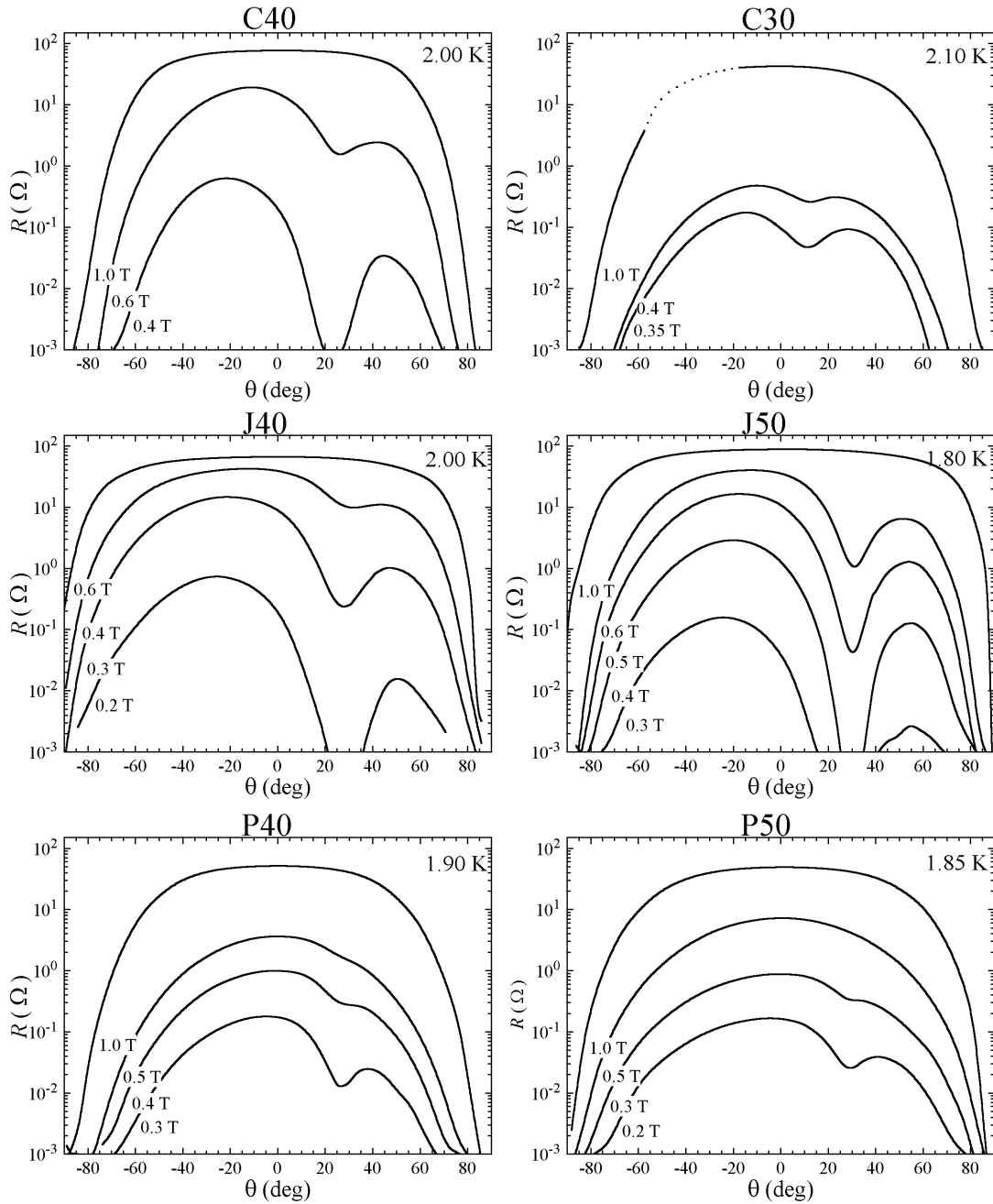
Figure 6.4: Resistance as a function of magnetic field orientation for given field/temperature combinations. Note the logarithmic resistance scale. Increased pinning for C-aligned fields is evident in all six samples. It is not possible to draw direct conclusions about the pinning strength from these plots, since the resistance reduction is dependent on the exact position in the vortex phase diagram. The dotted line in graph C30 for $-60° \leq \theta \leq -20°$ is a symmetric approximation used to interpolate missing data that resulted from interference of the magnetic field with the electronic equipment. This was avoided in later measurements by moving the equipment further away from the magnet.

of the normal state resistance R_N. Two effects lead to a reduction in R over many orders of magnitude when the field is rotated parallel to the film to $\theta = \pm 90°$. In fact, in many cases a truly superconducting phase with $R(\pm 90°) = 0$ will be entered. The first effect is a simple geometric one, which can be quantified by the demagnetising factor η, see for example [42]. For our thin films with in-plane dimensions much larger than the film thickness and the penetration depth λ, the demagnetising factor is approximately 1 for the field perpendicular configuration. Practically, this reduces the lower critical field $H_{c1\perp}$ to zero. In the field parallel case, however, with $\eta \approx 0$, the resulting lower critical field $H_{c1\parallel}$ is finite. But even when the lower critical field is exceeded, the resistance may remain zero up to very large fields, because of the layering of the films. The layered structure acts as a highly effective intrinsic pinning structure which suppresses any flux motion.

Beginning at $\theta = -90°$ and rotating the magnetic field out of the in-plane direction, at some angle, depending on field magnitude and temperature, a measurable resistance will set in. The resistance will then rise in some fashion over many orders of magnitude to the FFF or TAFF resistance for $\theta = 0°$, depending on whether the vortices are in the unpinned or pinned fluid phase for the chosen field and temperature combination. Without extended defects oriented at an angle β to the film normal, the resistance curve would be continued symmetrically for $0 \leq \theta \leq 90°$. For films with extended defects, however, the resistance at $\theta = \beta$ will be reduced compared to $\theta = -\beta$, because of enhanced pinning as the columnar angle is approached, resulting in a dip in the resistance curve. This is only true as long as the vortex matter is in its pinned liquid phase: for high enough fields and temperatures the curve is indeed expected to be symmetrical, even in the presence of extended pinning sites.

In figure 6.4 experimental $R(\theta)$ curves are given for all films. Each curve was taken at constant temperature and field as indicated in the graphs. Naturally, the curves with the smallest resistances were taken at the smallest field magnitudes. All curves follow the general expectation given in the above paragraph. For the right choice of field and temperature, all samples show a local minimum in resistance at some angle between approximately 10° and 30°, which is identified

as the direction of the columnar structure. Although it is not possible to draw simple conclusions about the pinning strength of the defects from the depth of the minimum, since the reduction in resistance is crucially dependent on the exact position in the H-T vortex phase diagram, it will be shown later that samples C40, J40 and J50 show much stronger pinning than the other three samples.

The minima caused by the columnar structure are relatively broad, which is probably the consequence of a distribution of columnar orientations. Due to the statistical film growth process, the columns are not strictly parallel. This leads to a distribution in the orientation as well as the pinning efficiency of the defect planes. This kind of pinning arrangement may even be beneficial in terms of flux pinning, as comparative studies on HTSC have shown, see for example reference [155]. For many of the curves in figure 6.4 the effects of the defects even extend into the negative or AC angular range with the consequence that the maximum resistance is measured for $\theta < 0$ instead of the perpendicular orientation.

From the minima the columnar orientation or C-direction was determined by assuming that the curves could by fitted by a second-order polynomial for a small angular range around the minimum. Because the "normal" resistance, that is, the resistance that would be expected without coplanar defects, is nonlinear and decreases with increasing $|\theta|$, this procedure may introduce a systematic error. That the minima are indeed non-symmetric is easily seen for the shallower ones, where the reduction of the resistance due to the defects is comparable to the reduction by geometric effects.

Extraction of the contribution of the columns only is not straight forward, because no theoretical description of the $R(\theta)$ curves exists. However, the two P-samples do suggest an alternative for determining the reduction in resistance due solely to the extended defect structure. For these two films the influence of the defects does not seem to extended into the negative θ-range, based on the observation that the maximum resistance was measured at $\theta \approx 0°$ for all fields. Taking the ratio of the resistances at positive θ (the C-branch) and negative θ (the AC-branch), $R_{\mathrm{C}}/R_{\mathrm{AC}}$, should result in a symmetrical minimum around the

columnar angle. Figure 6.5 gives curves calculated in this way for samples P40 and
P50. They are indeed symmetrical to a very good approximation, and even the
relatively shallow minima allow a quite accurate determination of the columnar
direction. There is however no significant deviation from the columnar direction
determined from the absolute resistance minimum. The same procedure was also
applied to the remaining four films, still resulting in symmetrical reductions of the
resistance, although the ratios at low angles clearly deviated from the expectations
since the experimental R_{AC} did not represent the undisturbed resistance value.
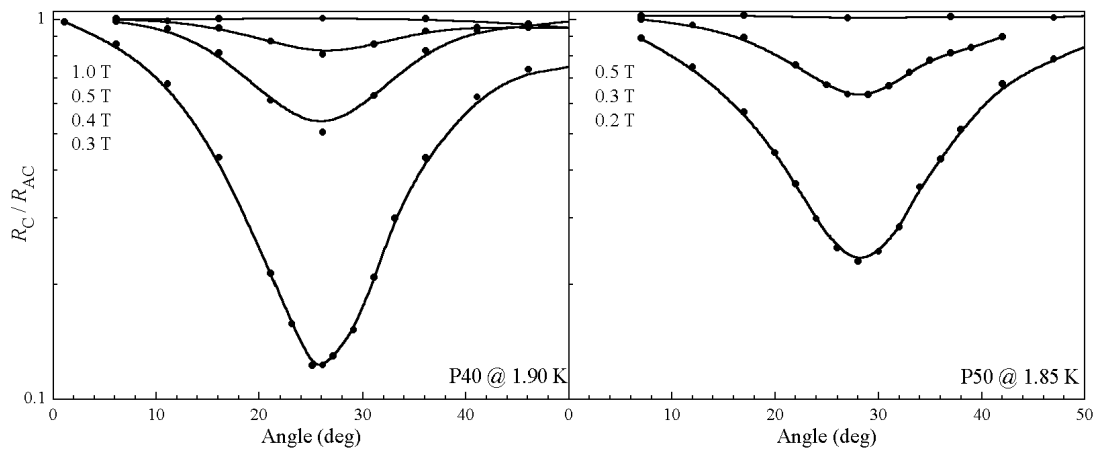

Figure 6.5: Relative reduction of the resistance due to extended defects in samples
P40 and P50. Plotted are the ratios of the resistance measured for positive θ over the
corresponding resistance for $-\theta$. Thereby, the changes in resistance due to layering and
the changing demagnetising factor are eliminated. The black lines are smooth curves
extrapolating between the data points (filled circles).

In table 6.2 values for the columnar direction obtained from these resistance
measurements are compared to the angles obtained directly form the defect struc-
ture seen in the TEM images (section 3.2). The angles of minimum resistance are
averaged values from the resistance minima and minima in the ratios R_C/R_{AC} for
different magnetic fields, as explained above. From the variations of the angles
obtained for the individual curves and the widths of the minima, it is estimated
that the given angles are accurate to within $\pm 2°$. Although the error bars do over-
lap, the angles determined from resistance measurements are consistently larger
than the defect angles derived from the TEM images.

Magnetisation measurements on YBCO containing columnar defects and twin-

Table 6.2: Comparison of columnar angles deter-
mined from resistance measurements as described in
this section and TEM photographs discussed in sec-
tion 3.2. The TEM images suggest an angular dis-
tribution in the columnar direction of approximately
$\pm 3°$ and a conservative estimate of the error in the
columnar angle determined from resistance measure-
ments gives $\pm 2°$. Although the experimental results
agree for these assumptions, the angles determined
from resistance measurements seem to be systemat-
ically larger.

	β	
	R	TEM
C30	12.0°	—
C40	23.8°	19.5°
J40	29.3°	26.8°
J50	30.3°	26.6°
P40	26.3°	25.5°
P50	28.6°	26.4°

planes at an angle of 32° to the c-axis gave clear evidence of vortex staircases [156].
The staircases developed due to competing pinning by the columnar defects, twin
planes parallel to the c-axis, and intrinsic pinning by the anisotropic crystal struc-
ture. Since the films in this study do not have any extended pinning sites cor-
responding to the twin planes in that YBCO single crystal, it is likely that the
minimum resistance occurs for field orientations slightly away from the colum-
nar direction, towards the film parallel direction. This assumption is based on
observations made in reference [156]. To verify the development of staircases in
these Ta_xGe_{1-x}/Ge -films magnetisation measurements or systematic studies of
homogeneous and multilayered films with columnar structure could be helpful.

All the conductance measurements in the C- and AC-direction were done for
magnetic fields aligned according to the angles obtained from resistance mea-
surements, simply because TEM images of the films were not available before
all conductance measurements had been done and the samples could be cut and
prepared for the TEM investigations.

6.4   Upper Critical Field $H_{c2}(T)$

The upper critical field $H_{c2}(T)$ will define the range of temperatures and magnetic
fields for which the samples are in the superconducting mixed phase. Informa-
tion about the upper critical field $H_{c2}(T)$ can be obtained from resistance versus
temperature measurements in the presence of an applied magnetic field. Figure
6.6 shows a typical example of a set of such resistance measurement taken from
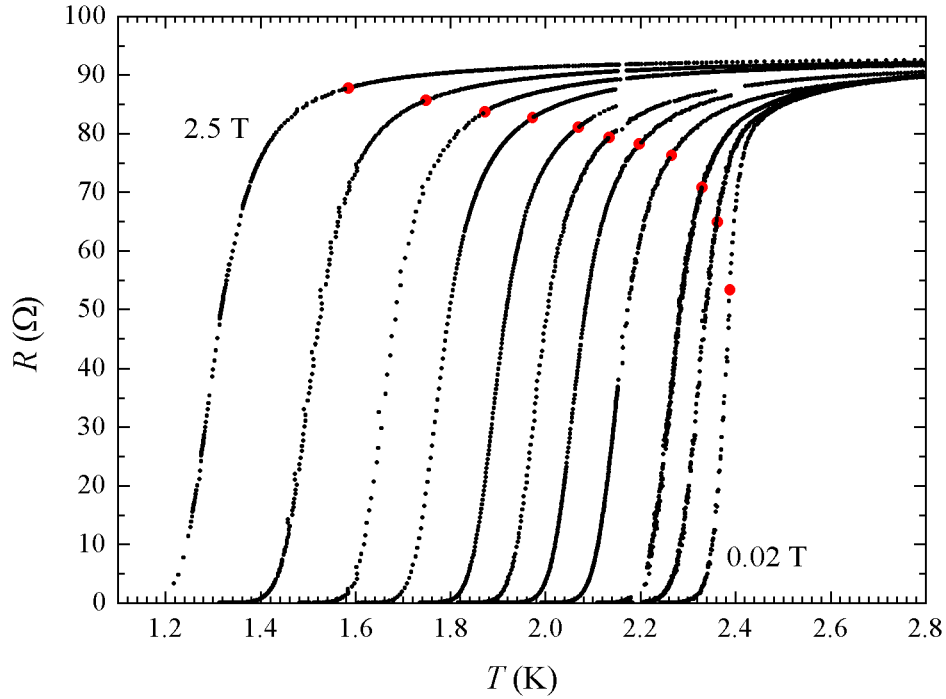sample C40 in fields ranging from 0.02 to 2.5 T applied in the C-direction. With

Figure 6.6:   Set of in-field R vs T data taken at magnetic fields H = 0.02, 0.1, 0.2, 0.4, 0.6, 0.8, 1.0, 1.3, 1.6, 2.0 and 2.5 T from right to left in the C-direction of sample C40. The highlighted, red data points mark $T_c(H)$ determined from fluctuation conductivity theory.

increasing field the critical temperature $T_c(H)$ decreases, and the transition becomes broader and less well defined. A rough estimate of T_c can be obtained from a 50 % *criterion*, that is, taking the temperature at which the resistance has dropped to $R_N/2$ as the critical temperature. From that we already obtain a linear relation between T_c and H. From GL theory one expects such a linear temperature dependence (eq. 5.11).

A much more accurate determination of the upper critical field is possible by applying the scaling relations of Ullah and Dorsey, equations 5.26 and 5.27. Depending on the dimensionality, a set of σ'-T curves, as it can be extracted from R-T data sets like that in figure 6.6, should collapse onto a single curve describing the scaling function F_x for appropriately scaled x- and y-axes. Assuming a linear relation between H_{c2} and T_c of the form $T_c(H) = T_c(0) + s \times H$, where s is the constant slope, leaves only one adjustable parameter, since $T_c(0)$ and R_N are already known from the zero-field resistance data. Both the 2D and 3D scaling

relations have been applied to the data, and again the 3D-form produced much better scaling, similar to the zero-field measurements (compare section 6.2).

In figure 6.7, the result of such a scaling procedure applied to the set of resistance measurements shown in figure 6.6 is shown. The rescaled fluctuation conductivity $\sigma'(H/T^2)^{1/3}$ is plotted versus a field-dependent reduced temperature $[T - T_c(H)]/(TH)^{2/3}$. For data above $T_c(H)$, equivalent to reduced temperatures larger than zero, the data sets collapse very nicely onto the scaling function F_{3D}. For lower temperatures the data fans out, since the measured conductivity is no longer determined by superconducting fluctuations but instead by the motion of flux lines.
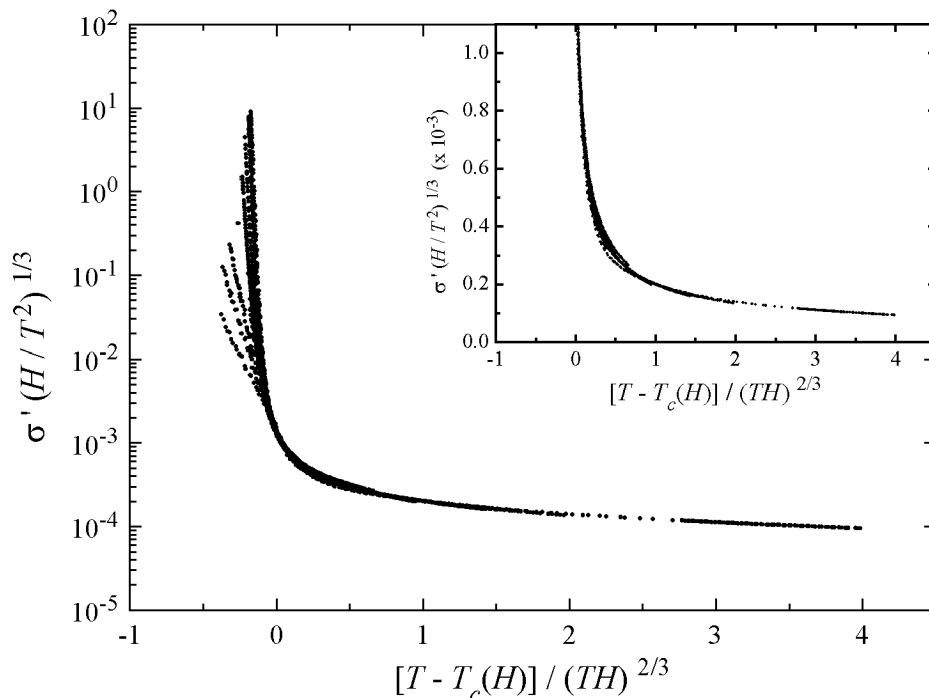

Figure 6.7: Data sets from figure 6.6 after scaling fluctuation conductivity according to the theory of Ullah and Dorsey, section 5.3. The rescaled fluctuation conductivity $\sigma'(H/T^2)^{1/3}$ is plotted versus the field dependent reduced temperature $[T - T_c(H)]/(TH)^{2/3}$. In the fluctuation dominated regime above $T_c(H)$ the scaling is very convincing. Below the critical temperature the curves do not collapse any longer because conductivity is dominated by flux motion. The inset shows a blow-up of the low conductivity part on a linear scale, demonstrating the very good scaling of the data.

From the slope s one can calculate the upper critical field linearly extrapo-

lated to zero temperature[3]. The resulting critical temperatures for the resistance curves in figure 6.6 are marked by the highlighted red data points. Obviously, the 50 *% criterion* underestimates the transition temperatures in high magnetic fields considerably. The perhaps unexpected high resistance below $T_c(H)$ is a consequence of flux motion, roughly given by the Bardeen-Stephen value for free flux flow, equation 5.32.

The scaling method described above has been successfully applied to all samples for fields applied in the C- and AC-direction. The slopes s extracted from these procedures vary from sample to sample, but are very similar for the two field directions. Numerical values for the extrapolated $H_{c2}(0)$ are given in table 6.3. The measurements were not taken for perpendicularly aligned fields, although the orientation was not too far from the normal direction, thus the calculated upper critical fields deviate from $H_{c2\perp}$ due to the layered nature of the films. The transformation rule, equation 5.14, allows one to estimate the deviation from $H_{c2}(0)$ for perpendicular fields. Even though anisotropy ratios γ have not been determined in this study, B. Ruck measured the anisotropy for similarly layered Ta/Ge and Ta_xGe_{1-x}/Ge films and found anisotropy ratios in the range $1/10 < \gamma \lesssim 1$ [32]. Figure 6.8 shows curves calculated according to equation 5.14 for $\gamma = 1/2$, $1/5$ and $1/10$. From this graph it can be inferred that the measured values of $H_{c2}(0)$ are no more than $15\,\%$ larger than the respective $H_{c2\perp}(0)$, and in many cases the difference is probably much less than $10\,\%$.

Using relation 5.18, $\xi_{ab}(0)$ can be derived approximately from these measurements. Since $\xi_{ab} \propto H_{c2\perp}^{-1/2}$, the systematic error, due to fields aligned in the C- and AC-direction, are even less. The values of the coherence lengths obtained in this section agree reasonably well with those derived from fitting zero temperature resistance measurements to the theory of fluctuation conductivity (6.2). At most the two values deviate by a factor of ≈ 2.5 from each other. The coherence lengths derived from measurements of the upper critical field are expected to be much more reliable. The other important parameter characterising these films, the penetration depth λ_{ab}, can be estimated from the following equation [157]

---

[3] Remember that the true upper critical field is less than the extrapolated value (see section 5.1).
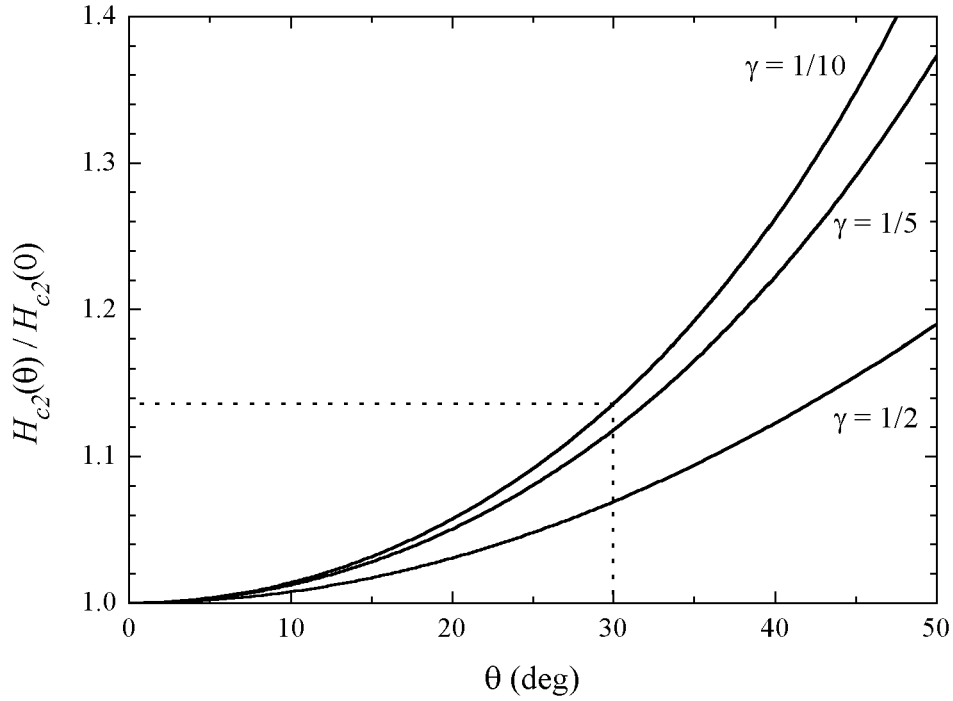
Figure 6.8: Theoretical $H_{c2}(\theta)/H_{c2\perp}(0)$ curves for different anisotropies as indicated according to the transformation rule for anisotropic superconductors, equation 5.14. The estimated maximum deviation of measured critical fields from $H_{c2\perp}(0)$ is given by the dashed lines.

$$\lambda_{ab}(0) \approx 1.05 \times 10^{-3}[\rho_N(0)/T_c(0)]^{1/2}. \tag{6.1}$$

All the superconducting parameters characterising the superconductivity of the multilayered films investigated are summarized in table 6.3. The large GL-parameters κ confirm the assumption of extremely type-II superconductors. A rough estimate of the lower critical field using relations 5.12 gives $H_{c1}(0) \approx 0.5\,\mathrm{mT}$. Together with a demagnetising factor η close to 1 this justifies setting $B = \mu_0 H$ for all applied fields in this study except for field orientations extremely close to parallel to the film surface.

Table 6.3: Summary of all the superconducting parameters characterising the films under investigation. The errors were determined as follows: the uncertainty in $T_c(0)$ was estimated from the maximum accuracy of the temperature measurement setup, for the case of $H_{c2}(0)$ and $\xi_{ab}(0)$ errors were derived from differences for the C- and AC-direction (where the analysis gave the same value for both directions, an error of the same magnitude as for the other samples is assumed), uncertainties in $\lambda_{ab}(0)$ are primarily due to uncertainties in the normal state resistances for which the extrapolated values from high temperature measurements were used, and errors in κ are calculated from the respective errors in ξ and λ.

	$T_c(0)$ [K]	$H_{c2}(0)$ [T]	$\xi_{ab}(0)$ [nm]	$\lambda_{ab}(0)$ [μm]	κ
C30	2.72 ± 0.01	5.5 ± 0.1	7.8 ± 0.1	1.14 ± 0.05	146 ± 7
C40	2.40 ± 0.01	7.4 ± 0.3	6.7 ± 0.2	1.43 ± 0.05	213 ± 10
J40	2.21 ± 0.01	7.0 ± 0.4	6.9 ± 0.2	1.62 ± 0.05	235 ± 10
J50	2.04 ± 0.01	8.4 ± 0.7	6.3 ± 0.3	1.85 ± 0.25	294 ± 42
P40	2.27 ± 0.01	7.3 ± 0.1	6.7 ± 0.1	1.67 ± 0.10	249 ± 15
P50	2.12 ± 0.01	6.5 ± 0.1	7.1 ± 0.1	1.96 ± 0.15	276 ± 21

6.5 Thermally Assisted Flux Flow and Activation Energies

Having defined the field and temperature range for which the films are in their superconducting state, information about the vortex behaviour in the superconducting mixed phase is derived from conductivity measurements. This was done by measuring the linear resistance in the limit of small applied currents as well as by probing the response of the vortex system to applied current densities, ranging from small up to or even exceeding the depairing current density. In this section, the activation energies for thermally activated flux flow are determined over a large range of magnetic fields. Strong effects of the columnar structure and the interlayer coupling will be deduced from these measurements.

Near $T_c(H)$, in the fluctuation conductivity regime and the free flux flow range, the influence of the columnar microstructure was not evident. Especially the magnetic field orientation with respect to defect direction had no significant influence on conductivity. As the temperature is lowered and the dynamics of the flux lines are expected to change from free flux flow to thermally activated

flux flow, the additional anisotropy of the inclined columnar microstructure is expected to reflect itself in conductivity differences for the C- and AC-direction. Qualitatively, this has already been demonstrated in section 6.3 by rotating the magnetic field with respect to the film geometry. In this section a more quantitative analysis of the differences for the two field orientations, C and AC, will be presented.

The temperature dependence of the resistance of a vortex liquid in the presence of disorder was discussed in section 5.5.3, and from equation 5.44 a strong exponential behaviour is expected in the TAFF-region of the vortex liquid phase. Therefore, it is most convenient to plot the resistance data in Arrhenius-style, that is the logarithm of R is plotted versus $1/T$. Plots of this kind are shown in figures 6.9 and 6.10 for samples C40, J40 and P40, respectively, for data taken with magnetic fields in the C and AC-direction. Experimental results for the three remaining samples were qualitatively similar.

Focusing on the graphs for samples C40 and J40 first, it is observed that they exhibit almost identical behaviour. At the lowest magnetic fields[4] (far left), the curves for the C (black) and AC (red) field orientations coincide, but as the field is increased the resistance for C-aligned fields is significantly reduced with respect to AC-oriented fields. Not only is the absolute resistance reduced, for medium field magnitudes the apparent gradient is steeper as well, i.e. the resistance vanishes much faster with temperature for the black curves than for the red. At the highest measured fields the resistance measured with magnetic fields aligned with the columnar structure is still less than for field orientations at large angles to it, but the gradients become similar again, as the detailed analysis below will show. Sample J50 (not shown) behaved in very much the same way as these two samples. Sample C30 on the other hand (also not shown), although showing a sharp drop in resistance, provided no clear evidence of pinning by extended defects, that is, over the whole measured field and temperature range the resistance data for the two distinct field directions were almost identical.

---

[4] The gap in the data for J40 at $H = 0.02\,\mathrm{T}$ and $1/T \approx 0.46\,\mathrm{K}^{-1}$ happens near the superfluid transition of the liquid helium. The lambda-anomaly of liquid helium near the superfluid transition [40] lead to difficulties controlling the temperature at the tens of mK level.
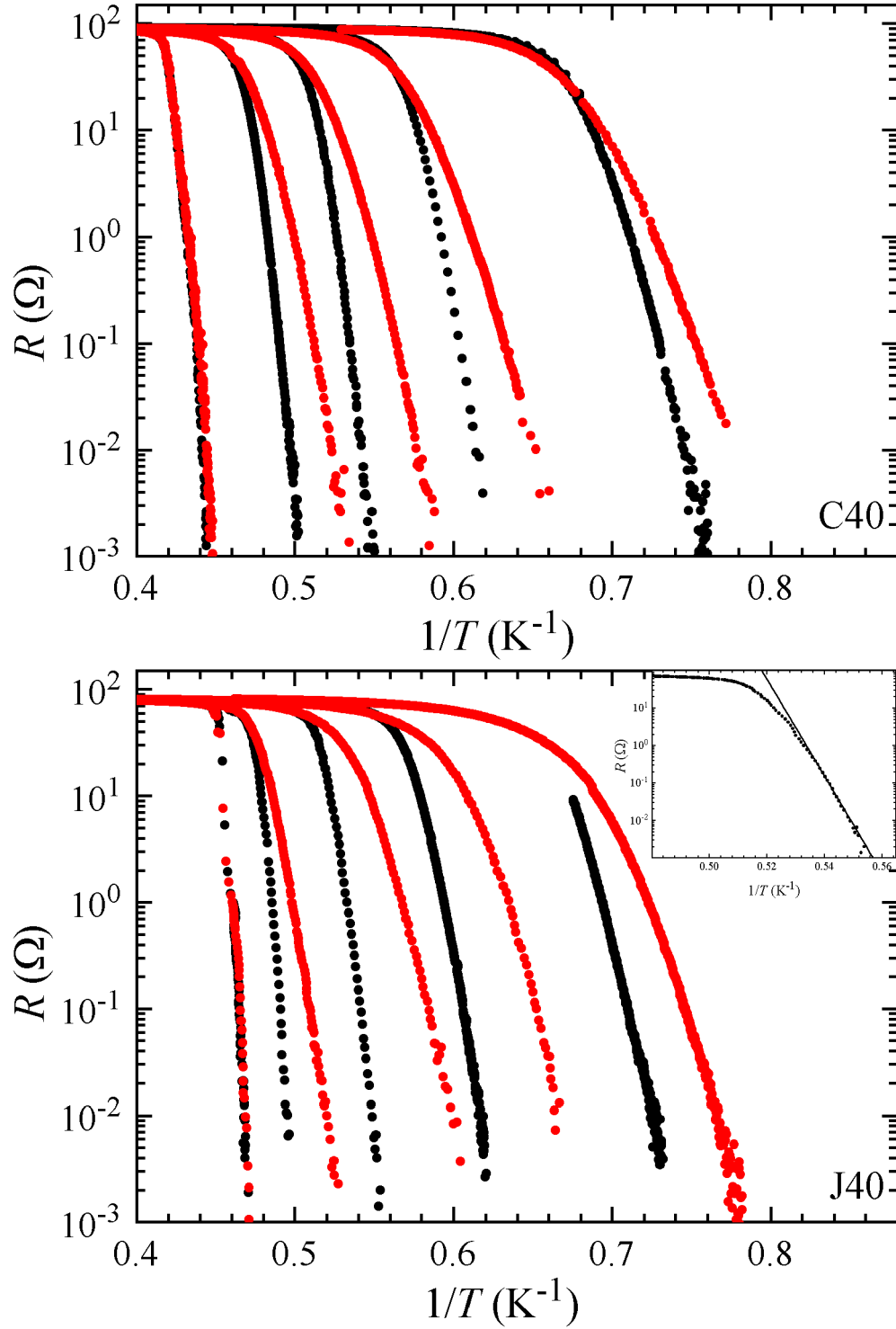
Figure 6.9: Selected *R-T* data from samples C40 (top) and J40 (bottom) plotted in Arrhenius-style for magnetic fields applied in the C (black) and AC (red) direction. Not all data sets are shown, allowing better illustration of the changes with changing magnetic field. The curves correspond to applied fields (from left to right) of $H =$ 0.02, 0.4, 0.8, 1.3, 2.0 T and $H =$ 0.02, 0.2, 0.6, 1.0, 1.6 T in the top and bottom graph, respectively. The inset in the lower graph shows the 0.6 T data for C-alignment together with a fitted curve according to equation 5.44.
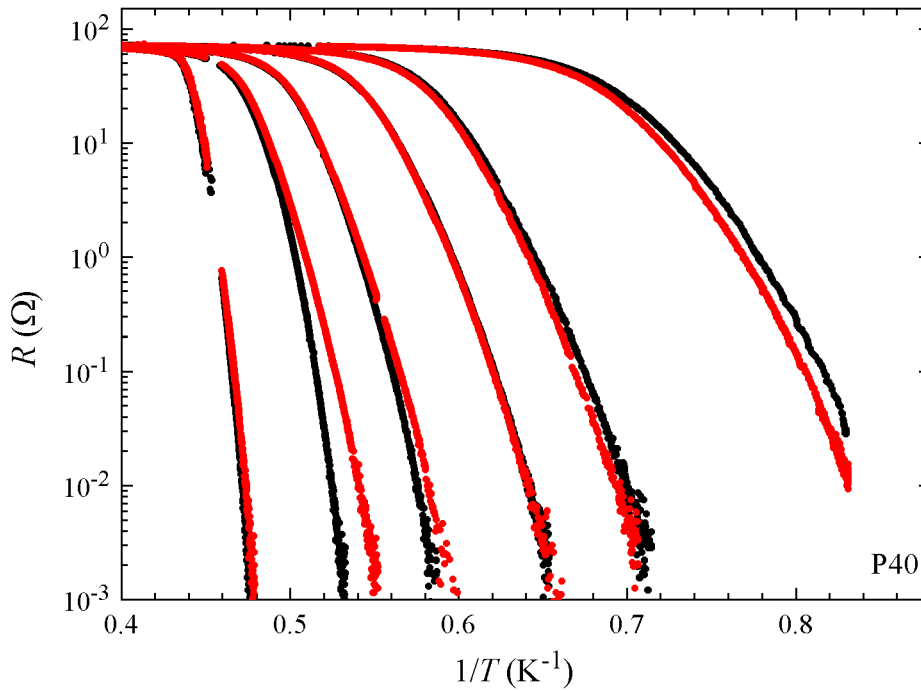
Figure 6.10: Similar plot as in figure 6.9 here for sample P40. The applied magnetic fields were $H = 0.02$, 0.3, 0.6, 1.0, 1.3, 2.0 T from left to right in the C (black) and AC-directions (red), respectively.

We now turn to the results for the more weakly coupled P-samples, as represented by the resistance measurements from P40, shown in figure 6.10. The P-samples display a similar resistance reduction for fields in the C-direction as for C40 and J40, but for a very limited field range only. At a field of 1.0 T the curves for columnar and anti-columnar orientation already coincide again, and for even higher fields the resistance seems to be even larger when the magnetic field is co-aligned with the defect structure.

Next, we will try to extract the field-dependence of the activation energies in the TAFF region. All the resistance curves in these Arrhenius-plots describe a reasonable straight line at low resistance. This suggests fitting the data with a simple exponential function of the form

$$y(x) = y_0 \exp(-U_A/x), \tag{6.2}$$

with a constant y_0 and the activation energy U_A. The inset in the lower graph

of figure 6.9 shows the result of fitting such a function to one particular set of resistance data and the agreement is reasonably good over $2 - 3$ orders of magnitude. Similarly, the low resistance parts of all data sets could be described by equation 6.2. Comparing equations 6.2 and 5.44, we can identify the fitting parameter U_A with the plastic barriers against vortex motion U_{pl}/k_B in units of Kelvin. The fact that the experimental data can be described with such a simple relation implies that the energy barriers U_{pl} are approximately constant over these relatively small temperature intervals. From equation 5.45 it follows that the activation energies should be proportional to the inverse square-root of the applied magnetic field, $U_A \propto 1/\sqrt{H}$.

The activation energies against plastic vortex creep have been studied previously for a homogeneous $Ta_{0.27}/Ge_{0.73}$-alloy film without columnar structure [32] where the activation energies could be described very well by the above inverse square-root dependence. In the following the results from this film are used as a guideline to discuss the influence of the additional anisotropies in the microstructured multilayer films.

Strongly-Coupled Samples

In figure 6.11 the field dependence of the activation energies for samples C30 and C40 for fields applied in the C and AC-directions are compared to the reference alloy film. Any power-law dependence on the applied field results in a straight line in this double logarithmic plot, thus the results from the alloy film are a straight line with gradient $-1/2$. This power-law dependence as predicted by equation 5.45 seems to hold for C30 for the measured field range. The values obtained in C and AC-direction are very similar and are even close in magnitude to the alloy film. Equation 5.45 even allows us to estimate the height of the plastic barriers, and inserting the appropriate penetration depth $\lambda(T)$ for e.g. $1\,T$, a value $U_{pl} \approx 270 \pm 30\,K$ is calculated for an anisotropy ratio $\gamma = 1$. Considering that certainly $\gamma < 1$ and that equation 5.45 is only a dimensional estimate, the measured values $U_A = 75$ and $87\,K$ for the AC and C-direction at $H = 1.0\,T$, respectively, are a strong indication that the resistance in this field and temperature range is indeed a consequence of plastic deformations in the flux liquid. On the other hand,
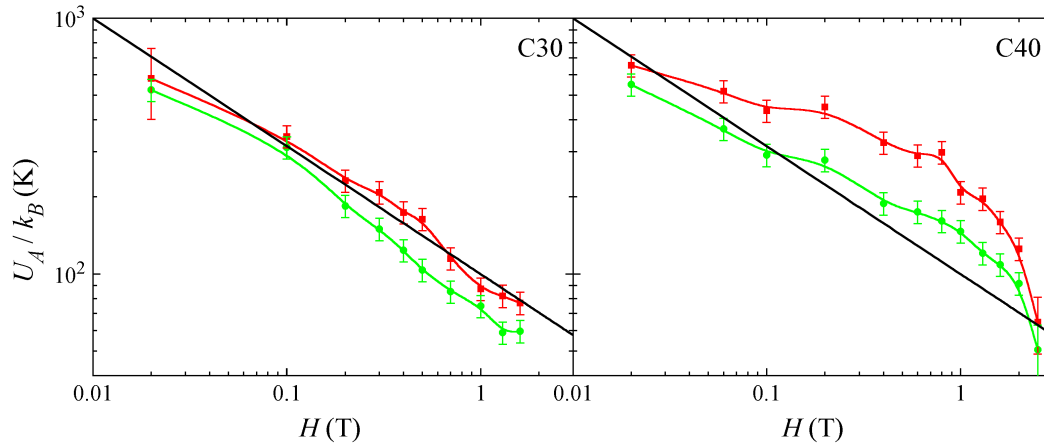
Figure 6.11: Activation energies for samples C30 (left) and C40 (right) for magnetic fields applied in the C (red) and AC (green) direction respectively, compared to a reference $Ta_{0.27}Ge_{0.73}$-alloy film [32] (straight black line). The colored lines are smooth interpolations between the data points and serve as guidelines. The error bars were estimated by varying the gradients of the fitting curves. Changes by $\pm 10\,\%$ could still describe the data reasonably well; for some data sets the errors had to be assumed to be even larger than $\pm 10\,\%$. The C30-sample preserved the $U_A \propto 1/\sqrt{H}$ dependence with little difference between C and AC aligned fields. Sample C40, on the other hand, shows an increase of $U_A(H)$ over a large range of applied fields, especially in the C-direction.

because the theoretical expression was derived for a weak pinning potential, it has to be concluded that the columnar microstructure is not developed well enough to significantly reduce dissipation through flux pinning by extended strong-pinning defects. In fact, the only clear indication that this film has correlated disorder to some degree has come from the rotation measurements in section 6.3.

The right graph in figure 6.11, however, gives substantial evidence for strong pinning caused by the columnar microstructure present in sample C40. At very low fields enhanced pinning by the coplanar defects is negligible, because the barriers against plastic vortex motion are already high compared to additional pinning provided by the extended defects. As the flux density increases, the plastic barriers provided by point-like pinning are reduced according to equation 5.45 and the contribution from the coplanar pinning sites leads to an increased activation energy compared to the reference film or C30. Increasing the magnetic field further means additional flux lines cannot be accommodated on planar defects any longer. They have to find their place at interstitial sites where they are at first still strongly pinned by the interaction with the flux lines localized at the

defects. But with ever increasing magnetic field, the average activation energy for flux flow falls back to the same level as for the alloy film without extended defects or the multilayer film C30 without effective columnar structure. From the field value at which the maximum increase in activation energy was measured, an estimate of the typical spacing between strong-pinning defects is possible. Taking that field as $H \approx 0.2\,\mathrm{T}$ a spacing of $d \approx 100\,\mathrm{nm}$ results.

In the AC-direction when the field is directed at large angles to the defect planes the activation energies are much more similar to those measured for C30 and the alloy film. A close inspection reveals, however, that all activation energies between applied fields of 0.2 and 2.0 T are higher than what is expected for a film without columnar structure. For the chosen geometry, the Lorentz-force is directed in such a way with respect to the pinning planes that the flux lines can *glide* along the planes, experiencing no additional pinning potential at least in a homogeneous film (compare figure 6.12 (a)). A study of a homogeneous
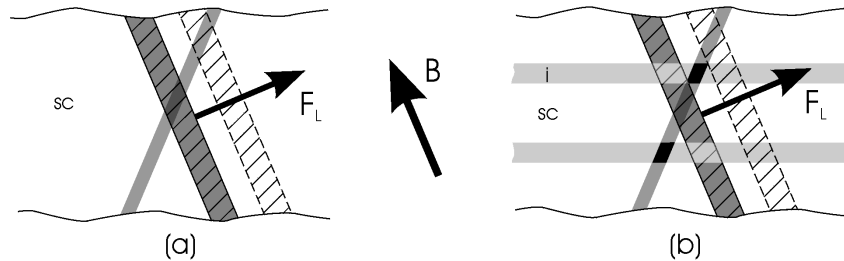

Figure 6.12: Schematic drawing of the pinning situation for fields oriented at large angles with respect to the coplanar orientation. The drawing is approximately to scale for sample C40 (b) compared to a non-layered superconductor with otherwise similar characteristics (a). In the homogeneous film a short section of the flux line is strongly pinned but it will *glide* along the defect in response to the Lorentz-force F_L. The only effective pinning potential is due to local variations resulting in weak point-like pinning very similar to a superconductor without coplanar pinning sites. In a layered superconductor (b) the section of the flux line in the potential valley has to cross the insulating layer. In a strongly-coupled superconductor a description in terms of a continuous flux line is still relevant, the Josephson-vortex in the insulating layer will experience much reduced pinning at the defect. Thus, the insulating layer effectively represents a barrier the flux line has to overcome to move in response to the Lorentz-force (see also [158]).

$Ta_{0.35}Ge_{0.65}$ film with columnar structure showed exactly this; enhanced pinning in the C-direction, but no additional pinning for fields at large angles [10]. In a multilayered film the situation is more like in figure 6.12 (b), which represents

a very schematic drawing for the situation of a strongly coupled film [158]. The drawing is approximately to scale for the situation in sample C40, only the horizontal extension of the defect is unknown. A flux line crosses a defect plane at a large angle, and the section of the flux line in the vicinity of the defect is in a deep valley of the potential the vortex experiences. In the homogeneous film this pinned section will just move along the defect and the only pinning force will come from variations in the pinning potential, thus it is effectively reduced to weak point-like pinning. In the layered sample this section has to cross the insulating layers as well, but there the pinning potential is not nearly as deep as in the superconducting layers, hence the pinned section of the flux line has to overcome a high potential barrier. This barrier is probably comparable to the barrier height C-aligned flux lines have to overcome. Contrary to the well-aligned case, the flux line is not pinned along its complete length, but only those parts that actually cross one of the defect planes. With the above estimate of the average distance between pinning sites of $\approx 100\,\mathrm{nm}$ and an angle between pinning planes and flux lines of $\approx 45°$, it follows that in about every 3$^{\mathrm{rd}}$ or 4$^{\mathrm{th}}$ superconducting layer the flux line is pinned this way.

To get the additional activation energy ΔU_A that is due to the coplanar defects, one can subtract the result that was obtained for the alloy film as that contribution that is due to pinning by point-like variations. To quantify the difference between C and AC-oriented fields one can look at the ratio $\Delta U_A^{AC}/\Delta U_A^C$ as a function of the applied field. This is shown in figure 6.13 for fields between 0.2 and 2.0 T. Although there is considerable scatter and the error bars are large, the ratio is approximately constant and a least-squares fit gives an average $\Delta U_A^{AC}/\Delta U_A^C \approx 0.29$. This coincides surprisingly well with the above estimation that roughly one third of the length of a flux line experiences enhanced pinning, even when the field is oriented at large angles to the defect structure.

The other strongly coupled films are the J-samples which have very similar interlayer-coupling to the C-samples but much thinner superconducting layers. The derived activation energies, as shown in figure 6.14, behave in a very similar way to C40, with no significant differences between J40 and J50. J40 shows a
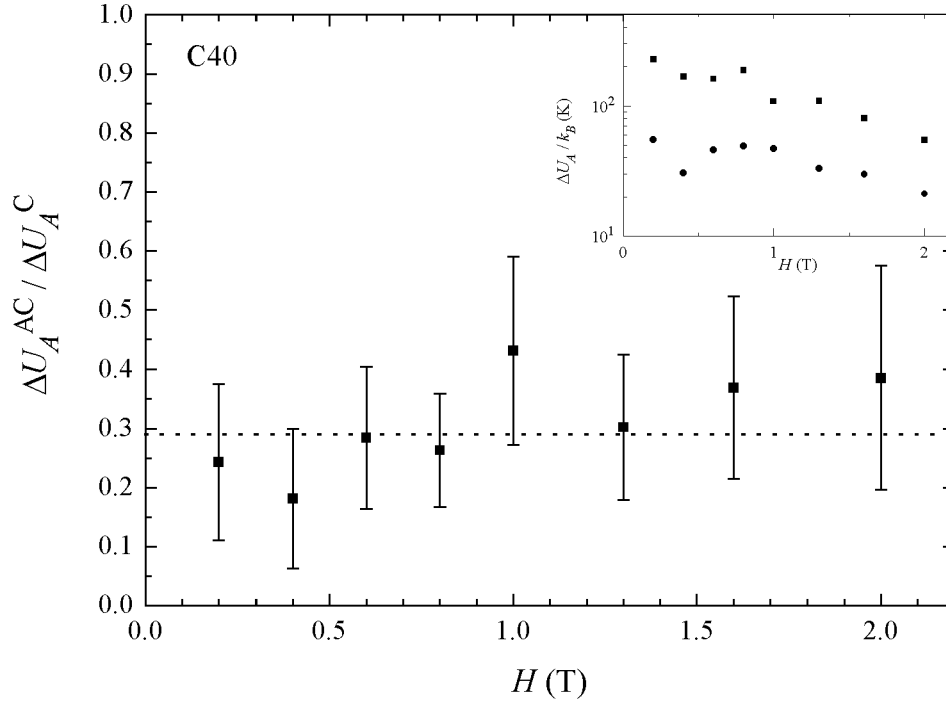
Figure 6.13: Relative increase in activation energy due to coplanar defects in C and AC-direction. The activation energy for the alloy film was subtracted from the results in figure 6.11, resulting in the additional contribution ΔU_A caused by the microstructure. The main plot shows the ratio $\Delta U_A^{AC}/\Delta U_A^{C}$ as a function of field, which is approximately constant. The dotted line is a least-squares fit giving the average ratio. Errors were calculated from the errors in U_A. Values for the C (square) and AC (circle) direction as a function of field H are shown in the inset.

maximum enhancement for a field $H \approx 0.2\,\mathrm{T}$ oriented in the C-direction while for J50 the maximum is shifted to a somewhat higher field of around $0.45\,\mathrm{T}$. For fields in the anti-columnar direction, both films show a slightly increased activation energy compared to the reference sample for fields $H > 0.1\,\mathrm{T}$, similar to the increase observed in C40. In fact, these three samples C40, J40 and J50, are so much alike in terms of their activation energy, that when all results are plotted in the same graph, as shown in the inset of the right graph of figure 6.14, they describe the same field dependence.

Weakly-Coupled Samples

A completely different picture emerges for the samples P40 and P50, which have superconducting layers of similar thickness to the C-samples, but are much more
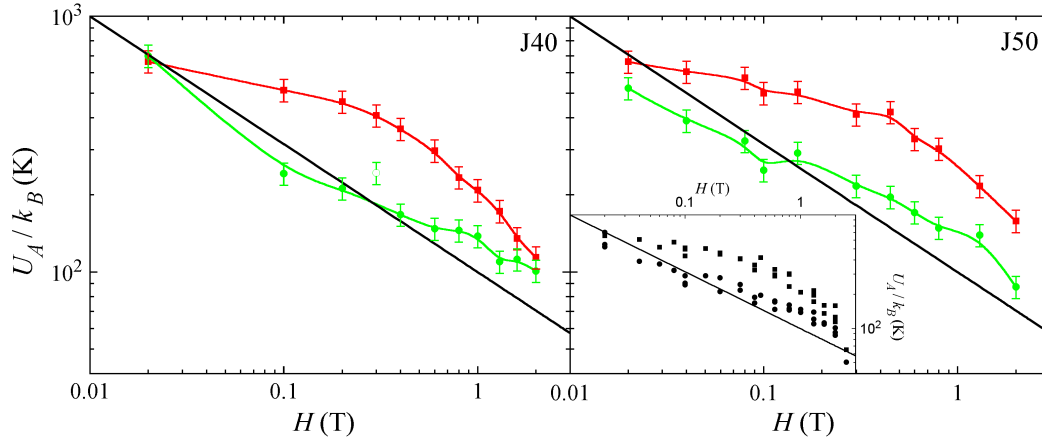
Figure 6.14: Activation energies for samples J40 (left) and J50 (right), again compared to the previously obtained activation energies for an unstructured alloy film (solid line). Resistance measurements were again taken in the C (red) and AC (green) directions for both samples. The data point represented by the open symbol in the left graph was excluded when drawing the interpolation line. The inset of the right graph shows the activation energies for samples C40, J40 and J50 in the same plot and C (squares) and AC (circles) aligned fields. Within the error margins, all three samples describe the same field dependence of the activation energies.
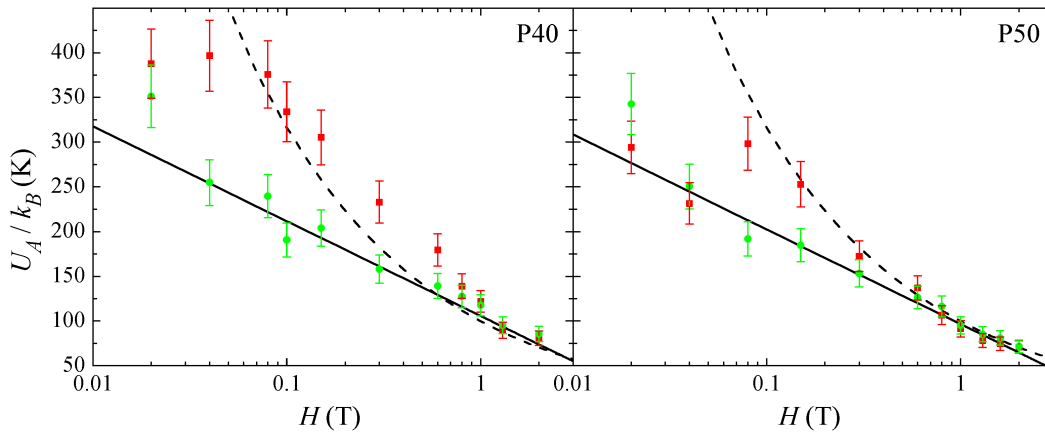

Figure 6.15: Activation energies for samples P40 (left) and P50 (right) here plotted on a linear scale versus the logarithm of the applied magnetic field. This way a logarithmic field dependence results in a straight line as observed for the AC-aligned fields (green data). The black solid lines are least-squares fits according to equation 5.46. For comparison the power-law curve which served as a guideline in the previous corresponding graphs is shown as the dashed line. Above $\approx 0.1\,\mathrm{T}$ and fields co-aligned with the defects (red data), the results can still be described approximately by a power-law dependence. At lower fields the data deviate from a power-law behaviour and approach the AC-data.

weakly coupled, due to the approximately twice as thick Ge-layers. As it turns out their activation energies do not show the same simple power-law behaviour as seen in C30 or the alloy film for either C or AC-aligned fields. In section 5.5.3 an alternative mechanism was presented which can also lead to a thermally activated resistance dependence, caused by the movement of unbound dislocations. As mentioned there, flux carrying dislocations are topologically forbidden in three dimensions, but possible in 2D or quasi-2D layered superconductors. Following equation 5.46 the activation energies for the P-samples in figure 6.15 are plotted versus the logarithm of the applied field.

Focusing first on the activation energies when the magnetic field was oriented at large angles to the defect structure (green symbols), the data describe a straight line to a good approximation and can be successfully fitted to an equation of the form 5.46. The fitting procedure had two fitting parameters, one of which was the characteristic field H_0 from equation 5.46 which should be of the order of the upper critical field H_{c2}. Best fits were achieved for $H_0 = 10.0$ and $8.2\,\mathrm{T}$ for P40 and P50, respectively, which compares relatively well to the upper critical fields determined from the fluctuation conductivity, which are 7.3 and $6.5\,\mathrm{T}$, respectively (compare to table 6.3). Using results given in tables 3.1 and 6.3, the pre-factor in equation 5.46 can also be calculated, giving a value of approximately 3, which is more than one order of magnitude less than the fitting parameter 46. Because equation 5.46 was derived for a two dimensional film and weak pinning, it is expected that the theory underestimates the magnitude of the activation energy for a film with weakly coupled superconducting layers and significant defect structure[5]. Therefore, it seems possible that the motion of unbound dislocations causes the observed thermally activated resistance.

For C-aligned fields (red data points) above $\approx 0.1\,\mathrm{T}$, the field dependence of the activation energy seems to be more like that in the previously discussed C and J-samples, although a clear enhancement due to the pinning by extended defects is not evident. For P40 the results are higher than what would be expected for an unstructured film, but far less than for example in C40 and J40, and the results

[5] For the AC configuration the defects are certainly not correlated, but the order parameter is still significantly reduced in their vicinity, thus causing stronger pinning.

for P50 follow almost exactly the same power-law dependence that was found for the reference alloy-film. At fields below $0.1\,\text{T}$, however, there is a clear deviation from the $1/\sqrt{H}$-dependence and it seems that the measured activation energies approach those determined for the AC field orientation. To see if the activation energy at very low applied fields does follow a logarithmic field dependence, the measurements would have to be expanded to lower fields. An extension to higher fields would be interesting as well. Because the two fitting curves almost coincide in the range $0.5\,\text{T} \leq H \leq 3\,\text{T}$, it is not possible to distinguish between two and three dimensional behaviour. For higher fields the two theoretical curves deviate again and it would be very interesting to study the evolution of the activation energies beyond the current field range, for fields aligned in the C- as well as the AC-direction. For this project, studying the conductivity at higher magnetic fields was excluded due to the temperature limit of $\approx 1.2\,\text{K}$.

From the available data it can be concluded that at fields above $0.1\,\text{T}$ in the C-direction samples P40 and P50 are dominated by three dimensional flux flow dynamics. The pancake vortices in the individual superconducting layers are pinned (most of the time) to the coplanar defects, thus they line up to form a one dimensional flux line made up of coupled segments. At lower fields the temperatures are higher, leading to thermally activated depinning of individual pancake vortices. This reduces the correlations along the defects and a crossover to 2D-behaviour occurs. However, at temperatures even closer to $T_c(0)$ or slightly above, in the fluctuation conductivity regime, the resistance could be explained within a three dimensional model (see sections 6.2 and 6.4) thus leaving some doubt about the dimensionality in this narrow field and temperature range. Similar recoupling effects, mediated by the presence of correlated defects, have also been observed in HTSC. This will be discussed in more detail in conjunction with the phase diagrams in section 6.8.

6.6   *IV*-Characteristics and Glass Scaling

As outlined in the theory chapter, current-voltage characteristics can give considerable information about the dynamics of the vortex system. Furthermore,

the possible second order phase transition between a pinned vortex glass and a vortex liquid will lead to a characteristic change of the *IV*-curves with temperature. Using a set of IV-curves taken for one sample at a particular magnetic field magnitude and direction, but varying temperature, the information that can be extracted will be discussed qualitatively. Thereafter, a quantitative analysis in the form of a glass transition will be attempted for all samples, applying the appropriate scaling equations from section 5.6. Furthermore, such a quantitative analysis of the *IV*-curves will allow us to gain information about the dissipation processes in the vortex glass phase and to construct vortex phase diagrams in sections 6.7 and 6.8, respectively. The behaviour of the samples characterised by strong interlayer coupling will be shown to be very much as expected from comparable studies of weakly anisotropic HTSCs like YBCO. The weakly-coupled P-samples on the other hand show a somewhat different behaviour, but not unlike more anisotropic HTSCs.
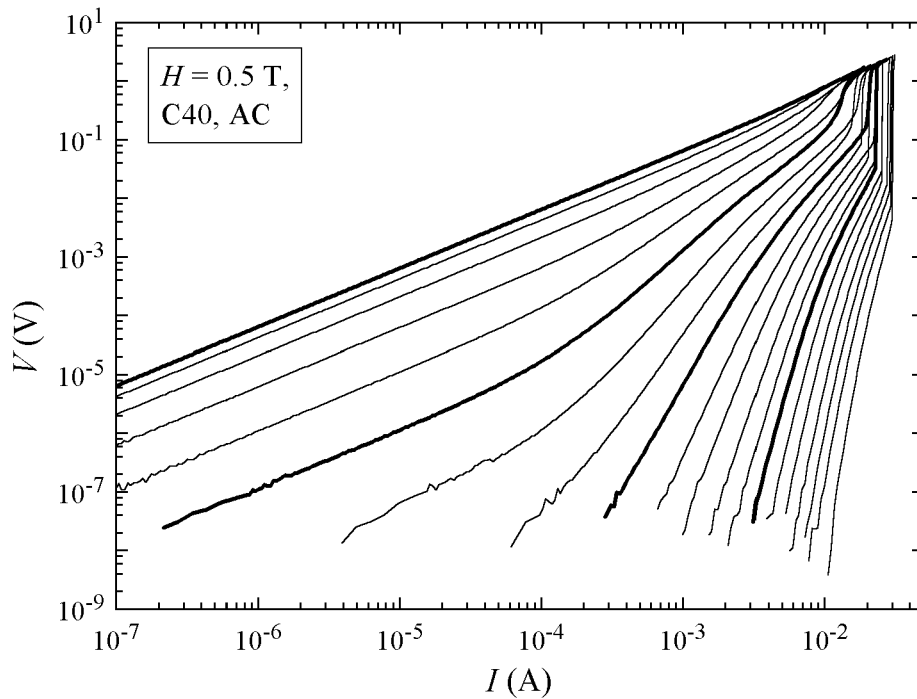

Figure 6.16: Log-log plot of the *IV*-characteristics for sample C40 with the magnetic field $H = 0.5$ T applied in the AC-direction. Temperatures range from 2.15 K for the topmost curve down to 1.195 K for the lowest one in intervals of 50 mK (55 mK for the last step). The changes with temperature are highlighted by the four bold curves and discussed in detail in the text.

In figure 6.16 a double logarithmic plot of IV-curves for sample C40 in an applied field of $0.5\,T$ in the AC-direction is shown[6]. The temperature varies from 2.15 to 1.195 K. At the highest temperature the sample exhibits free flux flow and ohmic resistance from the lowest measured current, 10 nA, to about 1 mA. From the upper critical field measurements it can be inferred that the sample is indeed in its superconducting state. The critical temperature at $H = 0.5\,T$ can be calculated to be $T_c = 2.233\,K$, which is significantly higher than 2.15 K, the measurement temperature. Using equation 5.32 the expected free flux flow resistance can also be calculated, and the resulting value of $R_{\mathrm{FFF}} = 62.2\,\Omega$ compares very well with the measured value of $63.6\,\Omega$ averaged over 5 orders of magnitude in excitation current. As will be seen more clearly below, at about 1 mA a very gradual transition to the normal state resistance sets in.

As the temperature is reduced the resistance drops rapidly. At the next high-lighted temperature of 1.90 K the resistance has dropped by more than 2 orders in magnitude. Now the linear region extends up to about $10\,\mu A$ only, at which point a nonlinear critical region is entered. As the current is further increased the free flux flow resistance value is approached, but never reached. Instead, at a second critical current the film turns normal conducting by a transition that becomes increasingly sharp with lower temperature.

As outlined in section 5.6 the glass transition temperature is characterised by a power-law IV-curve for all applied currents. The third emphasized curve in figure 6.16 can be described very well with a power-law dependence up to currents exceeding 1 mA. At even larger currents, the vortex velocity becomes so large that the pinning potential is smeared out and the curve deviates from the power-law behaviour. The transition to the normal state proceeds by an almost discontinuous jump to the normal state resistance. At even lower temperatures the IV-curves exhibit glassy behaviour with downward curved characteristics and

---

[6] Note about physical quantities: The equations derived for the glass theories are expressed in the material-dependent quantities, current density and electric field. However, only pro-portionalities were derived, which also hold for the sample-dependent quantities, current and voltage. Therefore, as long as only the glass exponents ν and z and the transition temperature T_g are of interest, it is sufficient to plot and analyse the IV-curves using the original data without converting them to the sample-independent quantities.

a very sharp jump to the normal state at high driving currents.

The transition into the normal state has not been investigated in detail in this study, but a few qualitative remarks can be made here. From equation 5.29 the depairing critical current density can be estimated. For the films studied, it is in the range $J_0(0) = 10^5 - 10^6 \, \text{A/cm}^2$. More specifically, using a relation that includes the pre-factor in equation 5.29 (e.g. [9]), the critical current density at zero temperature for sample C40 is $J_0 = (7.4 \pm 0.6) \times 10^5 \, \text{A/cm}^2$. For the power-law curve and those taken at lower temperatures the current density at which the discontinuity is observed is approximately $J_{\text{dis}} \approx 6 - 9 \times 10^3 \, \text{A/cm}^2$, a factor of 10 or more below the depairing current density at these temperatures. Therefore, it is likely that this discontinuity is caused by an instability calculated by Larkin and Ovchinnikov [96]. This assumption is based on extensive analysis of the instability in similar Ta/Ge multilayers by B. Ruck *et al.* [10, 32, 159]. They have also extended the theory by Larkin and Ovchinnikov to include the effects of pinning [97]. Even at higher temperatures the more gradual transition to the normal state is probably dominated by this instability. Although the depairing critical current density, $J_0 \propto t^{3/2}$, decreases more rapidly with increasing temperature than the current at which the instability occurs, it is still considerably higher for all T, except extremely close to $T_c(0)$.

More information about the transition from the vortex liquid to the pinned vortex phase can be extracted from these *IV*-characteristics when plotting the logarithmic gradient $\mathrm{d}(\log V)/\mathrm{d}(\log I)$ versus the current or, as in figure 6.17, versus $\log I$. For this plot the line for the highest temperature is at the bottom of the graph. Clearly, at the highest temperature the film shows linear behaviour for all but the highest currents, which results in the horizontal line at $y = 1$. As already mentioned above, at $I \approx 1 \, \text{mA}$ the gradient increases, marking the onset of the transition to normal conductivity.

In the TAFF region the ohmic behaviour is limited to low currents while in the critical regime the gradient increases with decreasing temperature. The transition to the normal phase becomes sharper, resulting in an increasingly pronounced peak in the gradient, which is not shown in figure 6.17 to keep the graph
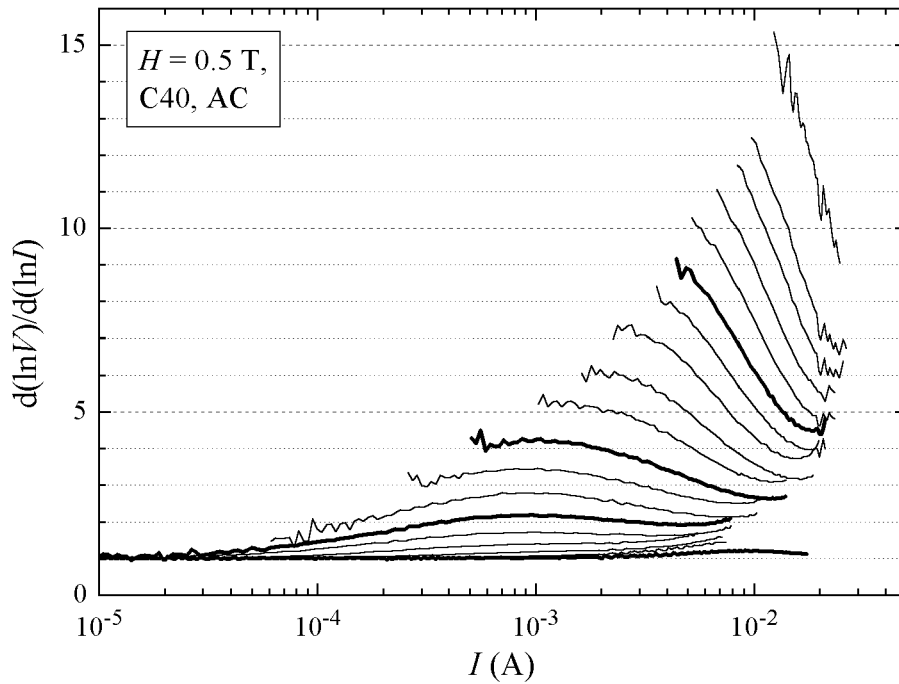
Figure 6.17: Logarithmic gradient $\mathrm{d}(\log V)/\mathrm{d}(\log I)$ plotted versus $\log I$ for the same data set shown in figure 6.16. In this representation the temperature decreases from the bottom to the top curve. Curves for the same temperatures as above are highlighted.

as concise as possible. According to equations 5.51 or 5.60, at the transition temperature from the unpinned vortex phase to the respective vortex or Bose-glass phase, the logarithmic gradient of the IV-curve should result in a horizontal line. The y-value of the horizontal line determines the dynamic critical exponent via the exponent in equation 5.51 or 5.60, depending on the glass theory applied. Although not absolutely conclusive, the bold curve near the proposed transition temperature has an approximately horizontal part at low currents, from which the dynamic exponent can be estimated using the respective scaling relation.

At low temperatures the IV-characteristics definitely have a negative curvature on a double-logarithmic plot, which is demonstrated by the sharply increasing gradient with decreasing current. As already anticipated in this discussion, the IV-curves show the typical temperature dependence predicted by the various glass theories. Before a detailed scaling analysis for all samples based on this more general description is discussed, a direct comparison for IV-curves taken in the C- and AC-direction is made.
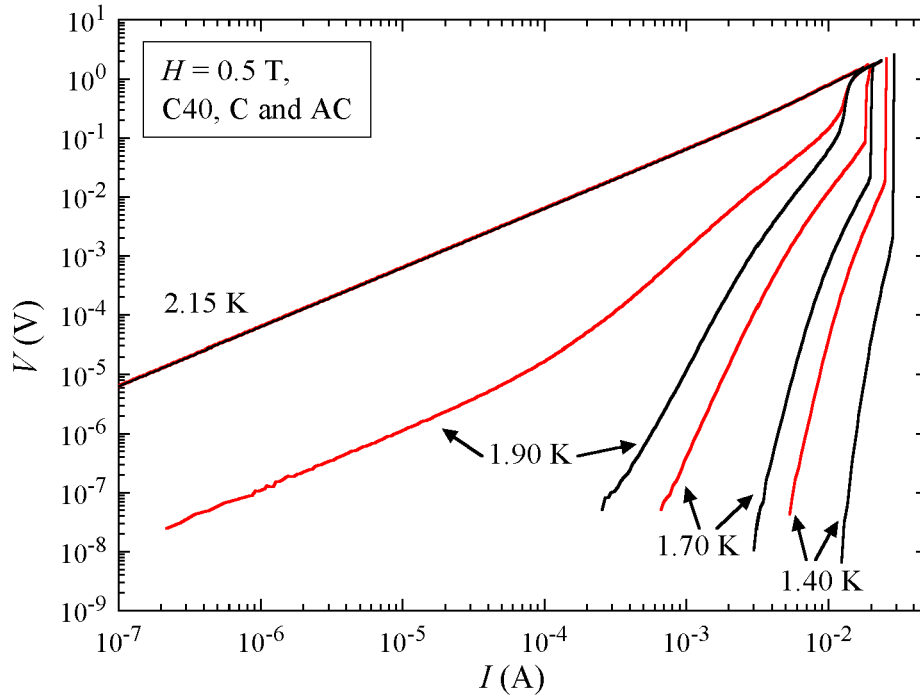
Figure 6.18: Selected *IV*-curves for sample C40 at a field of 0.5 T applied in the C-(black) and AC-direction (red). Temperatures were as indicated in the graph. The influence of enhanced pinning for fields aligned with the defect structure is clearly visible; the measured voltage for any given current and temperature is many orders of magnitude smaller in the C-direction compared to AC-oriented fields (except when the film is very close to its normal state resistivity).

In figure 6.18 a few selected *IV*-curves taken at $H = 0.5$ T in the C- (black) and AC-direction (red) are compared to each other. At high temperatures in the free flux flow regime, the two directions are indistinguishable and coincide with each other. But as the temperature is reduced the resistance drops much faster for fields aligned with the defect structure. Furthermore, at 1.90 K when the sample is still in the TAFF region for AC-aligned fields, the curve taken for C-orientation shows approximately power-law behaviour, indicative of the glass transition. Consequently, when the red curve shows a power-law dependence over a substantial range in applied currents, the black curve has negative curvature and the sample is already deep within the glass phase (1.70 K). Even at very low temperatures the resistance in the C-direction is many orders of magnitude smaller compared to when the field is at large angles to the defects. This very qualitative analysis already implies that the glass transition temperature strongly

depends on the magnetic field orientation for sample C40.

Following, a brief description of the procedure applied to analyse the IV-characteristics will be given. Sample-specific deviations from this method will be explained where necessary. The glass theories developed in section 5.6 offer many possible ways to determine the critical glass exponents and the transition temperature. Plotting the logarithmic gradient versus current as in figure 6.17, the transition temperature and the dynamic critical exponent can be estimated immediately. Further analysis was done using two independent methods. The first one is based on equations 5.52, 5.54 and 5.61, 5.63 for vortex glass and Bose-glass, respectively. The ohmic resistance at low currents was determined directly from the IV-measurements for those curves for which the ohmic part was accessible. The cross-over current between linear and critical behaviour was chosen as the current when the non-linear resistance had increased to twice the low current ohmic resistance[7]. The power-law scaling relations, equations 5.54 or 5.63, should then result in straight lines in a double-logarithmic plot from which the critical exponents can be determined. In practice, the previously estimated transition temperatures had to be adjusted to achieve successful scaling.

The other method is based on the prediction that the IV-curves taken at different magnetic fields and temperatures should all collapse, for the right choice of glass parameters, onto the universal functions $\mathcal{E}_{\pm}$ and $\mathcal{F}_{\pm}$ for vortex glass and Bose-glass, respectively. For this purpose a computer program was written that allowed adjustment of all relevant parameters, i.e. ν, z, and T_g, or the corresponding parameters for the Bose-glass, by increasing or decreasing them by a variable amount. This could be done for IV-sets for a specific magnetic field and for the complete set of IV-curves taken for one sample and magnetic field orientation. The resulting collapse was then checked visually as well as by calculating

---

[7] Of course, this definition of the cross-over current is arbitrary. However, using different criteria to define deviations from the linear behaviour result in very similar critical exponents.

a standard deviation[8] for the two branches of the universal functions. The value for the deviation should reach a global minimum for the best collapse. However, it proved to be very difficult to minimize it for the upper and lower branch simultaneously. Therefore, emphasis was put on the best visual collapse and fine adjustment of the parameters was done by trying to minimize the deviation.

If the vortex system is indeed undergoing a phase transition as proposed by these glass theories, both methods should give consistent values for the glass parameters and work equally well.

When the glass theories were discussed in section 5.6, it was already mentioned that the scaling relations for vortex glass and Bose-glass are very similar, thus it is not possible to distinguish between the two phases from the scaling of the *IV*-characteristics. Finding the characteristic cusp in the transition temperature for the Bose-glass when tilting the magnetic field from the defect direction was attempted. Probably due to the substantial distribution of columnar orientation in these films, an analysis following equation 5.64 was not conclusive. However, the rotation data presented in section 6.3 proved the additional anisotropy present in the films without doubt. Based on that and the structure of the films known from the TEM investigations, it is argued that the BG-theory is the appropriate model to describe the vortex system for fields aligned with the defect structure. For the other configuration (magnetic field in the AC-direction) no effective extended pinning sites are present and any possible pinned vortex phase at low temperatures should be adequately described using the VG-theory.

Sample C30

The first sample to be discussed in detail is C30, which has strongly-coupled superconducting layers and has shown relatively weak pinning in the C- and AC-directions, so far. In figure 6.19 the linear resistance and the cross-over current, separating the linear from the critical region, are shown versus $T - T_g$ in a double-

---

[8] Because no analytical expression for the scaling functions is known, standard fitting procedures could not be applied. Therefore, the scaled current range was divided into a certain number of x-value ranges. For each range, the standard deviation of the y-values that were falling into that range was calculated for the two branches and summed up. These sums for the lower and upper branch quantify, to some degree, the collapse of the *IV*-curves.
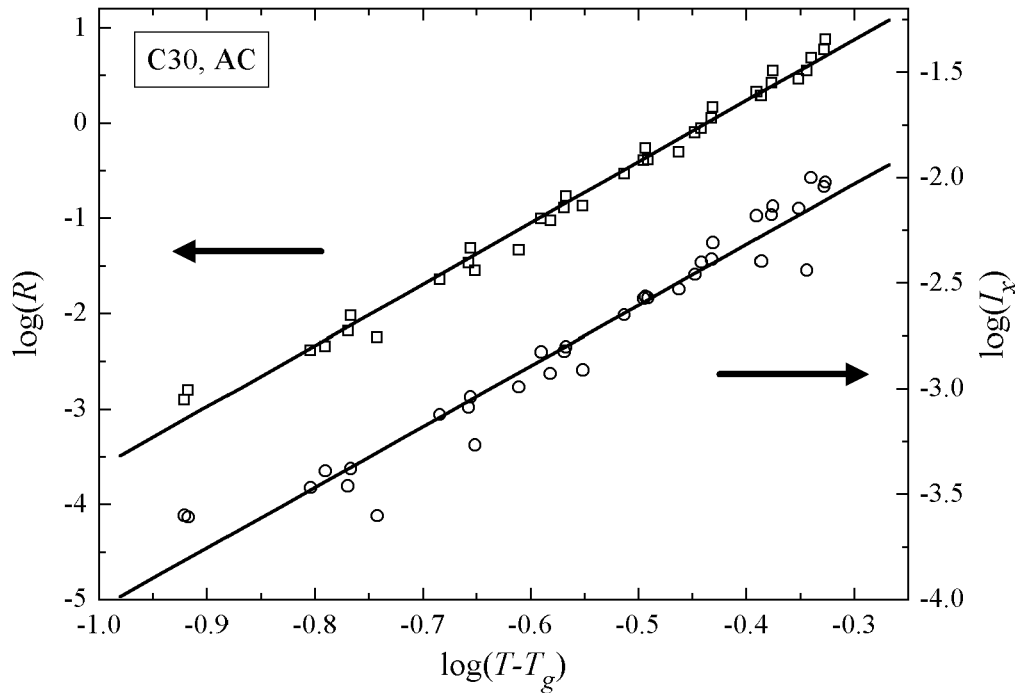
Figure 6.19: Double-logarithmic plot of linear resistance (squares, left axis) and critical current (circles, right axis) above T_g versus $T - T_g$ for sample C30. Data points are for fields $H = 0.35, 0.4, 0.45, 0.55, 0.8, 1.0,$ and $1.2\,\text{T}$ applied in the AC-direction. The straight lines are power-law fits to the data, from which the critical exponents can be calculated.

logarithmic plot for temperatures above T_g and magnetic fields as given in the caption of the figure. Only those magnetic fields were included in the graph and analysis for which for at least 3 different temperatures the linear resistance and cross-over current could be determined from the IV-curves. Initially, the field-dependent glass temperatures T_g were estimated from plots of the logarithmic gradient $\mathrm{d}(\log V)/\mathrm{d}(\log I)$ versus current I, similar to the example shown in figure 6.17 above. More precise estimates for the glass temperatures were obtained from independent efforts to collapse the IV-curves onto the universal scaling functions. All data points can be described by just one power-law function of $T - T_g$ for the linear resistance and the cross-over current, respectively. From the exponents of the respective power-laws the critical glass exponents ν and z can be calculated applying equations 5.52 and 5.54 assuming 3D VG-behaviour.

Using the glass exponents obtained in the way described above, the IV-data were scaled and a best possible collapse onto the scaling functions $\mathcal{E}_\pm$ was at-
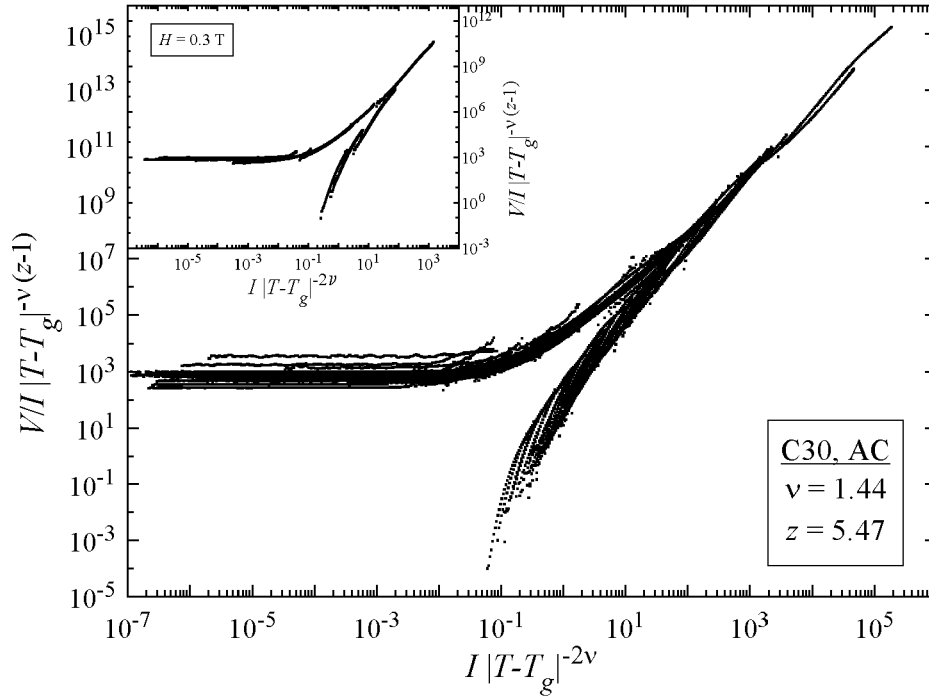
Figure 6.20: Scaled *IV*-curves for sample C30 taken at magnetic fields $H = 0.1, 0.2, 0.3, 0.35, 0.4, 0.45, 0.55, 0.8, 1.0,$ and $1.2\,\mathrm{T}$ (AC-direction) and various temperatures above and below the glass transition temperature. Glass scaling parameters are $\nu = 1.44$ and $z = 5.47$. The inset shows the scaling for just one set of *IV*-curves taken at $H = 0.3\,\mathrm{T}$.

tempted. All *IV*-curves taken in the AC-direction were included, except those in the free flux flow region, and ν and z were kept fixed, adjusting $T_g(H)$ only. Data taken for very high excitation currents close to the instability or the depinning current and above were not considered. If the glass temperatures had to be changed, the scaling of the linear resistance and cross-over current was repeated until consistent scaling could be achieved. The plot in figure 6.19 is for the final set of parameters. The resulting collapse onto the universal functions $\mathcal{E}_\pm$ of the *IV*-curves, including all measured magnetic fields ranging from 0.1 to 1.2 T, is shown in graph 6.20. The achieved scaling is very good considering the range of magnetic fields, and that for the three lowest fields from 0.1 to 0.3 T the glass exponents used were determined from the higher field values. Furthermore, looking at the set of *IV*-curves for each magnetic field individually, the collapse is qualitatively much better, as can be seen in the inset of figure 6.20. This kind of collapse was usually achieved when *IV*-data for only one magnetic field were

considered.

That the IV-curves taken at constant magnetic field usually scaled very well, but when comparing the scaling functions for all measured field values there was much less convincing scaling observed, is a general observation, holding for all films and field orientations. The original VG or BG models do not include any field-dependence of the critical functions. Studies on BSCCO containing columnar defects have shown no field-dependence of the scaling functions in accordance with the BG theory [151, 152, 160]. However, other authors reported a field-dependence of the scaling functions in YBCO films [161–163]. As pointed out by K. Moloni *et al.* these measurements can still be interpreted very successfully within an extended VG theory [163]. A detailed analysis along this extended VG theory is beyond the scope of the present project. But it should be kept in mind, that a less than perfect collapse of the IV-curves when data for all measured magnetic fields are included is not necessarily contradicting the universal character of the scaling analysis.

The situation for magnetic fields applied in the C-direction of C30 is not as consistent as for the AC-direction. The same procedure for analyzing the IV-curves was followed as above, only the respective equations for BG-theory were applied. Figure 6.21 shows the scaling behaviour of the linear resistance and the cross-over current for temperatures above T_{BG} and a range of magnetic fields, as given in the caption. Again, both quantities show scaling according to the glass theory and the extracted values for the Bose-glass exponents are given in the graph. However, the IV-curves could not be collapsed onto the BG-scaling functions using these values.

The only way to achieve scaling for the IV-curves was by allowing very different glass exponents, for approximately the same field-dependent $T_{BG}(H)$. The scaled IV-data and the exponents are shown in figure 6.22. The collapse was achieved by scaling the IV-sets taken for each magnetic field individually and finally using the averaged values for ν' and z'. This approach was very successful for temperatures below $T_{BG}(H)$. Above the transition temperature scaling of individual sets of IV-curves at constant magnetic field was also very good. How-
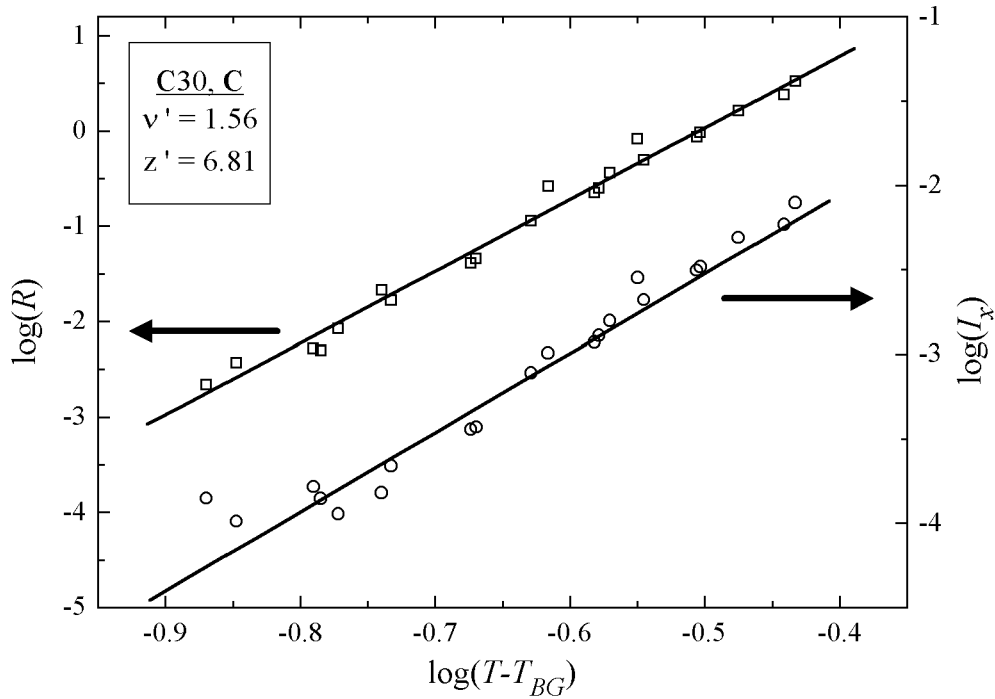
Figure 6.21: Scaling of the linear resistance and the cross-over current for C30 and magnetic fields $H = 0.4$, 0.45, 0.55, 0.8, 1.0, and $1.2\,\mathrm{T}$ applied in the C-direction. The straight lines are power-law fits to the data and the extracted glass exponents using BG-theory are given in the figure.

ever, the spread of data, looking at the complete set of *IV*-curves, is somewhat bigger than in the AC-case in figure 6.20. For comparison, the scaled *IV*-data taken at $H = 1.0\,\mathrm{T}$ in the C-direction using the glass exponents as derived from scaling the linear resistance and cross-over current above T_{BG}, is shown in the inset of figure 6.22. Although the scaling for isotherms above T_{BG} is very good, it fails for lower temperatures. Even for the higher temperatures when looking at the scaling behaviour for the complete range of magnetic fields, the data are spreading over a large range, comparable to the spread in the main graph of figure 6.22.

Since both sets of ν' and z' are in the range expected for a Bose-glass, it is not possible to rule out either one, although the values given in the main graph of figure 6.22 compare better with results for the other films (see below). From the analysis of C30 in the previous sections it is known that the columnar microstructure is very weakly developed. It is thus possible that the extended
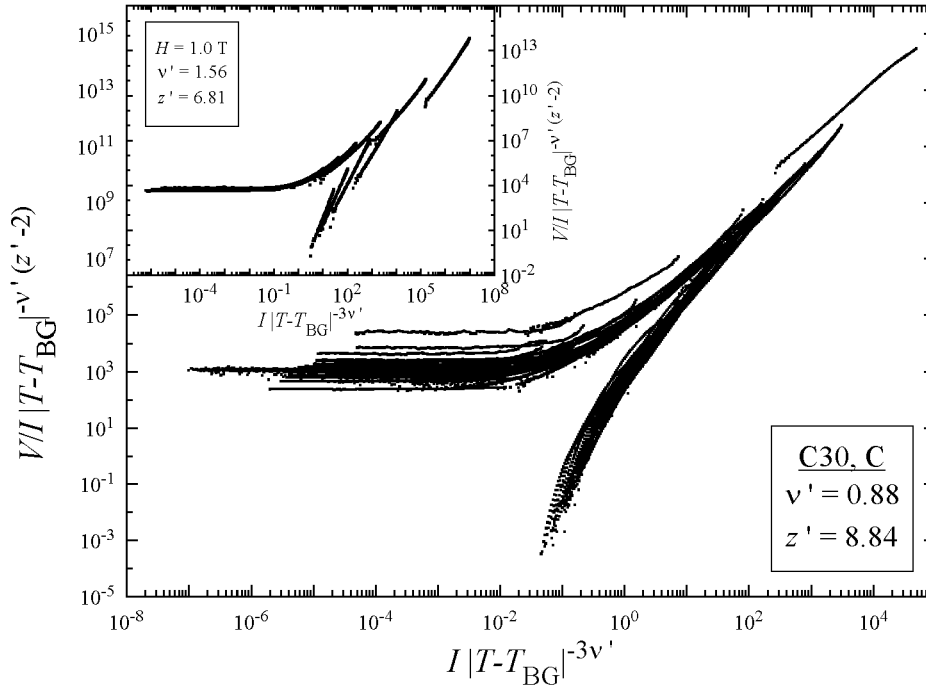
Figure 6.22: Scaled IV-curves for C30 taken at magnetic fields $H = 0.1, 0.2, 0.3, 0.35, 0.4, 0.45, 0.55, 0.8, 1.0,$ and $1.2\,\mathrm{T}$ in the C-direction. Very different glass parameters were used to achieve scaling compared to the values given in figure 6.21. The inset shows the scaling of IV-curves taken at $1.0\,\mathrm{T}$ using the other set of glass parameters, but the same T_{BG}.

defects are comparable in pinning strength to point-like defects in this film. Using VG-equations instead to scale the IV-curves gives qualitatively the same results, but the resulting VG exponents would be rather unusual. It seems possible that this film would have to be described by a theory which takes equal account of point and extended defects.

Sample C40

Sample C40 differs from the previous sample C30 by having much stronger flux pinning in the TAFF-region due to a more developed columnar structure. IV-curves for sample C40 have been discussed qualitatively at the beginning of this section, particularly in the case of AC-aligned fields. The quantitative analysis along the lines of a glass transition is given here. Graph 6.23 summarizes the scaling analysis for the case of AC-aligned fields. The main graph shows the scaling of the linear resistance and the cross-over current according to equations
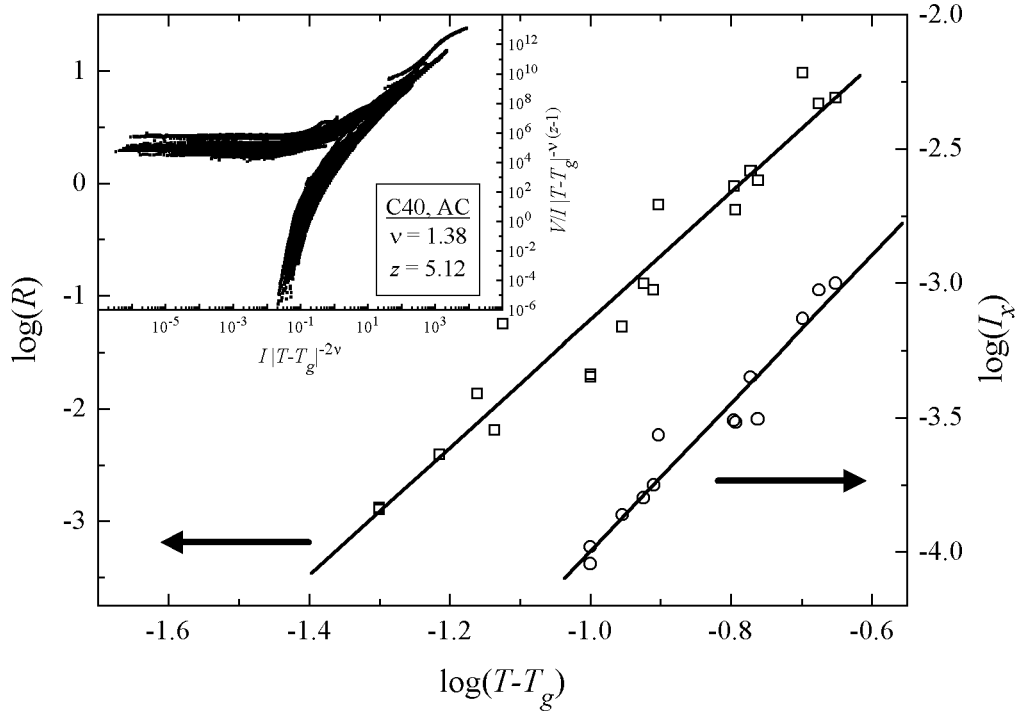
Figure 6.23: Ohmic resistance in the TAFF-region and cross-over current to the critical region for sample C40, AC-fields (0.1, 0.3, 0.5, 0.7, and 1.0 T), versus $T - T_g$. Again, the data can be described by a simple power-law given by the straight lines in this double-logarithmic plot. The inset shows the resulting scaling of the *IV*-curves and the glass exponents derived from the power-law exponents in the main graph for the magnetic field values given above, plus 0.05 and 1.3 T.

5.52 and 5.54, and the straight lines are power-law fits to the data. The resulting scaling of the *IV*-curves is shown in the inset, including all measured magnetic field values. Although scaling of the *IV*-curves for individual magnetic fields is very good, the data for all 7 field values together describe rather broad bands instead of the universal functions. However, there is a consistent trend of the data shifting towards the lower right corner of the graph with increasing magnetic field. Comparing the critical exponents ν and z to the results for C30 in the AC case, the values fall within the same range.

Scaling of the *IV*-characteristics for fields applied in the C-direction is shown in figure 6.24. Because of the strong pinning effect of the extended defects the vortex liquid phase is limited to a much smaller temperature range as will be shown later (section 6.8). Therefore, the number of data points available to check scaling of the linear resistance and cross-over current at temperatures above T_{BG}
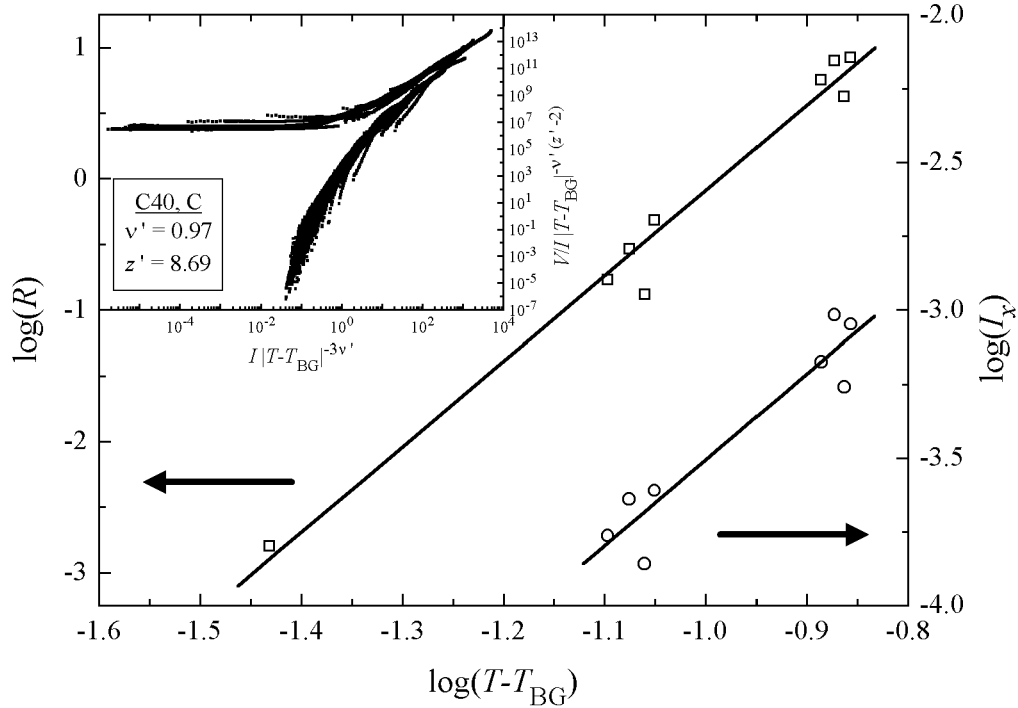
Figure 6.24: Scaling of *IV*-characteristics for film C40 with fields applied in the C-direction analogous to previous graphs. Due to the relatively small vortex liquid range, only a few data points ($H = 0.3$, 0.5, 0.7, and 1.0 T) are available to determine critical exponents from the fitted straight lines. The data still leads to successful scaling of the *IV*-curves, shown in the inset for the whole range of magnetic fields as in figure 6.23.

is much less than for previous examples. Nevertheless, the data was fitted to the respective power-laws and the resulting collapse of the *IV*-curves, including those for which no linear resistance data could be extracted, is reasonably good. The values of the critical exponents also fall within the expected range for a Bose-glass.

Sample J40

This film, which is also characterised by thin insulating layers and thus strong interlayer coupling comparable to the C-samples, exhibits similar scaling behaviour to sample C40, for which the evaporation angle of $\alpha = 40°$ was identical. The thinner sc-layers in the J-samples do have an effect on the pinning behaviour for AC-aligned fields and high current densities, which is, however, more pronounced in J50 and thus will be discussed below for that sample. Figure 6.25 shows the final outcome of the scaling analysis for fields applied in the AC-direction. The
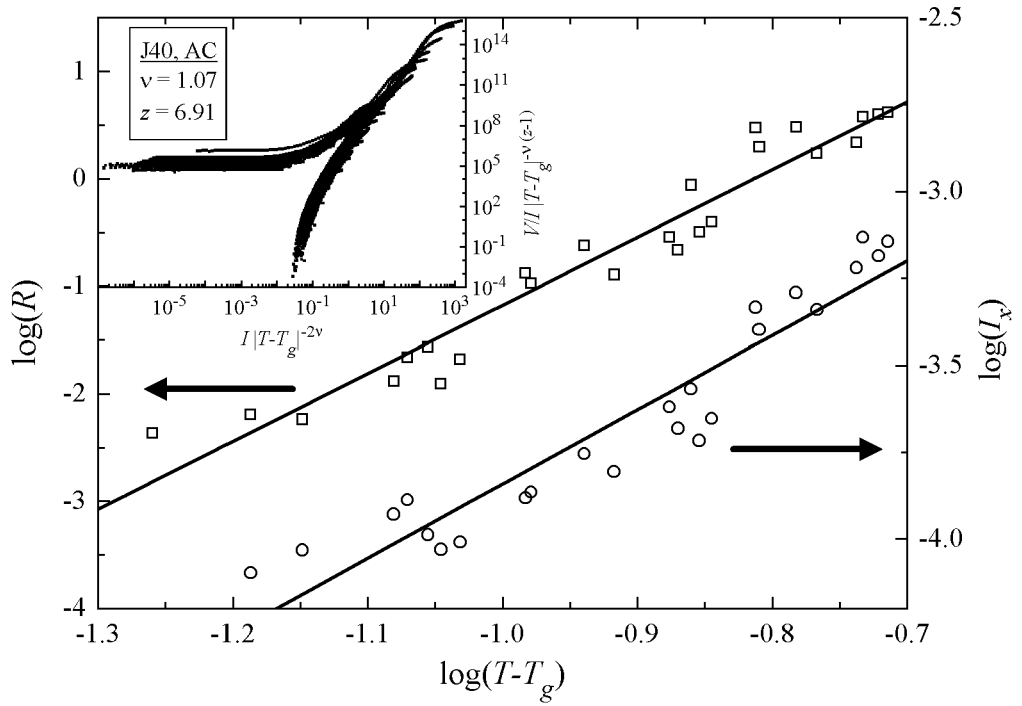
Figure 6.25: Scaling analysis for J40 analogous to previous samples. Magnetic fields $H = 0.1$, 0.2, 0.3, 0.4, 0.5, 0.6, 0.8, 1.0, and $1.3\,\text{T}$ were applied in the AC-direction.
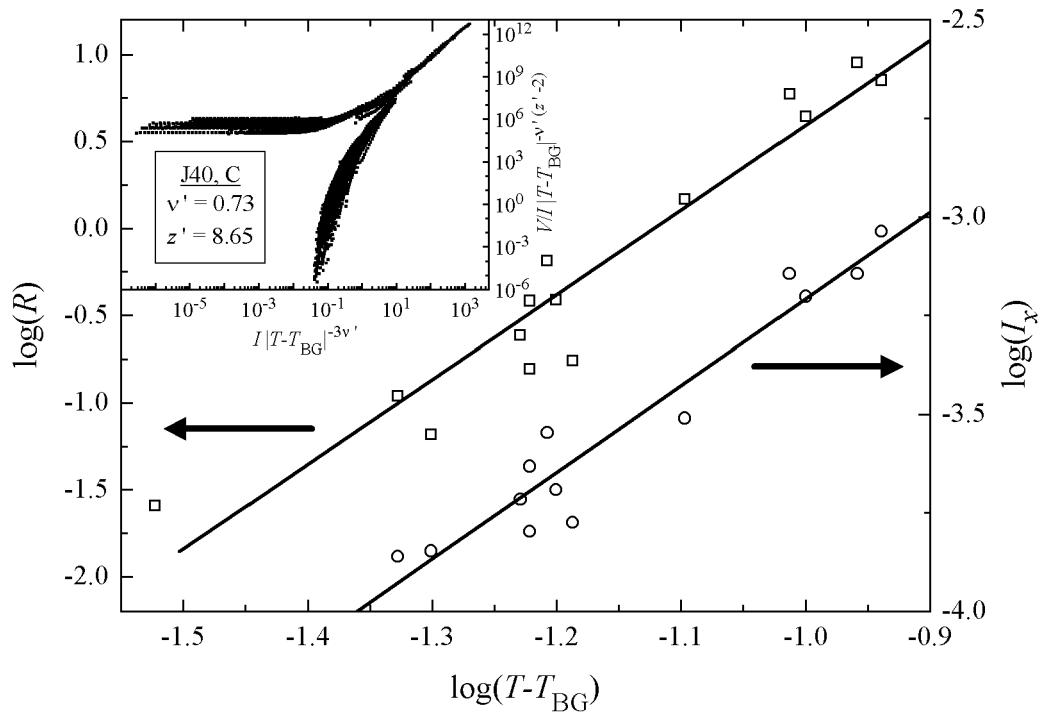

Figure 6.26: Similar graph as figure 6.25 for J40, but fields applied parallel to the extended pinning structure (C-direction).

achieved collapse of the IV-curves, as well as the power-law dependence of the linear resistance and the cross-over current on the reduced temperature $T - T_g$, have very much the same deviation from the ideal behaviour as seen in C40. However the resulting glass exponents, as given in figure 6.25 are different, although they are still within the range of reported values for a VG. A close look at the scaled IV-curves at very high current densities reveals a kink and deviation from the scaling behaviour for some of them. As mentioned above, this will be discussed in more detail for sample J50.

IV-curves taken for magnetic fields parallel to the extended defects can be well described within the BG-theory. The scaling analysis is summarized in figure 6.26, again showing the temperature dependence of resistance and cross-over current as well as the collapse of the IV-curves onto the universal functions. In this case, the obtained critical exponents are very similar to the BG-exponents for C40, supporting the idea of universal scaling.
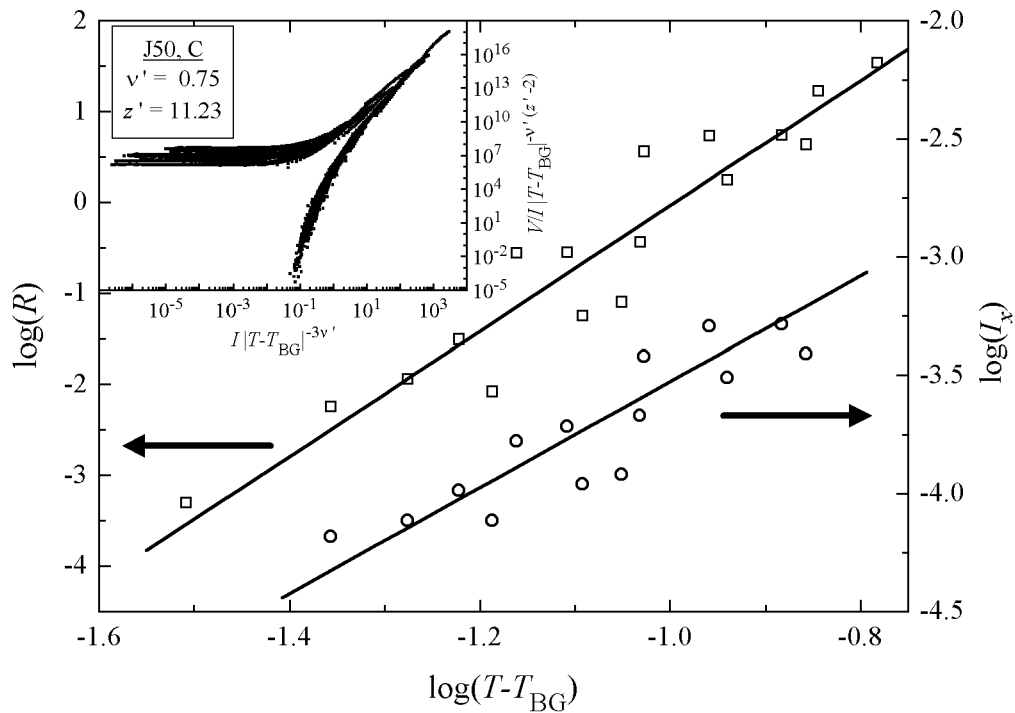
Sample J50

Figure 6.27:   Bose-glass scaling of sample J50 with magnetic fields $H =$ 0.05, 0.1, 0.3, 0.6, 0.8, 1.0, and 1.3 T applied in the C-direction.

The discussion of the *IV*-characteristics and the scaling behaviour for sample J50 will start with C-aligned fields, because for this field orientation J50 is similar to J40 and C40. Figure 6.27 shows the scaling analysis analogous to the previous films. Again, this film shows a considerable range of scaled linear resistances (the horizontal part of the upper branch of the scaling function). But more significantly, the dynamic critical exponent z' is very different compared to the previous two samples for which consistent BG-scaling was found. The *IV*-curves did not collapse assuming z' between 8 and 9, similar to the previous samples, even for drastically changed ν' and $T_{\text{BG}}(H)$.
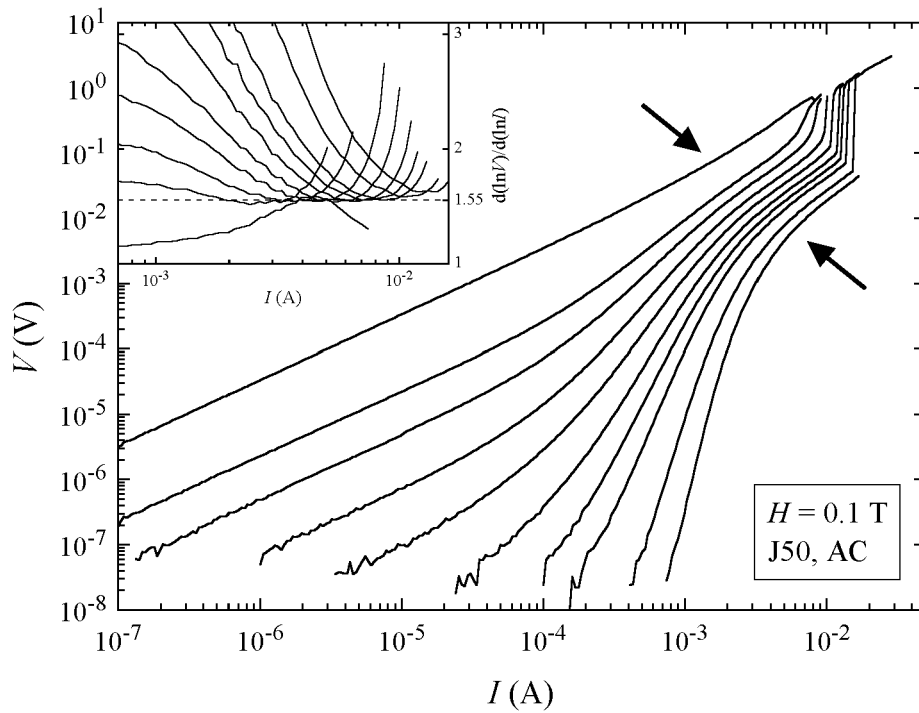

Figure 6.28:   *IV*-characteristics for sample J50 at an applied magnetic field H = 0.1 T in the AC-direction and different temperatures T = 1.70, 1.75, 1.80, 1.825, 1.85, 1.875, 1.90, 1.925, 1.95, and 2.00 K (right to left). At high critical currents, approximately indicated by the arrows, the curves deviated from the qualitative behaviour discussed at the beginning of this chapter. All curves are nearly parallel with a small gradient close to 1. The logarithmic gradient as a function of the applied current is shown in the inset, from which it can be determined to be ≈ 1.55 in this region.

J50 differs even more from the other strongly-coupled samples for AC-aligned magnetic fields. Figure 6.28 shows a set of isothermal *IV*-curves taken at H = 0.1 T. The first difference is a deviation from the the glassy behaviour at high

applied currents which could be seen in J40 and AC-aligned fields as well, but this variation is much more pronounced here.

At a high current value, indicated by the two arrows in the figure 6.28, the *IV*-curves flatten significantly and are nearly parallel for all measured temperatures. This is even more apparent in the inset of the graph, which shows the logarithmic gradient as a function of the applied current. All curves have a minimum gradient approximately equal to 1.55 before the transition to the normal conducting state (not shown in inset). That the *IV*-curve taken at the highest temperature in the free flux flow regime has a maximum also equal to 1.55 is probably coincidence. Similar *IV*-curves were also measured at 0.05 T, for which the logarithmic gradient is $\approx$ 1.50 before the instability. At the higher field value at 0.3 T for temperatures below 1.70 K this characteristic behaviour vanished, and the minimum logarithmic gradient, just before the sample turned normal conducting, increased with decreasing temperature just as can be seen in figure 6.17 for sample C40, but to a lesser extent. At even higher fields this behaviour was not observed, probably because the sample is normal-conducting or at least in the free flux flow regime at temperatures of 1.70 K or above. Signs of this behaviour have also been seen in sample J40 at small magnetic fields and high temperatures.
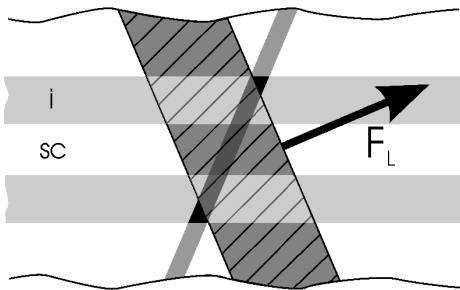

Figure 6.29: Vortex core in a layered superconductor with thin superconducting and thin insulating layers. In this schematic drawing the magnetic field is applied at large angles to the extended defect. The coherence length is large enough so that the vortex samples the pinning potential in the superconducting as well as in the adjacent insulating layers. Also, compare this graph to figure 6.12 for a superconductor with thick sc-layers.

The flattening of the *IV*-curves at a certain current value is interpreted as a dynamic depinning transition. Because the superconducting layers are reduced in thickness, above a certain temperature ($\approx$ 1.70 K for J50) the vortex core, given by the temperature-dependent coherence length, will always sample defect-areas

lying in the insulating layers as well as in the superconducting layers. This situation is schematically sketched in figure 6.29 and should be compared to figure 6.12 which gives the situation for the C-samples. Due to the thick superconducting layers in sample C40, for example, the pinning mechanism described in detail in section 6.5 is effective up to temperatures very close to $T_c(0)$. In the J-samples, however, the pinning-potential is considerably reduced at temperatures for which the coherence length is large enough to *overlap* into the insulating layers. This leads to a reduction of the depinning current density and hence to the observed quasi-free flux flow at high currents. This difference in the AC-pinning between sample C40 on one hand, and the samples J40 and J50 on the other hand, has not been observed in the measurements of the activation energies for plastic flux flow, because that method is much less sensitive to small changes in the pinning potential compared to the measurement of *IV*-curves over a large range of applied currents.

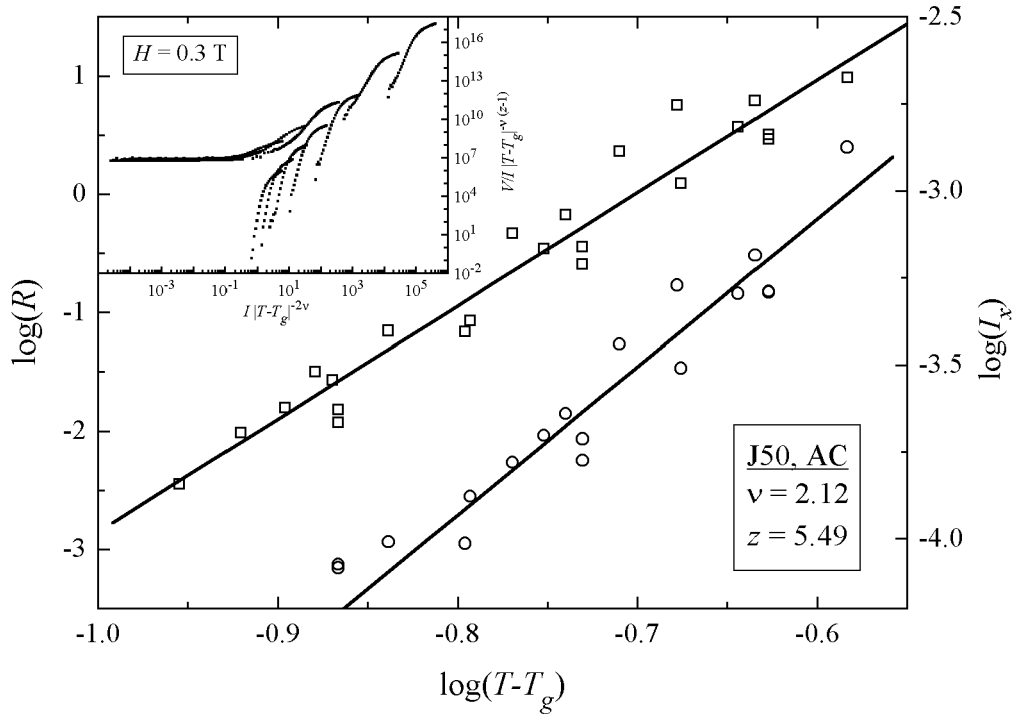

Figure 6.30: Glass scaling analysis for sample J50. Magnetic fields of $H = 0.05$, 0.1, 0.3, 0.6, 0.8, 1.0, and 1.3 T were applied in the AC-direction. Above the proposed glass transition temperature $T_g(H)$ scaling according to VG-theory is observed. However, below the transition temperature, no collapse of the *IV*-curves was achieved, as seen in the inset for a magnetic field $H = 0.3$ T.

The depinning transition for high applied current densities should not affect a possible glass transition, however. An analysis of the linear resistance and the cross-over current equivalent to the other films, is shown in figure 6.30. The data for different magnetic fields can be described by universal power-laws, comparable to the other samples. Scaling of the IV-curves, using the critical parameters derived from the power-law exponents, does produce a good collapse for those isotherms above $T_g(H)$, but fails below. Satisfactory collapse of the IV-data for all temperatures and fields could not be achieved, even for very different scaling exponents.

At the present stage, we have no explanation for why the scaling procedure fails for temperatures below the glass transition temperature. There are two points which may be important to note. Firstly, the static critical exponent ν is quite different from those found for the vortex glass phases in the other films. In this context, it may also be important to note the dissimilar dynamic exponent z' in the Bose-glass phase. Secondly, sample J50 showed some anomalies in the zero-field transition above $T_c(0)$ (figure 6.2), which could point to inhomogenities in this film. To what extent these observations are linked remains unclear.

Sample P40

Both weakly-coupled P-samples investigated in this study show some remarkable differences in their IV-characteristics compared to the other films. These differences are most obvious in the logarithmic gradient of the IV-curves. For sample P40, figure 6.31 shows three sets of logarithmic gradients for IV-curves taken at the indicated magnetic field values and oriented in the C-direction. The temperatures range from above an anticipated glass transition to well below, in steps of $50\,\mathrm{mK}$. At the lowest measured field of $0.1\,\mathrm{T}$, the IV-curves show the change from positive curvature at high currents to negative curvature below a well-defined transition temperature. Thus, from the sample geometries it is expected that the low-temperature vortex phase is a Bose-glass, analogous to the Bose-glass in the C- and J-samples.

For applied magnetic fields in the range 0.6 to $1.3\,\mathrm{T}$, this defining signature of a glass transition is completely absent, as seen for the $0.6\,\mathrm{T}$-data in the figure,
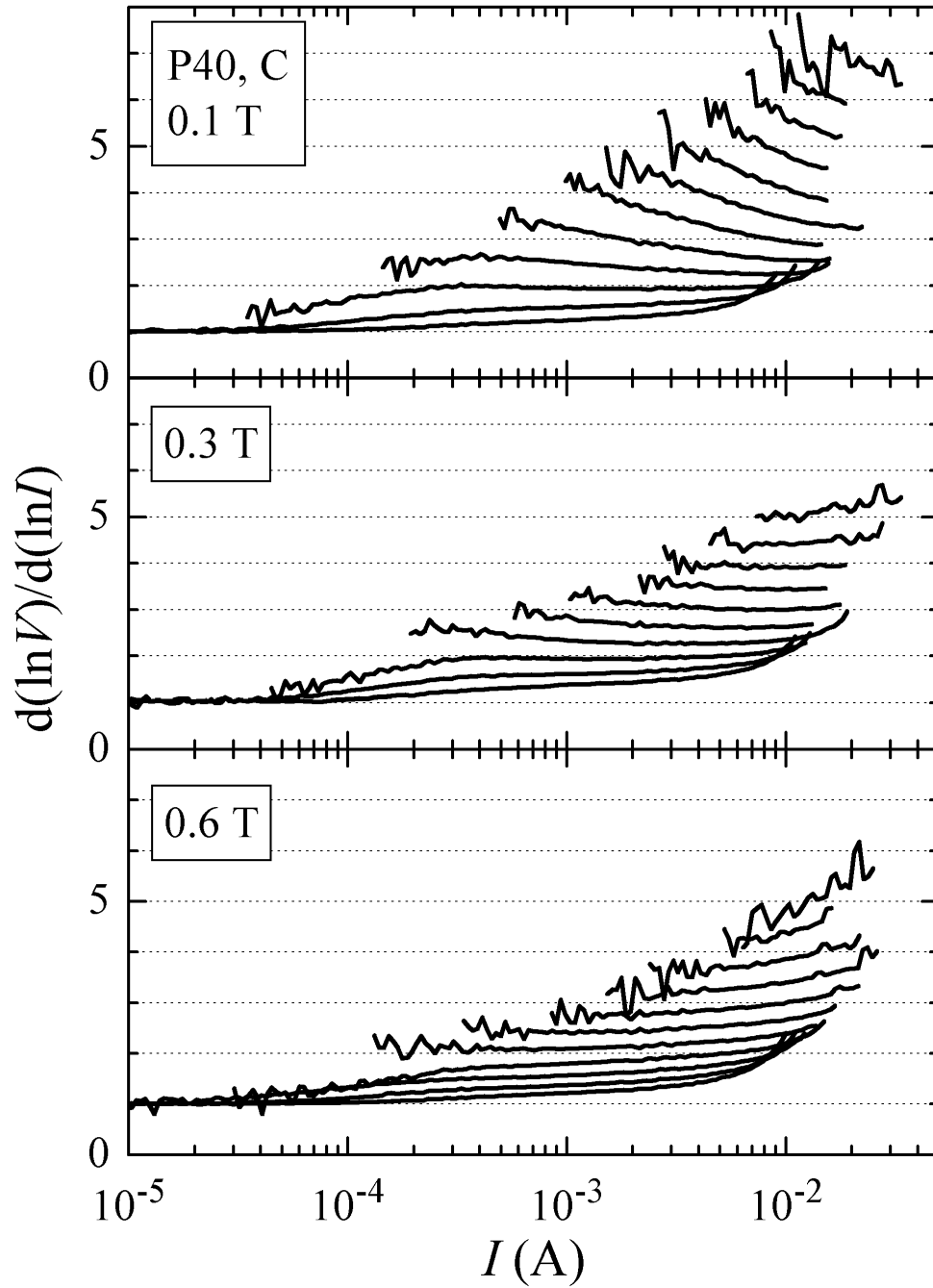
Figure 6.31: Logarithmic gradient of *IV*-characteristics for sample P40 with magnetic fields applied in the C-direction as given in the graphs. At 0.1 T the *IV*-curves show a change from positive to negative curvature comparable to those in figure 6.17, typical for a glass transition. At 0.6 T (and higher fields) all curves in the investigated temperature range have positive curvature and show no sign of a glass transition. At 0.3 T the film is in an intermediate state, where most curves exhibit power-law behaviour over an extended range of applied currents.

at least for the measured temperatures. The curves at high temperatures show the sign of a vortex liquid phase with a TAFF-region for small applied currents and the cross-over to a critical region, before turning normal conducting by the processes described earlier. However there are no curves with a negative gradient as in the top part of figure 6.31 or figure 6.17. At 0.3 T, P40 seems to be in an intermediate state. There are again curves following the expected behaviour of a vortex liquid and although there are no curves with negative gradient, above a certain temperature all the logarithmic gradients are approximately constant over an extended range of applied currents, up to an order of magnitude or more.

From the measurements of the activation energies for flux motion in the flux liquid phase it is known that both P-samples behave like 2D or quasi-2D superconductors, that is, their superconducting layers can be effectively decoupled, for certain magnetic fields and orientations. In section 5.6.1 it was mentioned that for truly two-dimensional superconductors no transition to a vortex glass phase is expected, except at $T = 0$ K. Nevertheless, a scaling law for the cross-over current, separating the ohmic part at low current densities from the critical region at higher currents, of the form $J_x^{2D} \propto T^{1+\nu}$ with $\nu = 2$ should hold. Power-law curves were fitted to the cross-over currents that could be extracted from the IV-curves, but this resulted in unreasonably high exponents of approximately 30 or higher.

For a successful scaling analysis according to the quasi-2D or 3D vortex glass theory given in section 5.6.1, it is important to have an estimate of the glass transition temperature. But since this estimate cannot be obtained from the IV-curves or their logarithmic gradients, an alternative method has to be used. Equation 5.52 gives the scaling relation for the linear resistance in the TAFF-region. This equation can be transformed to give the following relation:

$$[\mathrm{d}\left(\ln\rho\right)/\mathrm{d}T]^{-1} = \nu\left(z + 2 - D\right)|T - T_g|. \tag{6.3}$$

Setting $D = 4$ and replacing T_g, ν, and z by the corresponding BG expressions gives the respective relation for the case of a Bose-glass transition. Since the IV-curves give only a few data points within the critical region above the transition
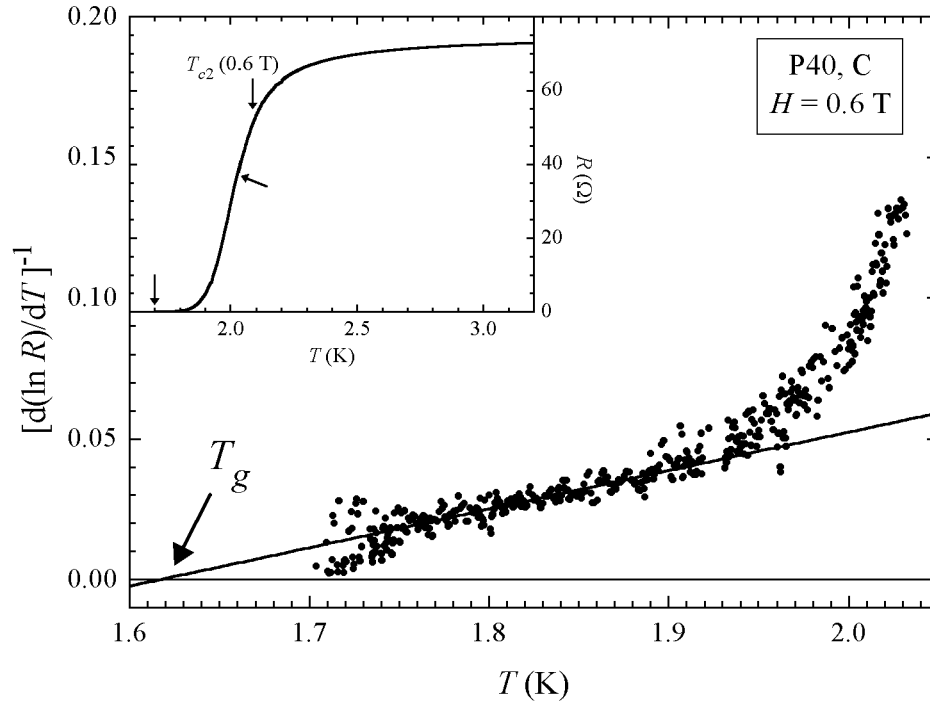
Figure 6.32: $[\mathrm{d}(\ln R)/\mathrm{d}T]^{-1}$ versus T for sample P40 at an applied magnetic field $H = 0.6\,\mathrm{T}$ in the C-direction. At low temperatures there is a linear part to which a line was fitted according to equation 6.3. The intersection with the x-axis gives an estimate for the glass transition temperature. The inset shows the original R-T curve. The lower two arrows mark the temperature and resistance range shown in the main graph. The upper arrow marks the critical temperature at $0.6\,\mathrm{T}$.

temperature, one has to resort to resistance versus temperature measurements from the previous sections in order to check the above expression. In figure 6.32 the resistance data for $H = 0.6\,\mathrm{T}$ applied in the C-direction, recalculated according to equation 6.3, is plotted versus the temperature. Below $1.9\,\mathrm{K}$ the data can be described very well by a linear relation. The solid line is a linear fit to the data between 1.7 and $1.9\,\mathrm{K}$. Extrapolation to $y = 0$ gives a transition temperature $T_g(0.6\,\mathrm{T}) = 1.618\,\mathrm{K}$. Even though the *IV*-curves taken at lower temperatures show no sign of negative curvature, this temperature was taken as an estimate for a hypothetical glass transition temperature. It is important to note that *IV*-curves were taken for temperatures well below the above determined transition temperature. In the case of $0.6\,\mathrm{T}$ aligned in the C-direction the lowest temperature for which *IV*-sweeps were measured was $1.41\,\mathrm{K}$. Similar analyses were carried out for all magnetic fields for which *IV*-characteristics were taken. The data did

not always allow the transition temperature to be determined reliably, in which case an extrapolation or interpolation from successfully determined transition temperatures was used. Additionally, the slope of the linear fit gives an estimate of $\nu(z + 2 - D)$. Due to large scattering of the data, it is not expected to be very accurate and was often dependent on the range of data being fitted.
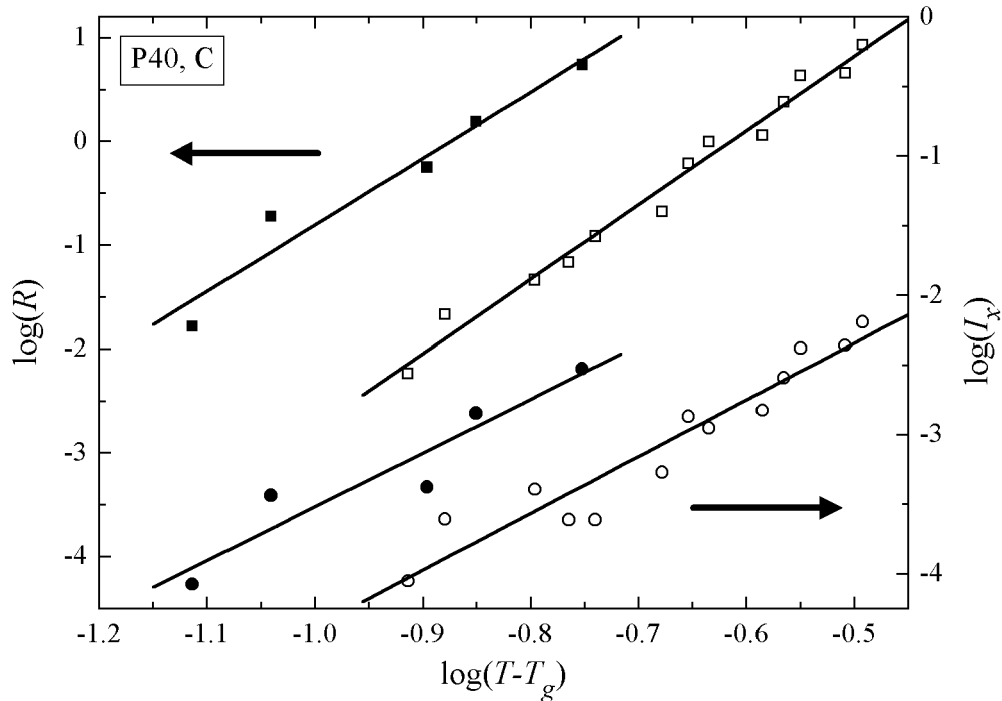

Figure 6.33: Linear resistances (squares) and cross-over currents (circles) versus $|T - T_g|$ in a double-logarithmic plot for sample P40 and magnetic fields parallel to the extended defects (C). The data split into two groups: those at low fields (0.1 and 0.3 T, filled symbols) and another set at higher fields (0.6, 0.8, 1.0, and 1.3 T, open symbols). For both sets the resistances and currents can be described by power-laws, as shown by the straight lines.

Despite these uncertainties, linear resistances and cross-over currents for P40 and fields in the C-direction showed good scaling when plotted versus $|T - T_g|$ on a double-logarithmic scale the same way as for the previous samples and using the above determined T_g. However, the scaling resulted in two power-laws for the linear resistance and the cross-over current. In line with the qualitative change in the IV-characteristics observed at about 0.3 T, the data for magnetic fields of 0.1 and 0.3 T can be described by one set of power-laws, and the data taken at higher fields of 0.6, 0.8, 1.0, and 1.3 T show power-law behaviour as well, but with

different exponents. The data as well as the fitted curves are plotted in figure 6.33. Since the 0.1 T *IV*-curves show the transition from positive to negative curvature, it is concluded that at low fields and temperatures the vortices form a Bose-glass, based on the geometry of the sample. The nature of the low-temperature phase at higher fields will be discussed in greater detail below. Using the VG scaling equations for $D = 2$ or 3 results in a set of critical exponents ν and z, which can be used to check the collapse of the *IV*-curves. If the *IV*-curves collapse, this is independent of the assumed dimensionality. On the other hand, this means that this analysis is not able to discriminate between a quasi-2D and a 3D vortex glass phase.
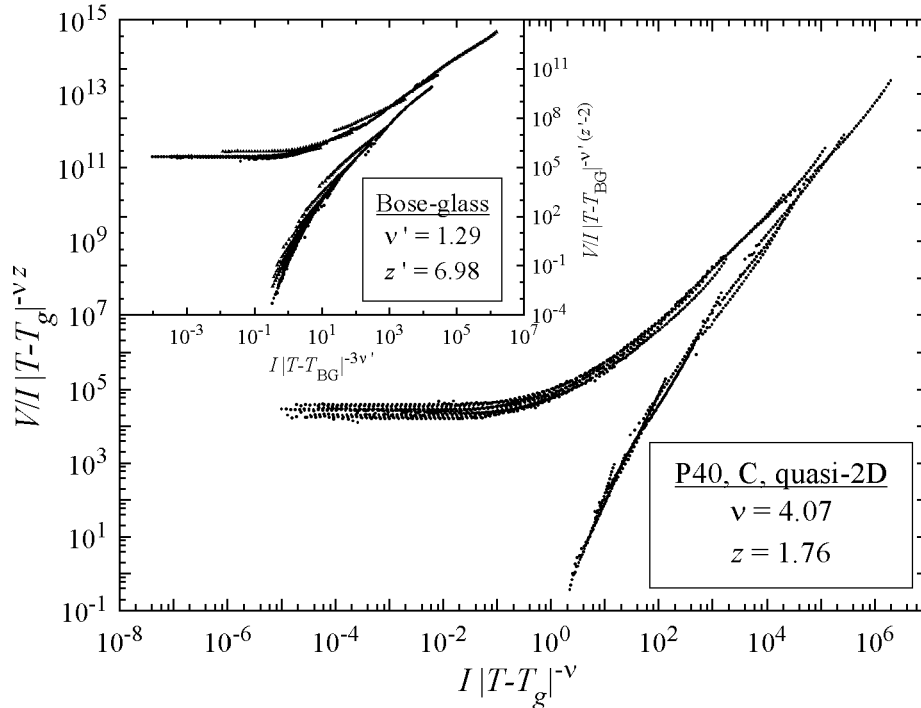
Figure 6.34: Scaled *IV*-curves for sample P40, C-aligned fields, in double-logarithmic presentation. The main graph shows high-field *IV*-curves and the critical exponents assuming quasi-2D VG. Alternative exponents for 3D VG are given in the text. The inset shows scaling for the low-field curves and exponents applying BG relations.

Figure 6.34 gives the resulting *IV*-scaling for fields $H \geq 0.6\,\mathrm{T}$ in the main graph and for smaller fields in the inset. For the lower magnetic fields glass exponents based on BG-theory are given, which compare favourably with BG-exponents obtained for the other samples. At higher fields and temperatures

above the possible transition temperature the IV-curves scale as well. Even at lower temperatures the IV-curves seem to collapse, but it is important to remember that individual data-sets did not show the negative curvature of the scaling function $\mathcal{E}_-$. Nevertheless, assuming that the vortices freeze into a disordered vortex solid, the question of the dimensionality of this vortex phase remains to be answered. In figure 6.34 the critical exponents assuming quasi-2D behaviour are given. These exponents would be highly unusual, compared to other published glass exponents. For a 3D vortex glass the exponents would be $\nu = 2.04$ and $z = 4.52$, well within the range of accepted critical exponents. Although this clearly favours the 3D over the quasi-2D scenario, the most plausible mechanism for the observed change with increasing magnetic field is a decoupling transition of the pancake vortices in this strongly anisotropic material. Such behaviour has been observed in the HTSC $Tl_2Ba_2Ca_2Cu_3O_{10-\delta}$ [164]. The unusual critical exponents for a quasi-2D VG may be caused by the relatively thick sc-layers in the P-samples.
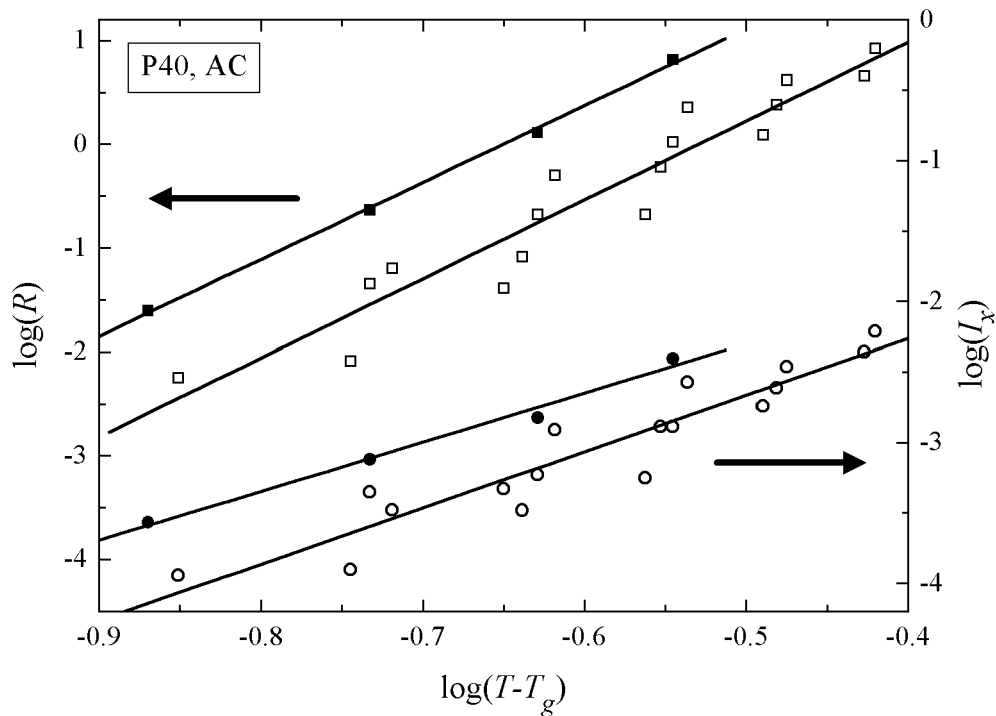

Figure 6.35: Linear resistance and cross-over current for P40 and AC-aligned fields, analogous to figure 6.33. The low-field phase (filled symbols) occurs for $H = 0.1\,\mathrm{T}$ only.
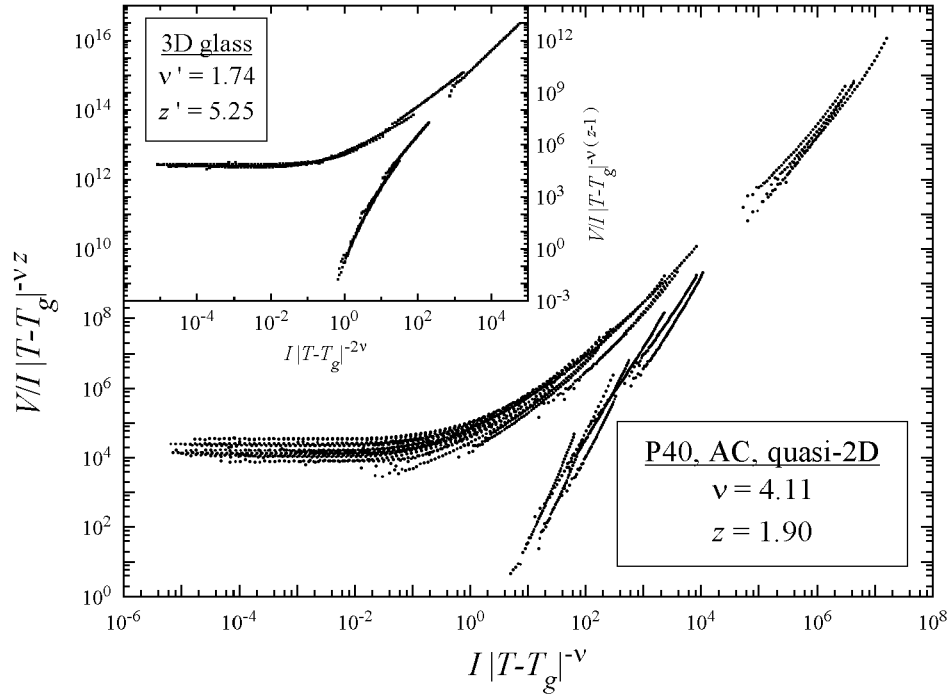
Figure 6.36: Scaled *IV*-curves for P40 and AC-aligned fields. The inset shows the *IV*-scaling at 0.1 T.

For AC-aligned fields, a very similar behaviour emerged. The *IV*-curves at high magnetic fields showed in principle the same characteristics. At 0.1 T a situation comparable to 0.3 T in the C-aligned case was observed, that is, below a certain temperature all curves exhibit power-law behaviour over an extended current range, before the instability occurs and the film turns normal. Consequently, at 0.3 T aligned in the AC-direction, the *IV*-curves showed no sign of the glass transition anymore. The same method as above was applied to estimate transition temperatures, anyway. Using these temperatures, scaling of the linear resistance and cross-over current at high temperatures was achieved. This time, only the data for the lowest field did not collapse onto the same power-laws as did the data for all the other fields, suggesting a different vortex phase at 0.1 T compared to higher magnetic fields. The scaling of the data together with the fitted power-laws are shown in figure 6.35.

From the power-law exponents the critical glass exponents could be retrieved. Due to the different geometry for AC-aligned fields, 3D VG was assumed for

the lowest field of 0.1 T. The fact that there seems to be a change in the *IV*-characteristics between 0.1 and 0.3 T even for the case of AC-oriented fields, is a further argument for a quasi-2D VG phase at higher fields. Consequently, in figure 6.36 showing the scaling of the *IV*-curves, the resulting critical exponents assuming quasi-two dimensionality are given. They are very similar to those obtained for C-aligned fields. The inset shows the 3D VG scaling for the lowest field together with the applied critical exponents. These conform very well with expectations for the respective vortex glass phase.

Sample P50
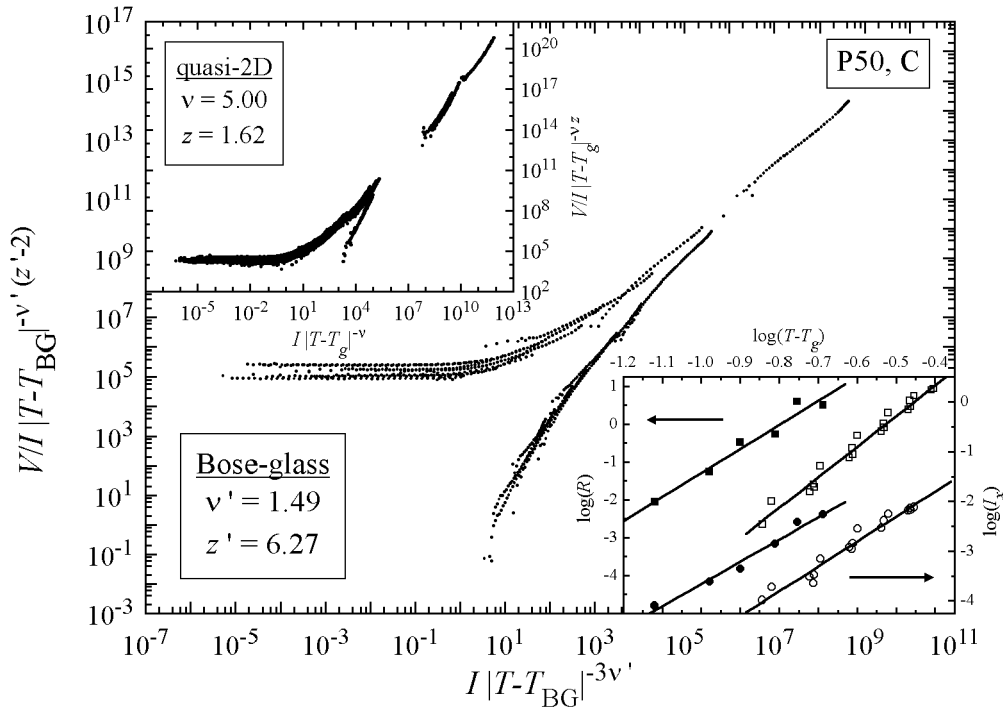
Figure 6.37: Scaling of *IV*-curves for sample P50 and $H = 0.1$ and 0.3 T applied in the C-direction in double-logarithmic plot. The upper inset shows scaling of *IV*-curves obtained at higher fields of 0.6, 0.8, 1.0, and 1.3 T, respectively. The power-law behaviour of the linear resistance and cross-over current employed to obtain the critical exponents, is shown in the lower inset. The respective glass theory and critical exponents are given with the *IV*-scaling curves.

Increasing the tilting angle to 50° during evaporation did not result in major changes in the *IV*-characteristics or the derived vortex phases. In the case of C-aligned fields the *IV*-characteristics show the same qualitative behaviour. At

the lowest fields (0.1, 0.3 T) there are indications of a BG transition at a field-dependent temperature, but at higher fields the hallmark of a change in curvature with temperature disappears. However, using true 2D VG-theory fails to describe the measured data. Resorting to the above described approach to extract possible glass transition temperatures is successful within the same limitations. The biggest problem is again that even those *IV*-curves measured below the derived transition temperature show no sign of negative curvature. Instead, they clearly bend upwards over the accessible voltage range.

Trying to apply BG and VG scaling laws for the low- and high-field *IV*-curves, respectively, is again surprisingly successful. The scaling is summarized in figure 6.37. For the low-field BG phase the glass critical exponents are very reasonable, assuming quasi-2D VG at higher fields leads again to an unusual combination of ν and z, but consistent with P40.
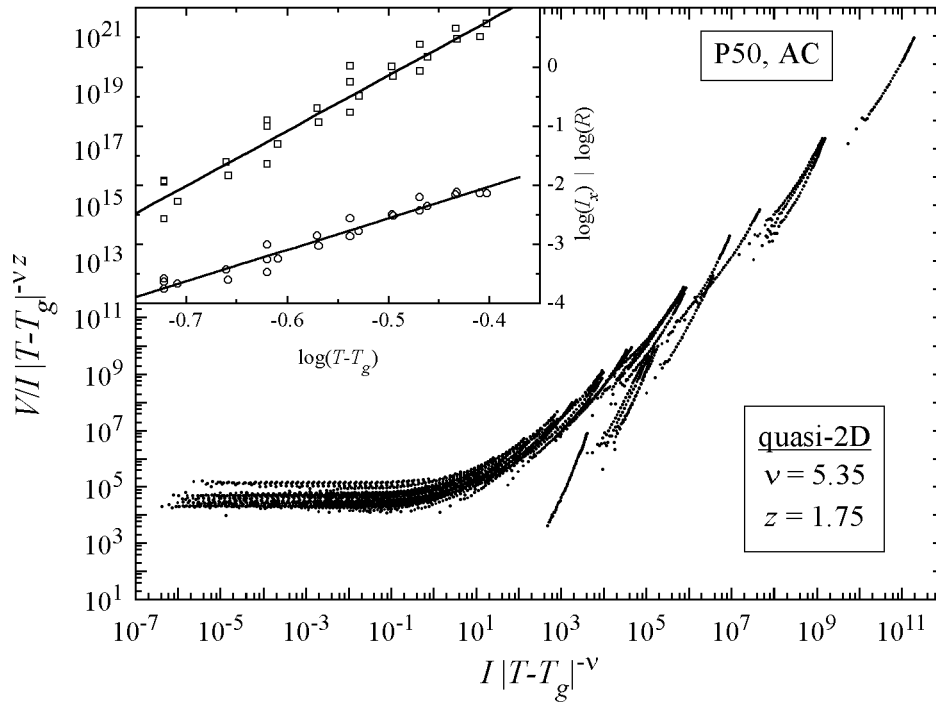

Figure 6.38: Summary of the vortex glass scaling for sample P50 and AC-oriented fields (magnitudes see figure 6.37). All *IV*-curves can be scaled assuming just one vortex solid phase, which is taken to be a quasi-2D VG in line with the analysis of P40. The inset shows the power-law dependence of the linear resistivity and the cross-over current in the vortex liquid phase.

The only difference for AC-aligned fields when compared to P40 is the absence of the proposed 3D-phase at low fields. Even for $H = 0.1\,\mathrm{T}$ all the measured IV-curves are curved upwards. After determining the transition temperatures by the procedure explained above, the linear resistances and the cross-over currents collapse onto only one power-law curve, respectively. This is shown in figure 6.38 together with the resulting collapse of the IV-curves onto universal functions. The critical exponents point towards a common vortex phase at high fields in P40 and P50, unaffected by the orientation of the magnetic field with respect to the defect structure.

6.6.1   Summary IV-Characteristics

The analysis of the IV-characteristics based on the various glass models of disordered vortex phases is summarized in table 6.4 for all samples investigated in this study and the two different magnetic field orientations, parallel and at large angles to the columnar microstructure. The results can be categorized into different groups, symbolized by the different shading, based on the glass models used to analyse the IV-curves and similarities and differences between the critical glass exponents.

Except for J50, the C- and J-samples present a very consistent picture, with the vortices condensing into a Bose-glass for fields parallel to the extended defects (grey) and a corresponding 3D vortex glass phase for AC-aligned fields (blue). The critical exponents are consistent across different samples, supporting the idea of universality of the proposed continuous glass transition. The exponents are even very similar to those published for comparable HTSCs (among many others see for example [113, 142, 145, 152, 165–167]). As already mentioned above, the reason why J50 seems to be different from these other samples is not entirely clear. It could be due to structural differences we are not aware of. Also, the critical exponents in the C-direction for C30 are consistent only when scaling is optimized for the low-temperature IV-curves. The parameters obtained for best possible scaling of the IV-curves at temperatures higher than T_{BG} are quite different (values in parenthesis in table 6.4).

Table 6.4: Summary of the glass scaling exponents of *IV*-curves for all films in this study. The colored shadings group the results into different vortex phases based on the model used and the resulting values for the glass exponents. The exponents given for the quasi-2D glass model in the C-direction are ν and z instead of ν' and z'. The errors are lower estimates, based on variations observed during the analysis. The values given in parentheses for C30 are those which resulted in better *IV*-scaling above the transition temperature. The quasi-2D phases in P40 and P50, respectively, may be different, judged by the differences in the static critical exponents ν.

| | C | | | AC | | |
	ν' (±0.2)	z' (±0.5)		ν (±0.2)	z (±0.5)	
C30	0.88 (1.56)	8.84 (6.81)	BG	1.44	5.47	3D
C40	0.97	8.69	BG	1.38	5.12	3D
J40	0.73	8.65	BG	1.07	6.91	3D
J50	0.75	11.23	BG	2.12	5.49	3D
P40	1.29	6.98	BG	1.74	5.25	3D
	4.07	1.76	q-2D	4.11	1.90	q-2D
P50	1.49	6.27	BG			
	5.00	1.62	q-2D	5.35	1.75	q-2D

In the P-samples, which had much thicker insulating layers, the *IV*-characteristics have to be further divided into those at low (green and blue) and high magnetic fields (red). Depending on the field orientation, the low-field phases can be interpreted as BG or 3D-VG phases below the transition temperature and probably three-dimensional vortex liquids above. The vortex glass for fields in the AC-direction was only observed in P40, but the derived vortex glass parameters are quite comparable to those obtained in the C- and J-films. The Bose-glasses in the C-aligned case have very consistent scaling parameters, although somewhat different from the BG-phase observed in the other samples. However, this could simply result from a systematic error in the determination of ν'. ν' is determined from the scaling behaviour of the cross-over current. z' on the other hand is determined from the exponent describing the decay of the linear resistance as T_{BG} is approached: $\nu'(z'-2)$. This exponent is very similar for all BG-phases in this study, thus the small z' values for P40 and P50 are a result of the relatively large static exponent ν'.

The high-field *IV*-curves of the P-samples were analysed in terms of a quasi-

2D vortex glass, despite the absence of IV-curves with negative curvature below the transition temperature. The resulting critical exponents are quite coherent for both films and field directions, yet very unexpected in magnitude. Support for this model of a decoupling transition from flux lines to pancake vortices comes from the results of the activation energies for plastic vortex motion section 6.5, at least for the case of C-oriented magnetic fields. Between about 0.1 and 0.5 T (0.3 T for P50) the activation energy is clearly enhanced and its dependence on the magnetic field can be interpreted within a three-dimensional model. At higher fields activation energies for fields in the C- and AC-direction are identical within the errors. Unfortunately, the 2D and 3D model predict very similar activation energies in this field range. But this does not rule out the possibility of 2D-behaviour of the vortices at these elevated field values oriented in the C-direction. Then again, the activation energies for AC-aligned fields can be explained within a 2D model over the whole range of applied fields, somewhat contradictory to the observed 3D-VG in P40. While there are some arguments in favour of the proposed decoupling transition from 3D to a quasi-2D behaviour, the unusual critical exponents and the lack of downwards curved IV-characteristics cast serious doubt on this scenario.

6.7   Vortex Dynamics in the Glass Phase

Careful analysis of the current-voltage characteristics taken at temperatures below the glass-transition temperature can give information about the dominant mechanism for flux creep in the glass phase. The vortex and Bose-glass theories make very precise predictions with regards to the exponent μ in the equations given in section 5.6.3. In order to extract the exponent μ in equations 5.67, 5.69, and 5.70, these equations can be recast and written in the following way:

$$\frac{\mathrm{d}(\ln E/J)}{\mathrm{d}J} = \frac{\mu E_k J_c^\mu}{k_B T} J^{-(\mu+1)}, \tag{6.4}$$

thus plotting $\ln[\mathrm{d}(\ln V/I)/\mathrm{d}I]$ versus $\ln I$ should result in a straight line with slope $-(\mu+1)$. IV-curves of all samples and for both magnetic field directions were
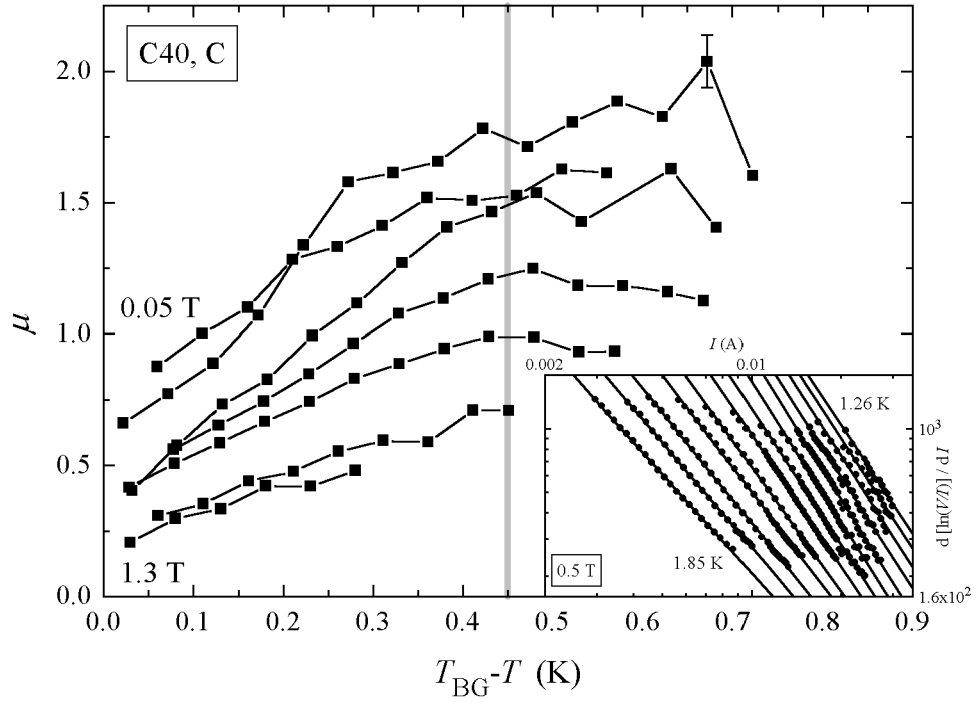
Figure 6.39: The glass exponent μ plotted versus the reduced temperature $T_{\mathrm{BG}} - T$ for sample C40 and magnetic fields $H = 0.05$, 0.1, 0.3, 0.5, 0.7, 1.0, and 1.3 T applied in the C-direction. The exponents were derived from plotting the IV-data according to equation 6.4 and shown in the inset. The lines are least-squares fits to the data enabling the derivation of μ. The lines in the main graph are guides to the eye, the grey vertical line marks the cross-over to the low-temperature constant μ. A typical error bar is given for the topmost data point.

analysed this way and the results can be categorized into two groups according to the interlayer coupling strength.

The strongly coupled C- and J-samples form the first group. The IV-curves within the glass-phase can be described by equation 6.4 over a considerable part of the measured current range, compare inset of figure 6.39. Those curves taken close to the transition temperature usually showed a deviation from the linear behaviour at very low currents. The calculated data points (not shown in inset) were below the extrapolated linear relation in the log-log plot. This could mean a cross-over to a different flux creep mechanism characterised by a reduced exponent μ or the onset of finite-size effects for thin films, resulting in effectively ohmic behaviour at very low current-densities, discussed briefly in section 5.6.3. However, due to the limited voltage resolution, no conclusive analysis of these

deviations was possible.

More importantly, the exponents μ derived from the linear parts in the inset of figure 6.39, showed a systematic field and temperature dependence. This is summarized for sample C40 and magnetic fields aligned in the C-direction in the main graph of figure 6.39. A very similar behaviour was observed in the AC-case as well as for the other strongly coupled samples. In the above figure, μ is plotted versus the reduced temperature $T_{\mathrm{BG}} - T$ for the applied magnetic fields given in the caption. As the temperature is reduced μ increases roughly linearly, until it reaches a reduced temperature of about 0.45 at which point the exponent remains approximately constant. The slope of the increase, as well as the low-temperature value of μ, decrease with increasing magnetic field. Clearly, the IV-curves can not be identified with any of the flux creep mechanisms presented in section 5.6.3, and it seems also not possible to explain the observed behaviour in a simple way within the theory of elastic flux creep mentioned in section 5.5.2, see also [9, 85, 86]. Given that the exponent μ seems to scale with the reduced temperature $T_{\mathrm{BG}} - T$, it is likely that the glass correlation length ξ_{BG}, or ξ_{VG} for the case of a vortex glass, plays an important part in the vortex creep mechanism in these superconductors.

The low-temperature glass phases observed in P40 and P50 show evidence of a very different flux creep mechanism. The derived values for μ in the Bose-glass of P40 at an applied field of $H = 0.1\,\mathrm{T}$ are shown in figure 6.40. The data from which μ was calculated could be fitted very well by a power-law, as seen in the inset, and within the errors the exponent is constant with an average $\bar{\mu} = 0.22$. It is worth noting, that the temperature range shown in figure 6.40 corresponds to the same range in which the strongly coupled samples show an undoubtedly increasing value of μ. However, the obtained averaged value for the glass exponent μ is below the theoretically predicted ones, especially it is only approximately half the expected value 0.5, based on the geometry of the sample having strong coplanar pinning sites (see section 5.6.3).

Unfortunately, the available IV-data did not allow the determination of μ as a function of magnetic field. At the next higher measured field of $0.3\,\mathrm{T}$, the IV-
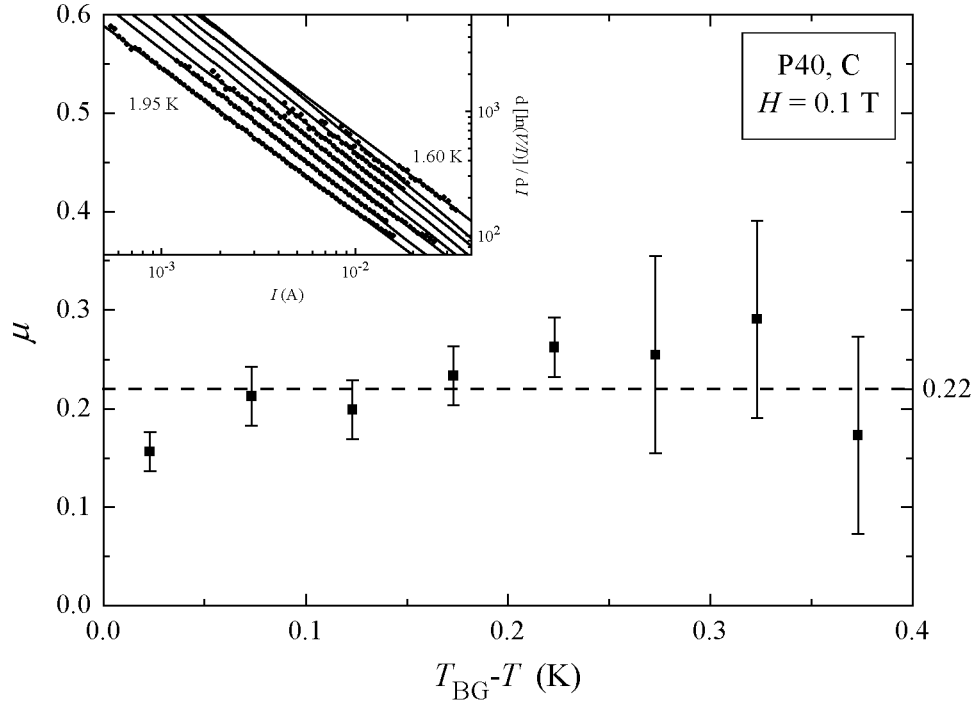
Figure 6.40: The glass exponent μ plotted versus the reduced temperature as in figure 6.39 for sample P40 and a C-aligned magnetic field $H = 0.1\,\mathrm{T}$. The inset shows the IV-data and the best fits of a power-law in a log-log plot. The dashed horizontal line is the average calculated from the data points. The errors give the range of μ obtained by fitting varying data ranges.

curves displayed power-law behaviour resulting in $\mu = 0$, although the scaling analysis suggested BG-behaviour at that field. The same is true for the AC-aligned field of $0.1\,\mathrm{T}$ and the BG-phase in P50. On the other hand, a small but positive μ would result in IV-characteristics that resemble power-law characteristics over a limited current range. For even higher fields the low-temperature IV-data can still be described by equation 6.4 over a not too large current range, but this would result in a negative glass exponent μ implying ohmic resistance in the limit of zero applied current, and thus no glassy behaviour.

6.8 Vortex Phase Diagrams

The preceding sections presented a thorough analysis of the conducting behaviour of the superconducting films studied in this project. The results of this analysis will be summarized in superconducting phase diagrams and the differences

between the samples will be discussed based on their different microscopic structures.

In figure 6.41 the phase diagrams for the four strongly coupled samples are shown next to each other for easy comparison. In order to make a quantitative comparison possible *reduced* phase diagrams are shown, i.e. $H/H_{c2}(0)$ is plotted versus $T/T_c(0)$ for each sample. In this representation the upper critical field in the GL approximation is a straight line with slope -1 intersecting the x-axis at $x = 1$, shown as the uppermost straight black line in the graphs. In all graphs, the full circles are the experimental results for the glass transition as a function of reduced temperature $T/T_c(0)$, where the black circles are results for C-aligned fields and red symbols are for the AC-case.

The discussion is begun with the well coupled, weakly pinning sample C30, in which case the glass transition lines for C- and AC-aligned fields are almost identical, although for C-oriented fields the transition consistently happens at slightly higher temperatures for the same applied field. Also shown in the graph for C30 are the results for a homogeneous $Ta_{0.27}Ge_{0.73}$-alloy film without columnar structure (open triangles), which already served as a reference in previous sections. Those results are well reproduced by the film C30, especially in the C-direction. As in the preceding sections, the zero-resistance glass phase for AC-aligned fields is assumed to belong to the class of 3D-vortex glasses. According to equation 5.55 the glass transition line was fitted to a power-law (black line). The data is described very well by a power-law relation (see also below), but the derived exponent of 2.60 is very different from the theoretically predicted value of 1.33. There are a number of possibilities for why the exponent deviates from the expected value, most importantly, the value of 1.33 was calculated for small applied fields. However, the applied fields in this study were always large enough for vortex-vortex interactions to be important. There is also the possibility that the exponent in equation 5.55 depends on the degree and nature of disorder in the film.

Although there is very little difference between the two field directions, and the data for C-aligned fields can be described by a power-law similar to the AC-

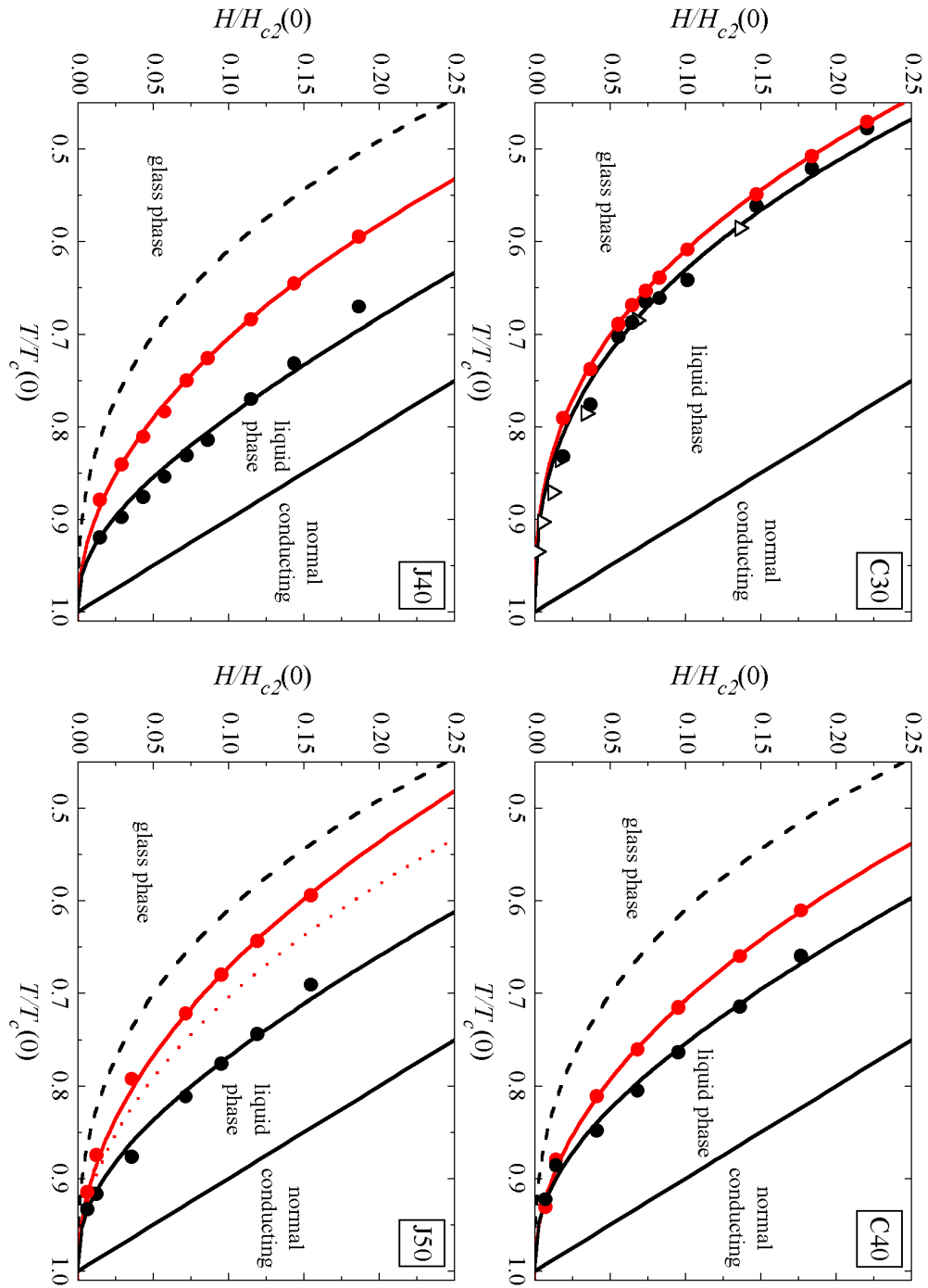Figure 6.41: Reduced $H - T$ phase diagrams for C- and J-samples, in all graphs field and temperature are scaled by the respective $H_{c2}(0)$ and $T_c(0)$. The upper critical field is the uppermost straight line. The glass transition lines are black (C) and red (AC), respectively. The Meissner-phase is basically identical to the x-axis on that scale. The graphs are described in detail in the text.

case, the experimental results in the C-direction were fitted according to equation 5.65 for the BG-transition line. Equation 5.65 relates the BG-transition to the melting line of a flux line lattice in a clean system. However, the FLL melting line is unknown, since we have never measured a step in resistance, reminiscent of the transition from a flux liquid to a FLL. Therefore, the result of the transition line in the AC-direction was used as an approximation to the melting line in the clean system. Not surprisingly, making this assumption the resulting disorder parameter is close to unity (see table 6.5), in other words there is very little disorder present in C30. This result was already suggested by the previous analysis of the conductivity data and the TEM photograph.

The much more pronounced columnar structure in film C40 results in a clear difference in the phase diagrams for C- and AC-aligned fields. For comparison the transition line for C30 in AC-field direction is shown as the dashed line in the graph for C40. As has been discussed for the activation energies in the TAFF-region, the columnar microstructure does not only affect the vortices for parallel applied fields, but in the case of layered superconductors, also when the magnetic field is directed at large angles to the extended coplanar pinning sites. In the phase diagram this is reflected by a clear shift of the transition line to higher fields and temperatures, thus extending the range of fields and temperatures for which this film has zero ohmic resistance. The data for the AC-aligned fields was again fitted according to equation 5.55. This time the results can be very well described using a parabolic relation between H and $T_c - T_g$. The resulting coefficient $\nu_0 = 1$ is still quite different from the theoretical result of $2/3$.

When the field is co-aligned with the defect structure the transition line moves to even higher temperatures and fields, but now the transition line can no longer be described using a power-law relation. Plotting the logarithm of H versus the logarithm of $T_c - T_g$, the AC-data are to a good approximation linear (see figure 6.42 below), but not so the glass transition temperatures for C-fields. Using the expression for the BG transition temperature (equation 5.65) we can however describe the data very satisfactorily, as demonstrated by the black solid line in the graph for C40.

The phase diagram for sample J40 is very similar to that of C40. The dashed black line in the graph is again the vortex glass transition line of C30, representative of a film with no or very little disorder. The vortex glass transition temperatures for J40 and AC-aligned fields can be described with a parabolic relation (red solid line) just as for C40, and not only is the functional dependence the same, but also the proportional factor within the errors. Thus, the transition in both films is described by the same line in this reduced phase diagram. This can be well understood within the proposed pinning mechanism for AC-aligned fields. Because the insulating layer thickness is approximately the same in the C- and J-samples, the barrier height and width responsible for the pinning is also approximately the same. This results in an equal shift of the vortex glass line to higher fields and temperatures.

For C-aligned fields, details of the microstructure, i.e. superconducting layer thickness and structure of the defects, are expected to be more important compared to AC-aligned fields. Indeed, the Bose-glass transition temperature in J40 is moved even closer to the upper critical field compared with the BG-line in C40. Whether this difference is caused by the changes in sc-layer thickness or differences in the columnar structure is speculative at best. However, the data could be explained very well again using the expression 5.65 (black solid line).

A very similar phase diagram was found for J50. The VG transition line (red) is also described very well by a quadratic relation. However, it lies in between that found for C30 (black dashed line) and that for C40 and J40 (red dotted line). The BG line is also lower than in J40 and comparable to that of C40. Because of the discrepancies found in J50 in the previous sections a conclusive interpretation of the phase diagram is not possible. It is still interesting to note that the phase diagram is very much alike, despite some of the unusual results obtained for J50.

As already mentioned in the discussion above, the VG transition lines in these strongly coupled samples could be well described based on equation 5.55, although with a different exponent $2\nu_0$. That a description using above equation is appropriate, can be seen best when plotting the applied field versus $T_c(0) - T_g$ on double-logarithmic scales. This is shown in figure 6.42 together with the
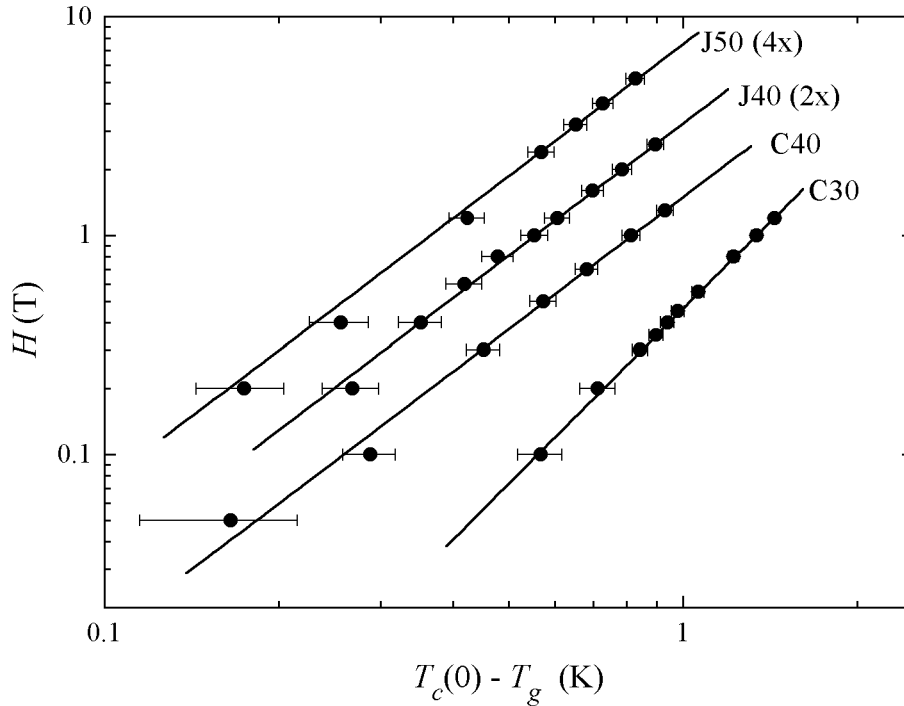
Figure 6.42: Double logarithmic plot of the applied field versus $T_c - T_g$, where T_g are the field-dependent VG transition temperatures for the four strongly coupled samples and with magnetic fields oriented in the AC-direction. For better discrimination the field values for samples J40 and J50 have been multiplied by a factor of 2 and 4, respectively. The error bars are estimates obtained during the analysis of the IV-characteristics. The solid lines are power-law least-square fits to the data with an exponent equal 2.60 for C30 and 2 for the other samples, respectively.

corresponding power-law lines obtained from a least-square fit to the respective data set. All four data sets follow a straight line as required from above equation. For C30 a best fit was achieved with an exponent equal to 2.60 or $\nu_0 = 1.30$. The data for the other three samples suggested very similar slopes. Leaving the exponent as a free parameter resulted in exponents equal $2 \pm 5\%$. Consequently, the same value of 2 as a fixed parameter was used to fit all three data sets.

In table 6.5 the disorder parameter χ obtained by fitting the BG line to the data is listed for all samples, as well as the VG exponent ν_0 discussed above. χ quantifies how far the transition line has been shifted towards the upper critical field. The parameter χ is defined such that a value of 1 means no shift and a value equal to 0 would imply the BG line being equivalent to the upper critical field. Thus, in J40 the microstructure has the most effect, extending the zero-

	χ (BG)	ν_0 (VG)
C30	0.93	1.3
C40	0.50	1.0
J40	0.38	1.0
J50	0.45	1.0
P40	0.64	1.3
P50	0.64	1.3

Table 6.5: Results from fitting the glass transition lines. χ is the disorder parameter which determines the position of the BG line (Eq. 5.65). The parameter ν_0 determines the exponent of the VG line, equation 5.55.

resistance glass phase to the highest fields and temperatures in these reduced phase diagrams. Blatter *et al.* [9] even relate the disorder parameter to the microscopic structure of columnar defects. But because the pinning sites in these films are expected to be coplanar and the expression for χ contains several parameters, such as average distance and size of the defects neither of which are well known, no attempt was made to extract these quantities from the disorder parameters.

It is interesting to compare these phase diagrams to those obtained for other superconductors with and without strong pinning defects. Qualitatively, they are very similar to results published for YBCO [139,140] and the isotropic $(K,Ba)BiO_3$ superconductor [142].

The discussion turns now to the phase diagrams of the weakly-coupled P-samples. The possible existence of a quasi-2D vortex glass phase in the P-samples has been thoroughly discussed in section 6.6. For the phase diagrams of these samples it will be assumed that they do undergo a continuous phase transition into a quasi-2D glass phase at low temperatures, despite the inconsistent *IV*-characteristics. Based on this conjecture the reduced phase diagrams for both samples are basically identical and will be presented and discussed together. Figure 6.43 shows the phase diagram for AC-aligned magnetic fields. As for the other phase diagrams the uppermost straight line is the upper critical field separating the normal from the superconducting phases. The experimental vortex glass transition temperatures for both samples together can be described using a power-law equivalent to that used for the C- and J-films, with an exponent very similar to C30 (compare table 6.5). However, the data deviate significantly
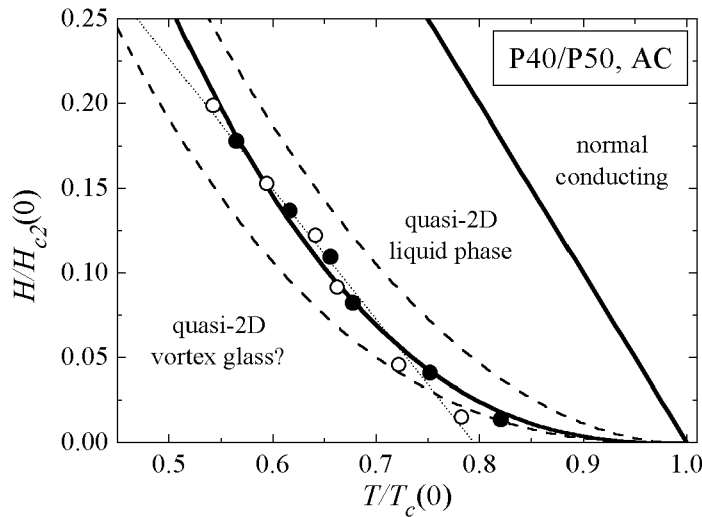
Figure 6.43: Combined reduced $H - T$ phase diagram for samples P40 (filled symbols) and P50 (open symbols) for fields in the AC-direction. The upper straight line is the upper critical field, the curved solid line is a power-law fit of the VG line to the data for both samples. The dashed lines are the VG lines of C30 and C40. The dotted straight line is an alternative linear fit to the glass transition.

more from the theoretical curve. This may be because of the larger uncertainty in the determination of $T_g(H)$. Alternatively, the data can also be described by a linear relation illustrated by the straight dotted line in the graph. To relate the transition line to the other samples, the transition lines for C30, lower dashed curve, and C40, upper dashed curve, are also plotted in figure 6.43. At high fields the transition is at considerably higher reduced temperature compared to C30, but at reduced fields ≤ 0.05 the difference is only marginal. Not shown in the phase diagram is the possible existence of a 3D VG at low fields for sample P40.

Interpreting all the available data in favour of a multitude of vortex phases and dimensional cross-overs, a phase diagram like that shown in figure 6.44 emerges for samples P40 and P50 when the magnetic field is parallel to the direction of the defect structure. This phase diagram is quite speculative however, and not all of the proposed phases and phase transitions may be realized. The most conclusive evidence coming from the IV-characteristics and the activation energies is for the existence of a Bose-glass phase at reduced fields below ≈ 0.05 (hatched area). At the BG transition line the vortex matter undergoes a continuous transition to a 3D vortex liquid. The experimental transition temperatures can be fitted
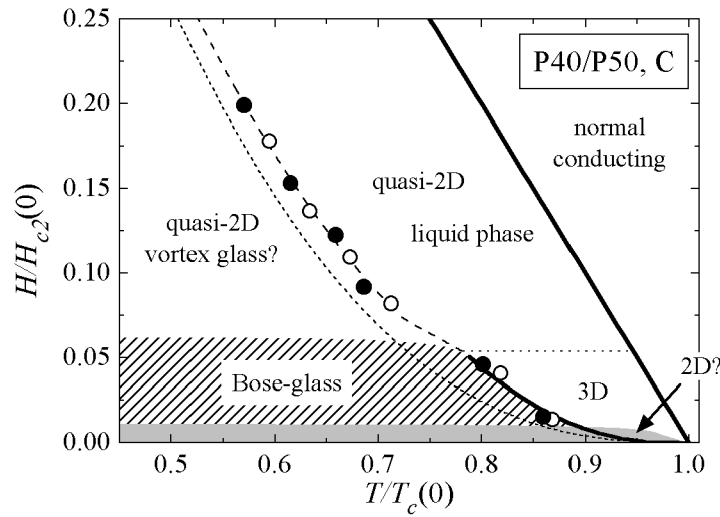
Figure 6.44: Speculative phase diagram for P40 and P50 for fields aligned in the C-direction. There is good evidence for a BG phase (hatched area) and a vortex liquid phase of 3D or quasi-2D character at high temperatures. Whether the quasi-2D vortex phase at high fields exists is not entirely clear. Furthermore, the activation energy results suggest a recurring 2D phase at very low magnetic fields (grey area). The dotted curve gives the position of the glass transition line for AC-fields.

reasonably well using equation 5.65; the extracted disorder parameter χ (see table 6.5) has to be taken cautiously due to the small field range and limited number of data points. At higher magnetic fields the temperature-dependence of the transition line changes noticeably and the solid vortex phase may well change to a quasi-2D vortex glass. The field-dependence of the activation energies can be interpreted in such a way that the vortex liquid is also undergoing a dimensional cross-over from 3D to 2D behaviour with increasing magnetic field. The transition temperatures at these higher fields follow a power-law dependence (dashed line) with an exponent between those obtained for C30 and C40, for example. The resulting glass exponent ν_0 was calculated to be 1.14.

The very striking deviation of the activation energies from the 3D expectation at very low magnetic fields (compare figure 6.15) suggest a recurring 2D dominated vortex behaviour in the grey region below $H/H_{c2}(0) \approx 0.01$. Since no IV-characteristics were taken at such low magnetic fields, no information about a possible transition between solid and liquid phases could be obtained. However, from the field-dependent resistance measurements as a function of temperature it is known that this 2D-regime does not extend all the way to the upper critical

field line. The field-dependent fluctuation conductivity could be explained using the 3D-model of Ullah and Dorsey for all measured fields, which extends from 0 up to ≈ 0.3 on the reduced magnetic field scale.

These phase diagrams may again be related to results obtained for other superconductors, this time of course to superconductors with increased anisotropy. Remarkable similarities can be found in the phase diagrams of moderately anisotropic $Bi_2Sr_2Ca_2Cu_3O_{10}$ [167] and especially $Tl_2Ba_2Ca_2Cu_3O_{10}$ [164] when compared to the phase diagram for C-orientation. The striking differences in the dimensional character of the vortices when the field is C- and AC-oriented respectively, can be understood as a defect-mediated recoupling of pancake vortices. Due to the strong pinning by the defects, most pancake vortices are lined up along the defects, and thus in the direction of the applied magnetic field in the C-case. This preserves the 3D character of the vortices to higher fields than for AC-alignment. In the AC-case the pancake vortices are still preferably in the vicinity of strongly pinning defects, but now this does not match the direction of the external field any more. This behaviour of recoupling pancake vortices due to extended defects has been found in experiments on BSCCO containing columnar defects directly probing the dimensionality of the vortices in the vortex liquid phase [168–170]. The findings of these experiments have also been supported recently by theoretical considerations [171]. It is thus very reasonable to assume a similar scenario in these weakly coupled Ta_xGe_{1-x}/Ge films.

Chapter 7

Conclusions

The conductivity of extremely type-II superconductors, such as the cuprate HTSC or highly disordered amorphous superconductors, in their mixed phase is dominated by the dynamic response of the penetrating flux lines to an applied transport current. To make full use of the potential application of HTSC materials it is of particular importance to gain a very good understanding of the dissipation processes caused by the movement of magnetic flux lines when subjected to an external current. Only then is it possible to maximize the range of temperatures and magnetic fields over which these materials show zero resistance current transport. It was the aim of this thesis to contribute to the understanding of the diverse superconducting phase diagram of anisotropic, extremely type-II superconductors.

A set of six multilayered amorphous Ta_xGe_{1-x}/Ge thin films, with $x \approx 0.31 - 0.37$ confirmed by RBS-measurements, was studied extensively over a considerable part of the $H - T$ plane in their superconducting phase diagram and close to the superconducting transition in the normal phase. The films differed from each other in their layering as well as in a deliberately introduced columnar microstructure resulting in nearly parallel correlated defects running at a tilted angle with respect to the normal direction across the films. These coplanar defects were thought to be very effective flux pinning sites. The layering as well as the orientation of the defects was verified and analysed employing TEM.

Critical temperatures in ambient magnetic field were determined by fitting the conductivity above $T_c(0)$ to the fluctuation conductivity by Aslamazov and

Larkin. Values ranged between $2.72\,\mathrm{K}$ for the least anisotropic and most homogeneous film and $2.04\,\mathrm{K}$ for a more anisotropic film with a strong defect structure. In this temperature range all films showed better agreement with the 3D-form of the AL fluctuation conductivity. Resistance versus temperature measurements in applied magnetic fields up to $2.5\,\mathrm{T}$ were used to determine the upper critical field. Again, all films showed 3D behaviour when using the scaling relations of Ullah and Dorsey for the fluctuation conductivity in the presence of a magnetic field and assuming a linear dependence of H_{c2} on T. The extrapolated upper critical field at zero temperature ranged between 5.5 and $8.4\,\mathrm{T}$ with no clear trend based on the films' microstructure.

These magnetoconductivity measurements together with the extrapolated normal state resistivity at zero temperature allow an estimate of the coherence length and the penetration depth within the GL theory. From $H_{c2}(0)$ the coherence lengths ξ_{ab} were calculated to be between 6.3 and $7.8\,\mathrm{nm}$ at zero temperature and the penetration depths $\lambda_{ab}(0)$ were determined in the range from 1.14 to $1.96\,\mu\mathrm{m}$. This resulted in very large GL parameters κ varying between 146 and 294. The coherence lengths are of the same order as in HTSC; due to the high normal-state resistivity of the $\mathrm{Ta_xGe_{1-x}/Ge}$ films the penetration depth is about a factor of 10 larger compared to YBCO and BSCCO.

Although all six samples could be described very well using 3D models for temperatures near the mean-field transition $H_{c2}(T)$, they fell into two different groups at lower temperatures, based on their interlayer coupling strength. The strongly coupled samples remained three dimensional for all temperatures and fields investigated. Of these four samples one had a very weakly developed columnar film structure which resulted in a phase diagram resembling that of a homogeneous $\mathrm{Ta_xGe_{1-x}}$ film studied previously. The other three strongly coupled films showed the expected strong pinning of the flux lines by the columnar microstructure when the fields were co-aligned with the defects. This was evident for all fields and temperatures below the very narrow free flux flow regime.

The activation energies for thermally activated plastic flux flow show a strong dependence on the orientation of the magnetic field with respect to the defect

structure. When the magnetic field and the defects are parallel the activation energy for flux flow is significantly increased. But the combined effects of coplanar defects and layering lead to a small enhancement of flux pinning even when the magnetic field is at large angles to the defects and the layered structure. A detailed analysis of the IV-curves gave strong support for the existence of vortex and Bose-glasses, respectively, in the low-temperature part of the phase diagrams. The increased pinning effects are reflected in these phase diagrams, which show a clear enhancement of the pinned glass phases towards higher temperatures and fields compared to an unstructured homogeneous film or the layered film with very weak columnar structure. Again, this was observed for both film directions, only with a much stronger effect for properly aligned fields. Further evidence for a glass phase came from derived glass exponents μ which showed an as yet unexplained temperature and field dependence in these 3D samples.

In the more weakly coupled samples, the activation energies for TAFF showed a qualitatively different behaviour when the magnetic field was co-aligned with the defect structure and at large angles to it, respectively. In the latter case the field-dependence of the activation energies could be explained as the thermally activated flux flow of unbound dislocations in quasi-2D superconductors. As in the case of the 3D samples the activation energies were significantly increased when the magnetic field was parallel to the extended pinning sites. Additionally, the field dependence for magnetic fields in a medium range between approximately 0.1 and 1 T resembled that expected for a 3D superconductor. At lower fields the results obtained in the AC-direction were approached. To conclusively decide if the flux lines at fields $\gtrsim 1\,\mathrm{T}$ are three or two dimensional, the measurements would have to be extended to higher fields and lower temperatures than it was possible in the present study.

The reduced coupling between the superconductor layers had possibly even greater consequences for the vortex phases at lower temperatures. Convincing evidence for a low-temperature glass phase was only found when small magnetic fields were applied in the C-direction. This pinned glass phase showed all the signs of a Bose-glass including signatures of variable-range hopping of the vortices,

although with an unexpectedly low glass exponent. At higher fields and for all fields applied at large angles to the defects the IV-curves were lacking the sign of a glassy behaviour, i.e. a negative curvature below the glass transition temperature. Although the IV-curves taken at higher temperatures indicate a possibly quasi-2D glass phase at low temperatures, the true nature of the low-temperature vortex phase remains to be clarified.

In summary, this study has come up with strong support in favour of a glass transition in disordered extremely type-II superconductors. Mainly the generally good scaling of the IV-characteristics and the universal scaling exponents for a range of superconductors with quite different microscopic structure strengthen the arguments for a continuous phase transition. However, the original proposal of universal scaling functions independent of the applied magnetic field needs to be reconsidered. In addition, the known theories for flux creep in the glassy phase could at best qualitatively describe the measured glass exponents. Further insight into the intriguing physics of vortices in type-II superconductors could be obtained by extending the present investigations into as yet unexplored regions of the phase diagram of these Ta_xGe_{1-x}/Ge multilayers and especially by combining them with complimentary measurements such as the macroscopic and microscopic magnetisation.

Appendix A

Temperature Accuracy

The overall accuracy of the temperature measurement was determined by the accuracy of the voltmeter (HP4378A), the current source (Yokogawa7651), and the gradient of the calibration curve $\mathrm{d}R/\mathrm{d}T$ for the resistor. From the manuals of the voltmeter and current source we get the following accuracy, respectively:

$$\Delta V = \pm(0.04\% + 4\,\mu\mathrm{V}), \tag{A.1}$$

$$\Delta I = \pm(0.02\% + 20\,\mathrm{nA}). \tag{A.2}$$

The offset for the Yokogama7651 was given to be much higher. However, independent measurements of the output current gave a offset usually at least a factor of 2 less than the assumed value of $20\,\mathrm{nA}$. The temperature-dependent $\mathrm{d}R/\mathrm{d}T$ values were taken from the calibration sheet #253413 supplied by *Lake Shore Cryotronics, Inc.* for this sensor.

The temperature uncertainty can then be calculated using

$$\Delta T = \frac{\mathrm{d}T}{\mathrm{d}R} \times \Delta R, \text{ with } \Delta R = R\sqrt{\left(\frac{\Delta V}{V}\right)^2 + \left(\frac{\Delta I}{I}\right)^2}. \tag{A.3}$$

Typical values for a number of temperatures are:

$$\begin{array}{rcll} \Delta T & = & 15\,\mathrm{mK} & (1.5\,\mathrm{K}) \\ \Delta T & = & 11\,\mathrm{mK} & (2.5\,\mathrm{K}) \\ \Delta T & = & 7\,\mathrm{mK} & (4.0\,\mathrm{K}) \\ \Delta T & = & 1.6\,\mathrm{K} & (300\,\mathrm{K}) \end{array} \tag{A.4}$$

A few notes at the end: Above estimate neglects the finite accuracy of the sensor calibration, which is given by *Lake Shore* to be about $4\,\mathrm{mK}$ between $T = 1 - 10\,\mathrm{K}$. Then again, liquid helium provides two temperature check points.

The first one is the boiling point at normal atmospheric pressure (4.222 K) and the other one is the superfluid transition at 2.177 K which confirmed the above calculated accuracy. Although the magnetoconductivity of carbon-glass resistors is small, it affects the accuracy of temperature measurements in an applied magnetic field, especially in fields $\gtrsim 1\,\mathrm{T}$.

Appendix B

Resistance Sensitivity and Accuracy

The tables below give the specifications of the voltmeter and current source used for the conductivity measurements.

K182 (Voltmeter)

$$
\begin{array}{ccc}
Range & Res & Acc(reading + offset) \\
\hline
3\,\text{mV} & 1\,\text{nV} & (80 + 16)\,\text{ppm} \\
30\,\text{mV} & 10\,\text{nV} & (80 + 6)\,\text{ppm} \\
300\,\text{mV} & 100\,\text{nV} & (80 + 6)\,\text{ppm} \\
3\,\text{V} & 1\,\mu\text{V} & (40 + 6)\,\text{ppm}
\end{array}
\tag{B.1}
$$

K224 (Amp-source)

$$
\begin{array}{ccc}
Range & Res & Acc(reading + offset) \\
\hline
10\,\mu\text{A} & 5\,\text{nA} & 0.05\% + 10\,\text{nA} \\
100\,\mu\text{A} & 50\,\text{nA} & 0.05\% + 100\,\text{nA} \\
1\,\text{mA} & 500\,\text{nA} & 0.05\% + 1\,\mu\text{A} \\
10\,\text{mA} & 5\,\mu\text{A} & 0.05\% + 10\,\mu\text{A} \\
100\,\text{mA} & 50\,\mu\text{A} & 0.1\% + 50\,\mu\text{A}
\end{array}
\tag{B.2}
$$

The noise level present during experiments limited the useful voltage resolution to several nV. The typical excitation current for resistance measurements was $10\,\mu\text{A}$, resulting in the smallest measurable resistance of about $1\,\mu\Omega$.

Appendix C

Source Materials

The following data are extracted from:

CRC Handbook of Chemistry and Physics, 59th edition, 1978-79, CRC Press Inc. and *www.webelements.com*.

C.1 Tantalum, Ta

atomic number	73
atomic weight	180.95 amu
melting point	3290 K
	(3rd highest of all elements)
boiling point	≈ 5730 K
mass density	16,654 kg/m^3
crystal structure (RT)	bcc
electrical conductivity (RT)	$13\,\mu\Omega$ cm
superconducting transition	4.47 K
energy gap $2\Delta(0)/k_B T_c$	3.6[a]

---

[a] data from [52], both superconducting parameters are for crystalline Ta

Its name is derived from the Greek mythological character *Tanalos, the Father of Niobe* (Tantalum is chemically very similar to Niobium). It was first discovered in 1802. Today it is widely used in special steel alloys and because of its immunity to body fluids and the body tolerating the metal well surgical appliances are often made using Ta-alloys. Tantalum oxide has a high index of refractivity and is therefore used for camera lenses. The material used in this study was a 99.95 % pure rod, purchased from *Princeton Scientific Corporation*.

C.2   Germanium, Ge

atomic number	32
atomic weight	72.61 amu
melting point	1211.4 K
boiling point	3093 K
mass density	$5,323\,\text{kg/m}^3$
crystal structure (RT)	ccp
electrical conductivity (RT)	$\approx 50,000\,\mu\Omega\,\text{cm}$
superconducting transition	none

Germanium (Latin Germania for Germany) was predicted by Mendeleev in 1871 and first extracted in 1886. It is an elemental semiconductor like Si and for example used doped with As, Ga or other elements in transistors. The source material were 99.999 % pure Ge granules, supplied by *Goodfellow*.

Bibliography

[1] H. K. Onnes, 'Further experiments with liquid helium. G. On the electrical resistance of pure metals, etc. VI. On the sudden change in the rate at which the resistance of mercury disappears.' *Leiden Comm.* **124c** (1911).

[2] W. Meissner and R. Ochsenfeld. *Naturwissenschaften* **21**, 787 (1933).

[3] F. London and H. London, 'The electromagnetic equations of the supraconductor'. *Proc. Roy. Soc. (London)* **A149**, 71 (1935).

[4] V. L. Ginzburg and L. D. Landau. *Zh. Eksperim. Teor. Fiz.* **20**, 1064 (1950).

[5] J. Bardeen, L. N. Cooper, and J. R. Schrieffer, 'Theory of superconductivity'. *Phys. Rev.* **108**, 1175 (1957).

[6] B. D. Josephson, 'Possible new effect in superconductive tunneling'. *Phys. Lett.* **1**, 251 (1962).

[7] J. G. Bednorz and K. A. Müller, 'Possible high T_c superconductivity in the Ba-La-Cu-O system'. *Z. Phys. B* **64**, 189 (1986).

[8] T. P. Sheahen, *Introduction to High-Temperature Superconductivity*, Plenum Press, New York (1994).

[9] G. Blatter, M. V. Feigel'mann, V. B. Geshkenbein, A. I. Larkin, and V. M. Vinokur, 'Vortices in high temperature superconductors'. *Rev. Mod. Phys.* **66**, 1125 (1994).

[10] J. C. Abele, H. J. Trodahl, B. J. Ruck, A. F. Lopez, L. J. Törnquist, T. R. Lee, and S. M. Robinson, 'Vortex dynamics in Ta-Ge films with columnar defects'. *Phys. Rev. B* **60**, 12448 (1999).

[11] L. F. Cohen and H. J. Jensen, 'Open questions in the magnetic behaviour of high-temperature superconductors'. *Rep. Prog. Phys.* **60**, 1581 (1997).

[12] M. P. A. Fisher, 'Vortex-Glass superconductivity: A possible new phase in bulk high-T_c oxides'. *Phys. Rev. Lett.* **62**, 1415 (1989).

[13] H. J. Trodahl, H. L. Johnson, A. B. Kaiser, C. K. Subramaniam, B. J. Ruck, and P. Lynam, 'Superconductivity in amorphous Ta/Ge multilayers'. *Phys. Rev. B* **53**, 15226 (1996).

[14] H. J. Trodahl, priv. communication (2001).

[15] G. L. Weissler and R. W. Carlson, *Vacuum Physics and Technology*, volume 14 of *Methods of Experimental Physics*, Academic Press (1979).

[16] F. L. Galeener, 'Optical evidence for a network of cracklike voids in amorphous germanium'. *Phys. Rev. Lett.* **27**, 1716 (1971).

[17] I. J. Hodgkinson, F. Horowitz, H. A. Macleod, M. Sikkens, and J. J. Wharton, 'Measurement of the principle refractive indices of thin films deposited at oblique incidence'. *J. Opt. Soc. Am. A* **2**, 1693 (1985).

[18] S. Kassam, I. J. Hodgkinson, Q. Wu, and S. C. Cloughley, 'Light scattering from thin films with an oblique columnar structure and with granular inclusions'. *J. Opt. Soc. Am. A* **12**, 2009 (1995).

[19] S. Rupp, *Obliqueliy deposited tantalum germanium multilayers electron transport and optical properties*, Master's thesis, Victoria University of Wellington, Wellington, New Zealand (1997).

[20] D. O. Smith, M. S. Cohen, and G. P. Weiss, 'Oblique-incidence anisotropy in evaporated permalloy films'. *J. Appl. Phys.* **31**, 1755 (1960).

[21] R. D. McMichael, C. G. Lee, J. E. Bonevich, P. J. Chen, W. Miller, and W. F. Egelhoff, Jr., 'Strong anisotropy in thin magnetic films deposited on obliquely sputtered Ta underlayers'. *J. Appl. Phys.* **88**, 5296 (2000).

[22] L. J. Törnquist, *Electrical Properties of Obliquely Deposited Thin Films*, Master's thesis, Uppsala University, Uppsala, Sweden (1997).

[23] J. D. Finegan and R. W. Hoffman, 'Stress anisotropy in evaporated iron films'. *J. Appl. Phys.* **30**, 597 (1959).

[24] H. van Kranenburg and C. Lodder, 'Tailoring growth and local composition by oblique-incidence deposition: a review and new experimental data'. *Mat. Sci. and Engineering* **R11**, 295 (1994).

[25] Y. D. Fan, X. P. Li, J. Yang, and J. P. Li, 'Microscopic model for columnar growth of thin films'. *phys. stat. sol. (a)* **134**, 157 (1992).

[26] K. Hara, K. Itoh, M. Kamiya, K. Okamoto, T. Hashimoto, and H. Fujiwara, 'A new type of columnar grain structure in obliquely deposited films'. *J. of Magn. and Magn. Mat.* **148**, 19 (1995).

[27] A. G. Dirks and H. J. Leamy, 'Columnar microstructure in vapor-deposited thin films'. *Thin Solid Films* **47**, 219 (1977).

[28] R. N. Tait, T. Smy, and M. J. Brett, 'Modelling and characterization of columnar growth in evaporated films'. *Thin Solid Films* **226**, 196 (1993).

[29] J. M. Nieuwenhuizen and H. B. Haanstra, 'Microfractography of thin films'. *Philips tech. Rev.* **27**, 87 (1966).

[30] L. Holland, *Vacuum Deposition of Thin Films*, Chapman & Hall Ltd. (1960).

[31] K. L. Chopra, *Thin Film Phenomena*, McGraw-Hill, New York (1969).

[32] B. J. Ruck, *Vortex Dynamics and Instabilities in $Ta_x Ge_{1-x}/Ge$ Multilayers*, Ph.D. thesis, Victoria University of Wellington, Wellington, New Zealand (1998).

[33] W.-K. Chu, J. M. Mayer, and M.-A. Nicolet, *Backscattering Spectrometry*, Academic Press Inc. (1978).

[34] L. Doolittle, 'Algorithms for the rapid simulation of Rutherford backscattering spectra'. *Nucl. Instr. and Meth.* **B9**, 344 (1985).

[35] A. Markwitz, 'Materials processing - elemental analysis with ion beams', in *Proc. of 1st Int. Conf. on Advanced Materials Processing*, 135 (2000).

[36] S. A. E. Johansson and J. L. Campbell, *PIXE*, John Wiley & Son Ltd. (1988).

[37] L. Reimer, *Transmission Electron Microscopy*, volume 36 of *Springer Series in Optical Sciences*, Springer-Verlag (1984).

[38] J. C. H. Spence, *Experimental High-Resolution Electron Microscopy*, Oxford University Press, second edition (1988).

[39] P. Munroe, 'TEM specimen preparation', priv. communications (2000).

[40] D. R. Tilley and J. Tilley, *Superfluidity and Superconducitivity*, Graduate Student series in Physics, Adam Hilger Ltd (1986).

[41] L. P. Gor'kov, 'Microscopic derivation of the Ginzburg-Landau equations in the theory of superconductivity'. *Zh. Eksperim. Teor. Fiz.* **36**, 1918 (1959). [Sov. Phys. – JETP **9**, 1364 (1959)].

[42] M. Tinkham, *Introduction to Superconductivity*, McGraw-Hill, Inc., New York, second edition (1996).

[43] A. A. Abrikosov, 'On the magnetic properties of superconductors of the second group'. *Zh. Eksperim. Teor. Fiz.* **32**, 1442 (1957). [Soviet Phys. – JETP **5**, 1174 (1957)].

[44] N. R. Werthamer, E. Helfand, and P. C. Hohenberg, 'Temperature and purity dependence of the superconducting critical field, H_{c2}. III. Electron spin and spin-orbit effects'. *Phys. Rev.* **147**, 295 (1966).

[45] G. Blatter, V. B. Geshkenbein, and A. I. Larkin, 'From isotropic to anisotropic superconductors: A scaling approach'. *Phys. Rev. Lett.* **68**, 875 (1992).

[46] W. Lawrence and S. Doniach, in *Proc. 12th Int. Conf. Low Temp. Phys.* (edited by E. Kanda), 361, Academic Press, Tokyo (1971).

[47] J. R. Clem, 'Two-dimensional vortices in a stack of thin superconducting films: A model for high-temperature superconducting multilayers'. *Phys. Rev. B* **43**, 7837 (1991).

[48] S. T. Ruggiero and D. A. Rudman (editors), *Superconducting Devices*, Academic Press, San Diego (1990).

[49] G. Bergmann, 'Amorphous metals and their superconductivity'. *Phys. Lett.* **27**, 159 (1976).

[50] H. L. Johnson, *Electron conduction processes in Tantalum-Germanium multilayers*, Ph.D. thesis, Victoria University of Wellington, Wellington, New Zealand (1993).

[51] N. W. Ashcroft and N. D. Mermin, *Solid State Physics*, CBS Publishing Asia Ltd. (1987).

[52] C. Kittel, *Introduction to Solid State Physics*, John Wiley & Sons, Inc., sixth edition (1986).

[53] G. Bergmann, 'Physical interpretation of weak localization: A time-of-flight experiment with conduction electrons'. *Phys. Rev. B* **28**, 2914 (1983).

[54] B. L. Alt'shuler and A. G. Aronov, *Electron-Electron Interactions in Disordered Systems*, chapter Electron-electron intersctions in disordered conductors, NORTH-HOLLAND, Elsevier Science Publishers (1985).

[55] L. G. Aslamazov and A. I. Larkin, 'The influence of fluctuation pairing of electrons on the conducitivity of normal metal'. *Phys. Lett.* **26A**, 238 (1968).

[56] H. Schmidt, 'The onset of superconductivity in the time dependent Ginzburg-Landau theory'. *Z. Physik* **216**, 336 (1968).

[57] R. S. Thompson, 'Microwave, flux flow, and fluctuation resistance of dirty type-II superconductors'. *Phys. Rev. B* **1**, 327 (1970).

[58] R. E. Glover, 'Ideal resistive transition of a superconductor'. *Phys. Lett.* **25A**, 542 (1967).

[59] K. Maki, 'Critical fluctuation of the order parameter in a superconductor. i'. *Prog. Theor. Phys.* **40**, 193 (1968).

[60] J. E. Crow, R. S. Thompson, M. A. Klenin, and A. K. Bhatnagar, 'Divergent fluctuations in superconducting films'. *Phys. Rev. Lett.* **24**, 371 (1970).

[61] W. J. Skocpol and M. Tinkham, 'Fluctuations near superconducting phase transitions'. *Rep. Prog. Phys.* **38**, 1049 (1975).

[62] S. Ullah and A. T. Dorsey, 'Critical fluctuations in high-temperature superconductors and the Ettingshausen effect'. *Phys. Rev. Lett.* **65**, 2066 (1990).

[63] S. Ullah and A. T. Dorsey, 'Effect of fluctuations on the transport properties of type-II superconductors in a magnetic field'. *Phys. Rev. B* **44**, 262 (1991).

[64] M. Yethiraj, D. M. Paul, C. V. Tomy, and E. M. Forgan, 'Neutron scattering study of the flux lattice in YNi_2B_2C'. *Phys. Rev. Lett.* **78**, 4849 (1997).

[65] T. M. Riseman, P. G. Kealey, E. M. Forgan, A. P. MacKenzie, L. M. Galvin, A. W. Tyler, S. L. Lee, C. Ager, D. M. Paul, C. M. Aegerter, R. Cubitt, Z. Q. Mao, T. Akima, and Y. Maeno, 'Observation of a square flux-line lattice in the unconventional superconductor Sr_2RuO_4'. *Nature* **396**, 242 (1998).

[66] M. Roulin, A. Junod, and E. Walker, 'Flux line lattice melting transition in $YBa_2Cu_3O_{6.94}$ observed in specific heat experiments'. *Science* **273**, 1210 (1996).

[67] A. Schilling, R. A. Fisher, N. E. Phillips, U. Welp, D. Dasgupta, W. K. Kwok, and G. W. Crabtree, 'Calorimetric measurements of the latent heat of vortex-lattice melting in untwinned $YBa_2Cu_3O_{7-\delta}$'. *Nature* **382**, 791 (1996).

[68] A. Schilling, R. A. Fisher, N. E. Phillips, U. Welp, W. K. Kwok, and G. W. Crabtree, 'Anisotropic latent heat of vortex-lattice melting in untwinned $YBa_2Cu_3O_{7-\delta}$'. *Phys. Rev. Lett.* **78**, 4833 (1997).

[69] F. A. Lindemann, 'Über die Berechnung molekularer Eigenfrequenzen'. *Phys. Z.* **11**, 609 (1910).

[70] R. Wördenweber, P. H. Kes, and C. C. Tsuei, 'Peak and history effects in two-dimensional collective flux pinning'. *Phys. Rev. B* **33**, 3172 (1986).

[71] W. K. Kwok, J. A. Fendrich, C. J. van der Beek, and G. W. Crabtree, 'Peak effect as a precursor to vortex lattice melting in single crystal $YBa_2Cu_3O_{7-\delta}$'. *Phys. Rev. Lett.* **73**, 2614 (1994).

[72] R. Liang, D. A. Bonn, and W. N. Hardy, 'Discontinuity of reversible magnetization in untwinned YBCO single crystals at the first order vortex melting transition'. *Phys. Rev. Lett.* **76**, 835 (1996).

[73] U. Welp, J. A. Fendrich, W. K. Kwok, G. W. Crabtree, and B. W. Veal, 'Thermodynamic evidence for a flux line lattice melting transition in $YBa_2Cu_3O_{7-\delta}$'. *Phys. Rev. Lett.* **76**, 4809 (1996).

[74] T. Ishida, K. Okuda, and H. Asaoka, 'Sequential vortex states upon lattice melting in untwinned single-crystal $YBa_2Cu_3O_7$'. *Phys. Rev. B* **56**, 5128 (1997).

[75] J. Shi, R. Ling, X. S. Liang, D. A. Bonn, and W. N. Hardy, 'Giant peak effect observed in an ultrapure $YBa_2Cu_3O_{6.993}$ crystal'. *Phys. Rev. B* **60**, 12 593 (1999).

[76] E. Zeldov, D. Majer, M. Konczykowski, V. B. Geshkenbein, V. M. Vinokur, and H. Shtrikman, 'Thermodynamic observation of first-order vortex-melting transition in $Bi_2Sr_2CaCu_2O_8$'. *Nature* **375**, 373 (1995).

[77] X. S. Ling, S. R. Park, B. A. McClain, S. M. Choi, D. C. Dender, and J. W. Lynn, 'Superheating and supercooling of vortex matter in a Nb single crystal: Direct evidence for a phase transition at the peak effect from neutron diffraction'. *Phys. Rev. Lett.* **86**, 712 (2001).

[78] W. F. Vinen, Superconductivity, Marcel Dekker, New York (1969).

[79] J. Bardeen and M. J. Stephen, 'Theory of the motion of vortices in superconductors'. *Phys. Rev.* **140**, 1197 (1965).

[80] A. I. Larkin and Y. N. Ovchinnikov, 'Electrodynamics of inhomogeneous type-II superconductors'. *Zh. Eksperim. Teor. Fiz.* **65**, 1704 (1973). [Sov. Phys. – JETP, **38**, 854 (1974)].

[81] A. I. Larkin and Y. N. Ovchinnikov, 'Pinning in type-II superconductors'. *J. Low Temp. Phys.* **34**, 409 (1979).

[82] Y. B. Kim, C. F. Hempstead, and A. R. Strnad, 'Critical persistent currents in hard superconductors'. *Phys. Rev. Lett.* **9**, 306 (1962).

[83] P. W. Anderson, 'Theory of flux creep in hard superconductors'. *Phys. Rev. Lett.* **9**, 309 (1962).

[84] P. W. Anderson and Y. B. Kim, 'Hard superconductivity: theory of the motion of Abrikosov flux lines'. *Rev. Mod. Phys.* **36**, 39 (1964).

[85] M. Feigel'man, V. Geshkenbein, A. Larkin, and V. Vinokur, 'Theory of collective flux creep'. *Phys. Rev. Lett.* **63**, 2303 (1989).

[86] T. Nattermann, 'Scaling approach to pinning: Charge-density waves and giant flux creep in superconductors'. *Phys. Rev. Lett.* **64**, 2454 (1990).

[87] M. V. Feigel'man and V. M. Vinokur, 'Thermal fluctuations of vortex lines, pinning, and creep in high-T_c superconductors'. *Phys. Rev. B* **41**, 8986 (1990).

[88] A. E. Koshelev, 'Effect of thermal fluctuations on pinning of 2D vortex lattice'. *Pis'ma Zh. Eksperim. Teor. Fiz.* **51**, 210 (1990). [Sov. Phys. – JETP Lett. **51**, 238 (1990)].

[89] V. Geshkenbein, A. Larkin, M. Feigel'man, and V. Vinokur, 'Flux pinning and creep in high-T_c superconductors'. *Physica C* **162-164**, 239 (1989).

[90] V. M. Vinokur, M. V. Feigel'man, V. B. Geshkenbein, and A. I. Larkin, 'Resistivity of high-T_c superconductors in a vortex-liquid state'. *Phys. Rev. Lett.* **65**, 259 (1990).

[91] V. M. Vinokur, V. B. Geshkenbein, A. I. Larkin, and V. M. Feigel'mann, 'Pinning of vortex fluid in high-T_c superconductors'. *Zh. Eksperim. Teor. Fiz.* **100**, 1104 (1991). [Sov. Phys. – JETP **73**, 610 (1991)].

[92] M. V. Feigel'man, V. B. Geshkenbein, and A. I. Larkin, 'Pinning and creep in layered superconductors'. *Physica C* **167**, 177 (1990).

[93] W. R. White, A. Kapitulnik, and M. R. Beasley, 'Collective vortex motion in a-MoGe superconducting thin films'. *Phys. Rev. Lett.* **70**, 670 (1993).

[94] D. Ephron, A. Yazdani, A. Kapitulnik, and M. R. Beasley, 'Observation of quantum dissipation in the vortex state of a highly disordered superconducting thin film'. *Phys. Rev. Lett.* **76**, 1529 (1996).

[95] O. Brunner, L. Antognazza, J.-M. Triscone, L. Miéville, and Ø. Fischer, 'Thermally activated flux motion in artificially grown $YBa_2Cu_3O_7/PrBa_2Cu_3O_7$ superlattices'. *Phys. Rev. Lett.* **67**, 1354 (1991).

[96] A. I. Larkin and Y. N. Ovchinnikov, 'Nonlinear conductivity of superconductors in the mixed state'. *Zh. Eksperim. Teor. Fiz.* **68**, 1915 (1975). [Sov. Phys. – JETP, **41**, 960 (1976)].

[97] B. J. Ruck, H. J. Trodahl, J. C. Abele, and M. J. Geselbracht, 'Dynamic vortex instabilities in Ta/Ge-based multilayers and thin films with various pinning strengths'. *Phys. Rev. B* **62**, 12 468 (2000).

[98] D. S. Fisher, M. P. A. Fisher, and D. A. Huse, 'Thermal fluctuations, quenched disorder, phase transitions, and transport in type-II superconductors'. *Phys. Rev. B* **43**, 130 (1991).

[99] D. A. Huse, M. P. A. Fisher, and D. S. Fisher, 'Are superconductors really superconducting?' *Nature* **358**, 553 (1992).

[100] S. F. Edwards and P. W. Anderson, 'Theory of spin glasses'. *J. Phys. F: Metal Phys.* **5**, 965 (1975).

[101] K. Binder and A. P. Young, 'Spin glasses: Experimental facts, theoretical concepts, and open questions'. *Rev. Mod. Phys.* **58**, 801 (1986).

[102] A. T. Dorsey, M. Huang, and M. P. A. Fisher, 'Dynamics of the normal to vortes-glass transition: Mean-field theory and fluctuations'. *Phys. Rev. B* **45**, 523 (1992).

[103] R. H. Koch, V. Foglietti, W. J. Gallagher, G. Koren, A. Gupta, and M. P. A. Fisher, 'Experimental evidence for vortex-glass superconductivity in Y-Ba-Cu-O'. *Phys. Rev. Lett.* **63**, 1511 (1989).

[104] P. Gammel, L. Schneemeyer, and D. Bishop, 'SQUID picovoltometry of $YBa_2Cu_3O_7$ single crystals: Evidence for a finite-temperature phase transition in the high-field vortex state'. *Phys. Rev. Lett.* **66**, 953 (1991).

[105] A. M. Petrean, L. M. Paulius, W.-K. Kwok, J. A. Fendrich, and G. W. Crabtree, 'Experimental evidence for the vortex glass phase in untwinned, proton irradiated $YBa_2Cu_3O_{7-\delta}$'. *Phys. Rev. Lett.* **84**, 5852 (2000).

[106] H. Safar, P. L. Gammel, and D. J. Bishop, 'SQUID picovoltometry of single crystal $Bi_2Sr_2CaCu_2O_{8+\delta}$: Observation of the crossover from high-temperature Arrhenius to low-temperature vortex-glass behavior'. *Phys. Rev. Lett.* **68**, 2672 (1992).

[107] P. Zheng, Y. Q. Zhou, Z. J. Chen, S. Luo, W. H. Wang, Y. S. He, and J. Duo, 'The vortex glass to liquid transition in Bi2212 whisker'. *Physica C* **316**, 210 (1999).

[108] J. Roberts, B. Brown, J. Tate, X. Xi, and S. Mao, 'Scaling of thin-film $Nd_{1.85}Ce_{0.15}CuO_{4-y}$ resistivity-current isotherms at low fields: Implications for vortex phase transitions and universality'. *Phys. Rev. B* **51**, 15281 (1995).

[109] J. Herrmann, M. C. de Andrade, C. C. Almasan, R. P. Dickey, M. B. Maple, W. Jiang, S. N. Mao, and R. L. Greene, 'Magnetoresistivity of thin films of the electron-doped highT_c superconductor $Nd_{1.85}Ce_{0.15}CuO_{4\pm\delta}$'. *Phys. Rev. B* **54**, 3610 (1996).

[110] T. Klein, L. Baril, C. Escripe-Filippini, J. Marcus, and A. G. M. Jansen, 'Flux motion and phse transtions in superconducting $(K,Ba)BiO_3$ single crystals'. *Phys. Rev. B* **53**, 9337 (1996).

[111] T. Klein, A. Conde-Gallardo, J. Marcus, C. Escribe-Filippini, P. Samuely, P. Szabó, and A. G. M. Jansen, 'Vortex-glass transition in the $(K,Ba)BiO_3$ cubic superconductor'. *Phys. Rev. B* **58**, 12411 (1998).

[112] N.-C. Yeh, D. S. Reed, W. Jiang, U. Kriplani, C. C. Tsuei, C. C. Chi, and F. Holtzberg, 'Universality, critical dynamics, and vortex diffusion in amorphous Mo_3Si films and $YBa_2Cu_3O_7$ single crystals'. *Phys. Rev. Lett.* **71**, 4043 (1993).

[113] P. Voss-de Haan, G. Jakob, and H. Adrian, 'High dynamic exponents in vortex glass transitions: Dependence of critical scaling on the electric-field range'. *Phys. Rev. B* **60**, 12443 (1999).

[114] P. Voss-de Haan, G. Jakob, and H. Adrian, 'Importance of the crossover-current density for a vortex-glass analysis'. *Physica C* **341**, 1387 (2000).

[115] M. Roulin, A. Junod, and E. Walker, 'Observation of second-order transitions below T_c in the specific heat of $YBa_2Cu_3O_x$: case for the melting of a vortex glass'. *Physica C* **296**, 137 (1998).

[116] C. Dekker, P. J. M. Wöltgens, R. H. Koch, B. W. Hussey, and A. Gupta, 'Absence of a finite-temperature vortex-glass phase transition in two-dimensional $YBa_2Cu_3O_{7-\delta}$ films'. *Phys. Rev. Lett.* **69**, 2717 (1992).

[117] H. H. Wen, H. A. Radovan, F. M. Kamm, P. Ziemann, S. L. Yan, L. Fang, and M. S. Si, '2D vortex-glass transition with $T_g = 0$ K in $Tl_2Ba_2CaCu_2O_8$ thin films due to high magnetic fields'. *Phys. Rev. Lett.* **80**, 3859 (1998).

[118] Z. Sefrioui, D. Arias, M. Varela, J. E. Villegas, M. A. López de la Torre, C. León, G. D. Loos, and J. Santamaria, 'Crossover from a three-dimensional to purely two-dimensional vortex-glass transition in deoxygenated $YBa_2Cu_3O_{7-\delta}$ thin films'. *Phys. Rev. B* **60**, 15423 (1999).

[119] L. Civale, A. D. Marwick, M. W. McElfresh, T. K. Worthington, A. P. Malozemoff, F. H. Holtzberg, J. R. Thompson, and M. A. Kirk, 'Defect independence of the irreversibility line in proton-irradiated Y-Ba-Cu-O crystals'. *Phys. Rev. Lett.* **65**, 1164 (1990).

[120] L. W. Lombardo, D. B. Mitzi, A. Kapitulnik, and A. Leone, 'Defect dependence of the irreversibility line in $Bi_2Sr_2CaCu_2O_8$ single crystals'. *Phys. Rev. B* **46**, 5615 (1992).

[121] M. Hawley, I. D. Raistrick, J. G. Beery, and R. J. Houlton, 'Growth mechanism of sputtered films of $YBa_2Cu_3O_7$ studied by scanning tunneling microscope'. *Science* **251**, 1587 (1991).

[122] D. G. Schlom, D. Anselmetti, J. G. Bednorz, R. F. Broom, A. Catana, T. Frey, C. Gerber, H.-J. Güntherodt, H. P. Lang, and J. Mannhart, 'Screw dislocation mediated growth of sputtered and laser-ablated $YBa_2Cu_3O_{7-\delta}$ films'. *Z. Phys. B* **86**, 163 (1992).

[123] J. Mannhart, D. Anselmetti, J. G. Bednorz, A. Catana, C. Gerber, K. A. Müller, and D. G. Schlom, 'Correlation between J_c and screw dislocation density in sputtered $YBa_2Cu_3O_{7-\delta}$ films'. *Z. Phys. B* **86**, 177 (1992).

[124] B. Roas, B. Hensel, H. S., S. Klaumünzer, B. Kabius, W. Watanabe, G. Saemann-Ischenko, L. Schultz, and K. Urban. *Europhys. Lett.* **11**, 669 (1990).

[125] L. Civale, A. D. Marwick, T. K. Worthington, M. A. Kirk, J. R. Thompson, L. Krusin-Elbaum, Y. Sun, J. R. Clem, and F. Holtzberg, 'Vortex confinement by columnar defects in $YBa_2Cu_3O_7$ crystals: Enhanced pinning at high fields and temperatures'. *Phys. Rev. Lett.* **67**, 648 (1991).

[126] V. Hardy, D. Groult, J. Provost, M. Hervieu, B. Raveau, and S. Bouffard, 'GeV-heavy ion irradiation effects in thallium-based superconducting copper oxides'. *Physica C* **178**, 255 (1991).

[127] L. Y. Vinnikov, L. A. Gurevich, G. A. Yemelchenko, and Y. A. Ossipyan, 'Direct observation of the lattice of Abrikosov vortices in high-T_c superconductor $YBa_2Cu_3O_x$ single crystals'. *Sol. Stat. Comm.* **67**, 421 (1988).

[128] G. J. Dolan, G. V. Chandrashekhar, T. R. Dinger, C. Feild, and F. Holtzberg, 'Vortex structure in $YBa_2Cu_3O_7$ and evidence for intrinsic pinning'. *Phys. Rev. Lett.* **62**, 827 (1989).

[129] G. Blatter, J. Rhyner, and V. M. Vinokur, 'Vortex pinning by twin boundaries in copper oxide superconductors'. *Phys. Rev. B* **43**, 7826 (1991).

[130] D. R. Nelson and V. M. Vinokur, 'Boson localization and pinning by correlated disorder in high-temperature superconductors'. *Phys. Rev. Lett.* **68**, 2398 (1992).

[131] D. R. Nelson and V. M. Vinokur, 'Boson localization and correlated pinning of superconducting vortex arrays'. *Phys. Rev. B* **48**, 13060 (1993).

[132] M. C. Marchetti and V. M. Vinokur, 'Low-temperature vortex dynamics in twinned superconductors'. *Phys. Rev. Lett.* **72**, 3409 (1994).

[133] M. Konczykowski, F. Rullier-Albenque, E. R. Yacoby, A. Shaulov, Y. Yeshurun, and P. Lejay, 'Effect of 5.3-GeV Pb-ion irradiation on irreversible magnetization in Y-Ba-Cu-O crystals'. *Phys. Rev. B* **44**, 7167 (1991).

[134] C. A. Durán, P. L. Gammel, R. Wolfe, V. J. Fratello, D. J. Bishop, J. P. Rice, and D. M. Ginsberg, 'Real-time imaging of the magnetic flux distribution in superconducting $YBa_2Cu_3O_{7-\delta}$'. *Nature* **357**, 474 (1992).

[135] M. C. Marchetti and V. M. Vinokur, 'Twin-boundary pinning of superconducting vortex arrays'. *Phys. Rev. B* **51**, 16 276 (1995).

[136] J. Lidmar and M. Wallin, 'Critical properties of Bose-glass superconductors'. *Europhys. Lett.* **47**, 494 (1999).

[137] D. R. Nelson and V. M. Vinokur, 'Bose glass scaling for superconducting vortex arrays revisited'. *Phys. Rev. B* **61**, 5917 (2000).

[138] T. Hwa, D. R. Nelson, and V. M. Vinokur, 'Flux-line pinning by competing disorders'. *Phys. Rev. B* **48**, 1167 (1993).

[139] L. Krusin-Elbaum, L. Civale, G. Blatter, A. Marwick, F. Holtzberg, and C. Feild, 'Bose-Glass melting in YBaCuO crystals with correlated disorder'. *Phys. Rev. Lett.* **72**, 1914 (1994).

[140] G. Nakielski, A. Rickertsen, T. Steinborn, J. Wiesner, G. Wirth, A. G. M. Jansen, and J. Kötzler, 'Enhancement of Bose-glass superconductivity in $YBa_2Cu_3O_{7-\delta}$ thin films'. *Phys. Rev. Lett.* **76**, 2567 (1996).

[141] J. C. Soret, L. Ammor, V. Ta Phuoc, R. De Sousa, A. Ruyter, A. Wahl, and G. Villard, 'Bose-glass behaviour in $Bi_2Sr_2Ca_{1-x}Y_xCu_2O_8$ crystals with columnar defects: Experimental evidence for variable-range hopping'. *Sol. Stat. Comm.* **109**, 461 (1999).

[142] T. Klein, A. Conde-Gallardo, I. Joumard, J. Marcus, C. J. van der Beek, and M. Konczykowski, 'Bose-glass melting in the cubic (k,ba)bio$_3$ high-ıt$_c$ oxide with columnar defects'. *Phys. Rev. B* **61**, 3830 (2000).

[143] M. Wallin and S. M. Girvin, '*I-V* characteristics of high-temperature superconductors with columnar defects'. *Phys. Rev. B* **47**, 14642 (1993).

[144] P. Sen, N. Trivedi, and D. M. Ceperley, 'Simulation of flux lines with columnar pins: Bose glass and entangled liquids'. *Phys. Rev. Lett.* **86**, 4092 (2001).

[145] S. A. Grigera, E. Morré, E. Osquilguil, C. Balseiro, G. Nieva, and F. de la Cruz, 'Bose-glass phase in twinned $YBa_2Cu_3O_{7-\delta}$'. *Phys. Rev. Lett.* **81**, 2348 (1998).

[146] A. W. Smith, H. M. Jaeger, T. F. Rosenbaum, A. M. Petrean, W. K. Kwok, and G. W. Crabtree, 'Vortex flow and transverse flux screening at the Bose glass transition'. *Phys. Rev. Lett.* **84**, 4974 (2000).

[147] A. W. Smith, H. M. Jaeger, T. F. Rosenbaum, W. K. Kwok, and G. W. Crabtree, 'Bose glass melting and the transverse Meissner effect in $YBa_2Cu_3O_{7-\delta}$ single crystals'. *Phys. Rev. B* **63**, 064514 (2001).

[148] B. I. Shklovskii and A. L. Efros, *Electronic Properties of Doped Semiconductors*, volume 45 of *Springer Series in Solid-State Sciences*, Springer, Berlin (1984).

[149] N. F. Mott, 'Conduction in non-crystalline materials III. Localized states in a pseudogap and near extremities of conduction and valence bands'. *Philos. Mag.* **19**, 835 (1969).

[150] J. R. Thompson, L. Krusin-Elbaum, L. Civale, G. Blatter, and C. Feild, 'Superfast vortex creep in $YBa_2Cu_3O_{7-\delta}$ crystals with columnar defects: Evidence for variable-range vortex hopping'. *Phys. Rev. Lett.* **78**, 3181 (1997).

[151] J. C. Soret, V. Ta Phuoc, L. Ammor, A. Ruyter, R. De Sousa, and E. Olive, 'Origin of the variable-range hopping in $Bi_2Sr_2Ca_{1-x}Y_xCu_2O_8$ with columnar defects'. *Phys. Rev. B* **61**, 9800 (2000).

[152] L. Ammor, R. De Sousa, J. C. Soret, V. Ta Phuoc, A. Ruyter, A. Wahl, and E. Olive, 'Vortex dynamics and phase diagram of BSCCO in the presence of columnar defects'. *J. Phys.: Condens. Matter* **12**, 4217 (2000).

[153] C. Dekker, W. Eidelloth, and R. H. Koch, 'Measurement of the exponent μ in the low-temperature phase of $YBa_2Cu_3O_{7-\delta}$ films in a magnetic field: Direct evidence for a vortex-glass phase'. *Phys. Rev. Lett.* **68**, 3347 (1992).

[154] D. A. W. Smith, 'Superconductive effects and weak localization in amorphous Ta/Ge superconductors: an exploration via magnetoresistance', Bachelor's thesis Lewis & Clark College, Portland, Oregon (2001).

[155] V. Hardy, M. Hervieu, J. Provost, C. Simon, and P. Lejay, 'Vortex pinning by a Gaussian splay of columnar defects in $YBa_2Cu_3O_7$'. *Phys. Rev. B* **62**, 691 (2000).

[156] A. Silhanek, L. Civale, S. Candia, G. Nieva, G. Pasquini, and H. Lanza, 'Evidence for vortex staircases in the whole angular range due to competing correlated pinning mechanisms'. *Phys. Rev. B* **59**, 13620 (1999).

[157] P. H. Kes and C. C. Tsuei, 'Two-dimensional collective flux pinning, defects, and structural relaxation in amorphous superconducting films'. *Phys. Rev. B* **28**, 5126 (1983).

[158] A. Engel, H. J. Trodahl, J. C. Abele, and S. M. Robinson, 'Flux pinning and phase diagrams in amorphous $Ta_{0.3}Ge_{0.7}$/Ge multilayers with coplanar defects'. *Phys. Rev. B* **63**, 184502 (2001).

[159] B. J. Ruck, J. C. Abele, H. J. Trodahl, S. A. Brown, and P. Lynam, 'Vortex dynamics and instabilities in layered and homogenous Ta/Ge superconductors'. *Phys. Rev. Lett.* **78**, 3378 (1997).

[160] L. Ammor, R. De Sousa, J. C. Soret, V. Ta Phouc, A. Ruyter, A. Wahl, and E. Olive, 'Universality of glass scaling in $Bi_2Sr_2Ca_{1-x}Y_xCu_2O_8$ single crystals in the presence of correlated disorder'. *Sol. Stat. Comm.* **113**, 633 (2000).

[161] J. Kötzler, M. Kaufmann, G. Nakielski, and R. Behr, 'Anisotropic dynamical scaling near the vortex-glass transition of twinned $YBa_2Cu_3O_{7-\delta}$'. *Phys. Rev. Lett.* **72**, 2081 (1994).

[162] J. Kötzler, G. Nakielski, M. Baumann, R. Behr, F. Goerke, and E. Brandt, 'Universality of frequency and field scaling of the conductivity measured by ac susceptibility of a $YBa_2Cu_3O_7$ film'. *Phys. Rev. B* **50**, 3384 (1994).

[163] K. Moloni, M. Friesen, S. Li, V. Souw, P. Metcalf, and M. McElfresh, 'Universality of glass scaling in a $YBa_2Cu_3O_{7-\delta}$ thin film'. *Phys. Rev. B* **56**, 14 784 (1997).

[164] Z. Q. Yu and W. J. Yeh, 'Scaling behavior and 3D-2D dimensional crossover in ceramic $Tl_2Ba_2Ca_2Cu_3O_{10-\delta}$ high-T_c superconductors'. *Physica C* **273**, 328 (1997).

[165] J. Roberts, B. Brown, B. Hermann, and J. Tate, 'Scaling of voltage-current characteristics of thin-film Y-Ba-Cu-O at low magnetic fields'. *Phys. Rev. B* **49**, 6890 (1994).

[166] J. Deak, M. McElfresh, J. R. Clem, Z. Hao, M. Konczykowski, R. Muenchausen, S. Foltyn, and R. Dye, 'Irreversibility line in $YBa_2Cu_3O_7$ thin

films: Correlation of transport and magnetic behavior'. *Phys. Rev. B* **49**, 6270 (1994).

[167] Q. Li, H. J. Wiesmann, M. Suenaga, and P. Motowidlow, L. nad Haldar, 'Observation of vortex-glass-to-liquid transition in the high-T_c superconductor $Bi_2Sr_2Ca_2Cu_3O_{10}$'. *Phys. Rev. B* **50**, 4256 (1994).

[168] M. Sato, T. Shibauchi, S. Ooi, T. Tamegai, and M. Konczykowski, 'Recoupling of decoupled vortex liquid by columnar defects in $Bi_2Sr_2CaCu_2O_{8+y}$'. *Phys. Rev. Lett.* **79**, 3759 (1997).

[169] M. Kosugi, Y. Matsuda, M. B. Gaifullin, L. N. Bulaevskii, N. Chikumoto, M. Konczykowski, J. Shimoyama, K. Kishio, K. Hirata, and K. Kumagai, 'Coupling transition of the vortex liquid in $Bi_2Sr_2CaCu_2O_{8+\delta}$ with columnar defects'. *Phys. Rev. Lett.* **79**, 3763 (1997).

[170] N. Morozov, M. P. Maley, L. N. Bulaevskii, V. Thorsmølle, A. E. Koshelev, A. Petrean, and W. K. Kwok, 'Structure of vortex liquid phase in irradiated $Bi_2Sr_2CaCu_2O_{8-\delta}$ crystals'. *Phys. Rev. Lett.* **82**, 1008 (1999).

[171] L. N. Bulaevskii, M. P. Maley, and V. M. Vinokur, 'Vortex phases in irradiated highly anisotropic layered superconductors'. *Phys. Rev. B* **57**, R5626 (1998).